Technische Universität München

Max-Planck-Institut für Astrophysik

Muon Creation and Effects in Supernovae

Dissertation von

Robert Günther Bollig

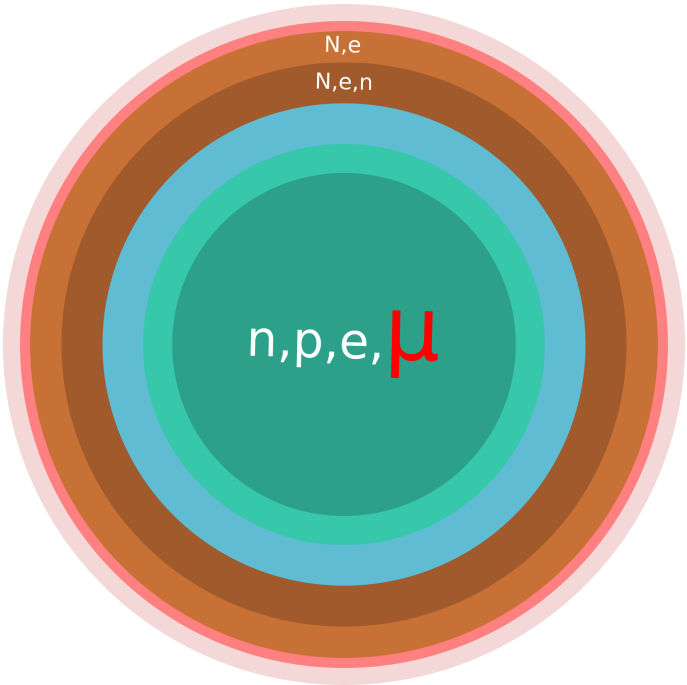

Technische Universität München

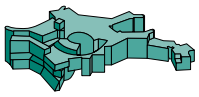

Max-Planck-Institut für Astrophysik

Muon Creation and Effects in Supernovae

Robert Günther Bollig

Vollständiger Abdruck der von der Fakultät für Physik der Technischen Universität München zur Erlangung des akademischen Grades eines

Doktors der Naturwissenschaften (Dr. rer. nat.)

genehmigten Dissertation.

Vorsitzender:		Prof. Dr. Lothar Oberauer
Prüfer der Dissertation:	1.	Prof. Dr. Hans-Thomas Janka
	2.	Prof. Dr. Björn Garbrecht
	3.	Prof. Dr. David Blaschke

Die Dissertation wurde am 15.03.2018 bei der Technischen Universität München eingereicht und durch die Fakultät für Physik am 17.09.2018 angenommen.

Contents

Chapter I
Introduction

Supernovae (SN) are the spectacularly bright events that accompany the violent deaths of stars. The name is derived from the Latin word "nova" for "new". It was coined to refer to the appearance of bright but transient events, which may seem like new stars spontaneously flashing up in the sky. In extension, a supernova is an exceedingly bright nova, often outshining their host galaxy for weeks or months. Supernovae, as we understand them today, are spawned by two very different mechanisms and origins.

Type Ia supernovae are thermonuclear explosions of degenerate white dwarfs that existed as old remnants of long-dead stars, "revived" by mass transfer from a companion star. The energy release is caused by the explosive fusion of the degenerate stellar material into iron that releases about 10^{51} erg (=1 bethe [B]) in total energy. Nearly all of this energy is contained in the expanding stellar gas in the form of internal and kinetic energy. Type 1a supernovae will, however, not be a part of this thesis since the effects we wish to investigate do not play a role in these events.

Core-collapse supernovae (CCSNe) occur when the central iron core that forms in massive stars during the last stage of their lives undergoes a gravitational collapse to a neutron star. The resulting shock wave propagates through the surrounding star and unbinds the stellar envelope. These events release up to a few 100 bethe in total energy, of which the major part is released in the form of neutrino radiation. In contrast to observable photons, which are released when the shock has passed the outer stellar layers and the stellar debris expands to transparency, neutrinos can escape the surrounding stellar shells on much shorter timescales as they are much more weakly interacting particles. In the case of the most famous recent supernova, SN 1987A, the visible signal of this event only reached Earth three hours after the first few neutrinos were detected. While the stellar medium around the neutron star is nearly transparent to neutrinos, the absorption of only a few percent of the energy carried by neutrinos can explain the observed canonical 1 B of kinetic energy contained in the expanding stellar gas.

The long-standing problem of CCSN theory is, to clarify the mechanism by which neutrinos can efficiently deposit such a large amount of energy despite their small interaction cross sections. In this thesis, we will try to shed light on some previously neglected components of the explosion mechanism that may prove beneficial to its success. The following introduction is mostly founded on the works of Refs. [5, 37, 15, 57, 103, 91], with a special emphasis on Ref. [91] in Sec. 1.1.3, and Ref. [103] in Sec. 1.2.

1.1 Core-collapse supernova paradigm

1.1.1 Road to collapse

The progenitors of core-collapse supernovae are massive stars, heavier than eight times our sun's mass ($M_\odot$), at the end of their lives. These stars have evolved through a sequence of burning stages in their struggle for an energy source that helps them maintain pressure support against their own tremendous gravitational attraction. The initial main-sequence phase of hydrogen core burning can last for millions of years. The initially inert helium fusion product concentrates in the center of the star and eventually becomes compact and hot enough to itself initiate fusion, replacing the energy source of central hydrogen core burning. The surrounding hydrogen then forms a burning shell around the new helium core. This cycle continues through carbon, neon, oxygen and silicon burning. Each of these successive burning stages produces less and less energy per reaction, requiring many more individual reactions to maintain similar power output, rapidly depleting the fuel supply. While the initial main-sequence phase may

have lasted millions of years, the duration of the last burning stage can be measured in days to hours.

Shortly before the collapse, the star has formed a nearly spherically symmetric concentric shell structure of active burning shells and an electron-degenerate hot iron core in the center. In contrast to a similarly degenerate white dwarf, thermal pressure provides additional support, raising the maximum sustainable core mass above the cold Chandrasekhar mass[①] of $M_{\mathrm{ch}} \propto 1.45727 M_{\odot} \cdot \left(2Y_{\mathrm{e}}\right)^2$. Eventually, the iron core becomes unstable to gravitational collapse due to electron capture onto iron group[②] nuclei and photodisintegration of iron group nuclei into alpha particles. The electron captures reduce the pressure support by degenerate electrons, as they are converted into electron neutrinos that immediately escape. As soon as the core density exceeds $\rho \sim 10^{12}\,\mathrm{g/cm^3}$, neutrino scattering on nuclei becomes frequent enough that the outward diffusion of neutrinos becomes slower than the infall of the collapsing core, and neutrinos begin to be advected with the fluid. This marks the onset of neutrino trapping and prevents further deleptonization of the inner core, i.e., the number of leptons per baryon $Y_{\ell} = Y_{\mathrm{e}} + Y_{\nu_{\mathrm{e}}}$ becomes effectively conserved inside the trapping radius.

The infall of the collapsing core is abruptly stopped when the nuclear saturation density of $\rho \sim 2.7 \cdot 10^{14}\,\mathrm{g/cm^3}$ is reached. At this point, all nuclei have dissolved, and repulsive strong forces between the free nucleons lead to a sudden stiffening of the equation of state. The remaining kinetic energy of the still infalling core slightly overcompresses the forming protoneutron star during the *bounce*. The rebounding neutron star then rams against the outer collapsing core and launches a shock wave. This shock wave, however, is quickly drained of energy as the infalling iron nuclei are disintegrated into free nucleons at the shock front, and initially trapped neutrinos begin to escape, leading the shock to stall after only a few milliseconds of propagation. The emission of a so-called ν_{e} breakout burst at the moment the shock reaches low-density, neutrino-transparent layers is a universal feature of CCSNe and signals the moment when the shock turns into an accretion shock, where the postshock matter is nearly hydrostatic[③] and allowed to settle onto the protoneutron star by neutrino emission. As the nascent neutron star, the protoneutron star (PNS), grows in mass and size, the neutrinos can escape from the lower-density material behind the shock, carrying away a part of the lepton number and liberated gravitational binding energy.

1.1.2 Neutrino-driven mechanism

The currently favored mechanism to revive the stalled shock is the neutrino-driven mechanism, first proposed in Refs. [22, 6]. This mechanism is based on estimates that a significant amount of the neutrino energy lost from the PNS can be reabsorbed in the matter between the PNS surface and the shock front. Even though neutrinos have an average mean free path on the order of hundreds of kilometers in the pre-shock stellar gas, the density and abundance of free nucleons in the post-shock gas allows a fraction of around 5%-10% of the ν_{e} and $\overline{\nu}_{\mathrm{e}}$ to deposit some or all of their energy, via scattering or absorption reactions, back into the gas. The most important neutrino interactions for this mechanism are the charged current beta-absorption processes on nucleons, $\nu_{\mathrm{e}} + \mathrm{n} \leftrightharpoons \mathrm{p} + \mathrm{e}^-$ and $\overline{\nu}_{\mathrm{e}} + \mathrm{p} \leftrightharpoons \mathrm{n} + \mathrm{e}^+$, which have the largest interaction opacity and can transfer all of the neutrino energy in a single interaction.

[①] Known as the maximum mass of an object purely supported against Newtonian gravity by the pressure of ultrarelativistic degenerate electrons .

[②] Iron group refers to elements from chromium to nickel.

[③] The gravitational force is perfectly balanced by the pressure gradient force.

The layer behind the shock and around the PNS surface, where accreted matter is settling on the higher-density inner core interior to the *neutrinosphere*[1] and cooled by neutrino emission, is called the *cooling layer*. The cooling layer has an energy loss rate that declines roughly proportional to the radius, scaling with $Q_{\rm E}^- \propto T^6 \propto r^{-6}$, whereas the rate of neutrino heating has an energy gain rate decreasing with $Q_{\rm E}^+ \propto r^{-2}$, cf. Ref. [57]. These radial distance dependencies imply a natural crossing point where heating just balances cooling, and exterior to which heating by neutrino absorption dominates. This point is called the *gain radius*; it demarcates the interior cooling layer from the exterior *gain layer*. The gain layer is the region where the majority of the neutrino heating takes place and extends up to the shock radius.

The neutrino energy deposition is given in terms of energy per second, implying that a mass element will receive more neutrino heating the longer it takes to pass through the gain layer. Ways to increase this so-called *dwell time* are, for example, to increase the effective path length via lateral turbulent motions and convective updrafts, which requires breaking the initial spherical symmetry of the progenitor. Another mechanism to aid in moving the shock outwards, increasing the gain layer volume, is by hydrodynamical instabilities like the *standing accretion shock instability* (SASI) (Ref. [8]). The SASI[2] is an advective-acoustic cycle of entropy and vorticity perturbations being advected towards the PNS surface, where they trigger aspherical pressure waves that rise back up towards the shock surface. These aspherical pressure waves in turn lead to oblique deformations of the shock front that cause larger transverse velocities in the postshock flow, thereby completing the feedback cycle (Refs. [36, 8]). This instability shows the fastest growth in the dipolar and quadrupolar modes, which take the form of a "sloshing" motion[3] along an axis or a spiral motion (Ref. [7]) around an axis.

1.1.3 Status of numerical simulations

The complexity of the radiation transport, the necessary range of length scales and the diversity of additional effects like magnetic fields, progenitor rotation, general relativity, and potentially dynamically relevant neutrino flavor oscillations, make the core-collapse supernova an incredibly challenging topic. Compounding on this complexity, the strong feedback between all components may obfuscate or suppress expected results, or enable unexpected results. Initially, simulations were only performed in spherical symmetry (1D), fitting the initial conditions provided by stellar evolution models. While adequate and efficient during phases where non-radial motions are small, for example during the initial iron core collapse or during the neutrino cooling evolution of the PNS left behind by the explosion, 1D alone cannot capture the dynamics between the shock front and the PNS surface in the critical phase of the stalled shock. The region between the PNS and shock can contain a gas moving at significant fractions of the sound speed in a turbulent and chaotic way. These non-radial motions and associated shock deformations are impossible in 1D, and the neutrino-driven mechanism is not successful except for particular low-mass progenitors with extreme density gradients between the central degenerate core and the outer layers (see e.g., Refs. [53, 84, 35, 88]).

The move to axisymmetric (2D) simulations has alleviated this constraint, allowing lateral motions but introducing a new artificial constraint in the form of the reflecting symmetry axis. The reflective boundary condition tends to channel lateral fluid flows hitting the boundary into channeled radial inflows or outflows. Correspondingly, the shock surface tends to be distorted into cigar or hourglass-like shapes around the axis with strong SASI sloshing modes

[1] The neutrinosphere is equivalent to the photosphere of a star, the radius where neutrinos on average interact a last time before they escape.

[2] See Ref. [37] for an experimental shallow water analogue of SASI (SWASI).

[3] Axisymmetric (2D) numerical simulations constrain the sloshing motion to the symmetry axis, while the sloshing and spiraling can happen in any direction in full 3D.

along the axis. Another shortcoming is the inverse energy cascade of turbulence in 2D that channels turbulent kinetic energy from small to large scales (Ref. [66]), opposite to the 3D case. The artificial effects of the symmetry axis and inverse energy cascade may have led to overly favorable conditions for explosions in 2D simulations compared to recent full 3D results (cf. Refs. [39, 40, 71, 83, 130]). Nonetheless, the move to 2D was a first necessary step in demonstrating the viability of the neutrino-driven mechanism, and the number of successful 2D explosion models is growing steadily, (e.g., Refs. [14, 12, 99, 127, 27, 105, 93, 90]).

1.2 Uncertainties in neutron star structure

Cold neutron stars and their nascent version, the protoneutron stars, are manifestations of the most extreme conditions in the universe not hidden behind an event horizon. Cold neutron stars can reach extremely high densities several times the saturation density, while hot protoneutron stars reach extremely high temperatures and densities a few[①] times the saturation density. NSs and PNSs also contain highly isospin asymmetric matter, i.e., a very high neutron to proton ratio, that is not stable at low densities. These conditions keep a detailed knowledge of the state of nuclear matter inside neutron stars still out of reach of experiments on Earth, as often only isolated aspects in isolated domains can be probed at once. The full range of density, temperature and isospin asymmetry can not be probed by experimental means, leaving only theoretical approaches for discussing the state of neutron star matter (cf. Ref. [49]).

1.2.1 Particle degrees of freedom

The equation of state (EOS) of matter above nuclear saturation density is highly uncertain, not only because of our incomplete knowledge of the forces between nucleons, but also with respect to its composition. It is useful here to introduce the concept of *particle degrees of freedom*. The basic degrees are the fundamental classical particles of neutrons, protons, electrons, and photons. These form the backbone of all EOS applicable to hot and dense matter; most available general-purpose EOS are limited to them. Additional particles added on top of this set tend to decrease the maximum pressure support a fluid can provide, as long as they do not themselves introduce a new stronger repulsive force. EOS containing additional particle degrees of freedom routinely come in conflict with the observational constraint of the heaviest currently measured pulsar PSRJ0348+0432 (Ref. [3]) being above $2.01M_\odot \pm 0.04M_\odot$.

In an ideal Fermi gas dominated by degeneracy pressure and at vanishing temperature, the more degrees of freedom introduced into a system, the lower the maximum pressure it can provide (e.g., Ref. [102]). Instead of paying the increasing energy penalty for compressing the degenerate matter even further, the system can instead prefer to convert fermion degeneracy energy of lighter particles into pure rest mass of alternative heavier particles. For example, the energy density of a gas composed of nonrelativistic degenerate light fermions scales according to $E_1 \propto n_1 \cdot \left(n_1^{2/3}/m_1 + m_1\right)$, whereas a nondegenerate gas composed of heavier fermions only scales with $E_2 \propto n_2 \cdot m_2$. This is valid as long as both particles remain nonrelativistic and $n_{1,2}$ and $m_{1,2}$ are their respective number densities and masses. There exists a natural crossing point, depending on the ratio between m_1 and m_2, after which the heavier particle is energetically favorable. For *baryonic degrees of freedom*, i.e., neutrons and protons, this point lies at several multiples of the saturation density, after which they could convert into their corresponding nondegenerate hyperon, i.e., their strange quark bearing equivalents. The simplified approach of an ideal gas is, however, not directly applicable to the hadronic[②] sector, as the strong force cannot be neglected and the exact nature of the governing many-body interactions in dense

[①] Few here means the densities can still reach multiples of saturation density but less than in fully cold neutron stars.

[②] Composite particles made up of quarks, interacting via the strong force. Grouped into baryons and mesons.

environments is even more poorly constrained for hyperons than for nucleons (cf. Ref. [101]). The appearance of hyperons and the associated softening of the EOS remains a conundrum to nuclear physicists, coined the "hyperon puzzle" (Ref. [76]), and is especially problematic for cold neutron stars. As we do not investigate hadronic degrees of freedom in this thesis, we leave the detailed discussion on this involved topic to the review paper of Ref. [103] and references therein.

1.2.2 Muons in neutron stars

A related process is an increase of the *leptonic degrees of freedom*. Degenerate electrons may then convert into heavier, nondegenerate muons. In contrast to the nucleon case, however, the electron chemical potential is already above the muon rest mass immediately after the birth of the neutron star, and the electron and muon gases behave like ideal Fermi gases. Increasing the leptonic degrees of freedom is accordingly not burdened by an uncertainty in the possible interactions between the particles.

A naive interpretation of muonization[①] would therefore expect the immediate conversion of a large proportion of degenerate electrons into nondegenerate muons. Looking at Fig. 1.1, this would result in the disappearance of the large electron chemical potential bump inside 10 km, until both electron and muon chemical potential have reached equilibrium, i.e., $\mu_\mathrm{e} = \mu_\mu$, probably close to the muon rest mass. This is equivalent to the system having reached neutrinoless *beta-equilibrium*, in which the net neutrino flavor number is assumed to be zero at all times. This is equivalent to the demand that neutrinos are not trapped and can effortlessly leave the PNS, which would result in the electron and muon chemical potentials being a strict function of the neutron and proton chemical potential difference, i.e., $\mu_\mathrm{e} = \mu_\mu = \mu_\mathrm{n} - \mu_\mathrm{p}$. The naive assumption of beta-equilibrium is however only applicable to the study of cold mature neutron stars that are transparent to neutrinos. This has allowed muons to be an accepted standard component of equations of state tailored to *cold* neutron stars.

The muonization of a PNS from birth becomes considerably more complicated when neutrinos are trapped and present in abundant numbers. The weak interactions, which e.g., produce muons and let electrons decay, conserve lepton flavor number, i.e., the net electron flavor number $L_\mathrm{e} = L_{\mathrm{e}^-} - L_{\mathrm{e}^+} + L_{\nu_\mathrm{e}} - L_{\overline{\nu}_\mathrm{e}}$ and net muon flavor number $L_\mu = L_{\mu^-} - L_{\mu^+} + L_{\nu_\mu} - L_{\overline{\nu}_\mu}$ cannot change by weak interactions alone. The evolution of the lepton numbers is now governed by separate conservation equations for the individual flavors, with diffusive fluxes of neutrinos as sourceterms, which need to be evolved forward in time. The diffusive losses are small in the domain of the PNS where neutrinos are trapped, and the system will quickly reach chemical equilibrium with the neutrinos. Chemical equilibrium means that the number densities of all involved particles are set by the relations $\mu_\mathrm{e} + \mu_\mathrm{p} = \mu_\mathrm{n} + \mu_{\nu_\mathrm{e}}$ and $\mu_\mu + \mu_\mathrm{p} = \mu_\mathrm{n} + \mu_{\nu_\mu}$, with $\mu_{\bar{\ell}} = -\mu_\ell\,(\ell \in [\mathrm{e}, \mu, \tau])$. The initial conditions of ν_e and ν_μ are vastly different however. ν_e and e^- are already highly degenerate (i.e., a large $L_\mathrm{e} = L_{\mathrm{e}^-} + L_{\nu_\mathrm{e}}$), whereas ν_μ and μ^- are initially not present (i.e., $L_\mu = 0$). This means the PNS will have to "de-electronize" by the diffusive loss of ν_e number, whereas it will muonize by the loss of $\overline{\nu}_\mu$ number.

The less dense outer domain of the PNS, where neutrino trapping generally does not hold, will quickly reach the aforementioned beta-equilibrium, and $\mu_\mathrm{e} = \mu_\mu$ holds to very good approximation. The muon production and muon decay rates may be out of equilibrium between the trapped and nontrapped domains of the PNS, and the muon number is a dynamically evolved quantity that depends sensitively on the microphysics governing the interactions between neutrinos and medium. The diffusion timescale of neutrinos, from the trapped domain to the nontrapped domain, sets the timescale for the complete de-electronization and muonization

[①] The production of an abundant net muon number in a NS.

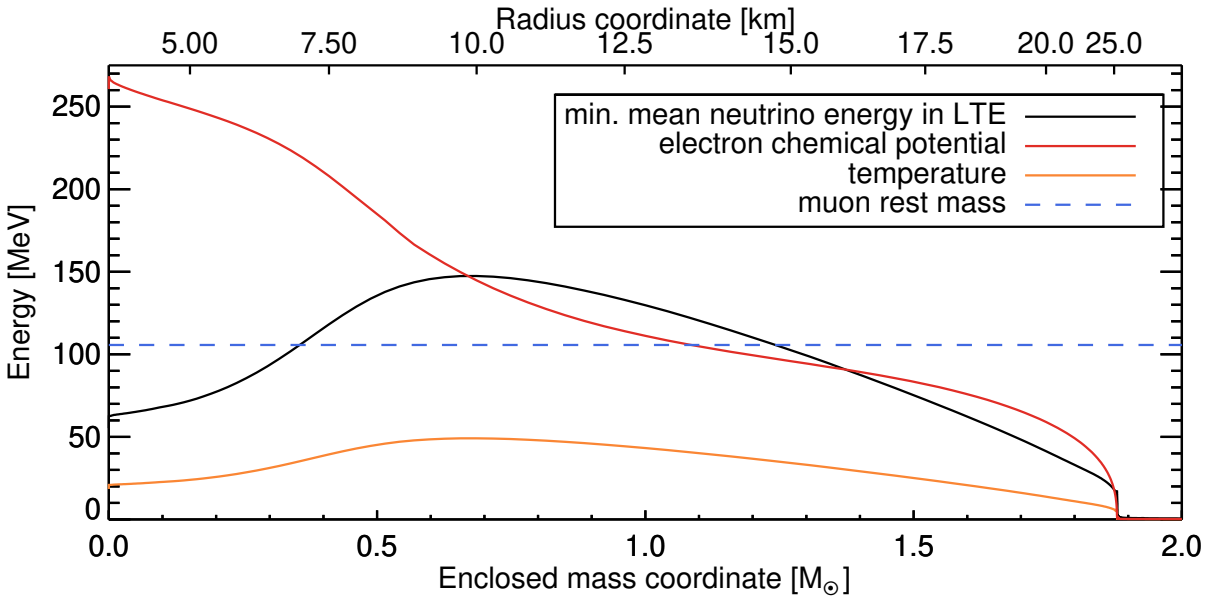

Figure 1.1: Typical conditions inside a protoneutron star 400 ms after bounce using the SFHo equation of state (Ref. [123]). The data is displayed as a function of the enclosed mass coordinate. An additional x-axis on top displays radius coordinates corresponding to the enclosed mass. The mean neutrino energy is given in terms of a Boltzmann gas in local thermodynamic equilibrium (LTE), being $\langle E \rangle_\nu^{\min} = 3T$, which sets the lower bound of the mean particle energy of a fermionic gas at arbitrary degeneracy.

of the PNS and is on the order of several seconds, but may vary depending on the accretion history of the PNS.

The evolution of the neutrino component is a crucial ingredient to the muonization of PNSs and is sensitively coupled to the evolution of density, temperature and lepton fractions of the PNS. The assumption of true beta-equilibrium is only rarely fulfilled and may only become applicable when the fate of the supernova has already long been decided. Investigating the implications of a muonic component in the EOS, from neutrino-rich conditions at birth of the PNS to full beta-equilibrium in the cold NS, therefore adds another degree of freedom that requires careful implementation into the neutrino sector. In this thesis, we have implemented the first fully self-consistent first-principles description of muons at arbitrary chemical potential as well as a fully consistent treatment of all six neutrino flavors with full coupling to electrons and muons.

1.3 Possible effects of muons in core-collapse supernovae

The common expectation among most researchers in the core-collapse supernova field was that, while muons may be present in cold neutron stars and slightly affect their cooling evolution (see e.g., Refs. [124, 2, 4]), they would be dynamically irrelevant in the first few seconds of a supernova or during black hole formation. This assumption was, however, formed at a time when the favored equations of state where still overly incompressible compared to recent developments. Current experimental bounds on the compressibility of nuclear matter favor relatively compact and dense neutron stars that may develop a high temperature already early after PNS formation, as shown in Fig. 1.1. The mean thermal energy of neutrinos can become larger than the muon rest mass after 100–200 ms, depending on the compactness[①] of the progenitor (cf. Ref. [100]). The combined conditions of high neutrino energy and high

[①] A high compactness at bounce implies large accretion rates.

electron chemical potential allow muons to be produced not only in the dense inner core, where the electron degeneracy is largest, but also in the extended hot mantle between $10^{12}\,\mathrm{g/cm^3} < \rho < 10^{14}\,\mathrm{g/cm^3}$. Here, muons may lead to a significant softening of the EOS, as the strong nuclear force effects are not yet dominant, and thermal and degeneracy pressure of nucleons and electrons determines the compression behavior. Muons may affect both of these pressure components, as the creation of muons taps both thermal energy and degeneracy energy and converts them into inert muon rest mass. This may happen by the combination of direct absorption processes, e.g., $\nu_\mu + \mathrm{n} \leftrightharpoons \mathrm{p} + \mu^-$; electron conversion processes, e.g., $\nu_\mu + \mathrm{e}^- \leftrightharpoons \nu_\mathrm{e} + \mu^-$; or thermal pair production, e.g., $\gamma + \gamma \leftrightharpoons \mu^- + \mu^+$. The result can be a faster contraction of the PNS mantle and a more compact PNS, as it can loose pressure support not only by neutrino emission but also by muon creation. Depending on the progenitor structure, muon creation could even be a more efficient channel of "pressure-loss" than neutrinos radiating away lepton number and thermal energy.

More compact PNS are found to be beneficial for the neutrino-driven mechanism, as both the neutrino luminosity as well as the mean neutrino energy are increased because of higher neutrinosphere temperatures (cf. Ref. [79]). More compressible EOS, however, may come into conflict with the lower bound of the TOV limit[①] being $2.01 M_\odot \pm 0.04 M_\odot$ (Ref. [3]), as modifying the strength of the strong interaction has a direct consequence on the stability of cold neutron stars. By introducing another leptonic degree of freedom that is most relevant in the early hot protoneutron star phase and smaller in cold neutron stars, muons can have an important effect during the phase most crucial to shock-revival, but do not reduce the TOV limit of cold NS significantly. Other possible scenarios involving hot compact objects, such as NS – NS mergers and PNS $\rightarrow$ BH collapse events might also be strongly modified since the metastability of these compact objects is aided by thermal pressure support. Muons might then sensitively affect the collapse timescale of hypermassive NS – NS merger remnants and metastable PNSs, by the aforementioned mechanisms. The influence of muons could therefore affect the neutrino and gravitational wave signals that can be detected from such events, as proven to be possible by the recent first measurement of gravitational waves from the NS – NS merger event GW170817 (Ref. [1]).

Muons may not only increase the luminosity and mean energy of all neutrinos but also imprint characteristic spectral differences on the emitted neutrinos, as both electron-flavor and μ-flavor neutrinos now also interact with the charged muons in the medium via weak interactions. μ-flavor neutrinos will experience the largest change as the ability to participate in charged current beta-reactions greatly change their diffusion properties. This not only has consequences for the neutrino-driven mechanism but may also affect for the detectability of these neutrinos on Earth in future galactic supernovae. Neutrinos, due to their finite mass, may undergo flavor oscillations that mix the different neutrino flavors. The possible relevance of muons for neutrino oscillations, however, requires a more complete understanding of the behavior of neutrino-flavor oscillations in the presence of dense neutrino background fields as present in and around protoneutron stars (see e.g., Ref. [88] for an overview). Since we do not treat neutrino oscillations in this thesis, we leave such an analysis to future work.

1.4 Outline of this thesis

Muons have up to now only been approximately integrated into evolution codes for neutron star cooling simulations that operate on the timescale of millions of years (e.g., Ref. [4]). The treatment of muons in the CCSN context has up to now been very limited, with at most some excursions into static modified equations of state with a muon beta-equilibrium contribution

[①] Tolman–Oppenheimer–Volkoff mass limit for the stability of cold, nonrotating neutron stars in general relativity.

(e.g., Refs. [109, 101]). We wish to alleviate this shortcoming and perform the first fully self-consistent and dynamic simulations of muon number formation in protoneutron stars; from the moment of birth to the transition to a warm[①] neutron star, including a full coupling between charged leptons and neutrinos of all flavors.

To achieve this goal, we first need to establish the basic framework of the thermodynamics of a muon gas, analogously to the standard electron gas component, in Chapter II. We can easily extend any publicly available general-purpose high-density equation of state for protoneutron stars with this noninteracting Fermi gas component.

The radiation-hydrodynamics simulation code PROMETHEUS-VERTEX, in which we will implement our changes, is introduced in Chapter III. The possible creation of net muon number is mediated by the interaction between neutrinos and the matter particles, which requires the calculation of both canonical production processes common to electron neutrinos and of the new production processes associated with the presence of muons. The theoretical framework for these processes is introduced in Chapter IV, mostly based on the work of Ref. [75]. As these processes require complex calculations for hundreds of thousands of discrete time evolution steps, they must be implemented as efficiently as possible, which is described in Chapter V. Additionally, the specifics of the flavor coupling needed for the implementation into the neutrino transport solver is discussed and relevant cross sections are presented.

Having established and implemented the necessary physical processes into our transport code, we will numerically simulate the classical core-collapse supernova scenario in spherical symmetry (1D) and axisymmetry (2D) in Chapter VI. To present a reference case for a standard scenario to the CCSN community, a 1D simulation of the accretion phase of a frequently used stellar progenitor is performed and further continued into the Kelvin-Helmholtz phase[②] in Sec. 11, after an artificial explosion trigger is applied. These 1D simulations will facilitate comparison and verification of the new muon physics in our models and their influence on the protoneutron star evolution. To evaluate a possible effect of the early onset of muonization on the self-consistent development of a supernova explosion, axisymmetric 2D simulations are performed in Sec. 12 for two different high-density equations of state to avoid a possible bias by specific high-density properties of a single selected EOS. As black hole formation might be especially sensitive to additional degrees of freedom in the equation of state as seen in previous simulations (cf. Refs. [56, 101, 107]), we investigate the consequences of abundant muon production on the collapse timescale of thermally stabilized metastable protoneutron stars.

The results of these studies provide a comprehensive assessment of the macroscopic influence of the early onset muonization on the protoneutron star and refute the default assumption of muons being irrelevant for the neutrino-driven explosion mechanism of CCSNe.

[①] Our simulations terminate when neutrino cooling becomes too inefficient to continue. These neutron stars still have temperatures of $T \sim 3\,\mathrm{MeV}$, but the neutron star structures are already close to their cold configuration.

[②] The cooling of the hot PNS by emission of energy and lepton number after a successful explosion.

Chapter II
Muonic equation of state

In this chapter, we will establish the underlying theoretical framework needed to calculate any noninteracting quantum statistical ideal gas, and demonstrate its application to an ideal gas of arbitrarily relativistic electrons and muons at an arbitrary state of degeneracy. The necessary calculations are based on the work of Refs. [59, 132], with which we calculate the tabulated leptonic quantities needed for the implementation into any general-purpose high-density equation of state. Furthermore, the high-density equations of state used in this thesis and their modifications are introduced, and the viability of these modified EOS in the CCSN context with respect to observational constraints is discussed.

2 Fundamentals

Charged lepton	Mass [MeV]	Neutrino
electron (e^-)	0.511	ν_e
positron (e^+)		$\overline{\nu}_e$
muon (μ^-)	105.66	ν_μ
antimuon (μ^+)		$\overline{\nu}_\mu$
tauon (τ^-)	1776.82	ν_τ
antitauon (τ^+)		$\overline{\nu}_\tau$

Table 2.1: Lepton species and masses (Ref. [89]).

The equation of state (EOS) for any noninteracting particle obeying Fermi-Dirac statistics can be fully described by various forms of Fermi-Dirac integrals over the particle phase-space volume

$$n_{\mathrm{FD}} \propto \int_0^\infty \frac{\mathrm{d}^3\vec{p}}{\exp\left(\left(E-\mu\right)/T\right)+1}\,, \tag{2.1}$$

which depending on the definition of the energy E can be used to calculate strictly nonrelativistic (NR), arbitrarily relativistic (AR) or ultrarelativistic (UR) particles. The general energy dispersion relation for an arbitrarily relativistic gas is the well-known

$$E_{\mathrm{AR}} = \sqrt{p^2+m^2}\,, \tag{2.2}$$

which is valid for all conditions but can complicate some calculations due to the appearance of the square root. For this reason, often the two limiting cases of an ultrarelativistic gas or a strictly nonrelativistic gas are used. If one, for example, wants to calculate the EOS of neutrinos then the small neutrino rest mass can be safely ignored, and

$$E_{\mathrm{UR}} = \sqrt{p^2+m_\nu^2} \xrightarrow[p\gg m]{} p \tag{2.3}$$

gives the correct energy dispersion relation. For more massive fermionic particles like nucleons or hyperons, the large rest mass dominates the relativistic energy, and the momentum of the

particle is only a small correction on top. This gives the classical nonrelativistic picture of the energy dispersion relation that can be derived from the relativistic energy spectrum by a simple series expansion around $p = 0$, resulting in

$$E_{\mathrm{NR}} = \sqrt{p^2 + m^2} \xrightarrow[p \ll m]{} \frac{p^2}{2m} + m\,. \tag{2.4}$$

The nonrelativistic picture is the method of choice for the baryonic matter at low-temperatures and sub-nuclear saturation density prevailing in pre-collapse stellar structure and can, with acceptable results, still be used above nuclear saturation density. A popular nonrelativistic EOS, for example, is the Lattimer&Swesty equation of state of Ref. [70]. In contrast to neutrinos and nucleons, the charged lepton energy dispersion relation cannot be assumed to be either strictly ultrarelativistic or nonrelativistic. Electrons, being the lowest mass charged lepton, can relatively safely be considered to be ultrarelativistic inside protoneutron stars. Outside the protoneutron star they can, however, become arbitrarily relativistic, and even nonrelativistic farther from the stellar core. Muons, being roughly 200 times heavier than electrons, never become ultrarelativistic, but are mildly relativistic inside the protoneutron star and nonrelativistic outside the protoneutron star. Tauons, being the most massive lepton at nearly twice the nucleon rest mass, can safely be assumed to be nonrelativistic everywhere inside a neutron star. Their high rest mass itself strongly suppresses their thermal production, and even in highly degenerate conditions the chemical potential of any particle never becomes large enough to trigger any abundant production. Tauons are accordingly neglected in all previous works including this one and, barring possible extreme conditions such as transient phases at the moment of collapse to a black hole, are unlikely to be present.

As we are in this work specifically interested in the equation of state of muons, we will employ the arbitrarily relativistic formulation of the Fermi gas in thermal and chemical equilibrium with the surrounding matter. This approach is valid since all possible electromagnetic muon reactions are sufficiently fast, and the muon spectrum can be defined by a single common chemical potential and temperature.

3 Ideal Fermi gas EOS of leptons

The calculation of an electron EOS at various degrees of degeneracy and relativity is a common problem for all so-called general-purpose stellar equations of state and many authors have explored multiple methods to formulate the Fermi-Dirac integrals in their most convenient form. For a small overview, we refer to Ref. [132] and references therein. The formulation we use in the calculation of our leptonic EOS allows for simple variation of the lepton rest mass and degeneracy.

The formula to calculate the number density of a fermion is given by the phase-space volume integral of the Fermi-Dirac function

$$n_\ell = \frac{g}{(hc)^3} \int_0^\infty \frac{\mathrm{d}^3\vec{p}}{\exp\left(E/T - \eta\right) + 1}\,, \tag{3.1}$$

where $\eta = \frac{\mu}{T}$ is the dimensionless degeneracy parameter, and g is the spin degeneracy of the fermion. The charged leptons have a spin degeneracy of $g = 2$, as a spin-up and a spin-down lepton can populate each phase-space volume. In contrast, neutrinos due to their chirality, i.e., left-handed neutrinos and right-handed antineutrinos, only have a spin degeneracy of $g = 1$, as only either a neutrino or an antineutrino can exclusively populate each phase-space volume.

The phase-space volume integral $\int \mathrm{d}^3\vec{p}$ can be expressed by $\int \mathrm{d}^3\vec{p} = 4\pi \int \mathrm{d}p\, p^2$, and the final form of the number density is

$$n_\ell = \frac{8\pi}{(hc)^3} \int_0^\infty \mathrm{d}p \, \frac{p^2}{\exp\left(E/T - \eta\right) + 1} \,. \tag{3.2}$$

While this form could already be directly numerically integrated, it is helpful to rewrite the formula in terms of the generalized Fermi-Dirac integrals, using following substitutions:

$$p = \sqrt{E^2 - m^2} \rightsquigarrow \mathrm{d}p = \frac{E}{\sqrt{E^2 - m^2}} \mathrm{d}E \,, \tag{3.3}$$

$$n_\ell = \frac{8\pi}{(hc)^3} \int_{m_\ell}^\infty \mathrm{d}E \, \frac{E\,\sqrt{E^2 - m^2}}{\exp\left(E/T - \eta\right) + 1} \,. \tag{3.4}$$

The rest mass appearing in the lower limit of the integral can further be removed by the substitution

$$x = \frac{E}{T} + \beta_\ell \rightsquigarrow E = Tx + m_\ell \rightsquigarrow \mathrm{d}E = T\mathrm{d}x \,, \tag{3.5}$$

leading to

$$n_\ell = \frac{8\pi}{(hc)^3} T^3 \int_0^\infty \mathrm{d}x \, \frac{\left(x + \beta_\ell\right)\,\sqrt{x\left(x + 2\beta_\ell\right)}}{\exp\left(x + \beta_\ell - \eta\right) + 1} \,. \tag{3.6}$$

By introducing the "kinetic" degeneracy parameter

$$\zeta_{\ell^\mp} = \eta_{\ell^\mp} - \beta_\ell \,, \tag{3.7}$$

we arrive at the final form of the number density of

$$n_{\ell^-} = \frac{8\pi}{(hc)^3} T^3 \int_0^\infty \mathrm{d}x \, \frac{\left(x + \beta_\ell\right)\,\sqrt{x\left(x + 2\beta_\ell\right)}}{\exp\left(x - \zeta_{\ell^-}\right) + 1} \,, \tag{3.8}$$

for the negatively charged lepton, and

$$n_{\ell^+} = \frac{8\pi}{(hc)^3} T^3 \int_0^\infty \mathrm{d}x \, \frac{\left(x + \beta_\ell\right)\,\sqrt{x\left(x + 2\beta_\ell\right)}}{\exp\left(x - \zeta_{\ell^+}\right) + 1} \,, \tag{3.9}$$

for the positively charged antilepton, where the parameter

$$\zeta_{\ell^+} = -\zeta_{\ell^-} - 2m_\ell = -\eta_{\ell^-} - m_\ell \,,$$

is the corresponding kinetic degeneracy of the antiparticle.

The parameter

$$\beta_\ell = \frac{m_\ell}{T} \,, \tag{3.10}$$

can be interpreted as a measure of the relevance of relativistic effects, where $\beta \gg 1$ implies the nonrelativistic regime. The dimensionless parameter

$$\zeta_{\ell^{\mp}} = \pm\frac{\mu_{\ell^-}}{T} - \beta_\ell \,, \tag{3.11}$$

can be interpreted as a measure for the degeneracy of the particle, where $\zeta \gg 1$ implies the degenerate regime.

The total density of leptons and antileptons, necessary to later account for the rest mass contained in the gas, is given by

$$n^{\text{tot}} = n_{\ell^-} + n_{\ell^+} \,. \tag{3.12}$$

The net number of leptons, given by

$$n^{\text{net}} = n_{\ell^-} - n_{\ell^+} \,, \tag{3.13}$$

is an important quantity in charge-neutral stars, where the positive charge of free or bound protons is perfectly balanced by the net negative charge. The net number of a gas is fully determined by the chemical potential, as a vanishing chemical potential implies that only perfect pairs of leptons and antileptons exist. One has to invert the lepton net number density numerically to determine any nonzero chemical potential fulfilling the charge-neutrality constraint. Typically, one uses bisection- and Newton-Raphson iterations to find the fitting chemical potential. Once it has been found, all further thermodynamic properties can be derived from it.

The internal energy density of the gas is simply the number density times the internal energy of each particle:

$$e^{\text{int}}_{\ell^-} = \frac{8\pi}{(hc)^3} T^4 \int_0^\infty \mathrm{d}x \, \frac{x(x+\beta_\ell)\,\sqrt{x\left(x+2\beta_\ell\right)}}{\exp\left(x-\zeta_{\ell^-}\right)+1} \,, \tag{3.14}$$

$$e^{\text{int}}_{\ell^+} = \frac{8\pi}{(hc)^3} T^4 \int_0^\infty \mathrm{d}x \, \frac{x(x+\beta_\ell)\,\sqrt{x\left(x+2\beta_\ell\right)}}{\exp\left(x-\zeta_{\ell^+}\right)+1} \,. \tag{3.15}$$

Note that this internal energy density does not yet contain the lepton rest mass and still needs to be corrected for the mass of thermally produced lepton pairs that are an intrinsic component of the gas.

As all antileptons of a positive net number density gas are created by the thermal component of the gas, the total number density of paired up leptons is simply twice the antilepton density,

$$\mathrm{e}^{\text{tot,pairs}} = e^{\text{int}}_{\ell^-} + e^{\text{int}}_{\ell^+} + 2m_\ell n_{\ell^+} \,. \tag{3.16}$$

The kinetic pressure of the gas is the relativistic velocity $v(p) = p/E$ of the gas times the momentum times the number density

$$P = \frac{8\pi}{3\,(hc)^3} \int_0^\infty \mathrm{d}p \, \frac{v(p)\cdot p\cdot p^2}{\exp\left(E/T-\eta\right)+1} = \frac{8\pi}{3\,(hc)^3} \int_0^\infty \mathrm{d}p \, \frac{p^4/E}{\exp\left(E/T-\eta\right)+1} \,, \tag{3.17}$$

where a factor of 1/3 is introduced to account for the isotropy of the gas. After applying the substitutions of Eqs. (3.3 – 3.7), we arrive at the final form of the Fermi pressure for leptons and antileptons:

$$P_{\ell^-} = \frac{8\pi}{3\,(hc)^3} T^4 \int_0^\infty \mathrm{d}x\, \frac{\sqrt{x\,(x+2\beta_\ell)}^3}{\exp\left(x-\zeta_{\ell^-}\right)+1}\,, \tag{3.18}$$

$$P_{\ell^+} = \frac{8\pi}{3\,(hc)^3} T^4 \int_0^\infty \mathrm{d}x\, \frac{\sqrt{x\,(x+2\beta_\ell)}^3}{\exp\left(x-\zeta_{\ell^+}\right)+1}\,. \tag{3.19}$$

The entropy of the gas can be determined using the thermodynamic potentials to be:

$$s_{\ell^-} = \left(e^{\text{int}}_{\ell^-} + P_{\ell^-}\right)/T - n_{\ell^-}\xi_{\ell^-}\,, \tag{3.20}$$

$$s_{\ell^+} = \left(e^{\text{int}}_{\ell^+} + P_{\ell^+}\right)/T - n_{\ell^+}\xi_{\ell^+}\,. \tag{3.21}$$

The final thermodynamic values of the equation of state are then simply the sum over all leptons and antileptons:

$$e^{\text{tot}} = e^{\text{int}}_{\ell^-} + e^{\text{int}}_{\ell^+} + m_\ell n^{\text{tot}} = e^{\text{tot,pairs}} + m_\ell n^{\text{net}}\,, \tag{3.22}$$

$$P^{\text{tot}} = P_{\ell^-} + P_{\ell^+}\,, \tag{3.23}$$

$$s^{\text{tot}} = s_{\ell^-} + s_{\ell^+}\,. \tag{3.24}$$

3.1 Regimes of the EOS

Depending on the lepton mass, temperature and density of leptons one can separate the equation of state into five separate regimes.

1. The nondegenerate, nonrelativistic regime at low densities and low temperatures
2. The nondegenerate, ultrarelativistic regime at low densities and high temperatures
3. The degenerate, nonrelativistic regime at high densities and generally low temperatures
4. The degenerate, ultrarelativistic regime at high densities and generally high temperatures
5. The intermediate regime where none of the above apply

Note that a degenerate gas can become ultrarelativistic even at low temperatures if the internal energy at the Fermi-surface is sufficiently larger than the lepton rest mass. The electron and muon EOS features all of these regimes, but the substantial difference in rest mass between both leptons will lead to significant shifts of the regime locations. A large rest mass, e.g., baryons and nuclei, will typically lead to the nonrelativistic regime being accurate in most conditions encountered in core-collapse supernovae. On the other hand, a vanishing rest mass, e.g., neutrinos and photons, will lead to these particles being ultrarelativistic in all conditions. For protoneutron star conditions, the ultrarelativistic regime with varying degrees of degeneracy is typically fulfilled for electrons. Muons, due to their 200 times larger rest mass, are however mostly either nonrelativistic or at most intermediate relativistic at no or intermediate degeneracy. In Fig. 3.1, we compare the above given regime locations for electrons, outlined in continuous lines, and for muons, outlined in dashed lines. We can immediately see that the regimes are qualitatively similar but shifted to higher densities and temperatures for the muon gas, and none of the approximations apply to typical hot neutron star conditions. This problem has further consequences for the treatment of the muon gas in the opacity calculations that will be discussed further in Chapter IV.

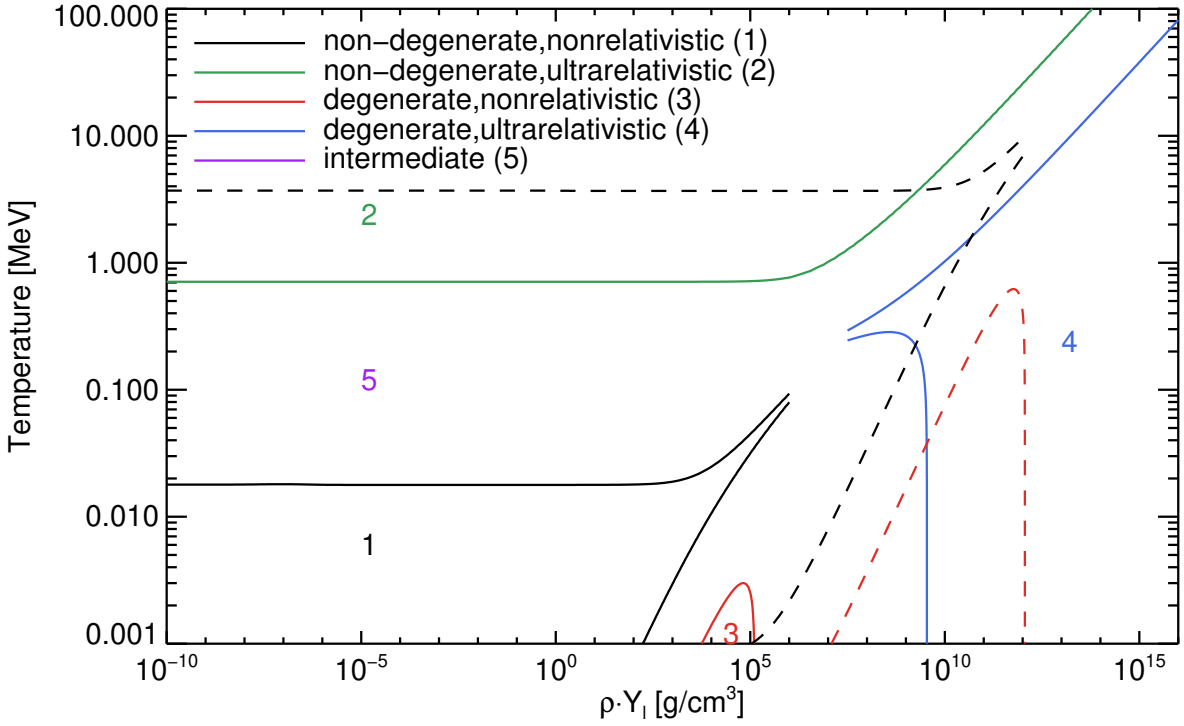

Figure 3.1: Regimes of the leptonic equation of state for electrons (solid) and muons (dashed). The regimes of the electron gas are labeled by the numbers.

The extended region of validity of the nondegenerate nonrelativistic approximation of the muon gas, however, allows us to efficiently and accurately extend the muon EOS down to lower temperatures and densities than tabulated using the analytic formulae for pressure, energy density, and entropy of a Boltzmann gas. Additionally, the chemical potential of muons can be inverted directly from the net number density, as we are still well below pair formation temperatures. This property is helpful to accurately track the decay of any present muon number, which requires an accurate chemical potential down to vanishing densities.

3.2 Thermodynamic quantities

The energy, pressure, and entropy per baryon of the muon equation of state are compared in the following figures to the corresponding quantities of the electron EOS. Note that the energy does not contain the net lepton rest mass contribution and is, therefore, the quantity $e^{\text{tot,pairs}}$ [MeV/by].

The energy per baryon in Fig. 3.2 shows the onset of pair gas formation by the sudden increase in line density, as the energy contained in the gas becomes uncoupled from any net lepton number. At nearly vanishing net electron density the pair gas already starts forming at 0.015 MeV, whereas the muon gas requires at least 2 MeV. These are 3% and 2% of the respective lepton rest mass, showing that the thermal tail already contains sufficient energy for abundant pair production. As the thermal pair number is only significant at large temperature and very small chemical potential, the energy per baryon will naturally decrease as the matter density grows. At high density, the energy contained in the net muon gas becomes larger than in the muon pair gas, as the rising chemical potential suppresses pair formation.

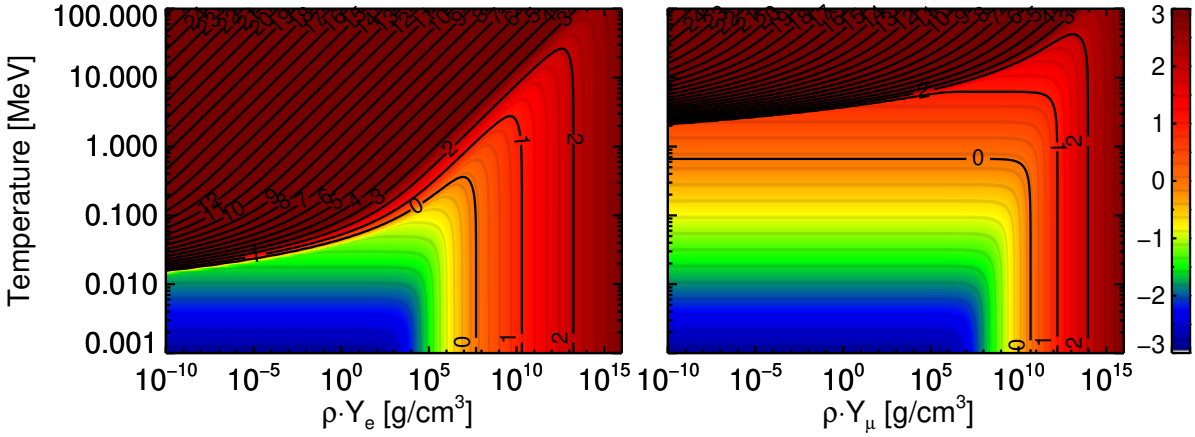

Figure 3.2: Logarithmic energy per baryon including pair rest masses $e^{\text{tot,pairs}}/n_{\text{B}}$. The electron energy is on the left side; the muon energy is on the right side.

The pressure will naturally follow the energy as they are linked by a relation of $P = \frac{1}{3}e^{\text{int}}$ for relativistic particles and $P = \frac{2}{3}e^{\text{int}}$ for nonrelativistic particles. There are only some slight differences as the pressure is a function of the pure internal energy without the pair rest masses, as seen in Fig. 3.3.

The entropy per baryon in Fig. 3.4 links the energy and pressure to the chemical potential. As a degenerate Fermi-Dirac gas is a highly ordered system and all energy levels are filled up to the Fermi-energy, the entropy will naturally decrease at high densities and low temperatures. The slope change of the isentropes, which happens at higher temperatures and densities in the muon gas, indicates the transition of a nonrelativistic to an ultrarelativistic gas as expected.

The chemical potential of the Fermi-Dirac gases approaches zero when the thermal lepton pairs (produced by photons with zero-chemical potential or by leptons with a summed chemical potential of zero) become abundant. As the chemical potential in Eq. 3.6 and $\mu_{\bar{\ell}} = -\mu_{\ell}$ determines the number densities at identical temperatures, equal number densities automatically imply that the only possible chemical potential to fulfill this is $\mu_{\ell} = 0$. The chemical potentials depicted in Fig. 3.5 are plotted as the relativistic chemical potential for electrons including rest mass and the nonrelativistic (kinetic) chemical potential for muons. Motivation for this is the large muon rest mass introducing a constant offset that would otherwise make the transition to a degenerate gas less visible. In the electron case, the transition begins at $\rho Y_{\text{e}} \sim 10^7$ g/cm^3,

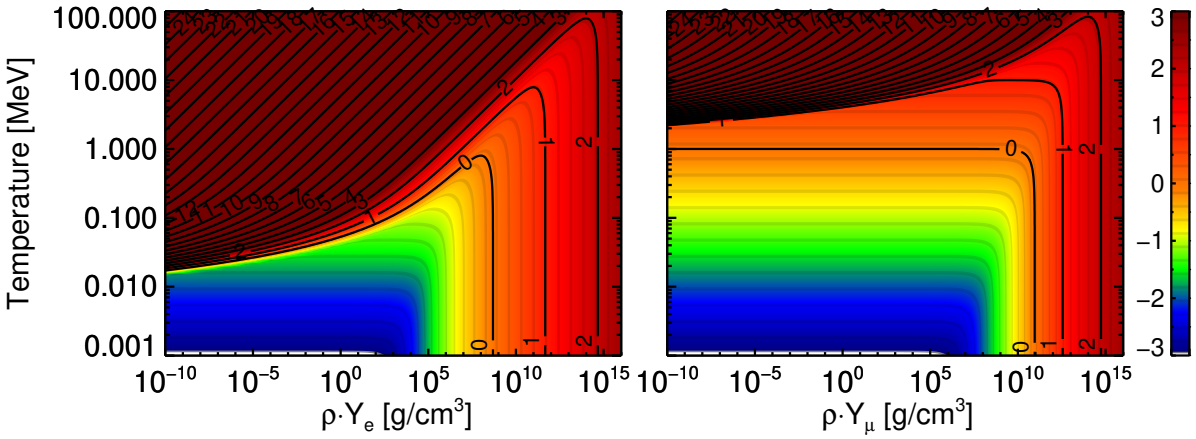

Figure 3.3: Logarithmic pressure per baryon $P^{\mathrm{tot}}/n_{\mathrm{B}}$. The electron pressure is on the left side; the muon pressure is on the right side.

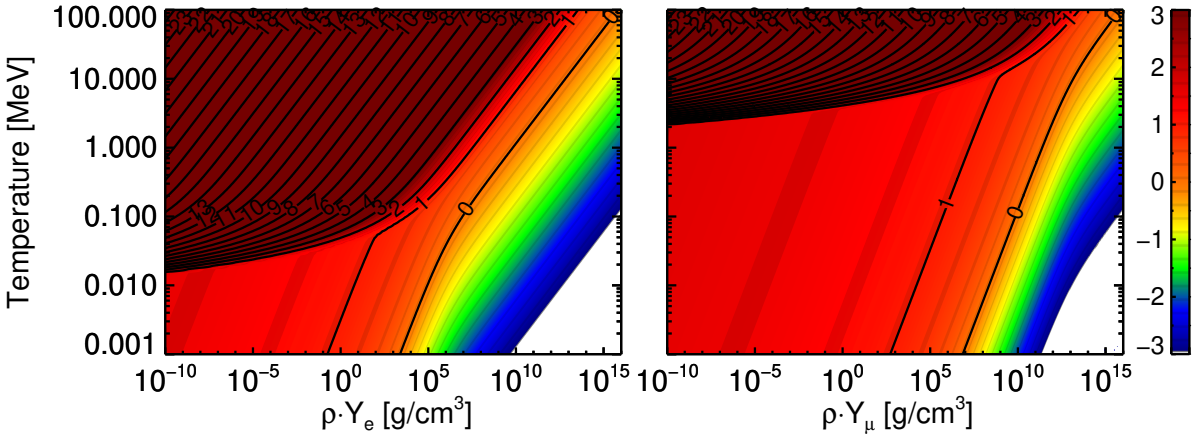

Figure 3.4: Logarithmic entropy per baryon $s^{\mathrm{tot}}/n_{\mathrm{B}}$. The electron entropy is on the left side; the muon entropy is on the right side.

equivalent to a net electron number density of $n_{\mathrm{e}} = \rho Y_{\mathrm{e}}/m_{\mathrm{B}} \sim 6 \times 10^{30}\,1/\mathrm{cm}^3$. The muons only transition to the degenerate regime later at $\rho Y_\mu \sim 10^{11}\,\mathrm{g/cm}^3$, equivalent to a muon density of $n_\mu \sim 6 \times 10^{34}\,1/\mathrm{cm}^3$. At a realistic muon fraction of $Y_\mu \sim 0.01$, this requires a minimum matter density of $\rho \sim 10^{13}\,\mathrm{g/cm}^3$. The transition to a pure muon pair gas is also further spread out compared to electrons, with some muon pairs starting to appear already at $T \sim 0.1\,\mathrm{MeV}$, signified by the nonrelativistic chemical potential becoming negative. The point of a pure muon pair gas is reached when the nonrelativistic chemical potential is equal the negative rest mass $\mu_\mu^{\mathrm{NR}} = -m_\mu \rightsquigarrow \mu_\mu^{\mathrm{R}} = 0$.

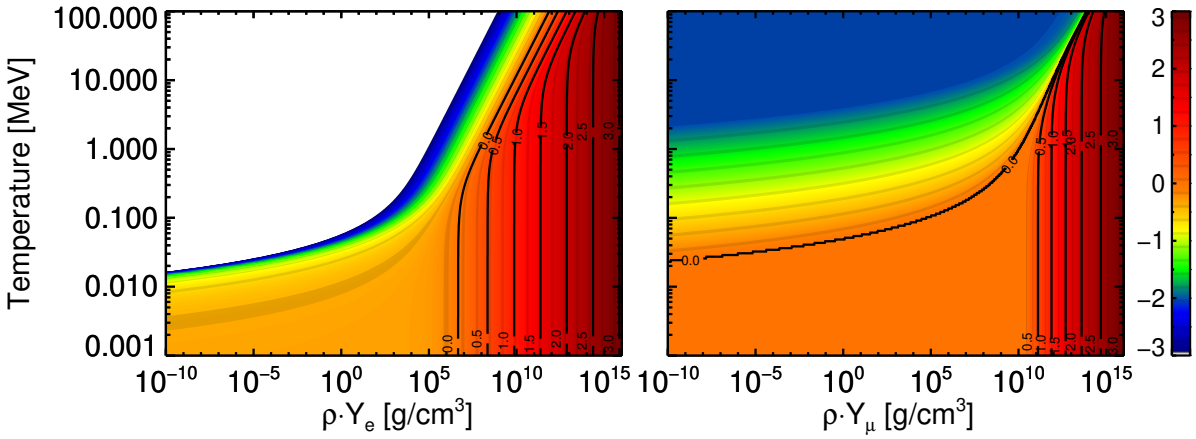

Figure 3.5: Logarithmic relativistic chemical potential including electron rest mass $\mu_{\mathrm{e}}^{\mathrm{R}}$ on the left side and logarithmic nonrelativistic chemical potential without muon rest mass $\mu_{\mu}^{\mathrm{NR}} = \mu_{\mu}^{\mathrm{R}} - m_{\mu}$ on the right side. Note that the plotted muon chemical potential is logarithmized according to the formula $\mu_{\mu}^{\mathrm{plotted}} = \mathrm{sign}(\mu_{\mu}^{\mathrm{NR}}) \log_{10}\left(\max\left(|\mu_{\mu}^{\mathrm{NR}}|, 1\right)\right)$, whereas the electron chemical potential is simply $\mu_{\mathrm{e}}^{\mathrm{plotted}} = \log_{10}\left(\mu_{\mathrm{e}}^{\mathrm{R}}\right)$.

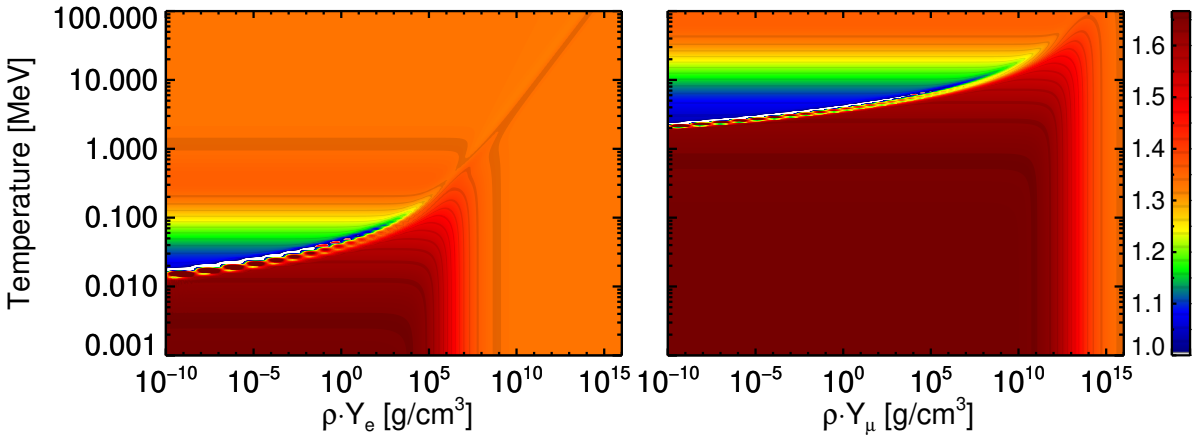

Figure 3.6: Adiabatic index $\Gamma_{\mathrm{s}} = \left(\frac{\partial \ln P}{\partial \ln \rho}\right)_{s,Y_\ell}$. The electron index is on the left side the; the muon index is on the right side.

The adiabatic index $\Gamma_{\mathrm{s}} = \left(\frac{\partial \ln P}{\partial \ln \rho}\right)_{s,Y_\ell}$ in Fig. 3.6, in combination with the pressure, gives the bulk modulus $K = \Gamma P$, which is a measure of the resistance of the gas to compression. Furthermore, the sound speed is equal to $v_{\mathrm{c}} = \sqrt{\frac{K}{(e^{\mathrm{tot}}+p)/c^2}}$, which converges towards $v_{\mathrm{c}}^{\mathrm{R}} = \frac{c}{\sqrt{3}}$ in an ultrarelativistic gas. The deep blue areas, with $\Gamma_{\mathrm{s}} \to 1$, are where the lepton–antilepton pair-instability begins. The formation of lepton pairs then consumes any additional temperature increase. In the electron gas, this happens at relatively low temperatures that are, however, still only reached in the cores of hyper-massive stars and lead to the pair-instability supernovae. A similar region also exists for muons but lies at significantly higher temperatures. These temperatures can only possibly be reached transiently in the short-lived remnants of NS–NS mergers, and during PNS → BH collapse.

4 High density equation of state

Densities far below nuclear saturation density, where the mean distance of the constituent particles is still large and the short-range nuclear interaction effects are dynamically insignificant, are easily modeled by treating the plasma as simple additive formally independent components. Baryonic particles only contribute by their statistical thermal motion and can be included as an ideal Maxwell-Boltzmann gas. Nuclear fusion and fission may happen if temperatures are high enough that nuclei can form and dissolve based on burning rate equations. The leptonic and photonic contributions further exist in the form of ideal Fermi and Bose gases, and are again independent contributions. As temperatures rise, nuclear burning can become fast enough that the forward and back-reactions reach the point of nuclear statistical equilibrium (NSE) and the baryonic composition becomes entirely determined by the Saha-equations. The approximation of ideal gases, however, breaks down as densities increase and particles begin to interact via strong forces. After this point, the nucleons and nuclei start to "feel" the other particles and corrections start to appear. The treatment of these corrections differ between the two EOS we employ in this thesis and can be separated into two categories.

1. Skyrme type zero-range interactions and the single nucleus approximation (SNA) as employed in the LS220 EOS of Ref. [70].

   Here the nucleons and nuclei are described by a Skyrme parametrization of the nuclear interaction in the mean field approximation and give the energy of the strongly interacting nucleons either contained inside nuclei at saturation density or outside nuclei as free nucleons. Additional corrections exist for the deformed shape of interacting nuclei to minimize their surface energy, as well as excluded volume effects. The treatment of the nuclear shape and binding energies follows the liquid drop model of Bethe-Weizsäcker. The single representative nucleus exists as a bubble of bound nucleons of a mean neutron and proton number determined by a minimization of the free energy and breakup occurs when it is energetically favorable to do so. This breakup typically happens at the point where the outside density of the unbound nucleons exceeds the nuclear saturation density or when the matter temperature is above the nucleus binding energy. The Skyrme parameters, which describe the strong nuclear interaction as an expansion around saturation density, can be directly fixed by experimentally determined values for symmetric matter. The chosen parameters of the LS220 EOS used in this thesis are the binding energy $B_0 = 16\,\mathrm{MeV}$, incompressibility $K_0 = 220\,\mathrm{MeV}$, symmetry energy $J = 29.3\,\mathrm{MeV}$ and a saturation density of $0.155\,\mathrm{fm}^{-3}$.

2. Relativistic mean field calculation for free nucleons and an excluded-volume nuclear statistical equilibrium for nuclei as employed in the SFHo EOS of Ref. [123]

   In the relativistic mean field approach, the nuclear interactions are treated using the quantum field theory, in which a mean field of mesons, described by the Klein-Gordon equations, surround the nucleons, described by the Dirac-equations. The interaction between nucleons is modeled by their coupling to the surrounding mean meson field. Mean field here means that the interactions are not calculated explicitly between nucleons. Instead, nucleons only feel the presence of surrounding nucleons by the expectation value of their meson field. The meson coupling constants and masses are some of the free parameters in the model and are still poorly constrained. The coupling constants and meson masses contained in the SFHo model are fitted to reproduce the experimental constraints of measured nuclei, as well as measured observational constraints on neutron star radii and masses of Ref. [25]. The resulting nuclear properties at saturation density fit the experimental constraints well, with a nuclear saturation density of $0.1583\,\mathrm{fm}^{-3}$, a binding energy of $B_0 = 16.19\,\mathrm{MeV}$, an incompressibility $K_0 = 245.4\,\mathrm{MeV}$, and a symmetry energy

$J = 31.57\,\mathrm{MeV}$. The nuclei contained in the matter are treated by a formally noninteracting NSE approach of many thousands of individual nuclei, with an individual treatment of their measured binding energy and shell effects where available. The excluded volume by the surrounding nuclei and nucleons provide a hard-body repulsion term, leading to their smooth dissolve when nuclear saturation density is reached. The exact prescription for the excluded-volume NSE is given in Ref. [44].

The equation of state of matter at supra-nuclear densities is still uncertain, and there exist many different approaches to try and tackle the issue. An excellent and exhaustive review on this topic is given in Ref. [103], and we will skip a discussion of this highly involved field as we do not modify the baryonic part of the EOS. The leptonic contribution remains in all cases an independent contribution which can be freely replaced or changed at will.

To see where changing the leptonic contribution actually can influence the EOS we refer to Fig. 4.1, where the relative proportion of gas pressure supplied by electrons to total gas pressure is shown. For this plot, the electron fraction was set to beta-equilibrium according to $\mu_{\nu_\mathrm{e}} = 0$ and $\mu_\mathrm{e} = \mu_\mathrm{n} - \mu_\mathrm{p}$. The blue areas are where the baryonic part of the EOS supplies nearly all of the pressure, and the system will exhibit barely any effect by a modification of the leptonic component. This area typically comprises the high-density part above nuclear saturation density, where the strong force and nuclear degeneracy pressure always dominates, as well as the relatively low density and temperature part, where the equilibrium net electron fraction and electron pair pressure is insignificant. The green and yellow areas, however, are representative of conditions in the extended protoneutron star mantle, where the freshly accreted matter slowly settles onto the protoneutron star and loses energy via neutrino radiation. Here, a change in the leptonic sector can affect the total behavior of the system by up to 30% percent, and is where we expect the appearance of muons to have the most significant dynamical effect. Furthermore, as the leptonic sector has practically no influence on cold matter, we do not expect extensive changes to the cold neutron star structure in accordance with previous studies in Ref. [4], who analyzed the effect of muons on the megayear timescale of cooling superfluid neutron stars.

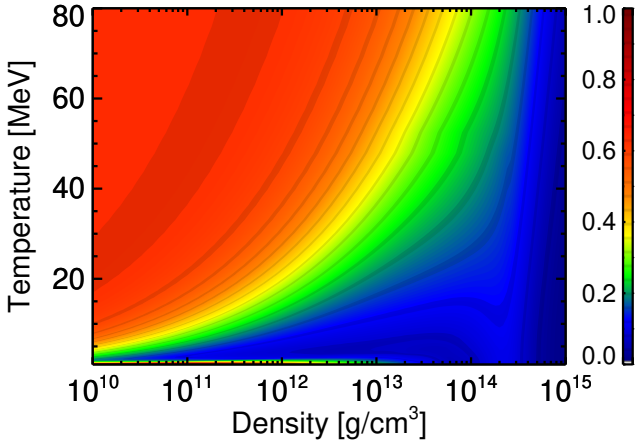

Figure 4.1: The relative contribution of the electron gas pressure to total gas pressure at an electron fraction Y_e set by beta-equilibrium of the SFHo EOS. Colors are set to the fraction $P_\mathrm{e}/P_\mathrm{total}$.

As the leptonic sector is only relevant in a hot protoneutron star and the minimum bound on the neutron star gravitational mass of Ref. [25] only constrains the cold neutron star mass our modified general-purpose finite-temperature EOS still fulfill the observational constraints as shown in the TOV solutions in Fig. 4.2. The LS220 EOS exhibits some sensitivity to the appearance of muons due to a shift in the weak equilibrium proton fraction, but the maximum mass is barely affected on the order of $\Delta m_\mathrm{TOV} \sim 0.01 M_\odot$. Both our employed EOS and all of

the other available EOS, which fulfill the constraints in Ref. [25], will remain viable even after the inclusion of muons. Further constraints on hot neutron star properties might be available in the future using gravitational wave observations of NS−NS merger remnants as predicted in Ref. [80].

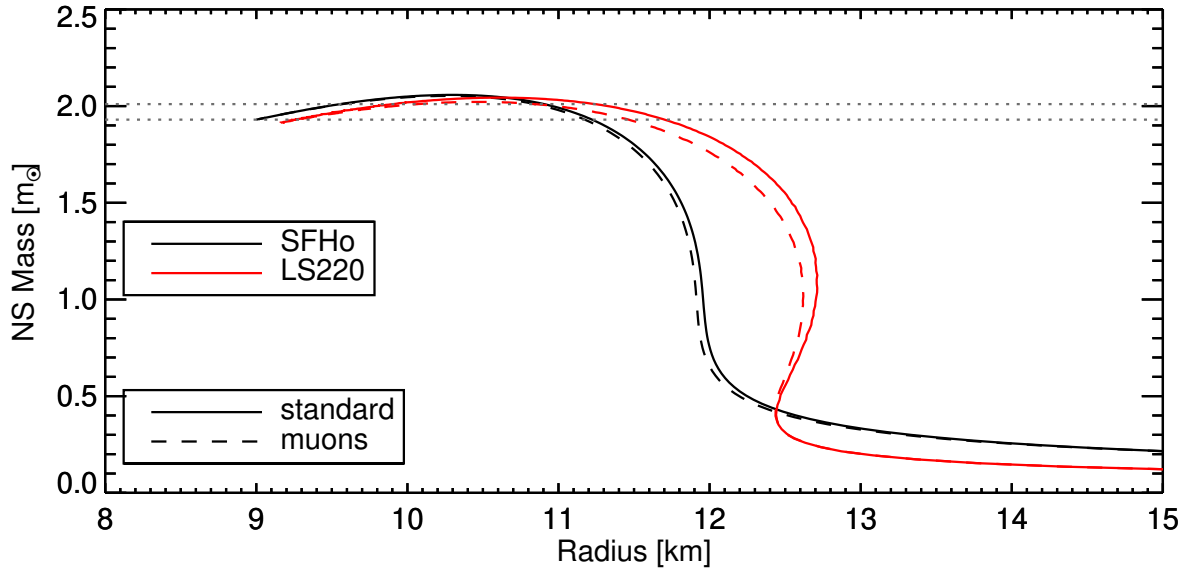

Figure 4.2: Mass-radius TOV solutions of hydrostatic cold neutrons stars with the SFHo EOS in black and the LS220 EOS in red. The TOV solutions without muons are solid lines, the solutions with muons are the dashed lines. The observational constraints of Ref. [25] are given by the two dotted lines at a 1σ confidence level.

Chapter III
PROMETHEUS-VERTEX

The radiation hydrodynamics equations at the core of every CCNS simulation require sophisticated tools to evolve all quantities forward in time from the given initial conditions. The neutrino transport solver currently used in the Garching Max-Planck CCSN group is the VERTEX[①] fully implicit transport solver, in combination with the PROMETHEUS explicit Newtonian hydrodynamics solver of Ref. [38], further upgraded and adapted to supernova physics in Ref. [62] and Ref. [64]. PROMETHEUS is a direct Eulerian, time-explicit Godunov-type solver implementation of the Piecewise Parabolic Method (PPM) of Ref. [21].

The VERTEX component has been developed in Ref. [114] initially for spherically symmetric (1D) geometry and has further been extended to axisymmetric (2D) in Ref. [14] and later to fully three-dimensional (3D) geometry in Ref. [41]. Additional work to implement a special axis-free "Yin-Yang" grid for the 3D version was done in Ref. [85], an improved effective GR gravitational potential of case A in Ref. [77], as well as an extension to CFC GR and improvements to numerical methods in Ref. [93].

5.1 Neutrino transport

As neutrinos are purely weakly interacting leptonic neutral particles, they can not a priori be assumed to be in equilibrium with the surrounding matter. This differentiates them from their charged lepton "cousins", the electron, muon, and tauon which interact via the significantly stronger electromagnetic force and have short interaction mean free paths. Equilibration can, therefore, be assumed to be instantaneous at temperatures and densities common in the stellar interior. Neutrinos, on the other hand, can have mean free paths which range from centimeters to millions of kilometers which defies a conventional treatment. The Euler equations for mass, momentum and energy conservation, which are valid for isotropic local equilibrium states, are sufficient for the stellar plasma surrounding the neutrinos, but the neutrinos themselves require the direct treatment of conservation equations applicable to nonequilibrium states.

The Boltzmann transport equation (BTE) is used to transport a statistical ensemble of quasi-massless neutrinos distributed in a phase-space volume of $\mathrm{d}^3\vec{r}\,\mathrm{d}^3\vec{p}$ by a particle distribution function $f\,(\vec{x},\vec{p},t)$. In the case of neutrino transport this is the Fermi-Dirac distribution. In the related case of photon transport, it would be the Bose-Einstein distribution. The natural coordinates of stellar transport are spherical coordinates. These coordinates result in the 7-dimensional problem of evolving $f\,(r,\Theta,\Phi,E,\theta,\varphi,t)$, where the large Greek letters are the space coordinates and the small Greek letters are the angle coordinates relatively to the radial direction of propagation $\vec{n}$, which is the surface normal on the area $\mathrm{d}A$ spanned by the solid angle $\mathrm{d}\Omega$. In our transport, only a "ray-by-ray" transport solution is solved, which separates the distribution function into a set of independent "spherically symmetric" 1D radial solutions for each combination of Θ and Φ. Even if the transport solution might vary in angle, the deviation from symmetry is assumed to be small enough that lateral or azimuthal fluxes will not develop. The neutrino distribution function is therefore assumed to be cylindrically symmetric around each rays axis of propagation $\vec{n}$, and the φ angle disappears. In this ray-by-ray transport, the phase-space distribution function reduces to a 4-dimensional form $f(r,E,\theta,t)$, in which the angular distribution θ around the propagation vector still needs to be evolved. Note that even in multi-dimensional simulations using PROMETHEUS-VERTEX, angular coupling between different propagation vectors is formally neglected and only approximately included via the "ray-by-ray plus" approximation detailed in Ref. [14]. The "plus" here refers to approximated

[①] **V**ariable **E**ddington factor **R**adiative **T**ransfer for supernova **Ex**plosions

angular neutrino momentum transfer in trapped conditions and angular advection with the fluid.

The traditional quantity evolved in radiation transport is the specific monochromatic intensity $\mathcal{I}$ that is related to the distribution function by

$$\mathcal{I}(r, E, \mu, t) = \frac{c}{(2\pi\hbar c)^3} f(r, E, \theta, t) \ , \tag{5.1}$$

where μ is the angle cosine $\mu = \cos\theta$. The Boltzmann radiative transfer equation for the evolution of this specific intensity is given in the comoving frame of the fluid but at fixed Eulerian space coordinates. The comoving frame introduces relativistic Doppler effects as well as advective transport, treated accurate to $\mathcal{O}(\beta)$, where $\beta = (v/c)$ is the local fluid velocity divided by the speed of light, sufficient for our Newtonian hydrodynamics. The Boltzmann transport equation is then (see Ref. [114]),

$$\begin{aligned}\left(\frac{1}{c}\frac{\partial}{\partial t} + \beta\frac{\partial}{\partial r}\right)\mathcal{I} + \mu\frac{\partial}{\partial r}\mathcal{I} + \frac{1-\mu^2}{r}\frac{\partial}{\partial \mu}I \\ + \frac{\partial}{\partial \mu}\left[\left(1-\mu^2\right)\left\{\mu\left(\frac{\beta}{r} - \frac{\partial\beta}{\partial r}\right) - \frac{1}{c}\frac{\partial\beta}{\partial t}\right\}\mathcal{I}\right] \\ - \frac{\partial}{\partial E}\left[E\left(\left(1-\mu^2\right)\frac{\beta}{r} + \mu^2\frac{\partial\beta}{\partial r} + \mu\frac{1}{c}\frac{\partial\beta}{\partial t}\right)\mathcal{I}\right] \\ + \left(\left(3-\mu^2\right)\frac{\beta}{r} + \left(1+\mu^2\right)\frac{\partial\beta}{\partial r} + \mu\frac{2}{c}\frac{\partial\beta}{\partial t}\right)\mathcal{I} = C(\mathcal{I}) \ .\end{aligned} \tag{5.2}$$

The left-hand side expresses the conservation equation of neutrino transport, while the right-hand side are the neutrino source terms contained in the "collision integral". The collision integral prescribes how many neutrinos are created, annihilated or redistributed in phase-space via scattering reactions and depends on the monochromatic intensities but also on the energy and angle-integrated intensities of its own or possibly multiple other neutrino species. This makes the Boltzmann transport equation an integro-differential equation that is computationally expensive and converges very slowly. This equation can still be solved directly via so-called S_n discrete ordinate methods that calculate the angular bins on discrete Gaussian spaced points and require complex angular coupling as the neutrino propagates. This method is for example used in 1D in Ref. [72] and in 2D genuinely multi-dimensional transport in Ref. [126]. An alternative approach is to evolve the angular moment representation of the BTE and only approximate the exact angular distribution. Angular moments of the BTE are a series expansion of the radiation intensity in increasing orders of angular integrations over the radiation intensity in the form of

$$I^{(i)}(r, E, t) = \frac{1}{2}\int_{-1}^{+1} \mathrm{d}\mu\, \mu^i \mathcal{I}(r, E, \mu, t) \ , \tag{5.3}$$

where the $I^{(i)}$ are the angular moments of order (i). The full series expansion, if continued to infinite order, encodes all information of the angular distribution of the radiation intensity. However, in practice, the moment equations are truncated after the second order, the so-called two-moment transport method. A caveat of the moment equation is however that these moments always require a closure, i.e., the next higher moment. In other words, if one wishes to solve the first angular moment of the BTE it needs to be closed by a gradient over the second moment and ad infinitum to higher and higher moments. These closures can be prescribed by an analytical expression of the most likely phase-space distribution given by the first two moments, the commonly called M1 neutrino transport, see for example Refs. [99, 61]. An alternative method is to solve a simplified formal solution of a model-Boltzmann equation that solves the monochromatic radiation intensity forgoing conservative neutrino energy and species

coupling. Utilizing the tangent-ray angular discretization (see Ref. [87]) also angular coupling between different radii is automatically included, and the model-BTE formally becomes a set of independently evolved tangent-rays that are ideally suited to handle a central luminosity source even at large radii.

VERTEX employs the moment formalism in combination with the tangent-ray discretization to apply the Variable Eddington factor method, where the right-hand side collision integral of Eq. 5.2 is supplemented by energy integrated angular moments, thereby taming the integro-differential nature. The closures required for the moment equations are itself computed from the solution of the model-Boltzmann equation. The coupled set of BTE and moment equation is then iterated against each other toward convergence.

The evolved moment equations in VERTEX are the first and second moment, whereas the third and fourth moment only appear as normalized moments of the model-BTE. The four evolved moments are

$$J^{\mathrm{BTE}}(r,E,t) = \frac{1}{2}\int_{-1}^{1} \mathrm{d}\mu\, \mu^0 \mathcal{I}(r,E,\mu,t) = \frac{c}{4\pi} E(r,E,t)\ , \tag{5.4}$$

$$H^{\mathrm{BTE}}(r,E,t) = \frac{1}{2}\int_{-1}^{1} \mathrm{d}\mu\, \mu^1 \mathcal{I}(r,E,\mu,t) = \frac{1}{4\pi} F(r,E,t)\ , \tag{5.5}$$

$$K^{\mathrm{BTE}}(r,E,t) = \frac{1}{2}\int_{-1}^{1} \mathrm{d}\mu\, \mu^2 \mathcal{I}(r,E,\mu,t) = \frac{c}{4\pi} P(r,E,t)\ , \tag{5.6}$$

$$L^{\mathrm{BTE}}(r,E,t) = \frac{1}{2}\int_{-1}^{1} \mathrm{d}\mu\, \mu^3 \mathcal{I}(r,E,\mu,t)\ . \tag{5.7}$$

The first moment can be identified to be equivalent to the neutrino energy density E; the second moment is equivalent to the neutrino energy flux density F. Both of these moments are evolved by the detailed moment equations of Eqs. 5.10 and 5.11 in a conservative fully energy-bin and species coupled way. The third moment can be identified to be the neutrino pressure tensor in the radial direction, i.e., P^{rr}, whereas the fourth moment does not have a traditional analogue quantity and only enters the neutrino energy flux equation via the velocity terms. The third and fourth moment are computed from the normalized results of the model-BTE and return the eponymous Variable Eddington factor

$$f_K = \frac{K^{\mathrm{BTE}}}{J^{\mathrm{BTE}}}\ , \tag{5.8}$$

and the fourth closure factor

$$f_L = \frac{L^{\mathrm{BTE}}}{J^{\mathrm{BTE}}}\ . \tag{5.9}$$

The first and second moment equation for a spherically symmetric background are calculated by integrating the BTE using the definitions of Eqs. 5.4 and 5.5 to be

$$\begin{aligned}\left(\frac{1}{c}\frac{\partial}{\partial t} + \beta\frac{\partial}{\partial r}\right) J + \frac{1}{r^2}\frac{\partial}{\partial r}\left(r^2 H\right) \\ - \frac{\partial}{\partial E}\left[E\left(\frac{\beta}{r}J(1-f_K) + \frac{\partial\beta}{\partial r} f_K J + \frac{1}{c}\frac{\partial\beta}{\partial t} H\right)\right] \\ + \frac{\beta}{r}J(3-f_K) + \frac{\partial\beta}{\partial r}J(1+f_K) + \frac{2}{c}\frac{\partial\beta}{\partial t}H = C^{(0)}\end{aligned} \tag{5.10}$$

and

$$\left(\frac{1}{c}\frac{\partial}{\partial t}+\beta\frac{\partial}{\partial r}\right)H+\frac{1}{r^2}\frac{\partial}{\partial r}\left(r^2 f_K J\right)+\frac{J\left(f_K-1\right)}{r} - \frac{\partial}{\partial E}\left[E\left(\frac{\beta}{r}\left(H-f_L J\right)+\frac{\partial\beta}{\partial r}f_L J+\frac{1}{c}\frac{\partial\beta}{\partial t}f_K J\right)\right] + \left(\frac{\beta}{r}+\frac{\partial\beta}{\partial r}\right)H+\frac{2}{c}\frac{\partial\beta}{\partial t}J\left(1+f_K\right)=C^{(1)}\,. \quad (5.11)$$

The higher moments are already implemented using the closure factors of Eqs. 5.8 and 5.9, and $C^{(i)}$ are the angular moments of the collision integral

$$C\left(\mathcal{I}\right)=B_{\mathrm{AE}}\left(\mathcal{I}\right)+B_{\mathrm{S}}\left(\mathcal{I}\right)+B_{\mathrm{IS}}\left(\mathcal{I}\right)+B_{\mathrm{TP}}\left(\mathcal{I}\right)\,. \quad (5.12)$$

Here,

$$B_{\mathrm{AE}}\left(\mathcal{I}\right)=j\left(E\right)\left(1-\mathcal{I}\left(r,E,\mu,t\right)\right)-\kappa\left(E\right)\mathcal{I}\left(r,E,\mu,t\right) \quad (5.13)$$

are absorption and emission reactions which are pure neutrino creation and annihilation operators.

$$B_S\left(\mathcal{I}\right)=2\pi\left(1-\mathcal{I}\left(r,E_1,\mu_1,t\right)\right)\int_{-1}^{1}\mathrm{d}\mu_3\int_0^\infty\mathrm{d}E_3\,E_3^2 R_{\mathrm{S}}^{\mathrm{in}}\left(E_1,E_3,\mu_{13}\right)\mathcal{I}\left(r,E_3,\mu_3,t\right) - 2\pi\mathcal{I}\left(r,E_1,\mu_1,t\right)\int_{-1}^{1}\mathrm{d}\mu_3\int_0^\infty\mathrm{d}E_3\,E_3^2 R_{\mathrm{S}}^{\mathrm{out}}\left(E_1,E_3,\mu_{13}\right)\left(1-\mathcal{I}\left(r,E_3,\mu_3,t\right)\right) \quad (5.14)$$

are any general scattering reaction which redistributes neutrinos in energy and angle.

$$B_{\mathrm{IS}}\left(\mathcal{I}\right)=2\pi E^2\left(1-\mathcal{I}\left(r,E,\mu_1,t\right)\right)\int_{-1}^{1}\mathrm{d}\mu_3\,R_{\mathrm{IS}}^{\mathrm{in}}\left(E,\mu_{13}\right)\mathcal{I}\left(r,E,\mu_3,t\right) - 2\pi E^2\mathcal{I}\left(r,E,\mu_1,t\right)\int_{-1}^{1}\mathrm{d}\mu_3\,R_{\mathrm{IS}}^{\mathrm{out}}\left(E,\mu_{13}\right)\left(1-\mathcal{I}\left(r,E,\mu_3,t\right)\right) \quad (5.15)$$

is a subset of scattering which only changes neutrino momentum but not energy resulting in only an angular redistribution.

$$B_{\mathrm{TP}}\left(\mathcal{I}\right)=2\pi\left(1-\mathcal{I}\left(r,E_1,\mu_1,t\right)\right)\int_{-1}^{1}\mathrm{d}\mu_3\int_0^\infty\mathrm{d}E_3\,E_3^2 R_{\mathrm{TP}}^{\mathrm{in}}\left(E_1,E_3,\mu_{13}\right)\left(1-\bar{\mathcal{I}}\left(r,E_3,\mu_3,t\right)\right) - 2\pi\mathcal{I}\left(r,E_1,\mu_1,t\right)\int_{-1}^{1}\mathrm{d}\mu_3\int_0^\infty\mathrm{d}E_3\,E_3^2 R_{\mathrm{TP}}^{\mathrm{out}}\left(E_1,E_3,\mu_{13}\right)\bar{\mathcal{I}}\left(r,E_3,\mu_3,t\right) \quad (5.16)$$

is a pair production reaction which couples different neutrino species in energy, angle and neutrino number.

The collision integral is the interface between the hydrodynamics and radiation transport part to maintain energy, momentum and lepton flavor number conservation. As only the moment equations are directly coupled to the hydrodynamics, the neutrino source terms entering the hydro solver are energy-integrated and summed angular moments of the collision integral.

$$Q_{\mathrm{E}}=-4\pi\int_0^\infty\mathrm{d}E\sum_\nu C_\nu^{(0)}\left(E\right)\,, \quad (5.17)$$

$$Q_{\mathrm{M}}=-\frac{4\pi}{c}\int_0^\infty\mathrm{d}E\sum C_\nu^{(1)}\left(E\right)\,, \quad (5.18)$$

$$Q_{\mathrm{N}}=-4\pi m_{\mathrm{B}}\int\mathrm{d}E\,\mathcal{C}_{\nu_{\mathrm{e}}}^{(0)}\left(E\right)-\mathcal{C}_{\bar{\nu}_{\mathrm{e}}}^{(0)}\left(E\right)\,, \quad (5.19)$$

where Q_{E} is the internal energy source term, Q_{M} is the momentum source term and Q_{N} is the electron number source term, $\mathcal{C}(E) = C(E)/E$ and m_{B} is the baryonic mass in gram. As an observer is interested in lab-frame (or inertial frame) quantities the comoving quantities evolved in our code need to be transformed $\mathcal{O}(\beta)$ accurate following Ref. [87]:

$$E^{\mathrm{lab}} = E + 2\beta F/c\,, \tag{5.20}$$

$$F^{\mathrm{lab}} = F + c\beta\,(J + K)\ . \tag{5.21}$$

Note however that these transformations are only valid for energy-integrated quantities, i.e., the total energy,flux and pressure density.

5.2 Hydrodynamics

The equation of hydrodynamics in the stellar interior can be described by the compressible Euler equations for an ideal, inviscid fluid in an equilibrium state which is characterized by a mass density ρ, a velocity vector $\vec{v}$ and a specific total energy density $\epsilon = e + \frac{1}{2}\vec{v}^2$. Just as in the radiation transport equations a closure is needed for the Euler equations, which is the gas pressure p. As the fluid is in thermodynamic equilibrium and all particles are isotropic and fully described by the respective distribution function, the gas pressure p is fully determined by the density, temperature and particle composition by the equation of state and is usually supplied in tabulated or analytical form. The Euler equations are

$$\partial_t \rho + \nabla\cdot(\rho\vec{v}) = 0\,, \tag{5.22}$$

$$\partial_t(\rho v_k) + \nabla\cdot(\rho\vec{v}\otimes\vec{v}) + \nabla P = -\rho\nabla\Phi + \vec{Q}_{\mathrm{M}}\,, \tag{5.23}$$

$$\partial_t(\rho\epsilon) + \nabla\left[(\rho\epsilon + P)\,\vec{v}\right] = -\rho\vec{v}\cdot\nabla\Phi + Q_{\mathrm{E}} + \vec{v}\cdot\vec{Q}_{\mathrm{M}}\,, \tag{5.24}$$

where the first equation is the mass conservation equation, the second is the momentum conservation equation and the third is the energy conservation equation.

Additional conservation equations are solved for the electron fraction $Y_{\mathrm{e}} = \frac{n_{\mathrm{e}^-} - n_{\mathrm{e}^+}}{n_{\mathrm{B}}}$

$$\frac{\partial\rho Y_{\mathrm{e}}}{\partial t} + \nabla\cdot\left(\rho Y_{\mathrm{e}}\vec{v}\right) = Q_{\mathrm{N_e}}\,, \tag{5.25}$$

and individual nuclear species if the system is not in nuclear statistical equilibrium

$$\frac{\partial\rho X_i}{\partial t} + \nabla\cdot(\rho X_i\vec{v}) = Q_{\mathrm{N}_i}\,, \tag{5.26}$$

where X_i are the nuclear mass fractions. Note that Q_{N_i} is here a nuclear source term by nuclear burning reactions, i.e., fusion or fission of nuclei, and is not the neutrino lepton number source term. As required by our goal to track muonization in the CCSN context, the electron fraction source terms and conservation equations were complemented by the corresponding muon fraction equations,

$$\frac{\partial\rho Y_\mu}{\partial t} + \nabla\cdot\left(\rho Y_\mu\vec{v}\right) = Q_{\mathrm{N}_\mu}\,, \tag{5.27}$$

which will be further detailed in the following sections.

5.3 Low-density equation of state

The low-density equation of state in PROMETHEUS-VERTEX is an analytical ideal Maxwell-Boltzmann gas using a tabulated nuclear statistical equilibrium (NSE) composition and supplemented by a tabulated electron ideal Fermi-Dirac gas with photon contributions. The assumption of an ideal gas without interactions, except by a simple Coulomb lattice correction, allows an independent superposition of all individual components without the intricacies of hot matter close to nuclear density. The thermodynamic variables of an ideal Boltzmann gas are a simple function of gas temperature and density, where

$$P_{\mathrm{B}} = \sum_i n_i T \,, \tag{5.28}$$

$$e_{\mathrm{B}} = \sum_i \frac{3}{2} n_i T \,, \tag{5.29}$$

$$s_{\mathrm{B}} = \sum_i n_i \left(\frac{5}{2} - \mu_i \right) , \tag{5.30}$$

are the pressure density, internal energy density and entropy density respectively. The sums are performed over the number densities of individual nucleons and nuclei n_i as given by the composition and mass number. The total thermodynamic variables of the low-density EOS are then a simple combination of all individual components

$$P_{\mathrm{LD}}\left(\rho, T, X_i, Y_{\mathrm{e}}, Y_\mu\right) = P_{\mathrm{B}} + P_{\mathrm{e}} + P_\mu + P_{\mathrm{Coulomb}} + P_\gamma \,, \tag{5.31}$$

$$e_{\mathrm{LD}}\left(\rho, T, X_i, Y_{\mathrm{e}}, Y_\mu\right) = e_{\mathrm{norm}} + e_B + e_{\mathrm{e}} + e_\mu + e_{\mathrm{Coulomb}} + e_\gamma \,, \tag{5.32}$$

$$s_{\mathrm{LD}}\left(\rho, T, X_i, Y_{\mathrm{e}}, Y_\mu\right) = s_{\mathrm{B}} + s_{\mathrm{e}} + s_\mu + s_{\mathrm{Coulomb}} + s_\gamma \,. \tag{5.33}$$

As the muon fraction is initially zero a negative net muon fraction cannot be excluded as for the case of electrons. The pressure, energy density and entropy of the muon gas not depending on the actual sign of the net fraction makes it possible to access the tabulated muon gas EOS using the absolute value of the net muon fraction. Only the sign of the resulting muon chemical potential then needs to be switched using $\mu_\mu\left(\rho,\, T,\, Y_\mu\right) = \mu_\mu\left(\rho,\, T,\, |Y_\mu|\right)\, \mathrm{sign}\left(Y_\mu\right)$. Note also that e_{norm} is a rest mass normalization term as used in the L&S EOS and is given by

$$e_{\mathrm{norm}} = n_i m_i + \frac{\rho}{m_{\mathrm{B}}}\left(Y_{\mathrm{e}} m_{\mathrm{e}} + Y_\mu m_\mu\right) + \frac{\rho}{m_{\mathrm{B}}}\left(-m_{\mathrm{n}} + E_0\right) \,, \tag{5.34}$$

where E_0 is a constant offset typically chosen to be the binding energy of ^{56}Fe. The calculation of the leptonic contributions is given in Sec. 3 for the muon and electron gas and will not be repeated here. In hydrodynamical simulations, one is usually interested in an inversion of the energy density with respect to temperature, to calculate the new hydrodynamic state after all source terms have been taken care of. For this purpose, the low-density EOS first performs bisection iterations to roughly bracket the total energy density e_{LD}, followed by Newton-Raphson iterations to converge quickly onto the correct temperature for given ρ, e_{LD}, Y_{e}, Y_μ.

The following steps can roughly characterize the procedure.

1. The nuclear composition is set by the tabulated NSE table using a bisection iteration in the energy density, and final linear interpolation between the bracketing tabulated points with density ρ and total proton fraction $Y_{\mathrm{p}} = Y_{\mathrm{e}} + Y_\mu$ kept constant. If the final tabulated temperature is above the critical temperature where we assume NSE holds then the nuclear composition is replaced by the current NSE composition for given ρ, T, Y_{p}.

2. Initial bisection iterations of the Boltzmann gas starting from the lowest and highest temperature of the tabulated electron EOS, as it spans the entire temperature range typically encountered in the cores of massive stars. The bracketing energy densities are calculated using Eq. 5.32 and the iteration is continued for a set number of times.

3. Final Newton-Raphson iterations using analytical derivatives for the baryonic and Coulomb component and numerical derivatives for the leptonic and photonic component until the desired accuracy has been reached.

4. After convergence of the Newton-Raphson method onto the final temperature, all thermodynamic state variables are output and fed back into the hydro calculation. To calculate the sound speed for the current gas mixture, the adiabatic index Γ_S for constant entropy is calculated via the following formula

$$\begin{aligned}
\Gamma_s = \quad & \left[P_\mathrm{B} \frac{\partial \ln P_\mathrm{B}}{\partial \ln \rho} + P_\mathrm{e} \frac{\partial \ln P_\mathrm{e}}{\partial \ln \rho} + P_\mu \frac{\partial \ln P_\mu}{\partial \ln \rho} + P_\mathrm{Coulomb} \frac{\partial \ln P_\mathrm{Coulomb}}{\partial \ln \rho} \right. \\
+ \quad & \left(P_\mathrm{B} \frac{\partial \ln P_\mathrm{B}}{\partial \ln T} + P_\mathrm{e} \frac{\partial \ln P_\mathrm{e}}{\partial \ln T} + P_\mu \frac{\partial \ln P_\mu}{\partial \ln T} + P_\gamma \frac{\partial \ln P_\gamma}{\partial \ln T} \right)^2 \\
/ \quad & \left. \left(e_\mathrm{B} \frac{\partial \ln e_\mathrm{B}}{\partial \ln \rho} + e_\mathrm{e} \frac{\partial \ln e_\mathrm{e}}{\partial \ln T} + e_\mu \frac{\partial \ln e_\mu}{\partial \ln T} + e_\gamma \frac{\partial \ln e_\gamma}{\partial \ln T} \right) \right] \\
/ \quad & \left(P_\mathrm{B} + P_\mathrm{e} + P_\mu + P_\mathrm{Coulomb} + P_\gamma \right) . \qquad (5.35)
\end{aligned}$$

5.4 High-density equation of state

The high-density equations of state used in PROMETHEUS-VERTEX are any publicly available general purpose equation of state for hot and dense matter. When approaching nuclear saturation density the simple Maxwell-Boltzmann gas approach breaks down and interactions between nucleons as well as nuclei come into play. The computational complexity of the required calculations then requires tabulated equations of state that are typically calculated on a fixed grid in ρ, T, Y_e parameter space and then interpolated using trilinear interpolation. As the tabulated high-density EOS, the tabulated electron EOS, and the tabulated muon EOS are generally calculated on varying grids in ρ, T, Y_e and Y_μ, a simple linear interpolation between the two bracketing total energy densities cannot be performed. Additionally, there might be several grid points of the leptonic EOS tables inside one high-density EOS table bracket with possibly varying derivatives. Nonetheless, the respective thermodynamic variables of the high-density region are given by

$$P_\mathrm{HD}\left(\rho, T, X_i, Y_\mathrm{e}, Y_\mu\right) = P_\mathrm{B} + P_\mathrm{e} + P_\mu + P_\gamma \,, \tag{5.36}$$

$$e_\mathrm{HD}\left(\rho, T, X_i, Y_\mathrm{e}, Y_\mu\right) = e_\mathrm{B} + e_\mathrm{e} + e_\mu + e_\gamma \,, \tag{5.37}$$

$$s_\mathrm{HD}\left(\rho, T, X_i, Y_\mathrm{e}, Y_\mu\right) = s_\mathrm{B} + s_\mathrm{e} + s_\mu + s_\gamma \,. \tag{5.38}$$

Note that P_B, e_B and s_B are now the tabulated values of the high-density equation for the purely baryonic case, either by subtracting the electronic and photonic component of the gas from the tabulated values, or by using a version of the tabulated EOS that is already provided for the purely baryonic case from the authors. The resulting table is now tabulated in ρ, T, Y_p where the proton fraction is again set by charge balance to be $Y_\mathrm{p} = Y_\mathrm{e} + Y_\mu$.

The method to converge onto the final temperature is similar to the low-density case.

1. Initial bisection iteration on the lowest and highest temperature of the high-density EOS using Eq. 5.37 to get the corresponding energy densities.

2. Once the bracketing high-density grid points are found, a final Newton-Raphson iteration inside left and right temperature grid points is performed using the constant numerical derivative of the tabulated HD-EOS, and the possibly varying numerical derivatives of the electron EOS and the muon EOS until the iteration has converged onto the final temperature.

3. Calculate the new adiabatic index using the same procedure as in Eq. 5.35.

Chapter IV
Muonic opacities

The collision integral of Eq. 5.12 contains the following opacities, whose implementation are described in Refs. [114, 13, 14] and this work.

Interactions	Reference
β-Processes	
$\nu_e + n \rightleftharpoons e^- + p$ $\overline{\nu}_e + p \rightleftharpoons e^+ + n$	[10, 86, 18]
$\nu_e + A_Z \rightleftharpoons e^- + A_{Z\text{-}1}$	[10, 86, 68]
$\nu_\mu + n \leftrightharpoons \mu^- + p$	[75, 18], this work
$\overline{\nu}_\mu + p \leftrightharpoons \mu^+ + n$	[75, 18], this work
Leptonic absorption	
$\nu_\mu + e^- \leftrightharpoons \nu_e + \mu^-$	[75], this work
$\overline{\nu}_\mu + e^+ \leftrightharpoons \overline{\nu}_e + \mu^+$	[75], this work
$\overline{\nu}_e + e^- \leftrightharpoons \overline{\nu}_\mu + \mu^-$	[75], this work
$\nu_e + e^+ \leftrightharpoons \nu_\mu + \mu^+$	[75], this work
Particle decay	
$\overline{\nu}_e + e^- + \nu_\mu \leftrightharpoons \mu^-$	[75], this work
$\nu_e + e^+ + \overline{\nu}_\mu \leftrightharpoons \mu^+$	[75], this work
Scattering	
$\nu + A \rightleftharpoons \nu + A$	[46, 11]
$\nu + A \rightleftharpoons \nu' + A'$	[69]
$\nu + N \rightleftharpoons \nu' + N'$	[10, 86, 17]
$\nu + e^\mp \rightleftharpoons \nu' + e^{\mp\prime}$	[86, 20]
$\nu_{\mu,\tau} + \nu_e \rightleftharpoons \nu'_{\mu,\tau} + \nu_e{}'$	[13]
$\nu + \mu^\mp \leftrightharpoons \nu' + \mu^{\mp\prime}$	[75, 86, 20], this work
Pair production	
$\nu + \bar{\nu} \rightleftharpoons e^- + e^+$	[10, 108]
$\nu_{\mu,\tau} + \bar{\nu}_{\mu,\tau} \rightleftharpoons \nu_e + \overline{\nu}_e$	[13]
Bremsstrahlung	
$\nu + \bar{\nu} + N + N \rightleftharpoons N' + N'$	[42]

Table 5.1: Overview of all neutrino interactions as included in our current numerical simulations. Symbols used in the table are ν to represent $\{\nu_e, \overline{\nu}_e, \nu_\mu, \overline{\nu}_\mu, \nu_\tau, \overline{\nu}_\tau\}$, N for free nucleons, A for heavy nuclei. Numerical implementation of the nonmuonic neutrino interaction rates is described in detail in Refs. [114, 13, 14].

6 Purely leptonic opacities

Purely leptonic opacities are defined as interaction rates that only involve leptons in the initial as well as the final state of the interaction vertex. These are interactions that can happen either via the neutral current channel by the exchange of a neutral Z^0-boson, the charged current channel by the exchange of a charged $W^{\mp}$-boson or a combination of both.

The neutral current Z^0-boson can only exchange energy and momentum between particles in the case of scattering or decay into a charge-neutral lepton pair in the case of pair production. An exchange of charge between particles is forbidden in the neutral current channel, but it has the advantage that all neutrino flavors can participate equally. Purely neutral current reactions between leptons relevant in the CCSN context include the classical case of μ/τ neutrino scattering on electrons or positrons (e.g., Ref. [133]) as well as the case of electron-positron annihilation into a μ/τ neutrino and antineutrino pair (e.g., Ref. [26]). These are supplemented by the related purely neutrinic reactions of electron neutrino pair annihilation into a μ/τ neutrino pair as well as a μ/τ (anti-)neutrino scattering on an electron (anti-)neutrino (Ref. [13]). These four reactions in combination with pair production of μ/τ neutrino pairs by nucleonic bremsstrahlung (Ref. [42]) form the dominant energy exchange and production channels of heavy-lepton flavor neutrinos currently included in simulation codes.

The charged current channel can in addition to energy and momentum also exchange charge between particles, which, in the leptonic case, transforms neutrinos into charged leptons and vice versa. Charged current channels between leptons in the current CCSN context are however only open to electron-flavor neutrinos, which act in addition to the neutral current channels and increase their respective cross-sections.

The inclusion of muons into the CCSN context opens additional charged current channels, which allow both net number generation of electrons and muons by neutrino absorption on charged leptons and decay of (anti-)muons into electrons/positrons, as well as a charged current scattering channel of μ (anti-)neutrinos on (anti-)muons. This increases the ability of electron and μ neutrinos to stay in chemical equilibrium even when final state blocking of nucleons or large interaction potential differences suppress the more traditional beta-reaction channels. Here we will first reiterate a general leptonic scattering kernel for arbitrary lepton mass that allows for neutral current and charged current pure scattering reactions on electrons and muons based on the work of Refs. [75, 86]. Note that we do not, as of yet, take muon-antimuon pair annihilation into account, even though it might be an additional production source of high energy μ neutrino pairs. As the production emissivities of bremsstrahlung and electron-positron pair annihilation are however already sufficiently large for μ neutrinos in these regions, and muon pairs are not abundant at the neutrinosphere, we do not expect a significant additional effect from including a new muon pair process and neglect it for now.

6.1 General leptonic scattering kernel

$\nu + \mathrm{e}^{\mp} \leftrightharpoons \nu' + \mathrm{e}^{\mp'}$	$\bar{\nu} + \mathrm{e}^{\pm} \leftrightharpoons \bar{\nu}' + \mathrm{e}^{\pm'}$
$\nu + \mu^{\mp} \leftrightharpoons \nu' + \mu^{\mp'}$	$\bar{\nu} + \mu^{\pm} \leftrightharpoons \bar{\nu}' + \mu^{\pm'}$

Table 6.1: Pure leptonic scattering reactions.

The angle-dependent scattering kernel for a general reaction $\nu_1 + \ell_2 \to \nu_3 + \ell_4$ of an incoming neutrino $\nu_1\,(E_1)$ scattering on any charged lepton ℓ_2 resulting in an outgoing neutrino $\nu_3\,(E_3)$ and an outgoing charged lepton ℓ_4 is

$$R_{\mathrm{NLS}}^{\mathrm{out}}\left(E_1, E_3, \theta_{13}\right) = \frac{G_{\mathrm{F}}^2}{2\pi^2}\left[\alpha_1 R_1\left(E_1, E_3, \theta_{13}\right) + \alpha_2 R_2\left(E_1, E_3, \theta_{13}\right) + \alpha_3 R_3\left(E_1, E_3, \theta_{13}\right)\right] , \quad (6.1)$$

with $\alpha_1 = \left(C_{\mathrm{V}} + C_{\mathrm{A}}\right)^2$, $\alpha_2 = \left(C_{\mathrm{V}} - C_{\mathrm{A}}\right)^2$, $\alpha_3 = C_{\mathrm{A}}^2 - C_{\mathrm{V}}^2$ being the combination of coupling constants for the considered neutrino-lepton pair and the functions $R_{1,2,3}\left(E_1, E_3, \theta_{13}\right)$ being the angle- and energy-dependent kinematic integrals of Ref. [75]. The out-direction of the kernel $R_{\mathrm{NLS}}^{\mathrm{out}}(E_1, E_3, \theta_{13})$ implies that a neutrino is scattered out of the respective (E_1, μ_1) phase-space into (E_3, μ_3). Conversely, the in-direction $R_{\mathrm{NLS}}^{\mathrm{in}}(E_1, E_3, \theta_{13})$ implies that a neutrino is scattered into the (E_1, μ_1) phase-space from (E_3, μ_3). The scattering angle $\cos\theta_{13}$ is the cosine of the angle between initial angle cosine μ_1 and final angle cosine μ_3.

The individual kinematic integrals are

$$R_1\left(E_1, E_3, \theta_{13}\right) = \int \mathrm{d}^3\vec{p}_2\,\mathrm{d}^3\vec{p}_4\,\frac{\left(\vec{p}_1\cdot\vec{p}_2\right)\left(\vec{p}_3\cdot\vec{p}_4\right)}{E_1E_2E_3E_4}\delta^4\left(\vec{p}_1 + \vec{p}_2 - \vec{p}_3 - \vec{p}_4\right) f_2\left(E_2\right)\left[1 - f_4(E_4)\right] , \quad (6.2)$$

$$R_2\left(E_1, E_3, \theta_{13}\right) = \int \mathrm{d}^3\vec{p}_2\,\mathrm{d}^3\vec{p}_4\,\frac{\left(\vec{p}_1\cdot\vec{p}_4\right)\left(\vec{p}_2\cdot\vec{p}_3\right)}{E_1E_2E_3E_4}\delta^4\left(\vec{p}_1 + \vec{p}_2 - \vec{p}_3 - \vec{p}_4\right) f_2\left(E_2\right)\left[1 - f_4(E_4)\right] , \quad (6.3)$$

$$R_3\left(E_1, E_3, \theta_{13}\right) = \int \mathrm{d}^3\vec{p}_2\,\mathrm{d}^3\vec{p}_4\,\frac{\left(\vec{p}_1\cdot\vec{p}_3\right)}{E_1E_2E_3E_4}\delta^4\left(\vec{p}_1 + \vec{p}_2 - \vec{p}_3 - \vec{p}_4\right) f_2\left(E_2\right)\left[1 - f_4(E_4)\right] , \quad (6.4)$$

where $\vec{p}_i$ are the particle four-momenta. These kinematic integrals have already been solved analytically up to a remaining integration over E_2 in Refs. [75, 86] and we repeat their results here.

$$R_1\left(E_1, E_3, \theta_{13}\right) = \frac{2\pi}{\Delta^5}\left(\tilde{A}_1 I_2 + \tilde{B}_1 I_1 + \tilde{C}_1 I_0\right) , \quad (6.5)$$

with the coefficients $\tilde{A}_1,\ \tilde{B}_1,\ \tilde{C}_1$ being given by

$$\tilde{A}_1 = E_1E_3\left(1 - \cos\theta_{13}\right)^2\left[E_1^2 + E_1E_3\left(3 + \cos\theta_{13}\right) + E_3^2\right] , \quad (6.6)$$

$$\tilde{B}_1 = E_1^2E_3\left(1 - \cos\theta_{13}\right)^2\left[2E_1^2 + E_1E_3\left(3 - \cos\theta_{13}\right) - E_3^2\left(1 + 3\cos\theta_{13}\right)\right] , \quad (6.7)$$

$$\tilde{C}_1 = E_1^3E_3\left(1 - \cos\theta_{13}\right)^2\left[E_1^2 - 2E_1E_3\cos\theta_{13} + E_3^2\left(-\frac{1}{2} + \frac{3}{2}\cos^2\theta_{13}\right)\right] + \frac{1}{2}E_1E_3\left(1 - \cos^2\theta_{13}\right)\Delta^2 m_2^2 . \quad (6.8)$$

$$R_2\left(E_1,\, E_3,\, \theta_{13}\right) = \frac{2\pi}{\Delta^5}\left(\tilde{A}_2 I_2 + \tilde{B}_2 I_1 + \tilde{C}_2 I_0\right)\,, \tag{6.9}$$

with the coefficients $\tilde{A}_2,\, \tilde{B}_2,\, \tilde{C}_2$ being given by

$$\tilde{A}_2 = E_1 E_3 \left(1-\cos\theta_{13}\right)^2 \left[E_1^2 + E_1 E_3 \left(3+\cos\theta_{13}\right) + E_3^2\right]\,, \tag{6.10}$$

$$\tilde{B}_2 = E_1 E_3^2 \left(1-\cos\theta_{13}\right)^2 \left[E_1^2 \left(1+3\cos\theta_{13}\right) + E_1 E_3 \left(-3+\cos\theta_{13}\right) - 2E_3^2\right]\,, \tag{6.11}$$

$$\begin{aligned}\tilde{C}_2 = {} & E_1 E_3^3 \left(1-\cos\theta_{13}\right)^2 \left[E_1^2\left(-\frac{1}{2}+\frac{3}{2}\cos^2\theta_{13}\right) - 2E_1 E_3\cos\theta_{13} + E_3^2\right] \\ & + \frac{1}{2} E_1 E_3 \left(1-\cos^2\theta_{13}\right)\Delta^2 m_2^2\,.\end{aligned} \tag{6.12}$$

$$R_3\left(E_1, E_3, \theta_{13}\right) = \frac{2\pi}{\Delta^5}\tilde{C}_3 I_0\,, \tag{6.13}$$

with the coefficient $\tilde{C}_3$ being given by

$$\tilde{C}_3 = \left(1-\cos\theta_{13}\right)\Delta^4 m_2^2\,. \tag{6.14}$$

The common coefficient Δ is given by

$$\Delta = \sqrt{E_1^2 - 2E_1 E_3\cos\theta_{13} + E_3^2}\,. \tag{6.15}$$

The energy integrals $I_k = \int_{E_-}^{\infty} \mathrm{d}E_2\, E_2^k f_2\left(E_2\right)\left[1 - f_4\left(E_2 + E_1 - E_3\right)\right]$ can be defined in terms of combinations of ultrarelativistic Fermi-Dirac integrals.

$$\begin{aligned} I_0 = {} & \int_{E_-}^{\infty} \mathrm{d}E_2\, f_2\left(E_2\right)\left[1 - f_4\left(E_2 + E_1 - E_3\right)\right] \\ = {} & T f_\gamma\left(\eta' - \eta\right)\left[F_0\left(\eta' - y\right) - F_0\left(\eta - y\right)\right]\,, \end{aligned} \tag{6.16}$$

$$\begin{aligned} I_1 = {} & \int_{E_-}^{\infty} \mathrm{d}E_2\, E_2 f_2\left(E_2\right)\left[1 - f_4\left(E_2 + E_1 - E_3\right)\right] \\ = {} & T^2 f_\gamma\left(\eta' - \eta\right)\left\{\left[F_1\left(\eta' - y\right) - F_1\left(\eta - y\right)\right] + y\left[F_0\left(\eta' - y\right) - F_0\left(\eta - y\right)\right]\right\}, \end{aligned} \tag{6.17}$$

$$\begin{aligned} I_2 = {} & \int_{E_-}^{\infty} \mathrm{d}E_2\, E_2^2 f_2\left(E_2\right)\left[1 - f_4\left(E_2 + E_1 - E_3\right)\right] \\ = {} & T^3 f_\gamma\left(\eta' - \eta\right)\left\{\left[F_2\left(\eta' - y\right) - F_2\left(\eta - y\right)\right]\right. \\ & \left. + \; 2y\left[F_1\left(\eta' - y\right) - F_1\left(\eta - y\right)\right] + y^2\left[F_0\left(\eta' - y\right) - F_0\left(\eta - y\right)\right]\right\}, \end{aligned} \tag{6.18}$$

with the lower limit of the integral given by

$$E_- = \frac{1}{2}\left\{\left(E_3 - E_1\right) + \sqrt{\left(E_1^2 + E_3^2 - 2E_1 E_3\cos\theta_{13}\right)\left[1 + \frac{2m_2^2}{E_1 E_3\left(1-\cos\theta_{13}\right)}\right]}\right\}. \tag{6.19}$$

The coefficients η, η' and y are defined as

$$y = \frac{E_-}{T}\,,$$
$$\eta = \frac{\mu_2}{T}\,,$$
$$\eta' = \eta - \frac{E_1 - E_3}{T}\,.$$

The appearing Fermi-Dirac integrals are

$$F_k\left(z\right) = \int_0^\infty \mathrm{d}x\, \frac{x^k}{\exp\left(x - z\right) + 1}\,, \tag{6.20}$$

and the function $f_\gamma\left(z\right)$ is given by

$$f_\gamma\left(z\right) = \frac{1}{\exp\left(z\right) - 1}\,. \tag{6.21}$$

The Fermi-Dirac integrals can easily be related to polylogarithms to ease computation, which will be demonstrated in Sec. 8.

In the case of forward scattering with no energy transfer, i.e., $E_1 \to E_3$, a limiting form of $\delta E = E_3 - E_1 \to 0$ needs to be developed following the results of Ref. [121] by replacing the integrals of Eqs. (6.16–6.18) with the following

$$I_0\left(E_1 = E_3\right) = T\left[F_{-1}\left(\eta - y\right)\right]\,, \tag{6.22}$$
$$I_1\left(E_1 = E_3\right) = T^2\left[F_0\left(\eta - y\right) + yF_{-1}\left(\eta - y\right)\right]\,, \tag{6.23}$$
$$I_2\left(E_1 = E_3\right) = T^3\left[2F_1\left(\eta - y\right) + 2yF_0\left(\eta - y\right) + y^2F_{-1}\left(\eta - y\right)\right]\,, \tag{6.24}$$

where

$$F_{-1}\left(z\right) = \frac{\exp(z)}{1 - \exp(z)}\,. \tag{6.25}$$

Note that all many-body corrections of interacting leptons as discussed in Ref. [52] are neglected in the calculations presented in this thesis, as the underlying EOS treats all leptons as perfect noninteracting ideal Fermi gases. The results of Ref. [52] show that including RPA-corrections of a correlated lepton gas interacting via the electromagnetic force can reduce the cross-section of neutrino–lepton scattering by up to an order of magnitude for low-energy neutrinos in a sufficiently dense plasma. The complexity of relativistic RPA and the sub-dominant opacity of neutrino–lepton-scattering at very high densities compared to the more tractable nonrelativistic RPA of neutrino–nucleon-scattering has however precluded their implementation.

6.2 Neutrino–lepton scattering

Having developed the general leptonic scattering kernel in Sec. 6.1 we can specialize the kernel to each reaction by appropriately inserting the correct coupling coefficients and lepton masses, which we will give here for all standard electronic scattering reactions and the new muonic scattering reactions.

Neutrino-electron scattering Here we present the coupling constants and rest masses to be used for the case of traditional neutrino–electron scattering $\nu_1 + \mathrm{e}^- \leftrightharpoons \nu_3 + \mathrm{e}^{-\prime}$ with $m_2 = m_4 = m_\mathrm{e} \approx 0.511\,\mathrm{MeV}$ and the Weinberg angle $\sin^2\theta_\mathrm{W} \approx 0.23$.

$\nu_{1,3}$	C_V	C_A
ν_e	$0.5 + 2\sin^2\theta_\mathrm{W}$	0.5
$\overline{\nu}_\mathrm{e}$	$0.5 + 2\sin^2\theta_\mathrm{W}$	-0.5
ν_μ	$-0.5 + 2\sin^2\theta_W$	-0.5
$\overline{\nu}_\mu$	$-0.5 + 2\sin^2\theta_\mathrm{W}$	0.5
ν_τ	$-0.5 + 2\sin^2\theta_\mathrm{W}$	-0.5
$\overline{\nu}_\tau$	$-0.5 + 2\sin^2\theta_\mathrm{W}$	0.5

Table 6.2: Constants used for neutrino–electron scattering.

Neutrino-positron scattering Here we present the coupling constants and rest masses to be used for the case of traditional neutrino–positron scattering $\nu_1 + \mathrm{e}^+ \leftrightharpoons \nu_3 + \mathrm{e}^{+\prime}$ with $m_2 = m_4 = m_\mathrm{e} \approx 0.511\,\mathrm{MeV}$ and $\sin^2\theta_\mathrm{W} \approx 0.23$.

$\nu_{1,3}$	C_V	C_A
ν_e	$0.5 + 2\sin^2\theta_\mathrm{W}$	-0.5
$\overline{\nu}_\mathrm{e}$	$0.5 + 2\sin^2\theta_\mathrm{W}$	0.5
ν_μ	$-0.5 + 2\sin^2\theta_\mathrm{W}$	0.5
$\overline{\nu}_\mu$	$-0.5 + 2\sin^2\theta_\mathrm{W}$	-0.5
ν_τ	$-0.5 + 2\sin^2\theta_\mathrm{W}$	0.5
$\overline{\nu}_\tau$	$-0.5 + 2\sin^2\theta_\mathrm{W}$	-0.5

Table 6.3: Constants used for neutrino–positron scattering.

Neutrino-muon scattering Here we present the coupling constants and rest masses to be used for the novel case of neutrino–muon scattering $\nu_1 + \mu^- \leftrightharpoons \nu_3 + \mu^{-\prime}$ with $m_2 = m_4 = m_\mu \approx 105.66\,\mathrm{MeV}$ and $\sin^2\theta_\mathrm{W} \approx 0.23$.

$\nu_{1,3}$	C_V	C_A
ν_e	$-0.5 + 2\sin^2\theta_\mathrm{W}$	-0.5
$\overline{\nu}_\mathrm{e}$	$-0.5 + 2\sin^2\theta_\mathrm{W}$	0.5
ν_μ	$0.5 + 2\sin^2\theta_\mathrm{W}$	0.5
$\overline{\nu}_\mu$	$0.5 + 2\sin^2\theta_\mathrm{W}$	-0.5
ν_τ	$-0.5 + 2\sin^2\theta_\mathrm{W}$	-0.5
$\overline{\nu}_\tau$	$-0.5 + 2\sin^2\theta_\mathrm{W}$	0.5

Table 6.4: Constants used for neutrino–muon scattering.

Neutrino-antimuon scattering Here we present the coupling constants and rest masses to be used for the new case of neutrino–antimuon scattering $\nu_1 + \mu^+ \leftrightharpoons \nu_3 + \mu^{+\prime}$ with $m_2 = m_4 = m_\mu \approx 105.66\,\mathrm{MeV}$ and $\sin^2\theta_\mathrm{W} \approx 0.23$.

$\nu_{1,3}$	C_V	C_A
ν_e	$-0.5 + 2\sin^2\theta_\mathrm{W}$	0.5
$\overline{\nu}_\mathrm{e}$	$-0.5 + 2\sin^2\theta_\mathrm{W}$	-0.5
ν_μ	$0.5 + 2\sin^2\theta_\mathrm{W}$	-0.5
$\overline{\nu}_\mu$	$0.5 + 2\sin^2\theta_\mathrm{W}$	0.5
ν_τ	$-0.5 + 2\sin^2\theta_\mathrm{W}$	0.5
$\overline{\nu}_\tau$	$-0.5 + 2\sin^2\theta_\mathrm{W}$	-0.5

Table 6.5: Constants used for neutrino–antimuon scattering.

6.2.1 Reverse reactions

The relation between the out-scattering kernel and the in-scattering kernel is given by the detailed-balance condition, which is the same for all scattering reactions included here:

$$R^\mathrm{in}_\mathrm{NLS}\left(E_1, E_3, \theta_{13}\right) = R^\mathrm{out}_\mathrm{NLS}\left(E_1, E_3, \theta_{13}\right) \exp\left[\left(E_3 - E_1\right)/T\right] . \tag{6.26}$$

The additional in/out-transpositional symmetry examined in Ref. [20] allows one to further reduce the numerical complexity by only calculating down-scattering neutrino energies of $E_1 > E_3$, and then exploiting the following symmetry for up-scattering energies of $E_3 > E_1$,

$$R^\mathrm{out}_\mathrm{NLS}\left(E_3, E_1, \theta_{13}\right) = R^\mathrm{in}_\mathrm{NLS}\left(E_1, E_{3,}\theta_{13}\right) . \tag{6.27}$$

6.3 Leptonic neutrino absorption reactions

The general leptonic scattering kernel framework of Sec. 6.1 can be reused for reactions, which are similar to neutral or charged current pure scattering reactions, but now also include different charged leptons ℓ_2 and ℓ_4 on opposite sites of the interaction vertex. In addition to the case of charged current neutrino-electron scattering, where an electron neutrino and an electron can interact via a W^--boson and exchange charge and identities, similar reactions can take place which transform electrons to higher mass leptons like muons and tauons and vice versa. The constraint of charge and flavor number conservation however only allows reactions to take place, which contain specific combinations of leptons that we will introduce in the following sections.

6.3.1 Lepton flavor exchange

$\nu_\mu + e^- \leftrightharpoons \nu_e + \mu^-$
$\overline{\nu}_\mu + e^+ \leftrightharpoons \overline{\nu}_e + \mu^+$

Table 6.6: Lepton flavor exchange reactions.

The novel case of lepton flavor exchange $\nu_\mu + e^- \leftrightharpoons \nu_e + \mu^-$ is introduced in Ref. [75] for the case of an electron emitting a W^--boson and becoming a neutral electron neutrino, while the incoming ν_μ absorbs the emitted W^--boson to itself become a muon. In addition to the negatively charged case presented in Ref. [75], we also include the positively charged case $\overline{\nu}_\mu + e^+ \leftrightharpoons \overline{\nu}_e + \mu^+$. As the rest mass of the electron and muon are different, the mass difference between initial and final state lepton gives an additional contribution to the transition rate that is taken into account by the additional terms introduced in Ref. [75]. The bolded parts will give these new terms in the following formulae.

The absorption kernel simplifies from Eq. 6.1 to

$$R^{\text{out}}_{\text{LFE}}(E_1, E_3, \theta_{13}) = \frac{2\pi}{\Delta^5}\alpha_1 \left(\tilde{A}_1 I_2 + \tilde{B}_1 I_1 + \tilde{C}_1 I_0\right) , \tag{6.28}$$

where the coefficients $\tilde{A}_1$, $\tilde{B}_1$, $\tilde{C}_1$ of Eqs. (6.6–6.8) are modified to be

$$\tilde{A}_1 = E_1 E_3 (1-\cos\theta_{13})^2 \left[E_1^2 + E_1 E_3 (3+\cos\theta_{13}) + E_3^2\right] , \tag{6.29}$$

$$\begin{aligned}\tilde{B}_1 = {} & E_1^2 E_3 (1-\cos\theta_{13})^2 \left[2E_1^2 + E_1 E_3 (3-\cos\theta_{13}) - E_3^2 (1+3\cos\theta_{13})\right] \\ & + \boldsymbol{Q\,(1-\cos\theta_{13})\left[E_1^3 + E_1^2 E_3\,(2+\cos\theta_{13}) - E_1 E_3^2\,(2+\cos\theta_{13}) - E_3^3\right]} ,\end{aligned} \tag{6.30}$$

$$\begin{aligned}\tilde{C}_1 = {} & E_1^3 E_3 (1-\cos\theta_{13})^2 \left[E_1^2 - 2E_1 E_3 \cos\theta_{13} + E_3^2\left(-\frac{1}{2} + \frac{3}{2}\cos^2\theta_{13}\right)\right] \\ & + \frac{1}{2} E_1 E_3 \left(1-\cos^2\theta_{13}\right)\Delta^2 m_2^2 \\ & + \boldsymbol{Q E_1\,(1-\cos\theta_{13})\left[E_1^3 - E_1^2 E_3 \cos\theta_{13} + E_1 E_3^2\left(-2+\cos^2\theta_{13}\right) + E_3^3\cos\theta_{13}\right]} \\ & + \boldsymbol{Q^2\left[E_1^2\cos\theta_{13} - E_1 E_3\left(\frac{3}{2} + \frac{1}{2}\cos^2\theta_{13}\right) + E_3^2\cos\theta_{13}\right]} ,\end{aligned} \tag{6.31}$$

with

$$\text{Q}=\boldsymbol{\frac{1}{2}\left(m_4^2 - m_2^2\right)} . \tag{6.32}$$

The lower integral bound E_- in Eqs. (6.16–6.18) also needs to be modified;

$$E_- = \frac{1}{2}\left\{(E_3 - E_1\,(\mathbf{1}+\boldsymbol{k}) + \sqrt{\left(E_1^2 + E_3^2 - 2E_1E_3\cos\theta_{13}\right)\left[(\mathbf{1}+\boldsymbol{k})^{\mathbf{2}} + \frac{2m_2^2}{E_1E_3\,(1-\cos\theta_{13})}\right]}\right\}, \tag{6.33}$$

with

$$\boldsymbol{k} = \frac{\boldsymbol{Q}}{\boldsymbol{E_1E_3}\,(\mathbf{1}-\cos\boldsymbol{\theta_{13}})}\,, \tag{6.34}$$

and

$$\begin{aligned} y &= \frac{E_-}{T}\,, \\ \eta &= \frac{\mu_2}{T}\,, \\ \eta' &= \eta - \frac{E_1 - E_3 + \boldsymbol{\mu_2} - \boldsymbol{\mu_4}}{T}\,. \end{aligned} \tag{6.35}$$

Using the amended framework introduced above we can calculate the two types of lepton flavor exchange via the following variable assignments.

Muon neutrino absorption on electron

$$\nu_1 \to \nu_\mathrm{e}, \quad \ell_2 \to \mathrm{e}^-, \quad \nu_3 \to \nu_\mu, \quad \ell_4 \to \mu^-, \quad m_2 = m_\mathrm{e}, \quad m_4 = m_\mu, \quad \alpha_1 = 4$$

Table 6.7: Particle assignments of $\nu_\mu + \mathrm{e}^- \leftrightharpoons \nu_\mathrm{e} + \mu^-$.

Antimuon neutrino absorption on positron

$$\nu_1 \to \overline{\nu}_\mathrm{e}, \quad \ell_2 \to \mathrm{e}^+, \quad \nu_3 \to \overline{\nu}_\mu, \quad \ell_4 \to \mu^+, \quad m_2 = m_\mathrm{e}, \quad m_4 = m_\mu, \quad \alpha_1 = 4$$

Table 6.8: Particle assignments of $\overline{\nu}_\mu + \mathrm{e}^+ \leftrightharpoons \overline{\nu}_\mathrm{e} + \mu^+$.

6.3.2 Lepton flavor conversion

$\overline{\nu}_{\mathrm{e}} + \mathrm{e}^- \leftrightharpoons \overline{\nu}_{\mu} + \mu^-$
$\nu_{\mathrm{e}} + \mathrm{e}^+ \leftrightharpoons \nu_{\mu} + \mu^+$

Table 6.9: Lepton flavor conversion reactions.

Lepton flavor conversion is a reaction where a charged electron reacts with its opposite antineutrino and converts into a second generation lepton pair. This is possible, as the lepton flavor number on both sides of the interaction vertex is zero and the net charge of ∓ 1 is conserved. As the kinematics of the process are slightly different to the lepton flavor exchange reaction, we need to modify a different portion of the general leptonic scattering kernel. The necessary modifications to include the rest mass difference between initial and final state charged leptons are however quite similar. We again include the additional positively charged process to the already derived negatively charged process from Ref. [75].

The absorption kernel simplifies from Eq. 6.1 to

$$R^{\mathrm{out}}_{\mathrm{LFC}}\left(E_1, E_3, \theta_{13}\right) = \frac{2\pi}{\Delta^5}\alpha_2 \left(\tilde{A}_2 I_2 + \tilde{B}_2 I_1 + \tilde{C}_2 I_0\right) , \tag{6.36}$$

where the coefficients $\tilde{A}_2$, $\tilde{B}_2$, $\tilde{C}_2$ of Eqs. (6.10–6.12) are modified in bold to be

$$\begin{aligned}
\tilde{A}_2 = \;& E_1 E_3 \left(1 - \cos\theta_{13}\right)^2 \left[E_1^2 + E_1 E_3 \left(3 + \cos\theta_{13}\right) + E_3^2\right] , && (6.37)\\
\tilde{B}_2 = \;& E_1 E_3^2 \left(1 - \cos\theta_{13}\right)^2 \left[E_1^2 \left(1 + 3\cos\theta_{13}\right) + E_1 E_3 \left(-3 + \cos\theta_{13}\right) - 2E_3^2\right] && (6.38)\\
+ \;& \boldsymbol{Q\left(1 - \cos\theta_{13}\right)\left[E_1^3 + E_1^2 E_3\left(2 + \cos\theta_{13}\right) - E_1 E_3^2\left(2 + \cos\theta_{13}\right) - E_3^3\right]} ,\\
\tilde{C}_2 = \;& E_1 E_3^3 \left(1 - \cos\theta_{13}\right)^2 \left[E_1^2 \left(-\frac{1}{2} + \frac{3}{2}\cos^2\theta_{13}\right) - 2E_1 E_3 \cos\theta_{13} + E_3^2\right] && (6.39)\\
+ \;& \frac{1}{2} E_1 E_3 \left(1 - \cos^2\theta_{13}\right) \Delta^2 m_2^2\\
+ \;& \boldsymbol{Q E_3\left(1 - \cos\theta_{13}\right)\left[E_1^3 \cos\theta_{13} + E_1^2 E_3\left(-2 + \cos^2\theta_{13}\right) - E_1 E_3^2 \cos\theta_{13} + E_3^3\right]}\\
+ \;& \boldsymbol{Q^2\left[E_1^2 \cos\theta_{13} - E_1 E_3\left(\frac{3}{2} + \frac{1}{2}\cos^2\theta_{13}\right) + E_3^2 \cos\theta_{13}\right]} ,
\end{aligned}$$

and E_-, Q, k and η' are the same as in Sec. 6.3.1.

We can again specialize the scattering kernel via the following replacements.

Electron antineutrino absorption on electron

$$\nu_1 \to \overline{\nu}_{\mathrm{e}}, \quad \ell_2 \to \mathrm{e}^-, \quad \nu_3 \to \overline{\nu}_{\mu}, \quad \ell_4 \to \mu^-, \quad m_2 = m_{\mathrm{e}}, \quad m_4 = m_{\mu}, \quad \alpha_2 = 4$$

Table 6.10: Particle assignments of $\overline{\nu}_{\mathrm{e}} + \mathrm{e}^- \leftrightharpoons \overline{\nu}_{\mu} + \mu^-$.

Electron neutrino absorption on positron

$$\nu_1 \to \nu_\mathrm{e}, \quad \ell_2 \to \mathrm{e}^+, \quad \nu_3 \to \nu_\mu, \quad \ell_4 \to \mu^+, \quad m_2 = m_\mathrm{e}, \quad m_4 = m_\mu, \quad \alpha_2 = 4$$

Table 6.11: Particle assignments of $\nu_\mathrm{e} + \mathrm{e}^+ \leftrightharpoons \nu_\mu + \mu^+$.

6.3.3 Summary

The results of Secs. 6.3.1 and 6.3.2 can easily be summarized using the definition of Eq. 6.1 with the above-introduced rest mass modifications to be

ν_1	ℓ_2	α_1	α_2	α_3
ν_e	e^+	0	4	0
$\overline{\nu}_\mathrm{e}$	e^-	0	4	0
ν_μ	e^-	4	0	0
$\overline{\nu}_\mu$	e^+	4	0	0

Table 6.12: Coupling constants for leptonic neutrino absorption reactions.

with zero for all other combinations.

6.3.4 Reverse reactions

The reserve reactions that convert muons back to electrons for lepton flavor exchange from Sec. 6.3.1 and for lepton favor conversion from Sec. 6.3.2, can again be calculated using the detailed-balance relations. Note however that the transpositional symmetry described in Ref. [20] does not link the positive and negative energy transfers anymore, due to the different initial and final state neutrinos. All combinations of incoming and outgoing neutrino energies therefore need to be calculated independently. The in/out-invariance $R^{\text{in}}\left(E_3, E_1, \theta_{13}\right) = R^{\text{out}}\left(E_1, E_3, \theta_{13}\right)$, arising out of lepton number conservation, however allows us to directly calculate the out-direction of the reversed rate $\nu_3 + \mu^{\mp} \to \nu_1 + \mathrm{e}^{\mp}$ that would otherwise require a separate calculation in addition to the out-direction of the original rate $\nu_1 + \mathrm{e}^{\mp} \to \nu_3 + \mu^{\mp}$.

Lepton flavor exchange

$$R^{\text{out}}_{\nu_{\mathrm{e}}+\mu^- \to \nu_\mu+\mathrm{e}^-}\left(E_{\nu_{\mathrm{e}}}, E_{\nu_\mu}, \theta_{13}\right) = R^{\text{out}}_{\nu_\mu+\mathrm{e}^- \to \nu_{\mathrm{e}}+\mu^-}\left(E_{\nu_\mu}, E_{\nu_{\mathrm{e}}}, \theta_{13}\right) \times \exp\left[\left(\mu_{\mu^-} - \mu_{\mathrm{e}^-} + E_{\nu_{\mathrm{e}}} - E_{\nu_\mu}\right)/T\right] = R^{\text{in}}_{\nu_\mu+\mathrm{e}^- \to \nu_{\mathrm{e}}+\mu^-}\left(E_{\nu_\mu}, E_{\nu_{\mathrm{e}}}, \theta_{13}\right), \quad (6.40)$$

$$R^{\text{out}}_{\overline{\nu}_{\mathrm{e}}+\mu^+ \to \overline{\nu}_\mu+\mathrm{e}^+}\left(E_{\overline{\nu}_{\mathrm{e}}}, E_{\overline{\nu}_\mu}, \theta_{13}\right) = R^{\text{out}}_{\overline{\nu}_\mu+\mathrm{e}^+ \to \overline{\nu}_{\mathrm{e}}+\mu^+}\left(E_{\overline{\nu}_\mu}, E_{\overline{\nu}_{\mathrm{e}}}, \theta_{13}\right) \times \exp\left[\left(\mu_{\mathrm{e}^-} - \mu_{\mu^-} + E_{\overline{\nu}_{\mathrm{e}}} - E_{\overline{\nu}_\mu}\right)/T\right] = R^{\text{in}}_{\overline{\nu}_\mu+\mathrm{e}^+ \to \overline{\nu}_{\mathrm{e}}+\mu^+}\left(E_{\overline{\nu}_\mu}, E_{\overline{\nu}_{\mathrm{e}}}, \theta_{13}\right). \quad (6.41)$$

Lepton flavor conversion

$$R^{\text{out}}_{\overline{\nu}_\mu+\mu^- \to \overline{\nu}_{\mathrm{e}}+\mathrm{e}^-}\left(E_{\overline{\nu}_\mu}, E_{\overline{\nu}_{\mathrm{e}}}, \theta_{13}\right) = R^{\text{out}}_{\overline{\nu}_{\mathrm{e}}+\mathrm{e}^- \to \overline{\nu}_\mu+\mu^-}\left(E_{\overline{\nu}_{\mathrm{e}}}, E_{\overline{\nu}_\mu}, \theta_{13}\right) \times \exp\left[\left(\mu_{\mu^-} - \mu_{\mathrm{e}^-} + E_{\overline{\nu}_\mu} - E_{\overline{\nu}_{\mathrm{e}}}\right)/T\right] = R^{\text{in}}_{\overline{\nu}_{\mathrm{e}}+\mathrm{e}^- \to \overline{\nu}_\mu+\mu^-}\left(E_{\overline{\nu}_{\mathrm{e}}}, E_{\overline{\nu}_\mu}, \theta_{13}\right) \cdot, \quad (6.42)$$

$$R^{\text{out}}_{\nu_\mu+\mu^+ \to \nu_{\mathrm{e}}+\mathrm{e}^+}\left(E_{\nu_\mu}, E_{\nu_\mu}, \theta_{13}\right) = R^{\text{out}}_{\nu_{\mathrm{e}}+\mathrm{e}^+ \to \nu_\mu+\mu^+}\left(E_{\nu_{\mathrm{e}}}, E_{\nu_\mu}, \theta_{13}\right) \times \exp\left[\left(\mu_{\mathrm{e}^-} - \mu_{\mu^-} + E_{\nu_\mu} - E_{\nu_{\mathrm{e}}}\right)/T\right] = R^{\text{in}}_{\nu_{\mathrm{e}}+\mathrm{e}^+ \to \nu_\mu+\mu^+}\left(E_{\nu_{\mathrm{e}}}, E_{\nu_\mu}, \theta_{13}\right). \quad (6.43)$$

6.4 Inverse lepton decay reactions

$\overline{\nu}_{\mathrm{e}} + \mathrm{e}^{-} + \nu_{\mu} \leftrightharpoons \mu^{-}$
$\nu_{\mathrm{e}} + \mathrm{e}^{+} + \overline{\nu}_{\mu} \leftrightharpoons \mu^{+}$

Table 6.13: Inverse muon decay reactions.

The case of inverse lepton decay $\nu_1 + \ell_2 + \nu_3 \leftrightharpoons \ell_4$ has a similar matrix element to the leptonic scattering reactions introduced above, and most of it can be reused by only changing particle momenta as in Ref. [75]. They are similar in structure to neutrino pair annihilation kernels, as one has two neutrinos in the initial state.

The three-body kernel for this reaction is

$$R_{\mathrm{ILD}}^{\mathrm{out}}\left(E_1, E_3, \theta_{13}\right) = \frac{G_{\mathrm{F}}^2}{2\pi^2}\alpha_1 R_1\left(E_1, E_3, \theta_{13}\right) , \tag{6.44}$$

with θ_{13} being the angle between the two ingoing neutrinos.

The angle- and energy dependent kinematic integral R_1 in Ref. [75] is given by

$$R_1\left(E_1, E_3, \theta_{13}\right) = \int \mathrm{d}^3\vec{p}_2\, \mathrm{d}^3\vec{p}_4\, \frac{\left(\vec{p}_1 \cdot \vec{p}_2\right)\left(\vec{p}_3 \cdot \vec{p}_4\right)}{E_1 E_2 E_3 E_4}\delta^4\left(\vec{p}_1 + \vec{p}_2 + \vec{p}_3 - \vec{p}_4\right) f_2\left(E_2\right)\left[1 - f_4\left(E_4\right)\right] . \tag{6.45}$$

This integral has again been solved analytically up to a remaining integration over E_2 in Ref. [75] and we repeat their formulae here.

$$R_1\left(E_1, E_3, \theta_{13}\right) = \frac{2\pi}{\Delta^5}\left(\tilde{A}_1 I_2 + \tilde{B}_1 I_1 + \tilde{C}_1 I_0\right) , \tag{6.46}$$

with the coefficients $\tilde{A}_1,\ \tilde{B}_1,\ \tilde{C}_1$ being given by

$$\tilde{A}_1 = E_1 E_3\left(1 - \cos\theta_{13}\right)^2\left[-E_1^2 + E_1 E_3\left(3 + \cos\theta_{13}\right) - E_3^2\right] , \tag{6.47}$$

$$\begin{aligned}\tilde{B}_1 = {} & E_1^2 E_3\left(1 - \cos\theta_{13}\right)^2\left[-2E_1^2 + E_1 E_3\left(3 - \cos\theta_{13}\right) + E_3^2\left(1 + 3\cos\theta_{13}\right)\right] \\ & + Q\left(1 - \cos\theta_{13}\right)\left[E_1^3 - E_1^2 E_3\left(2 + \cos\theta_{13}\right) - E_1 E_3^2\left(2 + \cos\theta_{13}\right) + E_3^3\right] ,\end{aligned} \tag{6.48}$$

$$\begin{aligned}\tilde{C}_1 = {} & -E_1^3 E_3\left(1 - \cos\theta_{13}\right)^2\left[E_1^2 + 2E_1 E_3\cos\theta + E_3^2\left(-\frac{1}{2} + \frac{3}{2}\cos^2\theta_{13}\right)\right] \\ & - \frac{1}{2}E_1 E_3\left(1 - \cos^2\theta_{13}\right)\Delta^2 m_2^2 \\ & + QE_1\left(1 - \cos\theta_{13}\right)\left[E_1^3 + E_1^2 E_3\cos\theta_{13} + E_1 E_3^2\left(-2 + \cos^2\theta_{13}\right) - E_3^3\cos\theta_{13}\right] \\ & + Q^2\left[E_1^2\cos\theta_{13} + E_1 E_3\left(\frac{3}{2} + \frac{1}{2}\cos^2\theta_{13}\right) + E_3^2\cos\theta_{13}\right] .\end{aligned} \tag{6.49}$$

The energy integrals $I_K = \int_{E_-}^{E+} \mathrm{d}E_2\, E_2^k f_2\left(E_2\right)\left[1 - f_4\left(E_2 + E_1 + E_3\right)\right]\Theta\left(k - 1\right)$ can again be defined in terms of combinations of ultrarelativistic Fermi-Dirac integrals as in Eqs. (6.16–6.18),

$$
\begin{aligned}
I_0 &= \int_{E_-}^{E_+} \mathrm{d}E_2\, f_2\left(E_2\right)\left[1 - f_4\left(E_2 + E_1 - E_3\right)\right]\Theta\left(k-1\right) \\
&= T f_\gamma\left(\eta' - \eta\right)\left\{\left[F_0\left(\eta' - y_-\right) - F_0\left(\eta - y_-\right)\right] - \left[F_0\left(\eta' - y_+\right) - F_0\left(\eta - y_+\right)\right]\right\}\,, \qquad (6.50) \\
I_1 &= \int_{E_-}^{\infty} \mathrm{d}E_2\, E_2 f_2\left(E_2\right)\left[1 - f_4\left(E_2 + E_1 - E_3\right)\right]\Theta\left(k-1\right) \\
&= T^2 f_\gamma\left(\eta' - \eta\right)\Big\{\left[F_1\left(\eta' - y_-\right) - F_1\left(\eta - y_-\right)\right] - \left[F_1\left(\eta' - y_+\right) - F_1\left(\eta - y_+\right)\right] \\
&+\, y_-\left[F_0\left(\eta' - y_-\right) - F_0\left(\eta - y_-\right)\right] - y_+\left[F_0\left(\eta' - y_+\right) - F_0\left(\eta - y_+\right)\right]\Big\}\,, \qquad (6.51) \\
I_2 &= \int_{E_-}^{E_+} \mathrm{d}E_2\, E_2^2 f_2\left(E_2\right)\left[1 - f_4\left(E_2 + E_1 - E_3\right)\right]\Theta\left(k-1\right) \\
&= T^3 f_\gamma\left(\eta' - \eta\right)\Big\{\left[F_2\left(\eta' - y_-\right) - F_2\left(\eta - y_-\right)\right] - \left[F_2\left(\eta' - y_+\right) - F_2\left(\eta - y_+\right)\right] \\
&+\, 2y_-\left[F_1\left(\eta' - y_-\right) - F_1\left(\eta - y_-\right)\right] - 2y_+\left[F_1\left(\eta' - y_+\right) - F_1\left(\eta - y_+\right)\right] \\
&+\, y_-^2\left[F_0\left(\eta' - y_-\right) - F_0\left(\eta - y_-\right)\right] - y_+^2\left[F_0\left(\eta' - y_+\right) - F_0\left(\eta - y_+\right)\right]\Big\}\,. \qquad (6.52)
\end{aligned}
$$

The lower and upper integral bounds are given by

$$
E_\pm = \frac{1}{2}\left[\left(E_3 + E_1\right)\left(k-1\right) \pm \sqrt{\left(E_1^2 + E_3^2 + 2E_1 E_3 \cos\theta_{13}\right)\left[\left(1-k\right)^2 - \frac{2m_2^2}{E_1 E_3\left(1 - \cos\theta_{13}\right)}\right]}\right]\,, \qquad (6.53)
$$

with Q, and k as in Eqs. (6.32 and 6.34) respectively. The upper limit and Heaviside function are a consequence of kinematic considerations, and especially the Heaviside function prohibits certain combinations of E_1, E_3 and $\cos\theta_{13}$ that are kinematically forbidden (see Ref. [75]). The Heaviside function also implies that a particle can not directly decay into a heavier particle, as that would violate momentum conservation. The Fermi-Dirac integrals F_k are defined as in Eq. 6.20 and the function f_γ is defined in Eq. 6.21.

The appearing coefficients are

$$
y_\pm = \frac{E_\pm}{T}\,, \qquad (6.54)
$$

$$
\eta = \frac{\mu_2}{T}\,, \qquad (6.55)
$$

$$
\eta' = \eta - \frac{E_1 + E_3 + \mu_2 - \mu_4}{T}\,. \qquad (6.56)
$$

Inverse muon decay

$$\nu_1 \to \overline{\nu}_{\mathrm{e}}, \quad \ell_2 \to \mathrm{e}^-, \quad \nu_3 \to \nu_\mu, \quad \ell_4 \to \mu^-, \quad m_2 = m_{\mathrm{e}}, \quad m_4 = m_\mu, \quad \alpha_1 = 4$$

Table 6.14: Particle assignments of $\overline{\nu}_{\mathrm{e}} + \mathrm{e}^- + \nu_\mu \leftrightharpoons \mu^-$.

Inverse antimuon decay

$$\nu_1 \to \nu_{\mathrm{e}}, \quad \ell_2 \to \mathrm{e}^+, \quad \nu_3 \to \overline{\nu}_\mu, \quad \ell_4 \to \mu^+, \quad m_2 = m_{\mathrm{e}}, \quad m_4 = m_\mu, \quad \alpha_1 = 4$$

Table 6.15: Particle assignments of $\nu_{\mathrm{e}} + \mathrm{e}^+ + \overline{\nu}_\mu \leftrightharpoons \mu^+$.

6.4.1 Reverse reactions

The reverse reaction of inverse muon decay and inverse antimuon decay can again be calculated using detailed balance where

$$R^{\mathrm{in}}_{\overline{\nu}_{\mathrm{e}}+\mathrm{e}^-+\nu_\mu \leftrightharpoons \mu^-}\left(E_{\overline{\nu}_{\mathrm{e}}}, E_{\nu_\mu}, \theta_{13}\right) = R^{\mathrm{out}}_{\overline{\nu}_{\mathrm{e}}+\mathrm{e}^-+\nu_\mu \leftrightharpoons \mu^-}\left(E_{\overline{\nu}_{\mathrm{e}}}, E_{\nu_\mu}, \theta_{13}\right) \exp\left(\frac{\mu_{\mu^-} - \mu_{\mathrm{e}^-} - E_{\overline{\nu}_{\mathrm{e}}} - E_{\nu_\mu}}{T}\right), \tag{6.57}$$

$$R^{\mathrm{in}}_{\nu_{\mathrm{e}}+\mathrm{e}^++\overline{\nu}_\mu \leftrightharpoons \mu^+}\left(E_{\nu_{\mathrm{e}}}, E_{\overline{\nu}_\mu}, \theta_{13}\right) = R^{\mathrm{out}}_{\nu_{\mathrm{e}}+\mathrm{e}^++\overline{\nu}_\mu \leftrightharpoons \mu^+}\left(E_{\nu_{\mathrm{e}}}, E_{\overline{\nu}_\mu}, \theta_{13}\right) \exp\left(\frac{\mu_{\mathrm{e}^-} - \mu_{\mu^-} - E_{\nu_{\mathrm{e}}} - E_{\overline{\nu}_\mu}}{T}\right). \tag{6.58}$$

In addition, the transpositional symmetry of neutrino species for a general inverse lepton decay reaction in both directions is

$$R^{\mathrm{in/out}}\left(E_1, E_3, \theta_{13}\right) = R^{\mathrm{in/out}}\left(E_3, E_1, \theta_{13}\right). \tag{6.59}$$

7 Semileptonic reactions

Semileptonic reactions are the well-known charged current reactions of $\nu_1 + \mathrm{N}_2 \leftrightharpoons \nu_3 + \mathrm{N}_4$ where $\mathrm{N}_{2,4}$ are either a neutron or proton. These reactions are typically called a charged beta reaction, and for ν_e and $\overline{\nu}_\mathrm{e}$ form the dominant opacity source in CCSN. These reactions are:

- absorption of electron neutrinos on free neutrons $\nu_\mathrm{e} + \mathrm{n} \leftrightharpoons \mathrm{e}^- + \mathrm{p}$
- absorption of electron antineutrinos on free protons $\overline{\nu}_\mathrm{e} + \mathrm{p} \leftrightharpoons \mathrm{e}^+ + \mathrm{n}$
- absorption of electron neutrinos on heavy nuclei $\nu_\mathrm{e} + \mathrm{A_Z} \leftrightharpoons \mathrm{e}^- + \mathrm{A_{Z+1}}$

We will concern our self only with the nucleonic reactions here, as nuclei do not exist at temperatures and densities where muons might exist in equilibrium.

The muonic reactions we will introduce here are

- absorption of μ neutrinos on free neutrons $\nu_\mu + \mathrm{n} \leftrightharpoons \mu^- + \mathrm{p}$
- absorption of μ antineutrinos on free protons $\overline{\nu}_\mu + \mathrm{p} \leftrightharpoons \mu^+ + \mathrm{n}$

The reaction kernel for electron (anti-)neutrino absorption is identical to the case of μ (anti-)neutrinos, and we can reuse the general formalism. However, due to the large rest mass of the muon, the common approximation of a massless final state ultrarelativistic charged lepton cannot be applied anymore. Instead, as in the purely leptonic reactions, we need to treat the muons as arbitrarily relativistic particles. Fortunately, the required changes to the interaction kernels for absorption reactions on nucleons remain small, as the target particles itself stay mostly nonrelativistic up to a few times the saturation density to good approximation (cf. Ref. [115]). The only significant modification is the separation of muon momentum and energy that introduces a lower limit to the minimum lepton energy, but the nucleonic kinematics can be retained in full generality.

Here we first introduce a simple modification of the Reddy elastic absorption kernel (Ref. [115]) for nonrelativistic interacting baryons, where initial and final state nucleon momenta are identical, and it is assumed that all surplus energy is transferred to the final state charged lepton. Furthermore, we will extend our modifications to the more involved calculation of inelastic absorption, where energy transfer to the nucleons can take place, and the energy transfer to the final state lepton becomes a function of the initial and final state nucleon energies.

7.1 Elastic case

The unmodified form for an ultrarelativistic massless lepton as presented in Ref. [115] in the elastic nonrelativistic interacting baryon approximation is

$$\frac{1}{\lambda}(E_1) = \frac{G_\mathrm{F}^2}{\pi}\left(G_\mathrm{V}^2 + 3G_\mathrm{A}^2\right) E_3^2 \left(1 - f_3(E_3)\right) \frac{n_2 - n_4}{1 - \exp\left(\left(\mu_4 - U_4 - \mu_2 + U_2\right)/T\right)}\,, \tag{7.1}$$

with

$$E_3 = E_1 + \Delta U + Q\,, \tag{7.2}$$

being the energy of the final-state lepton, and quantities with index 2 and 4 being the respective initial and final state nucleon quantities. The difference of the interaction potentials $\Delta U = U_2 - U_4$ is a result of the nonrelativistic dispersion relation

$$E_i^\mathrm{NR} = \frac{p_i^2}{2m_i^*} + U_i\,, \tag{7.3}$$

with the Landau effective masses of the respective nucleons m_i^* and the mass difference $Q = m_2 - m_4$. Accounting for a finite lepton mass is an easy task by the replacement of $E_3^2 \to p_3 E_3$ and $p_3 = \sqrt{E_3^2 - m_3^2}$. We will also include the Cabibbo-angle $V_{\mathrm{ud}} = \cos\theta_{\mathrm{C}} = 0.97427$ in the formula for quark flavor changing weak interactions. The final result is then simply

$$\frac{1}{\lambda}(E_1) = \frac{G_{\mathrm{F}}^2 V_{\mathrm{ud}}^2}{\pi}\left(G_{\mathrm{V}}^2 + 3G_{\mathrm{A}}^2\right)\sqrt{E_3^2 - m_3^2}E_3\left(1 - f_3(E_3)\right) \times \frac{n_2 - n_4}{1 - \exp\left(\left(\mu_4 - U_4 - \mu_2 + U_2\right)/T\right)}\Theta(E_3 - m_3)\,. \quad (7.4)$$

Note that for typical CCSN neutrino energies the approximation $p_{\mathrm{e}} \to E_{\mathrm{e}}$ is reasonable and reproduces the correct cross section. This, however, does not hold for μ neutrino absorption, where the large muon rest mass leads to a significantly smaller momentum of the final-state lepton, as well as setting a strict lower limit on the neutrino energies able to undergo an absorption reaction.

7.2 Inelastic case

The previous elastic case is calculated for the case of initial and final nucleon momenta being identical, i.e., $p_{\mathrm{n}} = p_{\mathrm{p}}$, where additionally the difference in kinetic energy of neutron and proton, expressed by $E_{\mathrm{n/p}} = \frac{p_{\mathrm{n/p}}^2}{2m_{\mathrm{n/p}}}$, is neglected and only the rest mass difference is kept. It is, however, possible to perform an inelastic calculation that takes nucleon thermal motions as well as neutrino energy and momentum transfer to the nucleons fully into account. In VERTEX-PROMETHEUS the inelastic absorption kernel is derived from the nonrelativistic formulae of Ref. [18], which include the effect of nucleon-nucleon correlations but assume a single nucleon mass. We will describe here the modifications required for including a finite lepton mass by Refs. [74, 75], as well as the effects of nucleon interaction potentials by Refs. [115, 74, 81].

The unmodified absorption opacity for vanishing lepton mass as given in Ref. [18] is

$$\frac{1}{\lambda}(E_1) = \frac{G_{\mathrm{F}}^2}{4\pi^2}\int_{-\infty}^{E_1}\mathrm{d}\omega\int_{-1}^{1}\mathrm{d}\cos\theta_{13}\,(E_1 - \omega)^2\,\frac{1 - f_3(E_1 - \omega)}{1 - \exp\left(-\left(\omega + \hat{\mu}\right)/T\right)}\Lambda^{\mu\nu}(\omega, q)\,\Im W_{\mu\nu}(\omega, q)\,, \quad (7.5)$$

with $\Lambda^{\mu\nu}(\omega, q)$ being the lepton trace; $\Im W_{\mu\nu}(\omega, q)$ being the imaginary part of the baryonic trace; $\hat{\mu} = \mu_2 - \mu_4$ and $E_3 = E_1 - \omega$. The momentum transfer is given by

$$q = \sqrt{E_1^2 + (E_1 - \omega)^2 - 2E_1(E_1 - \omega)\cos\theta_{13}}\,, \quad (7.6)$$

and the energy transfer by

$$\omega = E_1 - E_3\,. \quad (7.7)$$

The baryonic trace evaluates to

$$W_{ij}(\omega, q) = g_{\mathrm{A}}^2 W_{\mathrm{A}}(\omega, q)\,\delta_{ij} + g_{\mathrm{A}}^2 W_{\mathrm{T}}(\omega, q)\,q_i q_j\,, \quad (7.8)$$

$$W_{00}(\omega, q) = W_{\mathrm{V}}(\omega, q)\,, \quad (7.9)$$

where the tensor contribution W_{T} was dropped in the following derivation. Convoluting the lepton trace with the baryonic trace gives the form of the structure-function

$$S_0(\omega, q) = \Lambda^{\mu\nu}\Im W_{\mu\nu} = 2\left(1 + \cos\theta_{13}\right)\Im W_{\mathrm{V}}(\omega, q) + 2\left(3 - \cos\theta_{13}\right)g_{\mathrm{A}}^2\Im W_{\mathrm{A}}(\omega, q)\,. \quad (7.10)$$

To include correlations in the derivation of the vector and axial components of the polarization tensor the higher order Feynman diagrams of the potential model are summed over in the ring approximation (or Random Phase Approximation) (see Refs. [31, 18])

$$W_{\mathrm{V}}\left(\omega,q\right)=\frac{\Pi^{(0)}\left(w,q\right)}{1-2v_{1}\Pi^{(0)}\left(w,q\right)}\,, \tag{7.11}$$

$$W_{\mathrm{A}}\left(\omega,q\right)=\frac{\Pi^{(0)}\left(w,q\right)}{1-2v_{2}\Pi^{(0)}\left(w,q\right)}\,, \tag{7.12}$$

where $\Pi^{(0)}$ is the polarization function

$$\Pi^{(0)}\left(\omega,q\right)=-2\int\frac{\mathrm{d}^{3}\vec{p}}{\left(2\pi\right)^{3}}\,\frac{f\left(\left|\boldsymbol{p}\right|,\mu_{\mathrm{n}}\right)-f\left(\left|\boldsymbol{p}+\boldsymbol{q}\right|,\mu_{\mathrm{p}}\right)}{\omega+\boldsymbol{\epsilon}_{\boldsymbol{p}}-\boldsymbol{\epsilon}_{\boldsymbol{p}+\boldsymbol{q}}+i\eta}\,, \tag{7.13}$$

and v_1 and v_2 are zero-range potential models fitted to the Landau parameters of Fermi liquid theory as given in Refs. [116, 18].

To now evaluate $\Im W_{\mathrm{V}}$ and $\Im W_{\mathrm{A}}$ both the imaginary and real parts of the polarization function need to be calculated, which have been provided in Ref. [18],

$$\Im\Pi^{(0)}\left(\omega,q\right)=\frac{m^{*2}T}{2\pi q}\ln\left[\frac{1+\exp\left(-Q_{+}^{2}+\mu_{2}/T\right)}{1+\exp\left(-Q_{+}^{2}+\left(\mu_{4}-\omega\right)/T\right)}\right]\,, \tag{7.14}$$

$$\begin{aligned}\Re\Pi^{(0)}\left(\omega,q\right)=&\frac{m^{*2}T}{2\pi^{2}q}\int_{0}^{\infty}\frac{\mathrm{d}s}{s}\,\ln\left[\frac{1+\exp\left(-\left(s+Q_{+}\right)^{2}+\mu_{2}/T\right)\right)}{1+\exp\left(-\left(s-Q_{+}\right)^{2}+\mu_{4}/T\right)}\right]\\&+\;\left(Q_{+}\rightarrow Q_{-},\mu_{2}\rightarrow\mu_{4}\right)\,,\end{aligned} \tag{7.15}$$

where

$$Q_{\pm}=\sqrt{\frac{m^{*}}{2T}}\left(\mp\frac{\omega}{q}+\frac{q}{2m^{*}}\right)\,. \tag{7.16}$$

The imaginary part of the baryonic trace can now be expressed by combinations of the polarization functions

$$\Im W_{\mathrm{V}}\left(\omega,q\right)=\frac{\Im\Pi^{(0)}\left(\omega,q\right)}{\left(1-2v_{1}\Re\Pi^{(0)}\left(\omega,q\right)\right)^{2}+\left(2v_{1}\Im\Pi^{(0)}\left(\omega,q\right)\right)^{2}}\,, \tag{7.17}$$

$$\Im W_{\mathrm{A}}\left(\omega,q\right)=\frac{\Im\Pi^{(0)}\left(\omega,q\right)}{\left(1-2v_{2}\Re\Pi^{(0)}\left(\omega,q\right)\right)^{2}+\left(2v_{2}\Im\Pi^{(0)}\left(\omega,q\right)\right)^{2}}\,. \tag{7.18}$$

By inserting Eqs. (7.17–7.18) into Eq. 7.10 the final inverse mean free path for a correlated nonrelativistic medium in the formulation of Ref. [18] is now

$$\begin{aligned}\frac{1}{\lambda}\left(E_{1}\right)=\frac{G_{\mathrm{F}}^{2}}{2\pi^{2}}\int_{-\infty}^{E_{1}}\mathrm{d}\omega\int\mathrm{d}\cos\theta_{13}\,\left(E_{1}-\omega\right)^{2}\frac{1-f_{3}\left(E_{1}-\omega\right)}{1-\exp\left(-\left(\omega+\hat{\mu}\right)/T\right)}\\\times\left[\left(1+\cos\theta_{13}\right)\Im W_{\mathrm{V}}\left(\omega,q\right)+\left(3-\cos\theta_{13}\right)\Im W_{\mathrm{A}}\left(\omega,q\right)\right]\,.\end{aligned} \tag{7.19}$$

To include a finite lepton mass and mean-field potential interactions one needs to perform the following modifications to the kinematic integral by following additions (A. Lohs, personal communication [74]) printed in bold,

$$\frac{1}{\lambda}(E_1) = \frac{G_{\mathrm{F}}^2 \boldsymbol{V_{\mathrm{ud}}^2}}{2\pi^2} \int_{-\infty}^{E_1-\boldsymbol{m_3}} \mathrm{d}\omega \int_{-1}^{1} \mathrm{d}\cos\theta_{13} \sqrt{(\boldsymbol{E_1}-\boldsymbol{\omega})^2 - \boldsymbol{m_3^2}}\,(\boldsymbol{E_1}-\boldsymbol{\omega}) \times \frac{1-f_3(E_1-\omega)}{1-\exp\left(-(\omega+\hat{\mu})/T\right)} \left[(1+\boldsymbol{v_3}\cos\theta_{13})\,\Im W_{\mathrm{V}}(\omega,q) + (3-\boldsymbol{v_3}\cos\theta_{13})\,\Im W_{\mathrm{A}}(\omega,q)\right], \quad (7.20)$$

where

$$v_3 = \frac{p_3}{E_3} \quad (7.21)$$

is a measure of the relativistic velocity of the final state lepton, and we have again included the Cabibbo-angle V_{ud}.

The polarization functions now also include additional terms accounting for the potential differences of the neutron and proton

$$\Im\Pi^{(0)}(\omega,q) = \frac{m^{*2}T}{2\pi q} \ln\left[\frac{1+\exp\left(-\boldsymbol{Q_+^2} + \tilde{\boldsymbol{\mu}}_{\boldsymbol{2}}/T\right)}{1+\exp\left(-\boldsymbol{Q_+^2} + (\tilde{\boldsymbol{\mu}}_{\boldsymbol{4}} - \omega - \boldsymbol{\Delta U})/T\right)}\right], \quad (7.22)$$

$$\Re\Pi^{(0)}(\omega,q) = \frac{m^{*2}T}{2\pi^2 q} \int_0^\infty \frac{\mathrm{d}s}{s} \ln\left[\frac{1+\exp\left(-\left(s+\boldsymbol{Q}_+\right)^2 + \tilde{\boldsymbol{\mu}}_{\boldsymbol{2}}/T\right)\right)}{1+\exp\left(-\left(s-\boldsymbol{Q}_+\right)^2 + \tilde{\boldsymbol{\mu}}_{\boldsymbol{2}}/T\right)}\right] + \left(\boldsymbol{Q}_+ \to \boldsymbol{Q}_-, \tilde{\boldsymbol{\mu}}_{\boldsymbol{2}} \to \tilde{\boldsymbol{\mu}}_{\boldsymbol{4}}\right), \quad (7.23)$$

where

$$Q_\pm = \sqrt{\frac{m^*}{2T}}\left(\mp\frac{\omega}{q} + \frac{q}{2m^*} \mp \frac{\boldsymbol{\Delta U}}{\boldsymbol{q}}\right), \quad (7.24)$$

and

$$\tilde{\boldsymbol{\mu}}_{\boldsymbol{2,4}} = \mu_{2,4} - \boldsymbol{U_{2,4}}. \quad (7.25)$$

Charged current absorption of electron (anti-)neutrinos and μ (anti-)neutrinos can then easily be calculated by setting $m_3 = m_{\mathrm{e}}$ and $m_3 = m_\mu$ respectively. Note that our implementation of the Burrows&Sawyer ([18]) rates take the neutron/proton mass difference only approximately into account by again neglecting kinetic energy differences due to different nucleon masses and modifying the energy transfer to be $\omega := \omega + m_2 - m_4$.

7.3 Weak magnetism corrections

Additional corrections to the absorption cross section due to the effect of weak magnetism are provided in Ref. [47]. The weak magnetism correction is caused by the parity-violating interference of the weak magnetic moment of the nucleon which ordinarily cancels out in nonrelativistic calculations and only has a net contribution in a relativistic calculation where mixing of the vector-, axial-, and tensor-currents can happen. This energy-dependent correction increases the cross section for high energy neutrinos and decreases the cross section for high energy antineutrinos. The available analytic correction factor of Ref. [47] is written for massless leptons interacting with an initial nucleon at rest. This is an acceptable approximation

for the case of electron neutrino absorption at a relatively low density and temperature. It is however not acceptable for the case of μ neutrino absorption, as the large rest mass of the final-state muon changes the reaction kinematics dramatically. An improvement of the analytic weak magnetism is currently in works by A.Lohs (personal communication), however even there the lepton rest mass is still neglected as an analytic treatment of the appropriate terms is complex. We, therefore, apply the analytical weak magnetism correction only to the electron (anti-)neutrino absorption rates and ignore this correction for the μ (anti-)neutrino absorption rates. A fully relativistic inelastic implementation of weak magnetism into a general interaction kernel is available from Ref. [118], however, as work on nucleon-nucleon correlations in the relativistic framework is still under progress, we will delay implementation until the full relativistic correlated rates are available. For an overview of the effects of weak magnetism and the improvements of the scattering kernel to better include in-medium effects, please refer to Ref. [118] and references within.

7.4 Reverse reactions

The reverse reaction of neutrino absorption is the absorption of a charged lepton on a nucleon which can be calculated from the above inverse mean free paths using the detailed-balance condition given by

$$j\left(E_1\right) = \frac{1}{\lambda}\left(E_1\right) \exp\left(\frac{\mu_4 + \mu_3 - E_1 - \mu_2}{T}\right) = \frac{1}{\lambda}\left(E_1\right) \exp\left(\frac{\mu_4 + \mu_3 - E_1 - \mu_2}{T}\right) = \frac{1}{\lambda}\left(E_1\right) \exp\left(-\frac{E_1 - \mu_1^{\mathrm{eq}}}{T}\right), \quad (7.26)$$

where μ_1^{eq} is the equilibrium chemical potential of the neutrino being absorbed, i.e., $\mu_{\nu_\mathrm{e}}^{\mathrm{eq}} = \mu_{\mathrm{e}^-} + \mu_\mathrm{p} - \mu_\mathrm{n} - Q$ and $\mu_{\nu_\mu}^{\mathrm{eq}} = \mu_{\mu^-} + \mu_\mathrm{p} - \mu_\mathrm{n} - Q$.

Chapter V
Numerical implementation

In this chapter we will introduce our implementation of an efficient calculation of the new opacities introduced in chapter IV, beginning with a required method that sets the basis of our new muonic opacities and is unique to the calculation of arbitrarily relativistic particles. Having established this common core of the muonic opacities, we discuss the implementation of the scattering and absorption kernels into the collision integral of Eq. 5.12 and all required approximations to maintain stable convergence of the VERTEX transport solver. The hydrodynamic source terms governing the creation of net muon number are introduced, and the peculiarities of the coupling between electrons and muons as well as electron neutrinos and μ neutrinos are discussed. Finally, the inverse mean free paths of all new opacities are shown at representative protoneutron star conditions and mean energies.

8 Polylogarithms

The common aspect of all relativistic scattering and absorption rates is the presence of higher order Fermi-Dirac integrals $F_k(z)$that can not be solved analytically except for the lowest rank

$$F_0(z) = \int_0^\infty \mathrm{d}x \, \frac{1}{\exp(x-z)+1} = \ln(1+\exp(z)) \,, \tag{8.1}$$

which is sufficient for non-relativistic calculations of suitably heavy target particles like nucleons and nuclei and with some restrictions also muons. However as we aim to solve the rates in full generality, including all rest mass terms, the need to rapidly calculate the higher rank Fermi-Dirac integrals $F_1(z)$ and $F_2(z)$ cannot be avoided. One simple solution is to use appropriate Gauss-integrals to directly integrate the needed functions numerically. This, however, is met with limited accuracy and high computational effort to calculate the needed amount of exponential functions for each integration point. Another alternative approach is to use an appropriate fit for the values of $F_k(z)$ as given in Ref. [129] that has a sufficiently small error of less than 2%. As the opacities depend on differences of Fermi-Dirac integrals that are sensitive to numerical cancellation, we instead implement the integrals using their polylogarithmic representation of Refs. [65, 86] given by

$$S_n(z) = \frac{(-1)^{n-1}}{(n-2)!} \int_0^1 \mathrm{d}t \, \frac{\ln^{n-2}(t)\,\ln(1-zt)}{t} = \frac{z}{(n-1)!} \int_0^\infty \mathrm{d}t \, \frac{t^{n-1}}{e^t - z} \,, \tag{8.2}$$

$$F_n(z) = -n! S_{n+1}(-e^z) \,, \tag{8.3}$$

$$x = -e^z \,.$$

To speed up computation and maintain machine precision for all values of x, we implement several limiting cases in x via an expansion of the polylogarithm around specific points, in addition to a general purpose accelerated expansion of the polylogarithm for any other value. The primary goal is to avoid an excessive amount of transcendental calculations that otherwise would take up a significant amount of computation time.

In general, any series expansion of polylogarithms is limited to a convergence region of $-1 \leq x \leq 1$, requiring that we first apply the inversion formulas of Ref. [65] to represent any value of x outside the bounded region given above.

$$\begin{cases} S_2(x) = S_2(x) \,, & -1 \leq x \leq 1 \\ S_2(x) = -S_2\left(\frac{1}{x}\right) - \frac{1}{2}z^2 - \frac{\pi^2}{6} \,, & \text{else} \end{cases} \tag{8.4}$$

$$\begin{cases} S_3(x) = S_3(x)\,, & -1 \le x \le 1 \\ S_3(x) = S_3\left(\frac{1}{x}\right) - \frac{1}{6}z^3 - \frac{\pi^2}{6}z\,. & \text{else} \end{cases} \tag{8.5}$$

Once the function value has been rescaled to be between -1 and 1, we can start to solve the polylogarithms using the following cases based on series expansions performed using MATHEMETICA.

$$\begin{cases} S_1(x) = x\,, & |x| \le 4\times10^{-16} \\ S_1(x) = x + \frac{x^2}{2} + \frac{x^3}{3} + \frac{x^4}{4}\,, & 4\times10^{-16} < |x| \le 1\times10^{-4} \\ S_1(x) = -\ln(1-x)\,. & |x| > 1\times10^{-4} \end{cases} \tag{8.6}$$

Here a series expansion is performed even for the simple logarithm as the difference in magnitude between 1 and x can lead to a loss of precision that propagates into the higher ranked polylogarithms. This implementation maintains an exact representation of the logarithm in double precision, identical to truncated arbitrary precision calculations, for all values of x.

The dilogarithm and trilogarithm are a bit more complicated but otherwise follow the same procedure. Here $\hat{x}$ is either x or x^{-1}, depending on the case of Eqs. 8.4 and 8.5.

$$\begin{cases} S_2(\hat{x}) = \hat{x}\,, & |\hat{x}| \le 4\times10^{-16} \\ S_2(\hat{x}) = \hat{x} + \frac{\hat{x}^2}{4} + \frac{\hat{x}^3}{9} + \frac{\hat{x}^4}{16}\,, & 4\times10^{-16} < |\hat{x}| \le 1\times10^{-4} \\ S_2(\hat{x}) = \zeta(2) - \hat{x}_-\left(S_1(\hat{x})+1\right) - \hat{x}_-^2\left(\frac{S_1(\hat{x})}{2}+\frac{1}{4}\right) - \hat{x}_-^3\left(\frac{S_1(\hat{x})}{3}+\frac{1}{9}\right)\,, & 0.99 \le \hat{x} \le 1 \\ S_2(\hat{x}) = -\frac{\zeta(2)}{2} + \hat{x}_+\ln(2) + \frac{\hat{x}_+^2}{4}\left(\ln(4)-1\right) + \hat{x}_+^3\left(\frac{\ln(2)}{3}-\frac{5}{24}\right)\,, & -1 \le \hat{x} \le -0.99 \\ S_2(\hat{x}) \to \text{use series iteration}\,, & \text{else} \end{cases} \tag{8.7}$$

$$\begin{cases} S_3(\hat{x}) = \hat{x}\,, & |\hat{x}| \le 4\times10^{-16} \\ S_3(\hat{x}) = \hat{x} + \frac{\hat{x}^2}{8} + \frac{\hat{x}^3}{27} + \frac{\hat{x}^4}{64}\,, & 4\times10^{-16} < |\hat{x}| \le 1\times10^{-4} \\ S_3(\hat{x}) = \zeta(3) - \zeta(2)\hat{x}_- + \frac{\hat{x}_-^2}{12}\left(6S_1(\hat{x}) - \pi^2 + 9\right) & \\ \qquad + \frac{\hat{x}_-^3}{36}\left(18S_1(\hat{x}) - 2\pi^2 + 21\right)\,, & 0.99 \le \hat{x} \le 1 \\ S_3(\hat{x}) = -\frac{3\zeta(3)}{4} + \frac{\zeta(2)\hat{x}_+}{2} + \frac{\hat{x}_+^2}{24}\left(\pi^2 - 12\ln(2)\right) & \\ \qquad + \frac{\hat{x}_+^3}{36}\left(3 + \pi^2 - 18\ln(2)\right)\,, & -1 \le \hat{x} \le -0.99 \\ S_3(\hat{x}) \to \text{use series iteration}\,, & \text{else} \end{cases} \tag{8.8}$$

where $\hat{x}_- = 1 - \hat{x}$ and $\hat{x}_+ = 1 + \hat{x}$; ζ is the Riemann zeta function with values $\zeta(2) = \frac{\pi^2}{6}$ and $\zeta(3) \approx 1.2020569031595943$.

For the general case in $\hat{x}$ we use an accelerated series expansion of the polylogarithm based on Bernoulli numbers B_j introduced in Ref. [134] which we truncate once the desired accuracy has been reached.

$$S_2(\hat{x}) = \sum_{j=0}^{\infty} \frac{B_j}{(j+1)!} S_1(\hat{x})^{j+1}\,, \tag{8.9}$$

$$S_3(\hat{x}) = \sum_{j=0}^{\infty} \frac{C_3(j)}{(j+1)!} S_1(\hat{x})^{j+1}\,, \tag{8.10}$$

where

$$C_3(j) = \sum_{k=0}^{j} \binom{j}{k} \frac{B_{j-k}}{k+1} B_k \,. \tag{8.11}$$

To speed up the calculation of the coefficients, we precompute them in quad precision via their recursive definition

$$B_j = -\sum_{k=0}^{j-1} \binom{j}{k} \frac{B_k}{n-k+1} \,, \tag{8.12}$$

with $B_1 = 1$ and every uneven $B_{j\geq 3} = 0$.

Using this accelerated general expansion, in combination with the series expansions, allows a high-speed and highly accurate computation of the Fermi-integrals needed for the scattering and absorption kernels in the following sections, and can further be used for the relativistic neutrino-nucleon rates in Refs. [115, 116, 118].

9 Neutrino opacities

9.1 Neutrino–lepton scattering

The inelastic neutrino–lepton scattering rate is implemented into the collision integral as described in Ref. [114],

$$B_{\mathrm{S}}\left(E_1,\mu\right)=2\pi\int_0^\infty \mathrm{d}E_3\,E_3^2\Big\{\left(1-f_\nu\left(E_1,\mu\right)\right)\sum_{l=0}^{\infty}\left(2l+1\right)P_l\left(\mu\right)\phi_l^{\mathrm{in}}\left(E_1,E_3\right)L_l\left(E_3\right) \\ -f_\nu\left(E_1,\mu\right)\sum_{l=0}^{\infty}\left(2l+1\right)P_l\left(\mu\right)\phi_l^{\mathrm{out}}\left(E_1,E_3\right)\left(\delta_{l,0}-L_l\left(E_3\right)\right)\Big\}, \quad (9.1)$$

and its angular moments

$$B_{\mathrm{S}}^{(0)}\left(E_1\right)=2\pi\int_0^\infty \mathrm{d}E_3\,E_3^2\Big\{\sum_{l=0}^{\infty}\left(2l+1\right)\Big(\delta_{l,0}-L_l\left(E_1\right)\phi_l^{\mathrm{in}}\left(E_1,E_3\right)L_l\left(E_3\right)\Big) \\ -\sum_{l=0}^{\infty}\left(2l+1\right)L_l\left(E_1\right)\phi_l^{\mathrm{out}}\left(E_1,E_3\right)\left(\delta_{l,0}-L_l\left(E_3\right)\right)\Big\}, \quad (9.2)$$

$$B_{\mathrm{S}}^{(1)}\left(E_1\right)=2\pi\int_0^\infty \mathrm{d}E_3\,E_3^2\Big\{\sum_{l=0}^{\infty}\left[\delta_{l,1}-\left(l+1\right)L_{l+1}\left(E_1\right)-lL_{l-1}\left(E_1\right)\right]\phi_l^{\mathrm{in}}\left(E_1,E_3\right)L_l\left(E_3\right) \\ -\sum_{l=0}^{\infty}\left[\left(l+1\right)L_{l+1}\left(E_1\right)+lL_{l-1}\left(E_1\right)\right]\phi_l^{\mathrm{out}}\left(E_1,E_3\right)\left(\delta_{l,0}-L_l\left(E_3\right)\right)\Big\}, \quad (9.3)$$

where the Legendre moments $L_l\left(E\right)=\frac{1}{2}\int_{-1}^{1}\mathrm{d}\mu\,P_l\left(\mu\right)f\left(E,\mu\right)$ of the neutrino distribution function are used. These Legendre moments can be written as linear combinations of the angular moments of the neutrino distribution function $I^{(i)}\left(E\right)=\frac{1}{2}\int_{-1}^{1}\mathrm{d}\mu\,\mu^i f\left(E,\mu\right)$ that are evolved in the moment equations. The Legendre moments of the scattering kernel itself are defined as $\phi_l^{\mathrm{in/out}}\left(E_1,E_3\right)=\frac{1}{2}\int_{-1}^{1}\mathrm{d}\cos\theta_{13}\,P_l\left(\cos\theta_{13}\right)R^{\mathrm{in/out}}\left(E_1,E_3,\theta_{13}\right)$, where the scattering kernels of the in- and out-direction can be related using Eq. 6.26. In Ref. [122] it is shown that the cosine of the angle θ_{13} can be written as $\cos\theta_{13}=\mu\mu'+\sqrt{\left(1-\mu^2\right)\left(1-\mu'^2\right)}\cos\left(\phi-\phi'\right)$, and the addition theorem for Legendre polynomials implies

$$P_l\left(\cos\theta_{13}\right)=P_l\left(\mu\right)P_l\left(\mu'\right)+2\sum_{m=1}^{l}\frac{(l-m)!}{(l+m)!}P_l^m\left(\mu\right)P_l^m\left(\mu'\right)\cos\left[m\left(\phi-\phi'\right)\right],$$

which means integration over the θ and ϕ direction can be performed independently. For completeness, we list here the first four Legendre polynomials

$$P_0\left(\mu\right)=\mu^0,$$
$$P_1\left(\mu\right)=\mu^1,$$
$$P_2\left(\mu\right)=\frac{1}{2}\left(3\mu^2-1\right),$$
$$P_3\left(\mu\right)=\frac{1}{2}\left(5\mu^3-3\mu\right).$$

Note that, as we assume azimuthal symmetry of the neutrino distribution function around the radial propagation vector, the integral over ϕ can be performed analytically to result in the 2π factor seen above. In these pure scattering reactions the transpositional symmetry of $\phi_l^{\text{in}}(E_1, E_3) = \phi_l^{\text{out}}(E_3, E_1)$ (see Ref. [20]) as well as detailed balance, allows one to quickly verify that the neutrino number density $\int_0^\infty \mathrm{d}E_1\, E_1^2 B_{\text{S}}^{(0)}(E_1) = 0$ is conserved. The neutrino energy density $\int_0^\infty \mathrm{d}E_1\, E_1^3 B_{\text{S}}^{(0)}(E_1) \neq 0$ is however not conserved, and neutrinos can exchange energy with matter.

Reference [114] gives the source terms that enter the right-hand side of the moment equation and Boltzmann equation.

$$C_{\text{NLS}}(E_1, \mu) = \frac{c}{(2\pi\hbar c)^3} E_1^3 B_{\text{NLS}}(E_1, \mu)\ , \tag{9.4}$$

$$C_{\text{E,NLS}}^{(0)}(E_1) = \frac{c}{(2\pi\hbar c)^3} E_1^3 B_{\text{NLS}}^{(0)}(E_1)\ , \tag{9.5}$$

$$C_{\text{N,NLS}}^{(0)}(E_1) = \frac{c}{(2\pi\hbar c)^3} E_1^2 B_{\text{NLS}}^{(0)}(E_1)\ , \tag{9.6}$$

$$C_{\text{E,NLS}}^{(1)}(E_1) = \frac{c}{(2\pi\hbar c)^3} E_1^3 B_{\text{NLS}}^{(1)}(E_1)\ , \tag{9.7}$$

$$C_{\text{N,NLS}}^{(1)}(E_1) = \frac{c}{(2\pi\hbar c)^3} E_1^2 B_{\text{NLS}}^{(1)}(E_1)\ . \tag{9.8}$$

9.1.1 Neutrino–electron scattering

Neutrino–electron scattering as implemented in PROMETHEUS-VERTEX is based on the Legendre moments of the energy-dependent scattering rate as given in Ref. [139] and implement as in Ref. [114]. This implementation performs the angular integrals in the scattering rate analytically exact, with the caveat that the electron phase-space integration is calculated numerically only for the ultrarelativistic case $p_{\text{e}} = E_{\text{e}}$ using Gaussian quadrature. The neglection of the electron rest mass can lead to errors in conditions where electrons become non-relativistic, which we will explore further in App. A. Additionally this simplification rules out the application of the Yueh&Buchler scattering kernel ([139]) to the case of neutrino–muon scattering which we will demonstrate in Sec. 9.1.2.

Our new implementation of the neutrino–electron scattering rate of Sec. 6.1 has the advantage that it includes all terms of the lepton rest mass and calculates the lepton phase-space numerically exact using the polylogarithms of Sec. 8. The new implementation however has the caveat that it requires numerical integration over the scattering angle using Gaussian quadrature which introduces the complication that the width of this angle is a strong function of the matter temperature and initial lepton momentum. In the case of a target lepton at rest, the scattering angle effectively reduces to a δ-function for each energy transfer $\omega = E_1 - E_3$ that in theory would require an infinite number of Gaussian quadrature points to integrate accurately. In Fig. 9.1a one can see that the scattering angle quickly converges towards a single value in $\cos\theta_{13}$ that needs to be resolved by at least a few Gaussian points. In practice, we limit the number of Gaussian points in $\cos\theta_{13} = [-1 \ldots 1]$ to 24 points, which gives sufficiently accurate results even for non-relativistic but warm electrons as shown in Fig. 9.1b. In combination with precalculated values of the coefficients $\tilde{A}_i$, $\tilde{B}_i$ and $\tilde{C}_i$ of Eqs. (6.6 – 6.14), the quick calculation of the polylogarithms of Sec. 8 allows our new implementation of the scattering kernel to rival the performance of the NES scattering kernel of Refs. [114, 139].

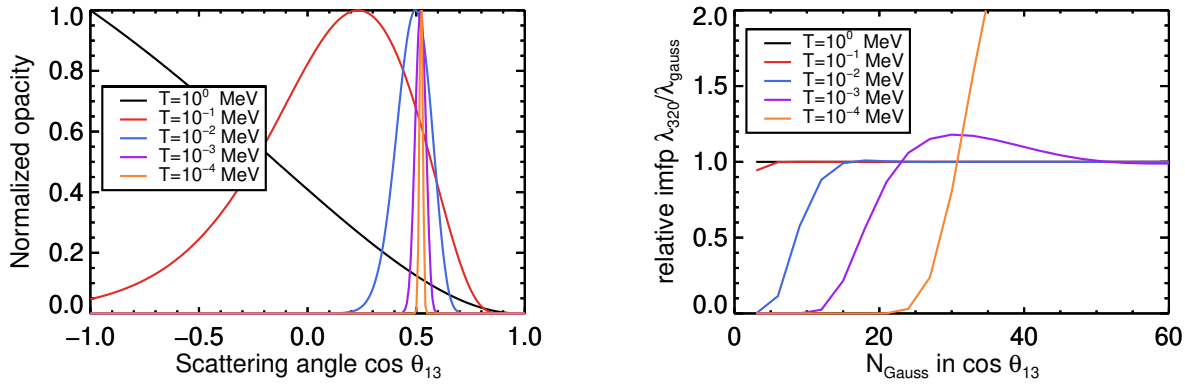

(a) Normalized scattering angle width using 320 Gaussian points.

(b) Relative inverse mean free path compared to an integration with 320 Gaussian points.

Figure 9.1: $\nu_e - e^-$ scattering at $E_1 = 15\,\text{MeV}$, $E_3 = 1\,\text{MeV}$ and $\mu_{e^-} = m_e$ at different temperatures.

9.1.2 Neutrino–Muon scattering

Analogously to the case of neutrino–electron scattering, neutrino–muon scattering can become an additional important contribution to the scattering opacity as well as energy exchange for neutrinos. Due to flavor conservation, μ neutrinos cannot undergo a charged current scattering interaction when scattering on electrons, resulting in a smaller vector current coupling constant of $C_{\text{V,NES}} = -0.5 + 2\sin^2\theta_W = -0.04$. This, in combination with $C_{\text{A,NES}} = -0.5$, leads to combined interaction coefficients of

$$\begin{aligned}
\alpha_1^{\text{NES}} &= \left(C_{\text{V,NES}}^{\nu\mu} + C_{\text{A,NES}}^{\nu\mu}\right)^2 = (-0.04 - 0.5)^2 &&\approx 0.29\,,\\
\alpha_2^{\text{NES}} &= \left(C_{\text{V,NES}}^{\nu\mu} - C_{\text{A,NES}}^{\nu\mu}\right)^2 = (-0.04 + 0.5)^2 &&\approx 0.21\,,\\
\alpha_3^{\text{NES}} &= \left(C_{\text{A,NES}}^{\nu\mu 2} - C_{\text{V,NES}}^{\nu\mu 2}\right) = (-0.5)^2 - (-0.04)^2 &&\approx 0.25\,,
\end{aligned}$$

where α_3 is typically neglected as it is proportional to m_e^2. Including the neutrino–muon scattering channel now adds a charged current channel on muons that allows for significantly larger interaction coefficients albeit with fewer target leptons to scatter on. As we will see, however, the increase in the individual cross section on each muon can compensate for the different abundances of electrons and muons. For μ neutrino-muon scattering the vector current coupling constant becomes $C_{\text{V,NMS}}^{\nu\mu} = 0.5 + 2\sin^2\theta_W = 0.96$ and the axial vector coupling constant becomes $C_{\text{A,NMS}}^{\nu\mu} = 0.5$. The individual combined interaction coefficients then become $\alpha_1^{\text{NMS}} = (0.96 + 0.5)^2 \approx 2.13$, $\alpha_2^{\text{NMS}} = (0.96 - 0.5)^2 \approx 0.21$ and $\alpha_3^{\text{NMS}} = 0.5^2 - 0.96^2 \approx -0.67$. A comparison with the interaction coefficients of μ neutrino–electron scattering shows a factor of ~ 7 difference in the α_1 coefficient, which is sufficient to compensate for the relative muon to electron abundance difference. In contrast to neutrino–electron scattering the α_3 term can also not be neglected anymore, as the squared muon rest mass $m_\mu^2 \approx 105.66^2\,\text{MeV}^2$ is of a similar energy scale as the incoming and outgoing neutrino energies. The influence of the large muon rest mass additionally complicates the problems mentioned in Sec. A as the factor $\beta = \frac{m_\mu}{T} \gg 1$ at all times during core-collapse and the ultrarelativistic approximation is inapplicable. Similarly, the muon rest mass, being only roughly 11% of the nucleon rest mass, is not sufficient for the nonrelativistic approximation to be applicable either. Neutrino–muon scattering can therefore

only be calculated using an arbitrarily relativistic formulation as shown in Eq. 6.1 during all stages of core-collapse supernovae.

The comparatively large rest mass of the muon also influences the energy transfer between a scattering neutrino and a muon as it roughly scales according to a factor of

$$E_3 = \frac{E_1}{1 + E_1/m_\mu \, (1 - \cos\theta_{13})} \,, \tag{9.9}$$

similar to the simple analytical energy scaling relation of Ref. [47] on neutrons. A neutrino of energy $E_1 = 30\,\mathrm{MeV}$ will therefore only transfer around $5-10\,\mathrm{MeV}$ to the medium in each scattering event, as also shown in Fig. 9.2 for other energies. As one can see, the increased rest mass of the muon leads to an energy transfer that is peaked at lower energies compared to the case of neutrino–electron scattering. The inclusion of neutrino–muon scattering for typical μ neutrino energies therefore mainly increases the transport opacity, as can be seen in Fig. 9.3 for μ neutrinos, without a large effect on thermalization. In contrast to neutrino–nucleon scattering, neutrino–muon scattering does not benefit from an extended scattering atmosphere at low temperatures, as muons are only abundant in the hot PNS mantle. We, therefore, expect neutrino-muon scattering to have no significant bearing on the neutrino–medium coupling.

An additional interesting property of Fig. 9.3 is that $\overline{\nu}_\mu$ scattering opacity on muons and antimuons is suppressed by about a factor of two compared to ν_μ scattering on muons and antimuons. This can again be explained by the same observation as in Ref. [133] for scattering on electrons. Helicity considerations reduce the scattering opacity of $\overline{\nu}_\mu$ on muons to be one-third of the scattering opacity on antimuons, as long as the muons are not degenerate or the incoming neutrino energy is not significantly larger than the muon chemical potential.

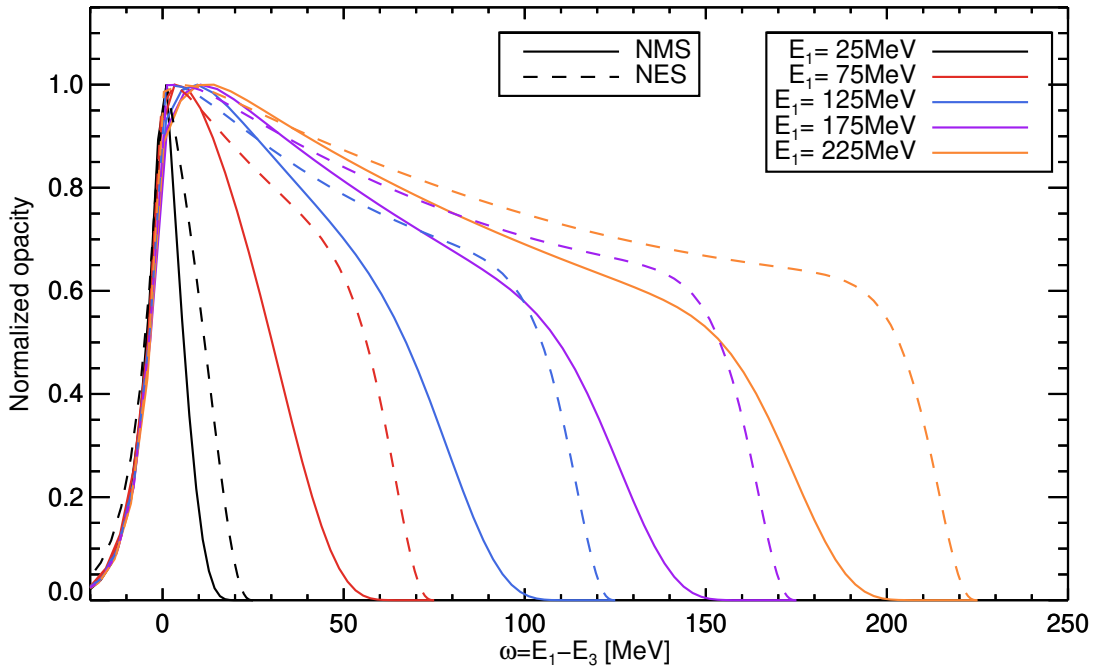

Figure 9.2: Normalized energy transfer of incoming neutrinos on muons (NMS) and electrons (NES) for $T = 5\,\mathrm{MeV}$, $\mu_{\mu^-} = m_\mu$ and $\mu_{\mathrm{e}^-} = m_\mathrm{e}$.

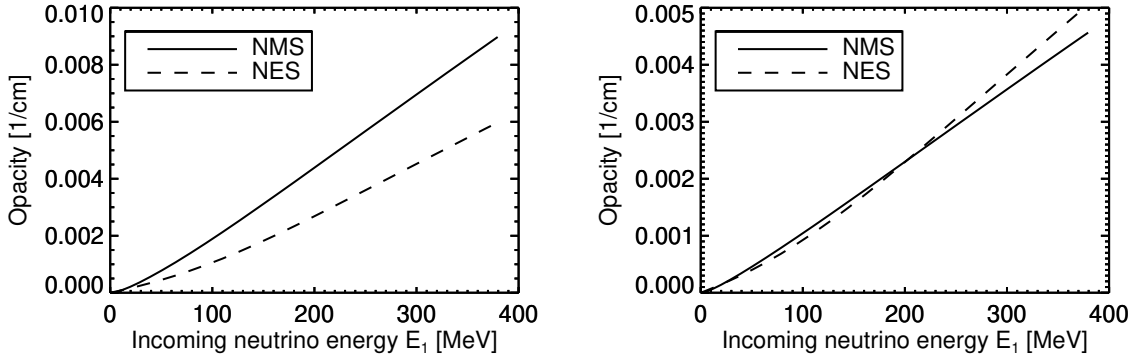

(a) $\nu_\mu - \mu^\mp$ and $\nu_\mu - \mathrm{e}^\mp$ scattering opacity into a free final phase-space.

(b) $\overline{\nu}_\mu - \mu^\mp$ and $\overline{\nu}_\mu - \mathrm{e}^\mp$ scattering opacity into a free final phase-space.

Figure 9.3: Opacity comparison between $\nu_\mu - \mu^\mp$ (NMS) and $\nu_\mu - \mathrm{e}^\mp$ (NES) scattering for $\rho = 2 \times 10^{14}\,\mathrm{g/cm^3}$, $T = 46\,\mathrm{MeV}$, $Y_\mathrm{e} = 0.2$ and $Y_\mu = 0.05$ using SFHo EOS.

9.2 Neutrino–lepton absorption

Neutrino–lepton absorption is implemented on the same principles as used for neutrino–lepton scattering, except that the final state neutrino ν_3 of energy E_3 is not of the same neutrino flavor as the initial state neutrino ν_1 of energy E_1. The implementation into the collision integral is

$$B^{\nu_1}_{\mathrm{NLA}}(E_1,\mu) = 2\pi \int_0^\infty \mathrm{d}E_3\, E_3^2 \Bigg\{ \Big(1 - f_{\nu_1}(E_1,\mu)\Big) \sum_{l=0}^{\infty} (2l+1)\, P_l(\mu)\, \phi_l^{\mathrm{in}}(E_1,E_3)\, L_l^{\nu_3}(E_3) \\ - f_{\nu_1}(E_1,\mu) \sum_{l=0}^{\infty} (2l+1)\, P_l(\mu)\, \phi_l^{\mathrm{out}}(E_1,E_3) \Big(\delta_{l,0} - L_l^{\nu_3}(E_3)\Big) \Bigg\}, \quad (9.10)$$

and its angular moments

$$B^{\nu_1(0)}_{\mathrm{NLA}}(E_1) = 2\pi \int_0^\infty dE_3\, E_3^2 \Bigg\{ \sum_{l=0}^{\infty} (2l+1) \Big(\delta_{l,0} - L_l^{\nu_1}(E_1)\, \phi_l^{\mathrm{in}}(E_1,E_3)\, L_l^{\nu_3}(E_3)\Big) \\ - \sum_{l=0}^{\infty} (2l+1)\, L_l^{\nu_1}(E_1)\, \phi_l^{\mathrm{out}}(E_1,E_3) \Big(\delta_{l,0} - L_l^{\nu_3}(E_3)\Big) \Bigg\}, \quad (9.11)$$

$$B^{\nu_1(1)}_{\mathrm{NLA}}(E_1) = 2\pi \int_0^\infty dE_3\, E_3^2 \Bigg\{ \sum_{l=0}^{\infty} \Big[\delta_{l,1} - (l+1)\, L_{l+1}^{\nu_1}(E_1) - l L_{l-1}^{\nu_1}(E_1)\Big]\, \phi_l^{\mathrm{in}}(E_1,E_3)\, L_l^{\nu_3}(E_3) \\ - \sum_{l=0}^{\infty} \Big[(l+1)\, L_{l+1}^{\nu_1}(E_1) + l L_{l-1}^{\nu_1}(E_1)\Big]\, \phi_l^{\mathrm{out}}(E_1,E_3) \Big(\delta_{l,0} - L_l^{\nu_3}(E_3)\Big) \Bigg\}, \quad (9.12)$$

with the Legendre moments defined in Sec. 9.1, except now for different neutrino species.

Note that the transpositional symmetry of Ref. [20] does not hold anymore and the in/out-Legendre moments are now only coupled by the detailed-balance condition of $\phi_l^{\mathrm{in}}(E_1,E_3) = \phi_l^{\mathrm{out}}(E_1,E_3)\, \exp\left[(\mu_4 - \mu_2 + E_1 - E_3)/T\right]$, where μ_4 and μ_2 are the chemical potential of the respective final and initial state charged lepton. This means that the neutrino number density of a single species is not conserved anymore by the absorption reaction, and in extension that also

the net neutrino number density is changed. Lepton flavor number conservation, therefore, requires that the net electron or net muon number also has to change in corresponding amounts,

$$Q_{\mathrm{N},4} = -4\pi m_{\mathrm{B}} \int_0^\infty \mathrm{d}E_1 \, \frac{c}{(2\pi\hbar c)^3} E_1^2 B_{\mathrm{NLA}}^{\nu_1(0)}(E_1) = -Q_{\mathrm{N},2}\,, \tag{9.13}$$

where m_{B} is the baryon mass in gram. Note however that the charge is conserved in this reaction and so the sum $Y_{\mathrm{e}} + Y_\mu$ of the net lepton number densities remains unchanged. As the number of charged leptons remains unchanged, lepton number conservation then also requires

$$\int_0^\infty \mathrm{d}E_1 \, E_1^2 B_{\mathrm{NLA}}^{\nu_1(0)}(E_1) = -\int_0^\infty \mathrm{d}E_3 \, E_3^2 B_{\mathrm{NLA}}^{\nu_3(0)}(E_3)\,. \tag{9.14}$$

Note also that the net fluid energy source term

$$Q_E = \sum_\nu -4\pi \int_0^\infty \mathrm{d}E_1 \, \frac{c}{(2\pi\hbar c)^3} E_1^3 B_{\mathrm{NLA}}^{\nu_1(0)}(E_1) \tag{9.15}$$

now contains a significant amount of net lepton rest mass being created or destroyed. For example, a reaction of type $\nu_\mu + \mathrm{e}^- \rightarrow \nu_{\mathrm{e}} + \mu^-$ with neutrino energies of $E_{\nu_\mu} = 150\,\mathrm{MeV}$ and $E_{\nu_{\mathrm{e}}} = 45\,\mathrm{MeV}$ does not result in a net internal energy gain of $Q_{\text{relativistic,heat}} = E_{\nu_\mu} - E_{\nu_{\mathrm{e}}} = 105\,\mathrm{MeV}$ but instead in $Q_{\text{internal,heat}} = E_{\nu_\mu} - E_{\nu_{\mathrm{e}}} + \mu_{\mathrm{e}} - \mu_\mu \approx 0\,\mathrm{MeV}$, if the chemical potentials are at their respective rest mass energies. Reactions that create muons are therefore mostly a net sink of neutrino energy that converts internal energy of the neutrino gas into rest mass energy. Conversely, muons transported to the PNS surface by convection, and then decay or are converted to an electron, release their stored rest mass energy in the form of high energy neutrinos. These might deposit a fraction of their energy in the gain layer, in addition to the highly energetic electrons which may thermalize and increase the temperature at the neutrinosphere.

As we are mostly interested in muon production at high temperatures and densities we can use the full formalism of Sec. 6.3.1 including the rest mass and chemical potential difference terms with a relatively low number of angular Gauss integration points in $\theta_{13} = [-1 \ldots 1]$ of only 8 points. The appearance of the rest mass and chemical potential difference terms allows both to compensate each other. This means the absorption kernel can tap the electron chemical potential to aid in the creation of a muon. To illustrate this effect we plot in Fig. 9.4 the normalized energy transfer of the $\nu_\mu + \mathrm{e}^- \rightarrow \nu_{\mathrm{e}} + \mu^-$ reaction for highly degenerate electrons. One can see that there is a significant amount of positive energy transfer to the final state neutrino even when nominally the incoming neutrino does not have sufficient energy to create a muon first. This means that for low energy incoming neutrinos E_1 a large amount of the freed electron chemical potential is transferred to the final state neutrino of $E_3 > E_1$. In combination with the necessary energy trapped in the muon rest mass, this causes a big net energy loss of this reaction if the final state neutrino can escape freely. Increasing incoming neutrino energies shift the curve slightly to the right, but a significant negative energy transfer always remains.

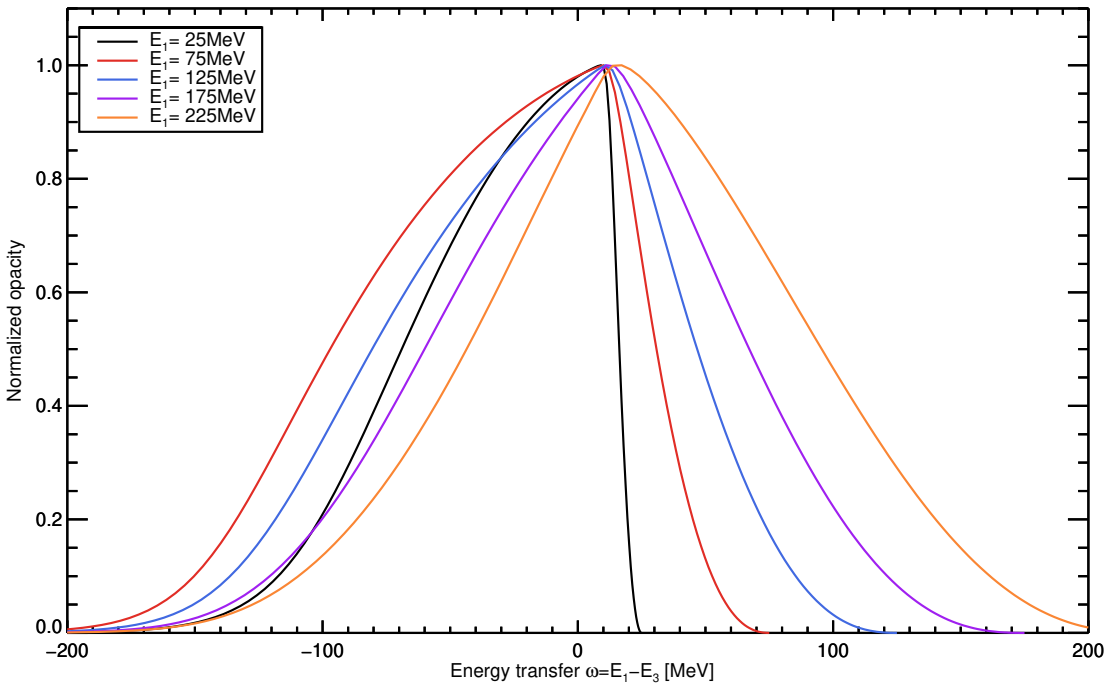

Figure 9.4: Normalized energy transfer spectrum of $\nu_\mu + \mathrm{e}^- \rightarrow \nu_\mathrm{e} + \mu^-$ at $T = 15\,\mathrm{MeV}$, $\mu_{\mathrm{e}^-} = 250\,\mathrm{MeV}$ and $\mu_{\mu^-} = 0\,\mathrm{MeV}$ for different incoming neutrino energies E_1.

9.2.1 Implementation into the transport solver

As the initial and final state neutrino is not of the same species, the numerical coupling of the neutrino species in the transport solver needs to be extended from the typical neutrino pairs $\nu + \bar{\nu}$, necessary for $\mathrm{e}^- - \mathrm{e}^+$ pair annihilation, to a fully coupled transport in which neutrinos can freely transform between any individual combinations. This requires not only significant computational overhead, as the matrix, in general, grows at least quadratically with the number of neutrinos species, but also numerical stability and speed of convergence are reduced as the necessary Jacobian drastically increases in size and complexity. To avoid these complications in this first implementation of the muonic rates, we focus our efforts on the most interesting regime where muons might play a role deep inside the protoneutron star. At sufficiently high densities and temperatures, the neutrino distribution functions can be assumed to be in chemical and thermal equilibrium with the surrounding fluid. The angle integrated neutrino spectrum can therefore be described very accurately by the equilibrium chemical potentials $\mu^{\mathrm{eq}}_{\nu_\mathrm{e}} = \mu_{\mathrm{e}^-} + \mu_\mathrm{p} - \mu_\mathrm{n} - Q$ and $\mu^{\mathrm{eq}}_{\nu_\mu} = \mu_{\mu^-} + \mu_\mathrm{p} - \mu_\mathrm{n} - Q$ in perfect isotropy. Inserting these equilibrium chemical potentials into the collision integrals of Eqs. (9.10 – 9.12) allows one to perform the integral over final state energies analytically, which reduces to

$$
\begin{aligned}
B_{\mathrm{NLA}}^{\nu_1,\mathrm{eq}}\left(E_1,\mu\right) &= 2\pi\int_0^\infty \mathrm{d}E_3\, E_3^2\Big[\Big(1-f_{\nu_1}\left(E_1,\mu\right)\Big)\,\phi_0^{\mathrm{in}}\left(E_1,E_3\right) f_{\nu_3}^{\mathrm{eq}}\left(E_3\right) \\
&\quad - f_{\nu_1}\left(E_1,\mu\right)\phi_0^{\mathrm{out}}\left(E_1,E_3\right)\Big(1-f_{\nu_3}^{\mathrm{eq}}\left(E_3\right)\Big)\Big] \\
&= \Big(1-f_{\nu_1}\left(E_1,\mu\right)\Big)\, j\left(E_1\right) - f_{\nu_1}\left(E_1,\mu\right)\kappa\left(E_1\right)\,, \qquad (9.16)\\
B_{\mathrm{NLA}}^{\nu_1,\mathrm{eq}(0)}\left(E_1\right) &= 2\pi\int_0^\infty dE_3\, E_3^2\Big[\Big(1-L_0^{\nu_1}\left(E_1\right)\phi_0^{\mathrm{in}}\left(E_1,E_3\right) f_{\nu_3}^{\mathrm{eq}}\left(E_3\right)\Big) \\
&\quad - L_0^{\nu_1}\left(E_1\right)\phi_0^{\mathrm{out}}\left(E_1,E_3\right)\Big(1-f_{\nu_3}^{\mathrm{eq}}\left(E_3\right)\Big)\Big] \\
&= \Big(1-L_0^{\nu_1}\left(E_1\right)\Big)\, j\left(E_1\right) - L_0^{\nu_1}\left(E_1\right)\kappa\left(E_1\right)\,, \qquad (9.17)\\
B_{\mathrm{NLA}}^{\nu_1,\mathrm{eq}(1)}\left(E_1\right) &= 2\pi\int_0^\infty dE_3\, E_3^2\Big[-L_1^{\nu_1}\left(E_1\right)\phi_0^{\mathrm{in}}\left(E_1,E_3\right) f_{\nu_3}^{\mathrm{eq}}\left(E_3\right) \\
&\quad - L_1^{\nu_1}\left(E_1\right)\phi_0^{\mathrm{out}}\left(E_1,E_3\right)\Big(1-f_{\nu_3}^{\mathrm{eq}}\left(E_3\right)\Big)\Big] \\
&= -L_1^{\nu_1}\left(E_1\right)\left[j\left(E_1\right)+\kappa\left(E_1\right)\right]\,. \qquad (9.18)
\end{aligned}
$$

Note that all higher orders of $L_l^{\nu_3}$ are zero as the equilibrium distribution is strictly isotropic.

The structure of these collision integral terms is identical to the terms for absorption and emission processes on nucleons. This can be easily understood as in our approximation, for example, $\nu_1 + \ell_2 \leftrightharpoons \nu_3 + \ell_4$ is similar in structure to the reaction $\nu_\mathrm{e} + \mathrm{n} \leftrightharpoons \mathrm{e}^- + \mathrm{p}$, if one assumes that all particles except ν_1 are described by their equilibrium distribution. Similarly, the detailed balance condition linking the in/out-scattering moments given by

$$
\phi_0^{\mathrm{in}}\left(E_1,E_3\right) = \phi_0^{\mathrm{out}}\left(E_1,E_3\right)\,\exp\left[\left(\mu_4-\mu_2+E_1-E_3\right)/T\right]\,, \qquad (9.19)
$$

reduces to

$$
\phi_0^{\mathrm{in}}\left(E_1\right) = \phi_0^{\mathrm{out}}\left(E_1\right)\,\exp\left[\left(E_1+\mu_4-\mu_2-\mu_3\right)/T\right] = \phi_0^{\mathrm{out}}\left(E_1\right)\,\exp\left[\left(E_1-\mu_\nu^{\mathrm{eq}}\right)\right]\,. \qquad (9.20)
$$

This allows us to describe the neutrino absorption on leptons collision integral in the form of a stimulated opacity, following the same implementation as in Sec. A1.1 of Ref. [114].

The collision integral term

$$
B_{\mathrm{NLA}}^{\nu_1,\mathrm{eq}}\left(E_1\right) = \Big(1-f_{\nu_1}\left(E_1,\mu\right)\Big)\, j\left(E_1\right) - f_{\nu_1}\left(E_1,\mu\right)\kappa\left(E_1\right)
$$

can be given in terms of a stimulated opacity

$$
\kappa_{\mathrm{NLA}}^*\left(E_1\right) \coloneqq \frac{1}{1-f_{\nu_1}^{\mathrm{eq}}\left(E_1\right)}\kappa\left(E_1\right) = j\left(E_1\right)+\kappa\left(E_1\right)\,, \qquad (9.21)
$$

resulting in

$$
\begin{aligned}
B_{\mathrm{NLA}}^{\nu_1,\mathrm{eq}}\left(E_1,\mu\right) &= \kappa_{\mathrm{NLA}}^*\left(E_1\right)\Big(f_{\nu_1}^{\mathrm{eq}}\left(E_1\right)-f\left(E_1,\mu\right)\Big)\,, \qquad (9.22)\\
B_{\mathrm{NLA}}^{\nu_1,\mathrm{eq}(0)}\left(E_1\right) &= \kappa_{\mathrm{NLA}}^*\left(E_1\right)\Big(L_{\mathrm{eq}}^{\nu 1}\left(E_1\right)-L_0^{\nu_1}\left(E_1\right)\Big)\,, \qquad (9.23)\\
B_{\mathrm{NLA}}^{\nu_1,\mathrm{eq}(1)}\left(E_1\right) &= -\kappa_{\mathrm{NLA}}^*\left(E_1\right)L_1^{\nu_1}\left(E_1\right)\,. \qquad (9.24)
\end{aligned}
$$

Identical to the case of neutrino absorption and emission on nucleons, the similar case of neutrino absorption and emission on leptons results in neutrino source terms that drive the neutrino distribution function towards its equilibrium value and towards isotropy. One complication not present in the nucleonic rates is that the change of the neutrino distribution function of ν_3 by the reverse reaction $\nu_3 + \ell_4 \leftrightharpoons \nu_1 + \ell_2$ is not automatically accounted for by the forward reaction. In contrast to electrons, the neutrino distribution function of ν_3 is independently evolved in phase-space in the next transport solver step, and correct spectral lepton number density conservation is not possible to uphold perfectly by a single integrated quantity. Instead we account for the reaction $\nu_3 + \ell_4 \leftrightharpoons \nu_1 + \ell_2$ by utilizing detailed-balance and express the out-direction kernel $\phi^{\text{out}}_{l,\nu_3+\ell_4\leftrightharpoons\nu_1+\ell_2}(E_3, E_1)$ by

$$\begin{aligned}\phi^{\text{out}}_{l,\nu_3+\ell_4\leftrightharpoons\nu_1+\ell_2}(E_3, E_1) &= \phi^{\text{in}}_{l,\nu_1+\ell_2\leftrightharpoons\nu_3+\ell_4}(E_1, E_3) \\ &= \phi^{\text{out}}_{l,\nu_1+\ell_2\leftrightharpoons\nu_3+\ell_4}(E_1, E_3)\, \exp\left[\left(E_1 - E_3 + \mu_4 - \mu_2\right)/T\right] , \quad (9.25)\end{aligned}$$

and

$$\phi^{\text{in}}_{l,\nu_3+\ell_4\leftrightharpoons\nu_1+\ell_2}(E_3, E_1) = \phi^{\text{out}}_{l,\nu_1+\ell_2\leftrightharpoons\nu_3+\ell_4}(E_1, E_3) . \quad (9.26)$$

The collision integral, assuming an equilibrium distribution for ν_1, becomes

$$\begin{aligned}B^{\nu_3,\text{eq}}_{\text{NLA}}(E_3, \mu) = & \quad 2\pi \int_0^\infty dE_1\, E_1^2 \Big[\Big(1 - f_{\nu_3}(E_3, \mu)\Big)\, \phi^{\text{in}}_0(E_3, E_1)\, f^{\text{eq}}_{\nu_1}(E_1) \\ & - f_{\nu_3}(E_3, \mu)\, \phi^{\text{out}}_0(E_3, E_1)\, \Big(1 - f^{\text{eq}}_{\nu_1}(E_1)\Big)\Big] \\ = & \quad \Big(1 - f_{\nu_3}(E_3, \mu)\Big)\, j(E_3) - f_{\nu_3}(E_3, \mu)\, \kappa(E_3) , \quad (9.27) \\ B^{\nu_3,\text{eq}(0)}_{\text{NLA}}(E_3) = & \quad 2\pi \int_0^\infty dE_1\, E_1^2 \Big[\Big(1 - L_0^{\nu_3}(E_3)\, \phi^{\text{in}}_0(E_3, E_1)\, f^{\text{eq}}_{\nu_1}(E_1)\Big) \\ & - L_0^{\nu_3}(E_3)\, \phi^{\text{out}}_0(E_3, E_1)\, \Big(1 - f^{\text{eq}}_{\nu_1}(E_1)\Big)\Big] \\ = & \quad \Big(1 - L_0^{\nu_3}(E_3)\Big)\, j(E_3) - L_0^{\nu 3}(E_3)\, \kappa(E_3) , \quad (9.28) \\ B^{\nu_3,\text{eq}(1)}_{\text{NLA}}(E_3) = & \quad 2\pi \int_0^\infty dE_1\, E_1^2 \Big[-L_1^{\nu_3}(E_3)\, \phi^{\text{in}}_0(E_3, E_1)\, f^{\text{eq}}_{\nu_1}(E_1) - \\ & - L_1^{\nu_3}(E_3)\, \phi^{\text{out}}_0(E_3, E_1)\, \Big(1 - f^{\text{eq}}_{\nu_1}(E_1)\Big)\Big] \\ = & \quad -L_1^{\nu_3}(E_3)\, [j(E_3) + \kappa(E_3)] . \quad (9.29)\end{aligned}$$

As an example, we demonstrate this for the case of electron neutrinos, where the net change of the neutrino distribution function is given by a combination of the reaction $\nu_\text{e} + \text{e}^+ \leftrightharpoons \nu_\mu + \mu^+$ and $\nu_\text{e} + \mu^- \leftrightharpoons \nu_\mu + \text{e}^-$. Of the two, only the first reaction is explicitly calculated by Eqs. (9.16 – 9.18), whereas the second reaction, with a significantly larger rate of change, is implicitly calculated by the reaction $\nu_\mu + \text{e}^- \leftrightharpoons \nu_\text{e} + \mu^-$ using Eqs. (9.25 – 9.29). The final absorption opacity can then again be transformed to a stimulated opacity via Eqs. 9.21 ff. Note that not directly coupling all involved neutrino species during the transport solve, and instead assuming equilibrium distributions for the final state neutrino, does not strictly conserve total lepton number if the neutrinos are not in equilibrium. This leads to non-convergence of the transport solver if the fluid lepton number source terms are always strictly implemented as in Eq. 9.13,

$$Q_{\text{N},4} = -4\pi m_\text{B} \int_0^\infty \text{d}E_1\, \frac{c}{(2\pi\hbar c)^3} E_1^2 B^{\nu_1(0)}_{\text{NLA}}(E_1) . \quad (9.30)$$

As the PROMETHEUS-VERTEX neutrino transport solver only couples neutrino flavor pairs in a flavor block, i.e., $\nu_\mathrm{e} + \overline{\nu}_\mathrm{e}$, $\nu_\mu + \overline{\nu}_\mu$ and $\nu_\tau + \overline{\nu}_\tau$, assigning a charged lepton source term to a neutrino that does not belong to that particular charged lepton's flavor group, e.g., $Q_{\mathrm{N},\mu} = -4\pi m_\mathrm{B} \int_0^\infty \mathrm{d}E_1 \, \frac{c}{(2\pi\hbar c)^3} E_1^2 B_\mathrm{NLA}^{\overline{\nu}_\mathrm{e}(0)}(E_1)$ in the case of $\overline{\nu}_\mathrm{e} + \mathrm{e}^- \leftrightharpoons \overline{\nu}_\mu + \mu^-$, will lead to an instability as this reaction will not maintain flavor number using our equilibrium assumption. An increase in net Y_{ν_e} due to the reduction of $Y_{\overline{\nu}_\mathrm{e}}$, is not balanced equally by a reduction in net Y_e. Subsequently during the operator-split $\nu_\mu + \overline{\nu}_\mu$ transport step the reaction $\overline{\nu}_\mu + \mu^- \leftrightharpoons \overline{\nu}_\mathrm{e} + \mathrm{e}^-$ does not balance net Y_{ν_μ} and net Y_μ. To circumvent this problem we instead always assign any change to net Y_e to an opposite change in net Y_{ν_e}, as well as any change to net Y_μ to an opposite change in net Y_{ν_μ}, no matter which side of the vertex the respective neutrino or charged lepton is located on. This is equivalent to either choosing $Q_{\mathrm{N},2}$ or $Q_{\mathrm{N},4}$ of Eq. 9.13 and conserving the respective net lepton flavor number of that particular neutrino flavor block, but possibly violating total lepton number conservation overall.

To limit our muonic reactions to conditions where neutrinos might be considered in equilibrium, we use a simple density and temperature dependent suppression factor

$$\phi_{l,\mathrm{effective}}^{\mathrm{in/out}} = \phi_{l,\mathrm{unmodified}}^{\mathrm{in/out}} \frac{1}{1 + (10^{10}\,\mathrm{g/cm^3}/\rho)^5} \frac{1}{1 + (2.5\,\mathrm{MeV}/T)^6} \,. \tag{9.31}$$

The density and temperature cut-offs are phenomenologically set values specifically chosen to exclude regions outside of the protoneutron star during both the earliest bounce phase using the temperature suppression and the density suppression during later phases. The exact structure of these suppression factors is not particularly critical, as muonic reactions become dynamically insignificant outside the protoneutron star, and accurately evolving the vanishing muon number becomes numerically unfeasible anyway.

9.2.2 Lepton flavor exchange

The Lepton flavor exchange (LFE) reaction $\nu_\mu + \mathrm{e}^- \leftrightharpoons \nu_\mathrm{e} + \mu^-$, as well as the corresponding reaction $\overline{\nu}_\mu + \mathrm{e}^+ \leftrightharpoons \overline{\nu}_\mathrm{e} + \mu^+$ for the positively charged leptons, is implemented following the formulae introduced in Sec. 6.3.1 by Ref. [75]. This reaction is, next to the charged beta-reactions, the main production channel of net muon number inside the protoneutron star, and can even exceed the opacity of beta-reactions for incoming neutrino energies E_1 of lower than the muon rest mass. This is explainable by the reaction being able to tap the additional energy supplied by the electron chemical potential of order $\mu_\mathrm{e} \sim 200\,\mathrm{MeV}$. The electron chemical potential can readily exceed the additional energy of $\Delta U \sim 40\,\mathrm{MeV}$, the interaction potential difference between neutron and proton in dense matter (cf. Ref. [32]). A caveat is however that a large electron chemical potential is usually correlated with a large electron neutrino chemical potential, as $\mu_{\nu_\mathrm{e}} = \mu_\mathrm{e} + \mu_\mathrm{p} - \mu_\mathrm{n} \sim 100\,\mathrm{MeV}$, which increases final state Pauli-blocking of the produced ν_e, This effect is absent in the beta reaction channel $\nu_\mu + \mathrm{n} \to \mathrm{p} + \mu^-$, where both final state particles are nondegenerate during the pre-explosion phase. Furthermore, the large number of trapped electron neutrinos will lead to a significant backreaction $\nu_\mathrm{e} + \mu^- \to \nu_\mu + \mathrm{e}^-$ that suppresses muon production, and prevents the rapid conversion of degenerate electrons into nondegenerate muons one might expect in a naive first expectation.

The production of muons is stopped once an equilibrium distribution of both ν_μ and ν_e is reached, identical to the beta-reaction equilibrium condition, and can therefore not lead to an increased muon number than the beta-reaction $\nu_\mu + \mathrm{n} \to \mathrm{p} + \mu^-$ by itself can produce. The benefit of this reaction is however an increased speed of chemical equilibration of μ neutrino energies lower than the muon rest mass at relatively low temperatures. From the moment of bounce up to several seconds postbounce before full deleptonization, this reaction surpasses the opacity of the beta-reaction close to the neutrinosphere as well as in the highly degenerate but cold PNS inner core up to 10km radius. This reaction, in combination with the inverse lepton decay reaction of Sec. 9.3, keeps the μ neutrinos very close to chemical equilibrium up to and slightly exceeding the neutrinosphere. The backreaction $\nu_\mathrm{e} + \mu^- \to \nu_\mu + \mathrm{e}^-$ is for electron neutrinos, however, only subdominant to the beta reaction $\nu_\mathrm{e} + \mathrm{n} \leftrightharpoons \mathrm{p} + \mathrm{e}^-$.

In the following, we will plot initial energy differential opacities of the neutrinos on both sides of the interaction vertex, for their respective forward opacity and stimulated opacity at a few select parameters ρ, T, Y_e, Y_μ. The opacity of the forward reaction $\nu_\mathrm{e} + \mu^- \to \nu_\mu + \mathrm{e}^-$ is calculated using the in/out-invariance and detailed balance conditions from Sec. 6.3.4, where for example

$$\begin{aligned}\frac{1}{\lambda}_{\nu_\mathrm{e}+\mu^-\to\nu_\mu+\mathrm{e}^-}(E_{\nu_\mathrm{e}}) = 2\pi \int \mathrm{d}E_{\nu_\mu}\, E_{\nu_\mu}^2 \phi^{\mathrm{out}}_{\nu_\mu+\mathrm{e}^-\to\nu_\mathrm{e}+\mu^-}\left(E_{\nu_\mu}, E_{\nu_\mathrm{e}}\right) \\ \times \exp\left[\left(\mu_{\mu^-} - \mu_{\mathrm{e}^-} + E_{\nu_\mathrm{e}} - E_{\nu_\mu}\right)/T\right] \\ = 2\pi \int \mathrm{d}E_{\nu_\mu}\, E_{\nu_\mu}^2 \phi^{\mathrm{in}}_{\nu_\mu+\mathrm{e}^-\to\nu_\mathrm{e}+\mu^-}\left(E_{\nu_\mu}, E_{\nu_\mathrm{e}}\right) . \quad (9.32)\end{aligned}$$

The corresponding stimulated absorption rates are calculated following Eq. 9.21 to be

$$\begin{aligned}\kappa^*_{\nu_\mu+\mathrm{e}^-\to\nu_\mathrm{e}+\mu^-}\left(E_{\nu_\mu}\right) = \left(1 + \exp\left[-\left(E_{\nu_\mu} - \mu_{\nu_\mu}\right)\right]\right) \\ \times 2\pi \int \mathrm{d}E_{\nu_\mathrm{e}}\, E_{\nu_\mathrm{e}}^2 \phi^{\mathrm{out}}_{\nu_\mu+\mathrm{e}^-\to\nu_\mathrm{e}+\mu^-}\left(E_{\nu_\mu}, E_{\nu_\mathrm{e}}\right)\left(1 - f^{\mathrm{eq}}_{\nu_\mathrm{e}}\left(E_{\nu_\mathrm{e}}\right)\right) , \quad (9.33)\end{aligned}$$

$$\kappa^{*}_{\nu_e+\mu^- \to \nu_\mu+e^-}\left(E_{\nu_e}\right) = \left(1+\exp\left[-\left(E_{\nu_e}-\mu_{\nu_e}\right)\right]\right) \times 2\pi \int \mathrm{d}E^2_{\nu_\mu}\, \phi^{\mathrm{in}}_{\nu_\mu+e^- \to \nu_e+\mu^-}\left(E_{\nu_\mu}, E_{\nu_e}\right)\left(1-f^{\mathrm{eq}}_{\nu_\mu}\left(E_{\nu_\mu}\right)\right). \quad (9.34)$$

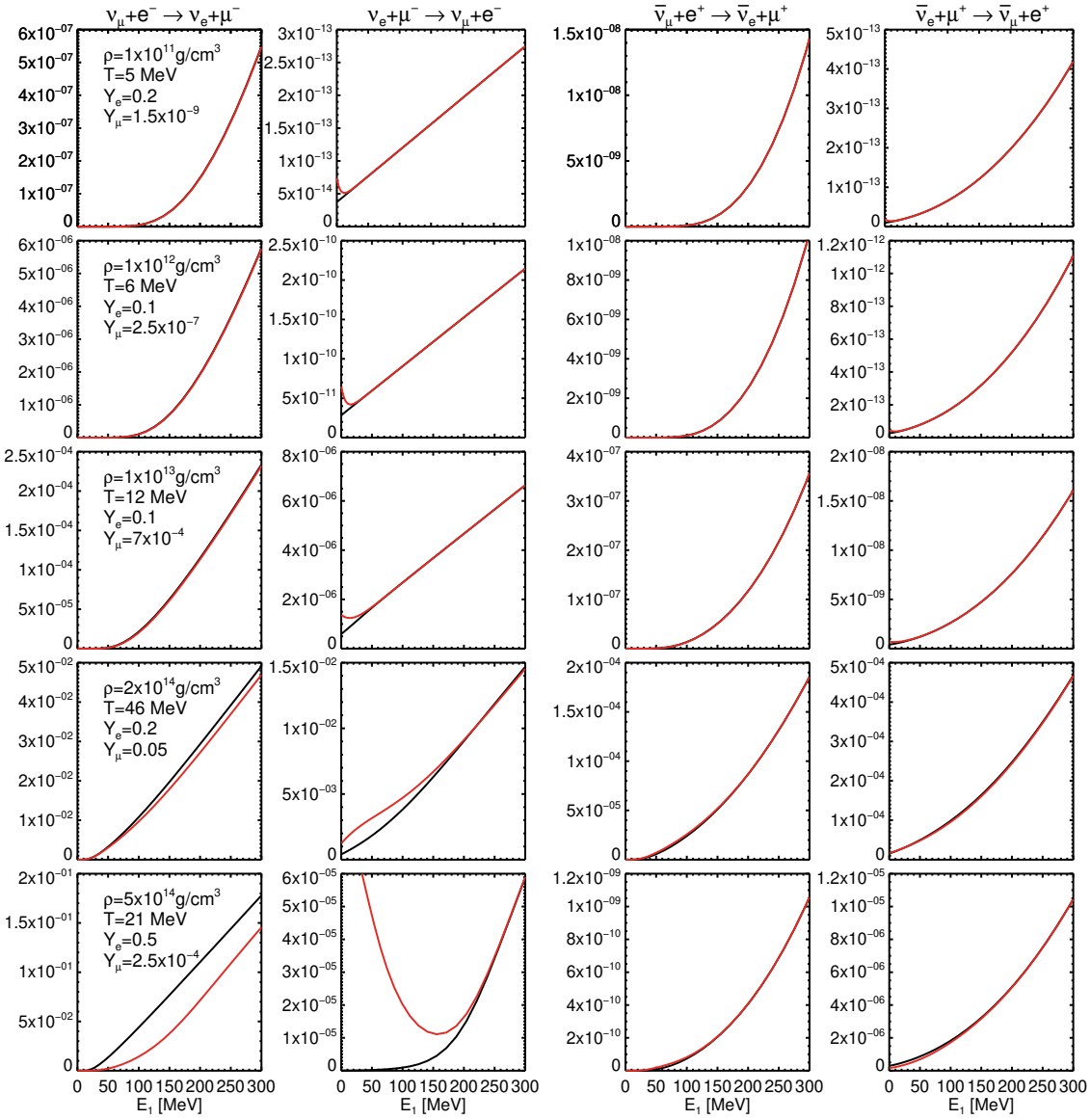

(a) $\nu_\mu + e^- \leftrightharpoons \nu_e + \mu^-$ opacity. (b) $\overline{\nu}_\mu + e^+ \leftrightharpoons \overline{\nu}_e + \mu^+$ opacity.

Figure 9.5: Lepton flavor exchange opacities for five select PNS conditions. The thermodynamic state used for each row is given in the first column, and the required chemical potentials are calculated using the SFHo EOS for the nucleonic part and our tables for the electron and muon chemical potentials. The y-axis of each plot is given in terms of either the inverse mean free path [1/cm] in black or the stimulated opacity [1/cm] in red and is unique in range to each plot. Note that the red lines contain blocking factors assuming a neutrino equilibrium distribution in the final state, whereas the black lines assume a free final state.

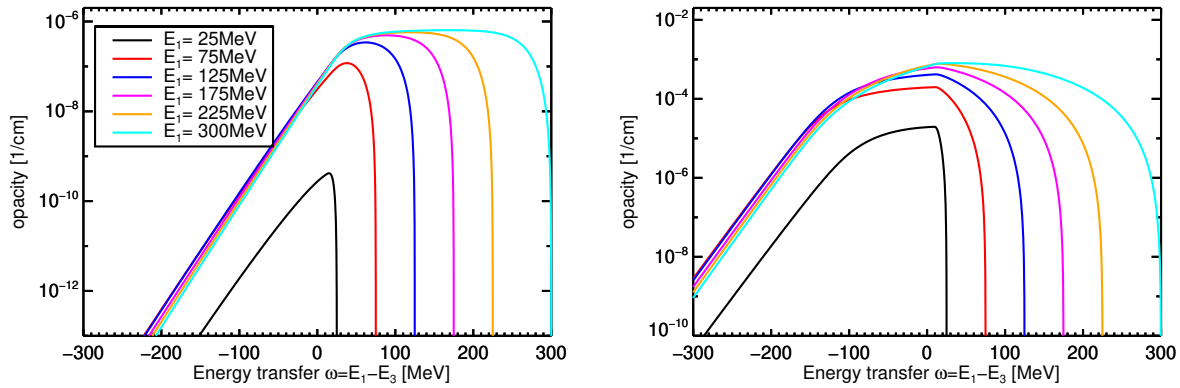

(a) Energy transfer in terms of the difference between initial and final state neutrino energy for $\mu_e = 25\,\mathrm{MeV}$.

(b) Energy transfer in terms of the difference between initial and final state neutrino energy for $\mu_e = 250\,\mathrm{MeV}$.

Figure 9.6: Energy transfer spectrum for a set of incoming ν_μ energies E_1 as given in the plot at fixed Temperature $T = 15\,\mathrm{MeV}$ and two fixed electron chemical potentials of $\mu_e = 25\,\mathrm{MeV}$ and $\mu_e = 250\,\mathrm{MeV}$ of process $\nu_\mu + e^- \leftrightharpoons \nu_e + \mu^-$. Chemical potential of the muon is set to $\mu_\mu = 0\,\mathrm{MeV}$ and final state blocking of ν_e is neglected.

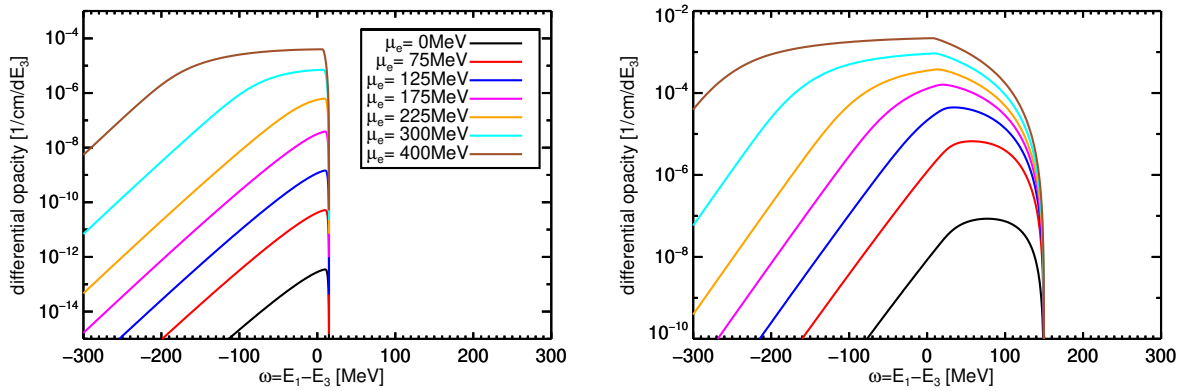

(a) Energy transfer in terms of the difference between initial and final state neutrino energy for $E_1 = 15\,\mathrm{MeV}$.

(b) Energy transfer in terms of the difference between initial and final state neutrino energy for $E_1 = 150\,\mathrm{MeV}$.

Figure 9.7: Energy transfer spectrum for a set of electron chemical potentials μ_e as given in the plot at fixed Temperature $T = 15\,\mathrm{MeV}$ and two fixed incoming ν_μ energies of $E_1 = 15\,\mathrm{MeV}$ and $E_1 = 150\,\mathrm{MeV}$ of process $\nu_\mu + e^- \leftrightharpoons \nu_e + \mu^-$. Chemical potential of the muon is set to $\mu_\mu = 0\,\mathrm{MeV}$ and final state blocking of ν_e is neglected.

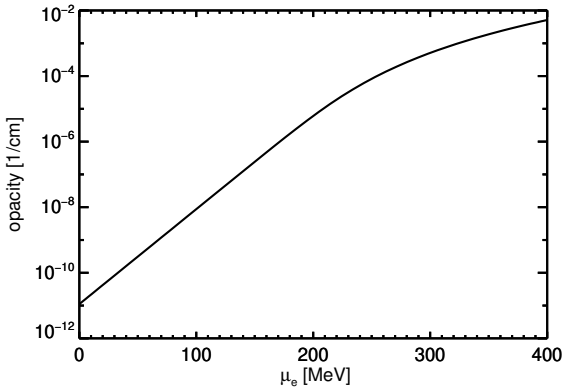

(a) Opacity for an incoming ν_μ energy of $E_1 = 15\,\mathrm{MeV}$.

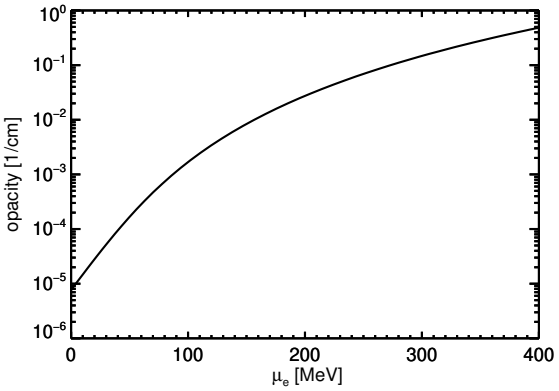

(b) Opacity for an incoming ν_μ energy of $E_1 = 150\,\mathrm{MeV}$.

Figure 9.8: Opacity depending on electron chemical potential μ_e at fixed Temperature $T = 15\,\mathrm{MeV}$ and two fixed incoming ν_μ energies of $E_1 = 15\,\mathrm{MeV}$ and $E_1 = 150\,\mathrm{MeV}$ of process $\nu_\mu + \mathrm{e}^- \leftrightharpoons \nu_\mathrm{e} + \mu^-$. Chemical potential of the muon is set to $\mu_\mu = 0\,\mathrm{MeV}$ and final state blocking of ν_e is neglected.

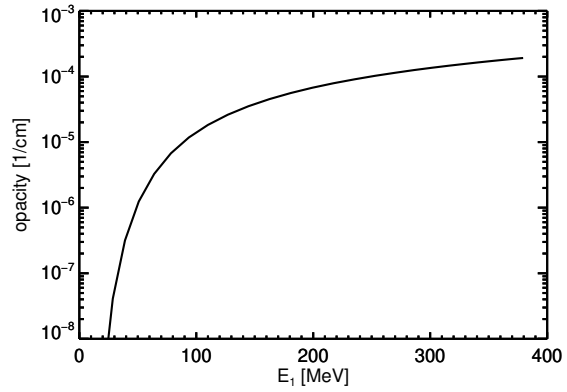

(a) Opacity for an electron chemical potential $\mu_\mathrm{e} = 25\,\mathrm{MeV}$.

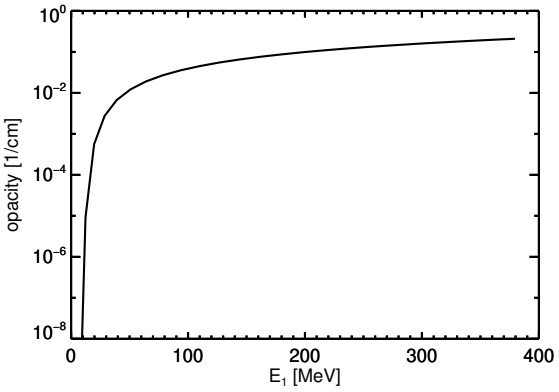

(b) Opacity for an electron chemical potential $\mu_\mathrm{e} = 250\,\mathrm{MeV}$.

Figure 9.9: Opacity depending on incoming ν_μ energy E_1 at fixed Temperature $T = 15\,\mathrm{MeV}$ and two fixed electron chemical potentials of $\mu_\mathrm{e} = 25\,\mathrm{MeV}$ and $\mu_\mathrm{e} = 250\,\mathrm{MeV}$ of process $\nu_\mu + \mathrm{e}^- \leftrightharpoons \nu_\mathrm{e} + \mu^-$. Chemical potential of the muon is set to $\mu_\mu = 0\,\mathrm{MeV}$ and final state blocking of ν_e is neglected.

9.2.3 Lepton flavor conversion

Lepton flavor conversion (LFC) is the reaction $\overline{\nu}_\mathrm{e} + \mathrm{e}^- \leftrightharpoons \overline{\nu}_\mu + \mu^-$, as well as the positively charged reaction $\nu_\mathrm{e} + \mathrm{e}^+ \leftrightharpoons \nu_\mu + \mu^+$. It is a similar reaction to lepton flavor exchange of Sec. 9.2.2, except for slightly changed kinematics. This reaction has the advantage, compared to lepton flavor exchange, that none of the final state particles are degenerate and therefore final phase space will usually be nearly completely unblocked. This comes with the downside that the initial state neutrino, the $\overline{\nu}_\mathrm{e}$, is strongly suppressed inside the densest part of the PNS core, as the degenerate electrons and trapped ν_e force vanishing number densities of $\overline{\nu}_\mathrm{e}$. Similarly, large number densities of ν_e in the case of the positively charged reaction imply vanishingly small positron densities. This limits the ability of the lepton flavor conversion reaction to produce muon number rapidly, and therefore, as in the case of LFE, can not rapidly convert degenerate electrons into nondegenerate muons. LFE can however still be important for the $\overline{\nu}_\mathrm{e}$ transport opacity. The traditionally dominant $\overline{\nu}_\mathrm{e}$ opacity, the beta-reaction on protons $\overline{\nu}_\mathrm{e} + \mathrm{p} \leftrightharpoons \mathrm{n} + \mathrm{e}^+$, has large final state blocking of the produced neutrons, a large energy penalty of the interaction potential ΔU, as well as additional suppression due to weak magnetism. Lepton flavor conversion has none of these disadvantages, but is still of similar overall strength as the beta-reactions, allowing the LFC reaction to become the dominant opacity source at conditions above nuclear saturation density. This can affect the neutrino-driven wind phase during PNS cooling when the accretion component has subsided and core luminosity takes over, as the neutrinospheres start to recede to higher densities.

Identical to the case of lepton flavor exchange, the forward direction of the backreaction $\overline{\nu}_\mu + \mu^- \rightarrow \overline{\nu}_\mathrm{e} + \mathrm{e}^-$ needs to be calculated via the in/out-invariance relation of Sec. 6.3.4, where

$$\begin{aligned}\frac{1}{\lambda_{\overline{\nu}_\mu+\mu^-\rightarrow\overline{\nu}_\mathrm{e}+\mathrm{e}^-}}(E_{\overline{\nu}_\mu}) &= 2\pi \int \mathrm{d}E_{\overline{\nu}_\mathrm{e}}\, E^2_{\overline{\nu}_\mathrm{e}} \phi^{\mathrm{out}}_{\overline{\nu}_\mathrm{e}+\mathrm{e}^-\rightarrow\overline{\nu}_\mu+\mu^-}\left(E_{\overline{\nu}_\mathrm{e}}, E_{\overline{\nu}_\mu}\right) \exp\left[\left(\mu_{\mu^-} - \mu_{\mathrm{e}^-} + E_{\overline{\nu}_\mathrm{e}} - E_{\overline{\nu}_\mu}\right)/T\right] \\ &= 2\pi \int \mathrm{d}E_{\overline{\nu}_\mathrm{e}}\, E^2_{\overline{\nu}_\mathrm{e}} \phi^{\mathrm{in}}_{\overline{\nu}_\mathrm{e}+\mathrm{e}^-\rightarrow\overline{\nu}_\mu+\mu^-}\left(E_{\overline{\nu}_\mathrm{e}}, E_{\overline{\nu}_\mu}\right) . \quad (9.35)\end{aligned}$$

The corresponding stimulated absorption rates are calculated following Eq. 9.21 to be

$$\begin{aligned}\kappa^*_{\overline{\nu}_\mathrm{e}+\mathrm{e}^-\rightarrow\overline{\nu}_\mu+\mu^-}\left(E_{\overline{\nu}_\mathrm{e}}\right) &= \left(1 + \exp\left[-\left(E_{\overline{\nu}_\mathrm{e}} + \mu_{\nu_\mathrm{e}}\right)\right]\right) \\ &\times 2\pi \int \mathrm{d}E_{\overline{\nu}_\mu}\, E^2_{\overline{\nu}_\mu} \phi^{\mathrm{out}}_{\overline{\nu}_\mathrm{e}+\mathrm{e}^-\rightarrow\overline{\nu}_\mu+\mu^-}\left(E_{\overline{\nu}_\mathrm{e}}, E_{\overline{\nu}_\mu}\right)\left(1 - f^{\mathrm{eq}}_{\overline{\nu}_\mu}\left(E_{\overline{\nu}_\mu}\right)\right) , \quad (9.36)\end{aligned}$$

$$\begin{aligned}\kappa^*_{\overline{\nu}_\mu+\mu^-\rightarrow\overline{\nu}_\mathrm{e}+\mathrm{e}^-}\left(E_{\overline{\nu}_\mu}\right) &= \left(1 + \exp\left[-\left(E_{\overline{\nu}_\mu} + \mu_{\nu_\mu}\right)\right]\right) \\ &\times 2\pi \int \mathrm{d}E_{\overline{\nu}_\mathrm{e}}\, E^2_{\overline{\nu}_\mathrm{e}} \phi^{\mathrm{in}}_{\overline{\nu}_\mathrm{e}+\mathrm{e}^-\rightarrow\overline{\nu}_\mu+\mu^-}\left(E_{\overline{\nu}_\mathrm{e}}, E_{\overline{\nu}_\mu}\right)\left(1 - f^{\mathrm{eq}}_{\overline{\nu}_\mathrm{e}}\left(E_{\overline{\nu}_\mathrm{e}}\right)\right) , \quad (9.37)\end{aligned}$$

and repeated analogously for the positively charged channel.

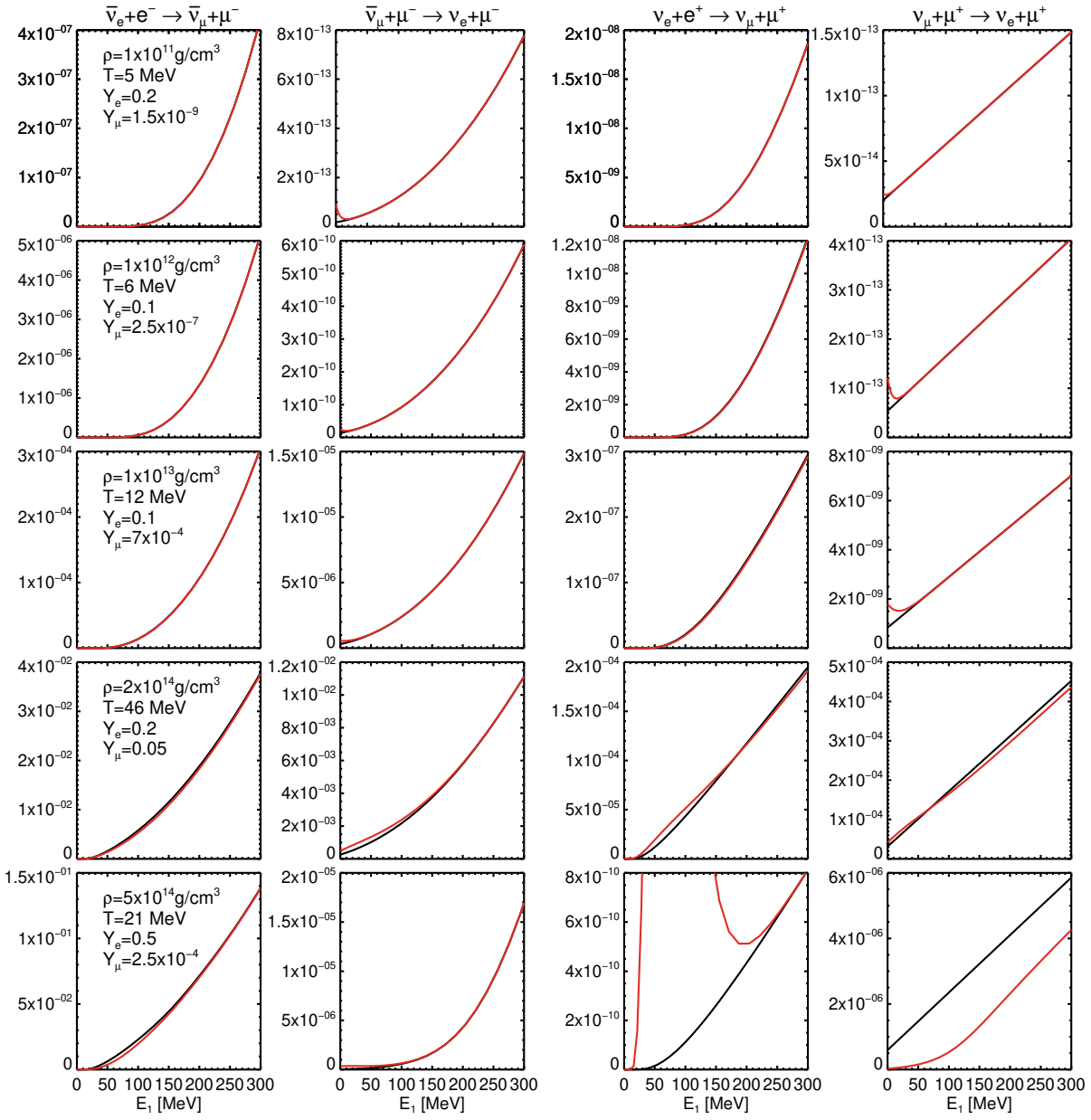

(a) $\overline{\nu}_e + e^- \leftrightharpoons \overline{\nu}_\mu + \mu^-$ opacity. (b) $\nu_e + e^+ \leftrightharpoons \nu_\mu + \mu^+$ opacity.

Figure 9.10: Lepton flavor conversion opacities for five select PNS conditions. The thermodynamic state used for each row is given in the first column, and the required chemical potentials are calculated using the SFHo EOS for the nucleonic part and our tables for the electron and muon chemical potentials. The y-axis of each plot is given in terms of either the inverse mean free path $[1/\text{cm}]$in black or the stimulated opacity $[1/\text{cm}]$ in red and is unique in range to each plot. Note that the red lines contain blocking factors assuming a neutrino equilibrium distribution in the final state whereas the black lines assume a free final state.

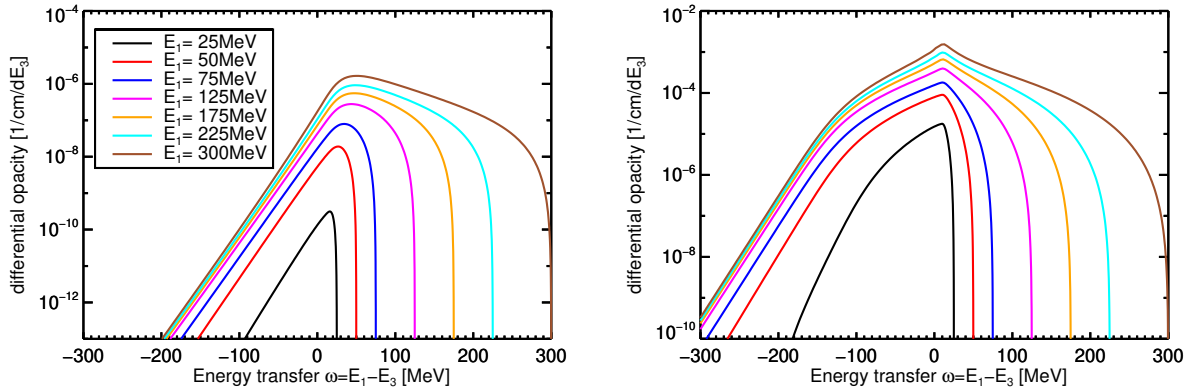

(a) Energy transfer in terms of the difference between initial and final state neutrino energy for $\mu_e = 25\,\mathrm{MeV}$.

(b) Energy transfer in terms of the difference between initial and final state neutrino energy for $\mu_e = 250\,\mathrm{MeV}$.

Figure 9.11: Energy transfer spectrum for a set of incoming $\overline{\nu}_e$ energies E_1 as given in the plot at fixed Temperature $T = 15\,\mathrm{MeV}$ and two fixed electron chemical potentials of $\mu_e = 25\,\mathrm{MeV}$ and $\mu_e = 250\,\mathrm{MeV}$ of process $\overline{\nu}_e + e^- \leftrightharpoons \overline{\nu}_\mu + \mu^-$. Chemical potential of the muon is set to $\mu_\mu = 0\,\mathrm{MeV}$ and final state blocking of $\overline{\nu}_\mu$ is neglected.

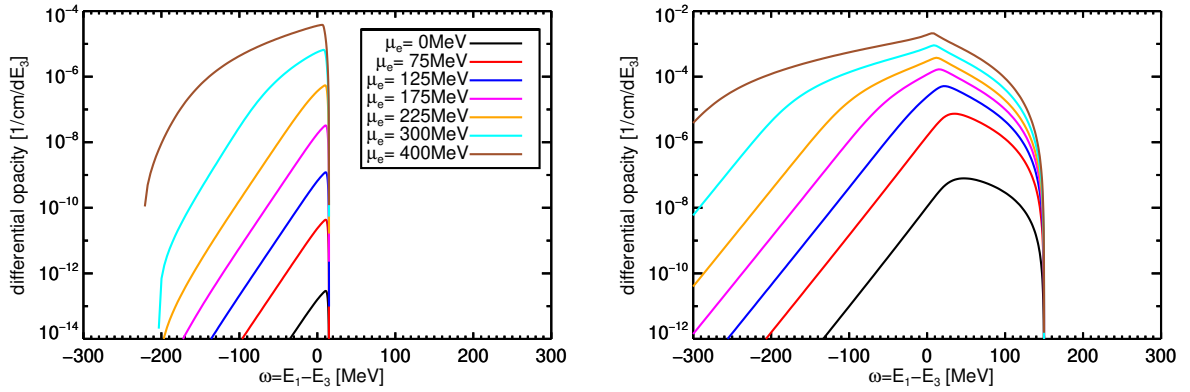

(a) Energy transfer in terms of the difference between initial and final state neutrino energy for $E_1 = 15\,\mathrm{MeV}$.

(b) Energy transfer in terms of the difference between initial and final state neutrino energy for $E_1 = 150\,\mathrm{MeV}$.

Figure 9.12: Energy transfer spectrum for a set of electron chemical potentials μ_e as given in the plot at fixed Temperature $T = 15\,\mathrm{MeV}$ and two fixed incoming $\overline{\nu}_e$ energies of $E_1 = 15\,\mathrm{MeV}$ and $E_1 = 150\,\mathrm{MeV}$ of process $\overline{\nu}_e + e^- \leftrightharpoons \overline{\nu}_\mu + \mu^-$. Chemical potential of the muon is set to $\mu_\mu = 0\,\mathrm{MeV}$ and final state blocking of $\overline{\nu}_\mu$ is neglected.

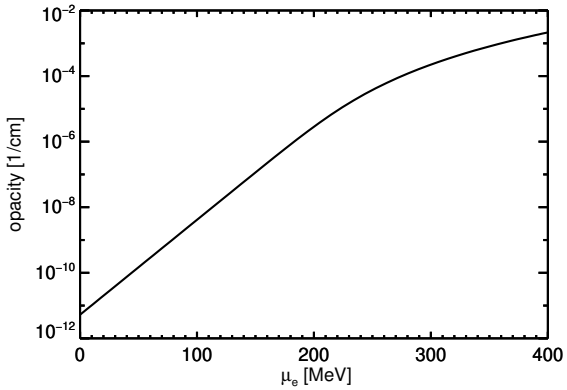

(a) Opacity for an incoming $\overline{\nu}_{\mathrm{e}}$ energy of $E_1 = 15\,\mathrm{MeV}$.

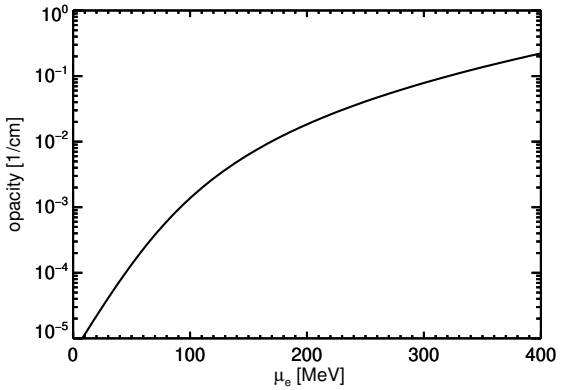

(b) Opacity for an incoming $\overline{\nu}_{\mathrm{e}}$ energy of $E_1 = 150\,\mathrm{MeV}$.

Figure 9.13: Opacity depending on electron chemical potential μ_{e} at fixed Temperature $T = 15\,\mathrm{MeV}$ and two fixed incoming $\overline{\nu}_{\mathrm{e}}$ energies of $E_1 = 15\,\mathrm{MeV}$ and $E_1 = 150\,\mathrm{MeV}$ of process $\overline{\nu}_{\mathrm{e}} + \mathrm{e}^- \leftrightharpoons \overline{\nu}_{\mu} + \mu^-$. Chemical potential of the muon is set to $\mu_{\mu} = 0\,\mathrm{MeV}$ and final state blocking of $\overline{\nu}_{\mu}$ is neglected.

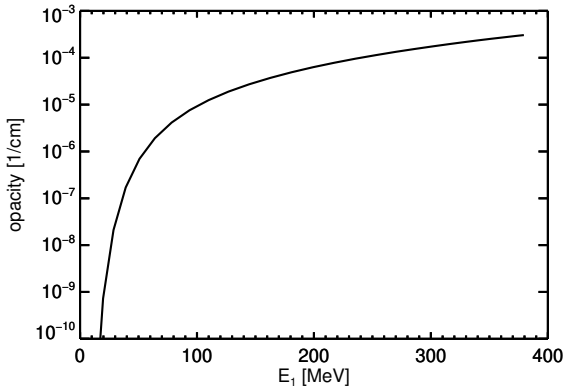

(a) Opacity for an electron chemical potential $\mu_{\mathrm{e}} = 25\,\mathrm{MeV}$.

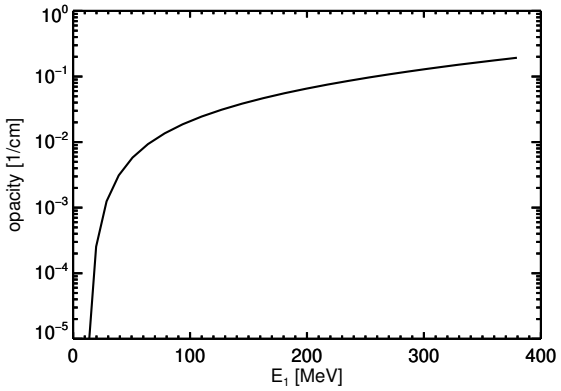

(b) Opacity for an electron chemical potential $\mu_{\mathrm{e}} = 250\,\mathrm{MeV}$.

Figure 9.14: Opacity depending on incoming $\overline{\nu}_{\mathrm{e}}$ energy E_1 at fixed Temperature $T = 15\,\mathrm{MeV}$ and two fixed electron chemical potentials of $\mu_{\mathrm{e}} = 25\,\mathrm{MeV}$ and $\mu_{\mathrm{e}} = 250\,\mathrm{MeV}$ of process $\overline{\nu}_{\mathrm{e}} + \mathrm{e}^- \leftrightharpoons \overline{\nu}_{\mu} + \mu^-$. Chemical potential of the muon is set to $\mu_{\mu} = 0\,\mathrm{MeV}$ and final state blocking of $\overline{\nu}_{\mu}$ is neglected.

9.3 Inverse lepton decay

Inverse lepton decay and here in its particular form of inverse muon decay (IMD) $\overline{\nu}_\mathrm{e} + \mathrm{e}^- + \nu_\mu \leftrightharpoons \mu^-$, is the inverse direction of the standard muon decay channel by which free muons can freely decay to a lighter electron and, due to flavor conservation, also into an additional $\overline{\nu}_\mathrm{e}$ and a ν_μ, $\mu^- \to \mathrm{e}^- + \overline{\nu}_\mathrm{e} + \nu_\mu$. It is therefore also the standard decay channel by which muons, advected closer to the PNS surface by convection, decay. The inverse direction, which produces net muon number, is weak, but has a nearly flat opacity spectrum that sets a new baseline opacity at very low neutrino energies. Additionally, as there are no neutrinos in the final phase-space and only nondegenerate muons, this reaction can proceed at a nearly constant opacity over a broad range of conditions regardless of the incident neutrino spectrum.

As it has two neutrinos in the initial state, this reaction is very similar to the case of thermal bremsstrahlung and pair annihilation kernels, and therefore the known collision integral terms can be reused. The collision integrals for pair annihilation kernels for a reaction as given in Ref. [108] for particles $\nu_1 + \ell_2 + \nu_3 \leftrightharpoons \ell_4$ read

$$B_\mathrm{IMD}^{\nu_1}(E_1,\mu) = 2\pi \int_0^\infty \mathrm{d}E_3\, E_3^2 \Bigg\{ \left(1 - f_{\nu_1}(E_1,\mu)\right) \phi_0^\mathrm{p}(E_1,E_3) - \sum_{l=0}^{\infty} (2l+1)\, P_l(\mu)\, \phi_l^\mathrm{p}(E_1,E_3)\, L_l^{\nu_3}(E_3) + f_{\nu_1}(E_1,\mu) \sum_{l=0}^{\infty} (2l+1)\, P_l(\mu)\, \hat{\phi}_l^\mathrm{a}(E_1,E_3)\, L_l^{\nu_3}(E_3) \Bigg\}, \quad (9.38)$$

and its angular moments

$$B_\mathrm{IMD}^{\nu_1(0)}(E_1) = 2\pi \int_0^\infty \mathrm{d}E_3\, E_3^2 \Bigg\{ \phi_0^\mathrm{p}(E_1,E_3) \left(1 - L_0^{\nu_1}(E_1) - L_0^{\nu_3}(E_3)\right) + \sum_{l=0}^{\infty} (2l+1)\, \hat{\phi}_l^\mathrm{a}(E_1,E_3)\, L_l^{\nu_1}(E_1)\, L_l^{\nu_3}(E_3) \Bigg\}, \quad (9.39)$$

$$B_\mathrm{IMD}^{\nu_1(1)}(E_1) = 2\pi \int_0^\infty \mathrm{d}E_3\, E_3^2 \Bigg\{ -\phi_0^\mathrm{p}(E_1,E_3)\, L_1^{\nu_1}(E_1) - \phi_1^\mathrm{p}(E_1,E_3)\, L_1^{\nu_3}(E_3) + \sum_{l=0}^{\infty} (2l+1)\, \hat{\phi}_l^\mathrm{a}(E_1,E_3)\, L_{l+1}^{\nu_1}(E_1)\, L_l^{\nu_3}(E_3) \Bigg\}, \quad (9.40)$$

with the Legendre moments defined in Sec. 9.1 and $\hat{\phi}_l^a(E_1,E_3) = \phi_l^\mathrm{p}(E_1,E_3) - \phi_l^\mathrm{a}(E_1,E_3)$, where ϕ_l^a is the absorption kernel, and ϕ_l^p is the production kernel. Pairwise symmetry implies $\phi_l^{\nu_1,\mathrm{a/p}}(E_3,E_1) = \phi_l^{\nu_1,\mathrm{a/p}}(E_1,E_3)$, and so we only need to calculate half the necessary energy bin couplings directly. The absorption kernel and production kernel are Legendre moments of the IMD kernel of Eq. 6.44 using the procedure in Sec. 9.1,

$$\phi_l^\mathrm{a/p} = \frac{1}{2} \int_{-1}^{1} \mathrm{d}\cos\theta_{13}\, P_l(\cos\theta_{13})\, R_\mathrm{IMD}^\mathrm{in/out}(E_1,E_3,\theta_{13}), \quad (9.41)$$

and the angular integration is performed via a numerical Gauss-Legendre integration using 6 Gaussian points in $\theta_{13} = \left[\theta_{13}^\mathrm{min} \ldots 1\right]$. As the Heaviside-Theta function appearing in the inverse

muon decay kernel can set a lower bound of the relative neutrino angle for each combination of neutrino energies due to

$$\Theta\left(k-1\right)=\Theta\left(\frac{Q}{E_1E_3\left(1-\cos\theta_{13}\right)}-1\right), \tag{9.42}$$

we can focus our Gauss integration onto the active angular region and maximize the resolution afforded by our limited number of points. The lower bound is then set to

$$-1\leq 1-\frac{Q}{E_1E_3}=\theta_{13}^{\min}<1\,. \tag{9.43}$$

As in the neutrino-lepton absorption reactions of Sec. 9.2, the net change in electron and muon number requires a corresponding change in net neutrino number where

$$\begin{aligned}Q_{\mathrm{N},4}=-4\pi m_{\mathrm{B}}\int_0^\infty \mathrm{d}E_1\,\frac{c}{\left(2\pi\hbar c\right)^3}E_1^2B_{\mathrm{IMD}}^{\nu_1(0)}\left(E_1\right)\\ =-4\pi m_{\mathrm{B}}\int_0^\infty \mathrm{d}E_3\,\frac{c}{\left(2\pi\hbar c\right)^3}E_3^2B_{\mathrm{IMD}}^{\nu_3(0)}\left(E_3\right)=-Q_{\mathrm{N},2}\,,\end{aligned} \tag{9.44}$$

and m_{B} is the baryon mass. As this is a pairwise reaction, the energy integrated neutrino number of both involved neutrinos must change by an identical amount and sign,

$$\int_0^\infty \mathrm{d}E_1\,E_1^2B_{\mathrm{IMD}}^{\nu1(0)}\left(E_1\right)=\int_0^\infty \mathrm{d}E_3\,E_3^2B_{\mathrm{IMD}}^{\nu_3(0)}\left(E_3\right)\,. \tag{9.45}$$

As neutrinos with different spectra can interact with each other, this, however, does not mean that the integrated neutrino energy density also has to change by the same amount. The net fluid energy source term is then

$$Q_{\mathrm{E}}=\sum_\nu -4\pi\int_0^\infty \mathrm{d}E_1\,\frac{c}{\left(2\pi\hbar c\right)^3}E_1^3B_{\mathrm{IMD}}^{\nu}\left(E_1\right)\,. \tag{9.46}$$

9.3.1 Implementation into the transport solver

As in Sec. 9.2.1, a fully consistent implementation of inverse muon decay requires full flavor coupling between ν_{e}, $\overline{\nu}_{\mathrm{e}}$, ν_μ, and $\overline{\nu}_\mu$. Otherwise the equality in Eq. 9.44 and Eq. 9.45 is not automatically fulfilled, and each neutrino does not know its partner neutrino spectrum. For this reason, we are again introducing an equilibrium assumption that all involved neutrinos can be sufficiently well described inside the PNS by an isotropic equilibrium distribution, given by the degeneracy factor $\eta=\mu_\nu^{\mathrm{eq}}/T$. By this assumption, we can forego the explicit flavor coupling and keep the simpler pairwise-coupling between $\nu-\bar{\nu}$ pairs. The Legendre moments of the distribution function in the collision integral can now be replaced by

$$L_0^{\nu_{\mathrm{e}3},\mathrm{eq}}\left(E_3\right)=\frac{1}{2}\int_{-1}^1 \mathrm{d}\mu\,f_{\nu_3}^{\mathrm{eq}}\left(E_3\right)=\frac{1}{2}\int_{-1}^1 \mathrm{d}\mu\,\frac{1}{\exp\left(\left(E_3-\mu_{\nu_3}^{\mathrm{eq}}\right)/T\right)+1}\,, \tag{9.47}$$

and

$$L_{l=1,\ldots,\infty}^{\nu_3,\mathrm{eq}}=0\,. \tag{9.48}$$

The collision integral reduces to

$$B_{\mathrm{IMD}}^{\nu_1,\,\mathrm{eq}}\left(E_1,\mu\right)=2\pi\int_0^\infty \mathrm{d}E_3\,E_3^2\Big\{\Big(\Big(1-f_{\nu_1}\left(E_1,\mu\right)\Big)\Big(1-L_0^{\nu_3,\mathrm{eq}}\left(E_3\right)\Big)\Big)\,\phi_0^{\mathrm{p}}\left(E_1,E_3\right) - f_{\nu_1}\left(E_1,\mu\right)\phi_0^{\mathrm{a}}\left(E_1,E_3\right)L_0^{\nu_3,\mathrm{eq}}\left(E_3\right)\Big\}, \quad (9.49)$$

and its angular moments

$$B_{\mathrm{IMD}}^{\nu_1,\mathrm{eq}(0)}\left(E_1\right)=2\pi\int_0^\infty \mathrm{d}E_3\,E_3^2\Big\{\Big(\Big(1-L_0^{\nu_1}\left(E_1\right)\Big)\Big(1-L_0^{\nu_3,\mathrm{eq}}\left(E_3\right)\Big)\Big)\,\phi_0^{\mathrm{p}}\left(E_1,E_3\right) - \phi_0^{\mathrm{a}}\left(E_1,E_3\right)L_0^{\nu_1}\left(E_1\right)L_0^{\nu_3,\mathrm{eq}}\left(E_3\right)\Big\}, \quad (9.50)$$

$$B_{\mathrm{IMD}}^{\nu_1,\mathrm{eq}(1)}\left(E_1\right)=2\pi\int_0^\infty \mathrm{d}E_3\,E_3^2\Big\{-L_1^{\nu_1}\Big(\phi_0^{\mathrm{p}}\left(E_1,E_3\right)\Big(1-L_0^{\nu_3,\mathrm{eq}}\left(E_3\right)\Big) + \phi_0^{\mathrm{a}}\left(E_1,E_3\right)L_0^{\nu_3,\mathrm{eq}}\left(E_3\right)\Big)\Big\}, \quad (9.51)$$

where we have kept the production and absorption kernels separate instead of applying the effective absorption kernel $\hat{\phi}_0^{\mathrm{a}}\equiv\phi_0^{\mathrm{p}}-\phi_0^{\mathrm{a}}$.

Using the definitions

$$j\left(E_1\right)=\int_0^\infty \mathrm{d}E_3\,E_3^2\phi_0^{\mathrm{p}}\left(E_1,E_3\right)\Big(1-L_0^{\nu_3,\mathrm{eq}}\left(E_3\right)\Big) \quad (9.52)$$

and

$$\kappa\left(E_1\right)=\int_0^\infty \mathrm{d}E_3\,E_3^2\phi_0^{\mathrm{a}}\left(E_1,E_3\right)L_0^{\nu_3,\mathrm{eq}}\left(E_3\right), \quad (9.53)$$

we arrive at

$$B_{\mathrm{IMD}}^{\nu_1,\mathrm{eq}}\left(E_1,\mu\right)=2\pi\left\{j\left(E_1\right)\left(1-f^{\nu_1}\left(E_1,\mu\right)\right)-\kappa\left(E_1\right)f^{\nu_1}\left(E_1,\mu\right)\right\}, \quad (9.54)$$

$$B_{\mathrm{IMD}}^{\nu_1(0),\mathrm{eq}}\left(E_1\right)=2\pi\left\{j\left(E_1\right)\Big(1-L_0^{\nu_1}\left(E_1\right)\Big)-\kappa\left(E_1\right)L_0^{\nu_1}\left(E_1\right)\right\}, \quad (9.55)$$

$$B_{\mathrm{IMD}}^{\nu_1(1),\mathrm{eq}}\left(E_1\right)=2\pi\left\{-L_1^{\nu_1}\left[j\left(E_1\right)+\kappa\left(E_1\right)\right]\right\}. \quad (9.56)$$

As in the neutrino-lepton absorption process, we can express the emissivity and opacity by a combined stimulated opacity form of

$$\kappa_{\mathrm{IMD}}^{\nu_1*}\left(E_1\right)=\frac{1}{1-f_{\mathrm{eq}}^{\nu_1}\left(E_1\right)}\kappa\left(E_1\right)=j\left(E_1\right)+\kappa\left(E_1\right), \quad (9.57)$$

and the collision integrals again reduce to a form that directly enforces an equilibrium spectrum of the incoming neutrino

$$B_{\mathrm{IMD}}^{\nu_1,\mathrm{eq}}\left(E_{1,}\mu\right)=\kappa_{\mathrm{IMD}}^{\nu_1*}\left(E_1\right)\Big[f_{\mathrm{eq}}^{\nu_1}\left(E_1\right)-f^{\nu_1}\left(E_1,\mu\right)\Big], \quad (9.58)$$

$$B_{\mathrm{IMD}}^{\nu_1,\mathrm{eq}(0)}\left(E_1\right)=\kappa_{\mathrm{IMD}}^{\nu_1*}\left(E_1\right)\Big[L_0^{\nu_1,\mathrm{eq}}\left(E_1\right)-L_0^{\nu_1}\left(E_1\right)\Big], \quad (9.59)$$

$$B_{\mathrm{IMD}}^{\nu_1,\mathrm{eq}(1)}\left(E_1\right)=-\kappa_{\mathrm{IMD}}^{\nu_1*}\left(E_1\right)L_1^{\nu_1}\left(E_1\right), \quad (9.60)$$

and vanishes once the neutrino distribution has arrived at its isotropic equilibrium distribution. This is repeated for the partner neutrino ν_3, where one assumes the neutrino ν_1 to be in equilibrium. A caveat of this treatment is that any deviation of each neutrino from its equilibrium spectrum results in a mismatch of the distribution function source terms and breaks neutrino number conservation. The condition of Eq. 9.45 is not necessarily upheld, as

$$\int_0^\infty \mathrm{d}E_1\, E_1^2 \kappa_{\mathrm{IMD}}^{\nu_1 *}(E_1)\left[L_0^{\nu_1,\mathrm{eq}}(E_1) - L_0^{\nu_1}(E_1)\right] \neq \int_0^\infty \mathrm{d}E_3\, E_3^2 \kappa_{\mathrm{IMD}}^{\nu_3 *}\left(E_{_3}\right)\left[L_0^{\nu_3,\mathrm{eq}}(E_3) - L_0^{\nu_3}(E_1)\right] ,$$

and the equilibrium spectrum of the partner neutrino does not necessarily mirror the actual distribution function. This also removes the natural quenching of the inverse muon decay absorption rate, as both neutrino distribution functions would become strongly forward peaked in the free streaming region and the transverse component would become small. To alleviate this, we suppress this rate using the suppression factor as used for the NLA rate of Eq. 9.31, which switches off the rate outside the PNS or at very low temperatures. The caveat of this method is that the production rate by muon decay to electrons and neutrinos is also actively suppressed. In practice, the muon number outside the protoneutron star has, however, already been reduced enough that any further decay is dynamically insignificant.

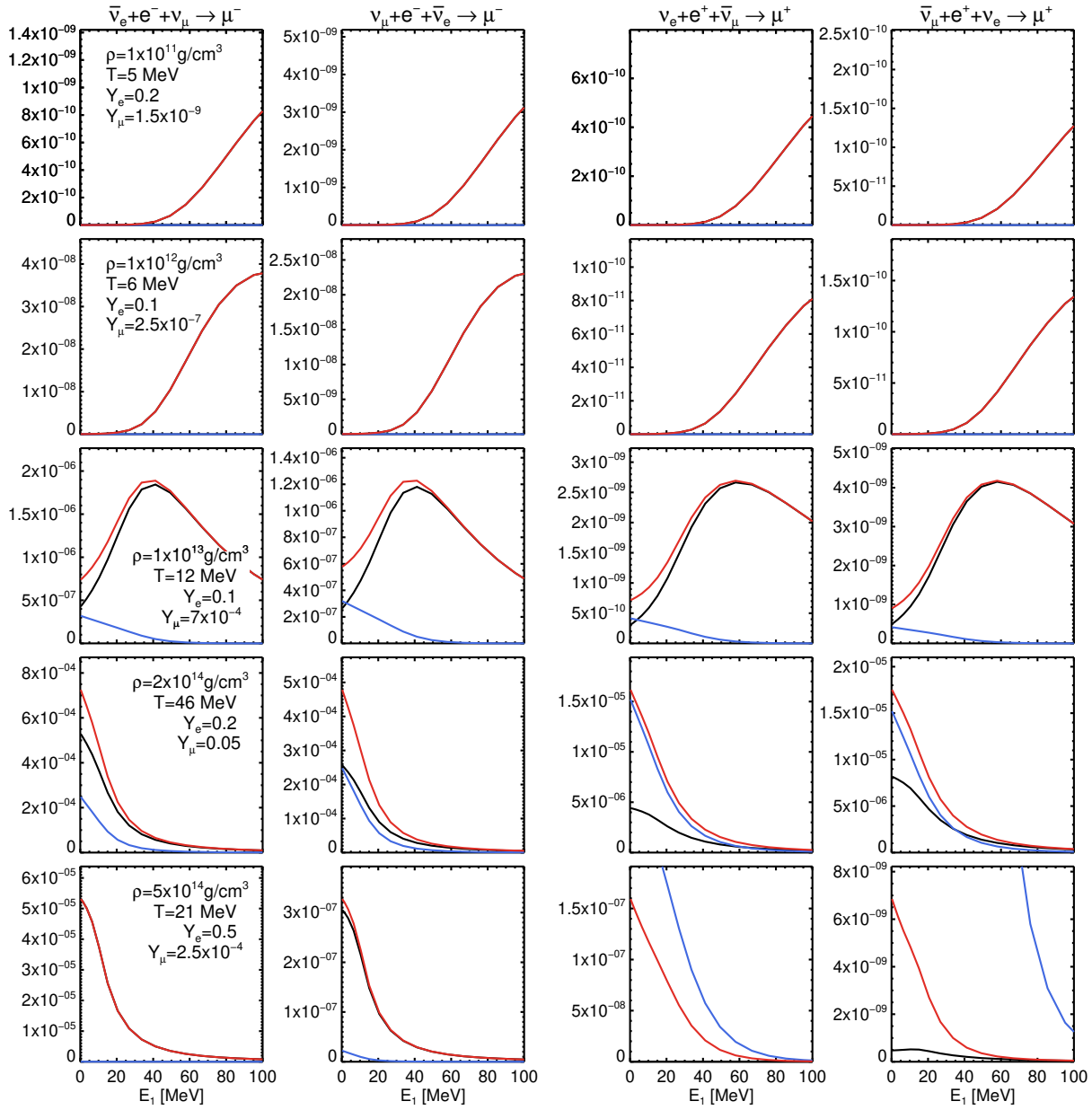

(a) $\bar{\nu}_e + e^- + \nu_\mu \leftrightharpoons \mu^-$ opacity. (b) $\nu_e + e^+ + \bar{\nu}_\mu \leftrightharpoons \mu^+$ opacity.

Figure 9.15: Inverse muon decay opacities for five select PNS conditions. The thermodynamic state used for each row is given in the first column, and the required chemical potentials are calculated using the SFHo EOS for the nucleonic part and our tables for the electron and muon chemical potentials. Note that the right column switches ν_1 and ν_3. The y-axis of each plot is given in terms of either opacity $[1/\text{cm}]$ in black, the stimulated opacity $[1/\text{cm}]$ in red or the emissivity [1/cm] in blue. Note that the red and black lines assume that the partner neutrino is in an equilibrium distribution while the blue line is assuming no blocking.

9.4 Beta-reactions

The muonic charged beta-reactions $\nu_\mu + \mathrm{n} \leftrightharpoons \mu^- + \mathrm{p}$, as well as $\overline{\nu}_\mu + \mathrm{p} \leftrightharpoons \mu^+ + \mathrm{n}$ are implemented exactly as in the standard case of electron (anti-)neutrino charged absorption, and we refer here to the discussion in Refs. [14, 114] about the exact prescription. The collision integral of the absorption and emission process is originally of the same structure as the scattering processes. The assumption that the final state lepton, in this case, the muon, is in perfect chemical equilibrium is, however, automatically upheld, and we can directly formulate the collision integral via the emissivity $j\left(E_1\right)$ and opacity $\kappa\left(E_1\right)$ without any loss of accuracy,

$$B_{\mathrm{AE}}^{\nu_1}\left(E_1,\mu\right) = j\left(E_1\right)\left[\left(1-f^{\nu_1}\right)\left(E_1,\mu\right) - f\left(E_1,\mu\right)\kappa\left(E_1\right)\right] . \tag{9.61}$$

Using the stimulated opacity κ^*, defined as in the preceding sections, the collision integral can be simplified to be

$$B_{\mathrm{AE}}^{\nu_1}\left(E_1,\mu\right)\kappa^*\left(E_1\right)\left[f_{\mathrm{eq}}^{\nu_1}\left(E_1\right) - f^{\nu_1}\left(E_1,\mu\right)\right] , \tag{9.62}$$

with the angular moments

$$B_{\mathrm{AE}}^{\nu_1(0)}\left(E_1\right) = \kappa^*\left(E_1\right)\left[L_0^{\nu_1,\mathrm{eq}}\left(E_1\right) - L_0^{\nu_1}\left(E_1\right)\right] , \tag{9.63}$$

$$B_{\mathrm{AE}}^{\nu 1(1)}\left(E_1\right) = -\kappa^*\left(E_1\right)L_1^{\nu_1}\left(E_1\right) . \tag{9.64}$$

As for the case of electron neutrinos, the interaction potential difference of neutron and proton can strongly influence the absorption rate. In the case of ν_μ absorption, a positive interaction potential difference allows neutrinos well below the muon rest mass energy to be absorbed onto a neutron and produce a muon and a proton. Additionally, as we use a fully inelastic absorption kernel, the thermal energy and chemical potential of the neutron can be used to increase the energy available to the muon. This practically removes the usual hard energy cutoff of $E_1 + \Delta U + \Delta Q \overset{!}{\geq} m_\mu$ if one were to do an elastic calculation for high densities and temperatures.

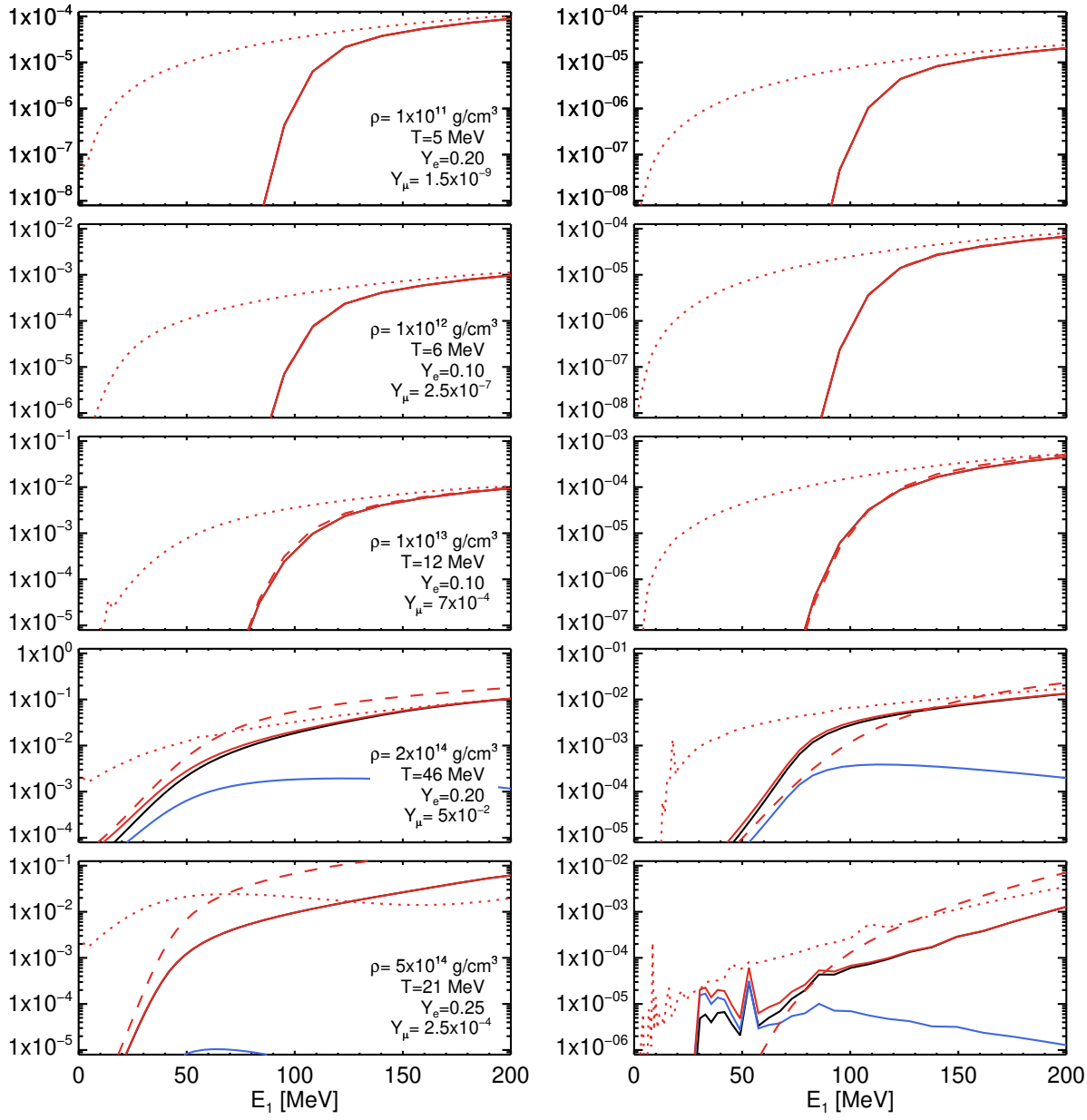

(a) $\nu_\mu + n \leftrightharpoons p + \mu^-$ opacity.

(b) $\overline{\nu}_\mu + p \leftrightharpoons n + \mu^+$ opacity.

Figure 9.16: Beta-process opacities for five select PNS conditions. The thermodynamic state used for each row is given in the first column, and the required chemical potentials are calculated using the SFHo EOS for the nucleonic part and our tables for the electron and muon chemical potentials. The y-axis of each plot is given in terms of either opacity [1/cm] in black, the stimulated opacity [1/cm] in red or the emissivity [1/cm] in blue. As a comparison, the opacity for correlated ν_e and $\overline{\nu}_e$ absorption with $e^\mp$ in the final state are the dotted lines. The solid lines and dotted lines are including the effects of nucleon-nucleon correlations; the dashed lines are for uncorrelated matter. The noisy behavior, seen at low $\overline{\nu}_\mu$ energies and high densities, is due to resonances in the correlated medium, and is a physical feature of the RPA.

Chapter VI
Simulations

10 Common numerical Setup

The simulations to be explored in this chapter are calculated using a $20M_\odot$ ZAMS (zero-age main sequence) progenitor of solar metallicity evolved in spherical symmetry in Ref. [136]. This progenitor does not include any asphericities induced by possible rotation as explored in Refs. [128, 67, 131, 96] nor by multidimensional first principle convection during the last burning stages before iron core collapse (see for example Refs. [24, 23, 92, 95, 94]). The set of progenitors by Woosley & Heger (2007) spanning the mass range from $12M_\odot - 40M_\odot$ has been vigorously explored in the community in 1D, 2D and 3D by various groups (see for example Refs. [12, 127, 99, 27, 105, 88, 83, 90]). The $20M_\odot$ progenitor in particular has been in the focus of different groups and has shown itself to be sensitive to variations in microphysics (see in particular Ref. [83]). Due to this sensitivity, we can more visibly quantify the effects that small changes might have on the result, with explosion or nonexplosion being the most extreme differentiator. However, even slight changes can shift the onset of shock expansion by several hundred milliseconds. For this reason, we try to keep changes between different sets of microphysics to the minimum and explore the impact of each variation in isolation.

The common base of our test runs is called "standard" and implements the microphysics on the level of sophistication as described in Refs. [114, 14], but extended to account for nucleon potential effects. For the case of tabulated equations of state including a light cluster component, we have extended our base set of opacities to approximately treat the contained light clusters by a quasi-unbound nucleon approximation. For this, the individual nucleons contained in the light clusters are treated as if they are unbound in the iso-energetic kinematics, but the energy required to unbind them is first subtracted from the final state lepton energy. This gives similar results as in Ref. [33] but with a slightly exaggerated cross section as the correlated state of the lightly bound nucleons is not consistently taken into account.

The case "muons" builds upon the "standard" set of opacities as described above but modified to include all muonic neutrino reactions as described in this thesis plus the muonic EOS component. These two setups form the basis of our comparisons and remain unchanged during all 1D and 2D simulations. The common neutrino energy grid spans the range of $0\,\mathrm{MeV} - 380\,\mathrm{MeV}$ divided into 15 geometrically spaced bins. The radial hydro and transport grid extend out to $10000\,\mathrm{km}$ and is initially divided into respectively 400 and 233 zones. As the protoneutron star gravitationally contracts due to continued accretion and energy loss in the neutrino channel, the continually steepening density gradient at the PNS surface is tracked via periodic radial remapping onto finer grids. The goal is to maintain a radial density resolution of about 20 points per density decade at all times and ending with a finest grid resolution of about 40m per cell around the PNS surface. To increase the angular resolution in the 2D simulations, we employ the static mesh refinement method (SMR) of Ref. [85], which allows us to increase the angular resolution of the hydrodynamic part by a factor of two above the gain radius. The minimum angular resolution of all our 2D runs is $1.125°$ in θ in both transport and hydro, and increases to $0.5625°$ above the gain radius in the hydro grid. Having different angular resolutions of the hydro and transport grid is an acceptable compromise, as the neutrino mean free path above the gain radius is significantly longer than the length scale of any small-scale hydro fluctuation. As a result, the thermodynamic variables can safely be interpolated from the high-resolution hydro grid onto the lower resolution transport grid without loss of accuracy. As the hydrodynamic component is comparatively less time intensive to compute, this allows us to track the turbulent energy down to smaller length scales (cf. Refs. [112, 110]), while keeping the computationally expensive neutrino transport part unchanged.

11 1D simulations

Muons are a component of the stellar gas that only exists stably and in abundant number in the densest and hottest regions of the protoneutron star. In this environment, uniquely multi-dimensional effects due to turbulence are only of low importance, and we can perform a first study of PNS muonization in spherical symmetry, i.e., 1D, without loss of generality. The dominant effect of muonization is a secular reduction of thermal and degenerate pressure in the PNS mantle, which can be examined in 1D with great ease and accuracy.

1D simulations can serve as excellent verification of our implementation of muons into Prometheus-Vertex in a quasi-steady state accretion situation without genuinely multi-dimensional effects and instabilities like neutrino-driven convection or the standing accretion shock instability (SASI) superimposing strong time-dependent fluctuations onto the neutrino signal. The steady-state PNS convection can, if required, be approximated to high accuracy using mixing-length theory (MLT) as described in Refs. [55, 88]. The Ledoux-criterion (cf. Ref. [63]) describes the convectively unstable region well, allowing us to take the slower contraction of the PNS and enhanced neutrino luminosity into account. Note however that due to the multi-component nature of our mixed electron and muon gas and the variable degree of neutrino trapping, the error in our mixing-length theory increases and MLT calculations including muons will need to be recalibrated against 2D simulations in future work. The MLT long-time cooling calculations presented in this section are therefore not the final result and might change slightly once the MLT mechanism has been finalized. The discussion of PNS contraction including convection will consequently only be discussed in the 2D simulation section.

11.1 Steady-state accretion

Spherical simulations of CCSN, except in special cases of progenitors with very steep density profiles like the $9.6 M_\odot$ ZAMS zero-metallicity progenitor discussed in Refs. [84, 111] or oxygen-neon-magnesium progenitors undergoing an electron-capture supernova (ECSN) as discussed in Refs. [53, 35, 111], do not explode and enter a steady-state accretion phase after the collapse, bounce and subsequent stalling of the shock. This phase will not end until the simulation has been ended or the continued accretion leads to further collapse to a black hole after several seconds. As the time-variability of the accretion is very low, this allows us to get an unambiguous and stable neutrino signal from the superimposed diffusion flux escaping from the protoneutron star and the mainly electron-flavor neutrino accretion component created from the infalling deleptonizing shocked matter. As we want to observe variations of the neutrino diffusion component from the PNS in this scenario, it is beneficial to not have "hydrodynamic noise" from time-variable turbulent accretion obfuscating the possibly small effects we wish to observe.

For this reason, we will evolve the s20.0 progenitor of Ref. [136] from initial collapse through bounce into the steady-state accretion phase for up to several hundred milliseconds postbounce using the SFHo RMF EOS of Ref. [123] and our standard numerical setup. We will simulate first the standard physics case without muons, called s20.0-SFHo-standard, using four neutrino species $\nu \in [\nu_e, \overline{\nu}_e, \nu_x, \bar{\nu}_x]$. Then a second simulation called s20.0-SFHo-muons in which we switch on muons at the moment of bounce, defined as the point of time when the post-shock entropy has reached $3.2\,k_B$, as well as include all six neutrino species $\nu \in \left[\nu_e, \overline{\nu}_e, \nu_\mu, \overline{\nu}_\mu, \nu_\tau, \overline{\nu}_\tau\right]$. Note that we neglect the effects of PNS convection in these particular simulations. In the following, we will discuss snapshots of protoneutron star profiles at select times to analyze the effects of muons in the EOS, as well as the influence of muonic opacities on the location of the neutrinospheres.

Pre-collapse profiles

The initial profiles of the progenitor at the beginning of our simulation are shown in Fig. 11.1. The most relevant plot here is the relation of the different pressure contributions. Initially, the inner $10000\,\mathrm{km}$ are mainly supported by the degenerate relativistic electron pressure with photonic pressure taking over in the still active burning layers above the inert iron core. The noninteracting baryonic pressure is unimportant everywhere. Note that the tabulated SFHo EOS is applied during the collapse phase at densities above 10^8 g/cm^3, and the analytic Maxwell-Boltzmann EOS is applied at densities below that. As the conserved energy density is mapped onto the grid via an inversion of the density, electron fraction and pressure, the original pressure profile as supplied by the stellar evolution calculation is maintained without perturbations. Temperature, entropy, energy density and other composition dependent variables, however, might be affected by variations in the EOS employed and a small discontinuity at the interface between the high- and low-density EOS remains. This can be explained by the different treatment of the nuclear statistical equilibrium (NSE) composition, which in the case of the SFHo EOS is applied down to temperatures of $0.1\,\mathrm{MeV}$ using thousands of nuclei. Our Maxwell-Boltzmann-EOS, however, requires a minimum temperature of $0.5\,\mathrm{MeV}$ for NSE, includes only 23 nuclei, and uses the original progenitor composition below this temperature.

11.1.1 Snapshots

Iron-core collapse As the phase of iron-core collapse is already well analyzed in many of its dependencies in exhaustive detail, for example, in Ref. [125], we will skip a detailed treatise on this phase. This is motivated by us not introducing any new physics before bounce and we instead only give a brief overview of the major effects. The degenerate iron core is susceptible to electron capture onto nuclei in addition to being further weakened by photodisintegration of iron nuclei into alpha particles, and the collapse is already underway at the start of our simulation. The core initially only slowly deleptonizes via electron capture and starts a slow subsonic collapse. The produced neutrinos can still escape freely from the core, and the total lepton number is free to change. As continued deleptonization leads to reduced pressure support, which leads to further contraction, ending up with more deleptonization, this is a self-reinforcing cycle that speeds up towards the last few tens of milliseconds before collapse. Eventually, the collapsing core splits up into a supersonic outer infalling part and a subsonic inner infalling part.

As soon as a density of $\rho \sim 10^{12}\,\mathrm{g/cm^3}$ has been exceeded, the electron neutrinos start becoming trapped due to frequent scattering on nuclei, after which the total lepton number becomes conserved and neutrinos are dragged with the medium. This neutrino trapping already during collapse leads to the substantial electron fraction remaining in the protoneutron star, and is the quantity that needs to leak out before one can speak of the protoneutron star as having deleptonized. Electrons and electron neutrinos are in chemical equilibrium in these conditions, and can freely convert between each other to maintain equilibrium as the core collapses further. The increasing degeneracy of the trapped electron neutrinos, however, prevents a total conversion of electrons into neutrinos. This degenerate electron neutrino gas will in the later stages after the bounce also suppress muon formation in the innermost core, but at this moment muons are yet to appear in the gas in any relevant amount. This allows us to keep muons switched off during the collapse and our two simulations are identical during the collapse phase.

The collapse is followed up to a critical maximum central density of $\rho = 1.4 \times 10^{14}\,\mathrm{g/cm^3}$ after which the next phase of our simulation begins and strong interactions between the nucleons lead to a prompt stiffening of the gas, signifying the birth of a protoneutron star.

Pre-bounce At the beginning of the bounce phase when the matter at the center enters its bulk nuclear matter phase, we switch from evolving only the electron neutrino transport to evolving the full set of neutrino species we wish to evolve for the remainder of the simulation.

In the case of the standard physics simulation this means evolving the neutrinos ν_e, $\bar{\nu}_e$, ν_x and $\bar{\nu}_x$, where ν_x and $\bar{\nu}_x$ represent the indistinguishable set of heavy lepton neutrino ν_μ, ν_τ and antineutrino $\bar{\nu}_\mu$, $\bar{\nu}_\tau$. As we neglect heavy-lepton charged current opacities in the standard physics set and neutral currents do not distinguish between neutrino flavors, the transport properties of ν_μ and ν_τ are identical and we can treat both flavors by a single representative neutrino. Due to the effects of weak magnetism and lepton helicity, the heavy-lepton neutrinos, however, have a different transport opacity than antineutrinos even in the absence of charged currents.

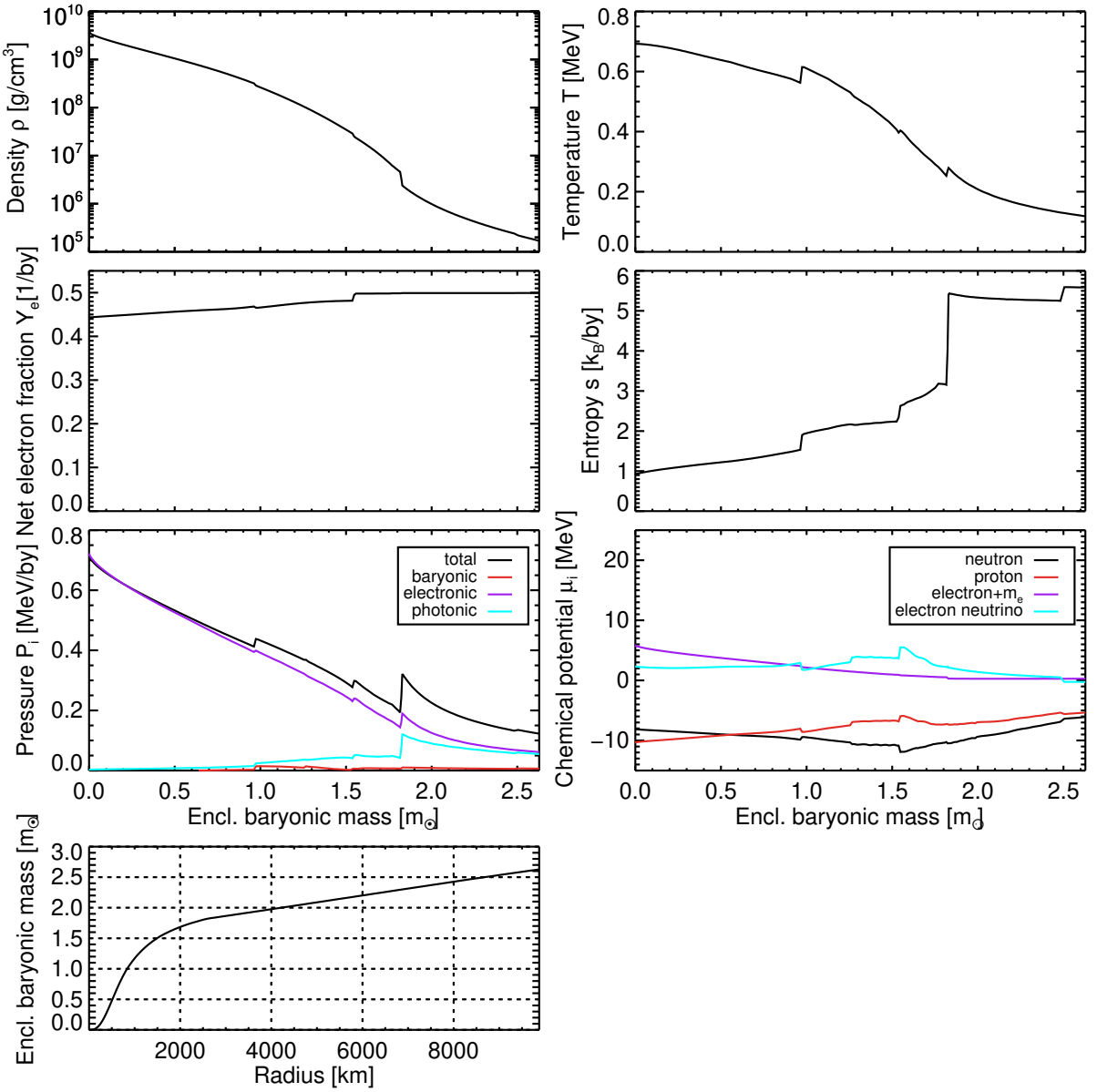

Figure 11.1: Initial profiles of the s20.0 progenitor mapped onto our numerical grid as a function of enclosed baryonic mass. Shown are the density, temperature, electron fraction, entropy per baryon, pressure per baryon, chemical potentials, and the location of each enclosed mass shell. The pressure has been further subdivided into its individual components.

Different spectra for neutrinos and antineutrinos will then develop, as already described in Ref. [47].

In the case of the muon physics simulation, we switch to evolving all six neutrino flavors ν_e, $\overline{\nu}_\mathrm{e}$, ν_μ, $\overline{\nu}_\mu$, ν_τ, $\overline{\nu}_\tau$ individually, as the spectra of ν_μ and $\overline{\nu}_\mu$ will now be significantly changed by the presence of muons and the single heavy-lepton neutrino approximation breaks down. Every neutrino flavor will, therefore, have its own flux and spectrum. Up to the postbounce stage, we will however still neglect muons, as the EOS enters a complicated phase-transition bridged by a Maxwell construction in which the pressure cannot easily be disentangled into its components. Previous tests, where muons were already switched on before the bounce, however, have shown that the postbounce phase is not sensitive to any pre-bounce muon presence. As the infalling matter continues to accrete onto the forming protoneutron star at the center, the kinetic energy is transformed into internal energy and the PNS heats up. The increased heat leads to abundant pair production of ν_x and $\bar{\nu}_\mathrm{x}$ by the thermal pair processes of bremsstrahlung and electron-positron pair annihilation, making the heavy-lepton neutrinos rapidly achieve thermal equilibrium. As all neutrinos are, however, still trapped in the PNS, they cannot escape from their production sites. The continuously infalling supersonic matter leads to a slight overcompression of the forming PNS which begins to rebound like a spring. This bounce has sufficient kinetic energy to launch a shock-wave that begins to propagate outwards. The exact moment of bounce is defined as the time when the entropy at the shock front exceeds $3.2\,k_B$ per baryon. In our case, the bounce happens at $t_\mathrm{b} = 328.1\,\mathrm{ms}$, after which we normalize our time coordinate to the so-called postbounce time $t_\mathrm{pb} = t - t_\mathrm{b}$ so that $t_\mathrm{pb} = 0\,\mathrm{ms} \coloneqq t_\mathrm{b}$.

The moment of bounce is when our two simulations will begin to diverge, and the last identical profiles of both simulations are given in Fig. 11.2. The temperature in the nascent PNS has reached $10-15\,\mathrm{MeV}$, and the pressure shows a sharp increase in the baryonic component as strong interactions resist further compression. The electronic pressure is still substantial at roughly equal proportion to the baryonic pressure, but the situation will change quickly as the trapped lepton number escapes the PNS and the densities increase to multiples of the saturation density. The chemical potentials show degenerate electrons and electron neutrinos as expected and the nucleons remain nondegenerate for now. Note however that the nucleon chemical potential contains a contribution by the respective interaction potentials that are attractive around saturation density and therefore reduce the apparent chemical potentials. The trapped net neutrino fraction in the plot has been defined as

$$\begin{aligned}\text{net } Y_\nu^{\text{trapped}} = \frac{4\pi}{c}\left\{\left[\int \mathrm{d}E\,\mathcal{J}_\nu\left(E\right)\right] - \left[\int \mathrm{d}E\,\mathcal{H}_\nu\left(E\right)\right]\right\} \\ - \frac{4\pi}{c}\left\{\left[\int \mathrm{d}E\,\mathcal{J}_{\bar{\nu}}\left(E\right)\right] - \left[\int \mathrm{d}E\,\mathcal{H}_{\bar{\nu}}\left(E\right)\right]\right\}, \quad (11.1)\end{aligned}$$

where $\mathcal{J} = J/E$ is the respective number density and $\mathcal{H} = H/E$ is the respective number flux density, following the definitions of Eqs. 5.10 and 5.11.

Postbounce At the beginning of the postbounce phase we continue evolving the standard physics case without changes, except a remapping of the Lagrangian comoving grid-coordinates to a fixed Eulerian grid with optimized resolution. We perform the same for the muon physics case, except we additionally switch on the treatment of muons and all additional muonic opacities, thereby beginning the different evolution track for both simulations. As visible in Fig. 11.2, the muons and μ neutrinos quickly achieve chemical equilibrium within a few numerical time-steps, showing that muon production is quick and very efficient at high densities. The system enters beta-equilibrium in respect to muons, i.e., $\mu_{\nu_\mu} \approx 0\,\mathrm{MeV}$, everywhere inside the nascent PNS, as shown by the blue chemical potential. The equilibrium muon fraction at the current temperatures is still tiny at a maximum value of $Y_\mu \approx 0.0004$ and the muon

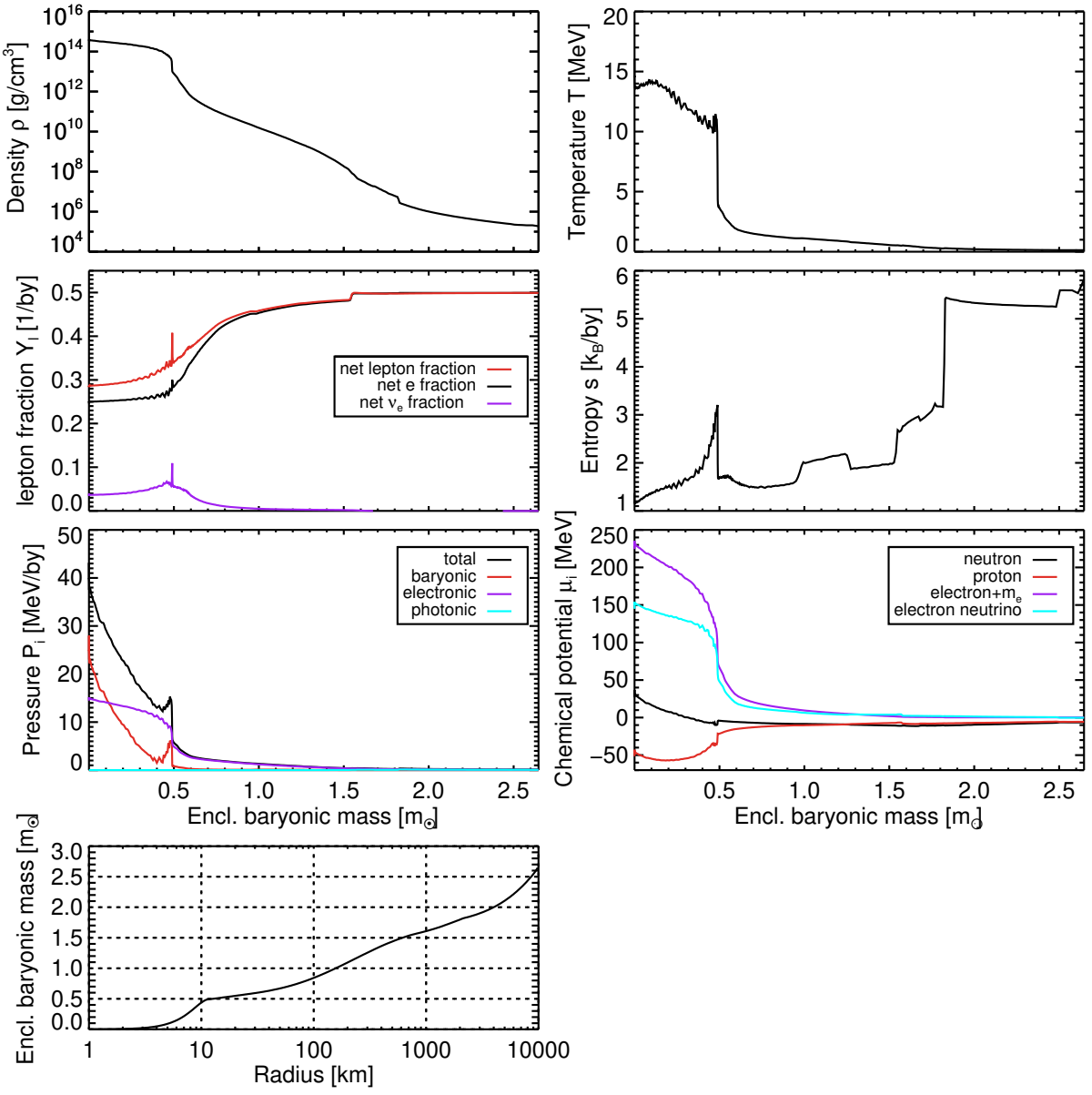

Figure 11.2: Last common profiles at the moment of bounce at $t_\mathrm{b} = 328.1\,\mathrm{ms}$. Plot contents are mostly identical to Fig. 11.1, except now the lepton fraction has been further subdivided into its components and the total conserved lepton fraction in the trapping region. The enclosed baryonic mass vs. radius plot has also been changed to a logarithmic axis to provide more information in the critical area around the PNS.

fraction profile closely tracks the temperature profile. The negligible muon fraction does not affect the hydrodynamics at this time, but the production of muons has already resulted in a corresponding negative net μ neutrino fraction. As there were no initial muons present, any muons produced must result in a surplus of $\overline{\nu}_\mu$ as fixed by the conserved muon lepton number $Y_{\ell_\mu}(t_{\rm pb} = 0) = 0 = \text{net } Y_\mu + \text{net } Y_{\nu_\mu}$ for trapped conditions. As μ neutrinos start to diffuse outwards and inwards from their main production regions, the net μ lepton fraction can become nonzero, resulting in the final net muon number already predicted in Ref. [51].

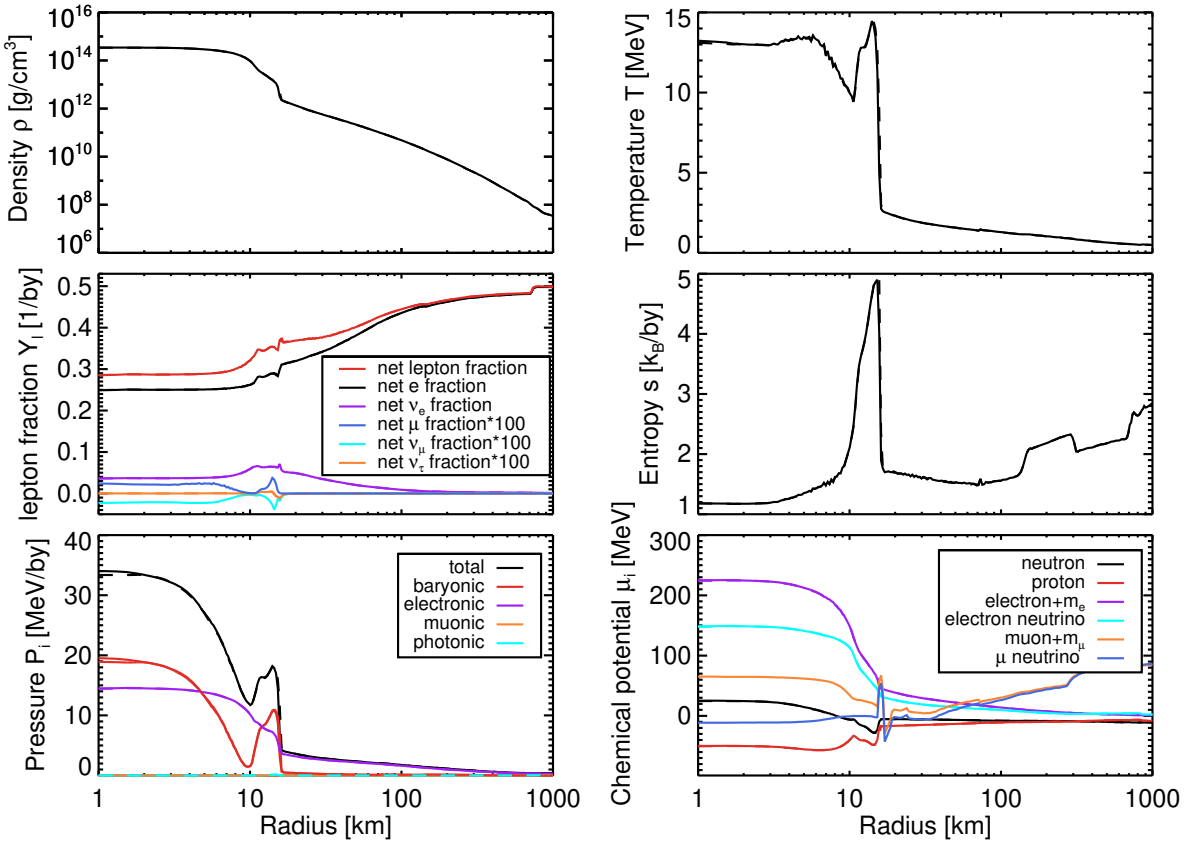

Figure 11.3: Profiles of case s20.0-SFHo-muons in solid lines and s20.0-SFHo-standard in dashed lines at $t_{\rm pb} = 0.15\,$ms and $t_{\rm pb} = 0.16\,$ms respectively. The plots are now all displayed as a function of the logarithmic radial coordinate from $0\,$km to $1000\,$km to capture both the PNS as well as the gain layer and pre-shock region. In enclosed mass plots the gain layer would not be visible due to the small contained mass, but Fig. 11.2 can be referred to, to relate radius and enclosed mass if necessary. As we have switched muons on, we now additionally track the muonic pressure contribution, additional net lepton fractions, and chemical potentials. Note that the net muon, net μ neutrino and net τ neutrino fraction have been multiplied 100-fold to make them visible. The representative heavy-lepton neutrino of case s20.0-SFHo-standard has been given the same cyan color as the τ neutrinos from case s20.0-SFHo-muons.

In Fig. 11.4 we show the densities at which the effective optical depth of each interaction and neutrino energy becomes smaller than $2/3$ at the time of $t_{\rm pb} = 0.15\,$ms. The effective optical depth at every radius for each opacity is defined following Ref. [113] to be

$$\tau_{{\rm eff},i}\left(r,\, E_1\right) = \int_r^\infty {\rm d}r' \sqrt{\frac{1}{\lambda_i\left(r',\, E_1\right)}\left[\frac{1}{\lambda_{\rm T}\left(r',\, E_1\right)} + \frac{1}{\lambda_i\left(r',\, E_1\right)}\right]}\,, \tag{11.2}$$

where λ_i is the mean free path of each rate i, and λ_T is the transport mean free path of the summed nearly elastic scattering mean free path on nucleons and nuclei. The motivation behind the introduction of an effective optical depth lies in the forced random walk by successive rapid scattering events that increase the effective total distance a neutrino has to travel as it diffuses out of the PNS. Neglecting the transport opacity would otherwise assume that neutrino trapping conditions do not exist. The radius where $\tau_{\text{eff},i}$ for each neutrino energy becomes smaller than $2/3$ is then the radius where neutrinos of this energy will stop interacting via the specified interaction. Following the definitions of Ref. [113] this allows us to define radii where certain kinds of interactions cease to be effective. These are the

1. **Number sphere** until where neutrino number can be created and destroyed via thermal pair annihilation and bremsstrahlung reactions; net neutrino number via charged current beta-reactions and the new muonic reactions. In the s20.0-SFHo-standard case, only ν_e and $\overline{\nu}_e$ can participate in the net neutrino number creating reactions, whereas in the s20.0-SFHo-muons case, also ν_μ and $\overline{\nu}_\mu$ can participate. In contrast, the thermal pair annihilation and bremsstrahlung reactions are open to all neutrinos, but can only create $\nu - \bar{\nu}$ pairs that leave net number unchanged. The interesting issue will now be to see, whether the new muonic reactions can become the dominant production reactions for ν_μ and $\overline{\nu}_\mu$ compared to the traditional pair reactions.

2. **Energy sphere** until where neutrinos can thermalize with the surrounding matter via energy exchanging scattering reactions like neutrino–electron scattering, neutrino–neutrino scattering and to some extent neutrino–nucleon scattering. As scattering on nucleons can only transfer a small amount of energy in each single scattering event, this opacity operates akin to a continuous neutrino flux in energy-space rather than by discrete large-magnitude events. Here we wish to see whether neutrino–muon scattering can become relevant for ν_μ and $\overline{\nu}_\mu$.

3. **Scattering sphere** until where neutrinos can still scatter on nucleons or nuclei with or without energy exchange. This typically leaves the spectrum unchanged in each scattering reaction, but can still lead to a changed flux spectrum measured at the decoupling region due to energy dependent transport effects. Weak magnetism, for example, can lead to different ν and $\bar{\nu}$ flux spectra by affecting the scattering opacity of each neutrino energy with opposite sign.

Note that this simple separation into three discrete spheres is only possible for the case of ν_τ and $\overline{\nu}_\tau$, where typically the number sphere lies before the energy sphere, which is followed by the scattering sphere. In the case of ν_e and $\overline{\nu}_e$, this is considerably more difficult, as charged current beta-reactions have the largest cross section and are typically the last reaction by which an electron-flavor neutrino interacts. The number sphere therefore effectively becomes the last active sphere and the effects cannot be disentangled as easily. Here we will try to identify whether this is now also the case for ν_μ and $\overline{\nu}_\mu$, where the large muon rest mass will create a strongly energy dependent number sphere radius. Low energy ν_μ and $\overline{\nu}_\mu$ might behave more like ν_τ and $\overline{\nu}_\tau$, whereas high energy neutrinos might act more like ν_e and $\overline{\nu}_e$. Looking at Fig. 11.4 we can see that the addition of muonic interactions lead to no effective change for ν_e, as charged-current absorption on neutrons remains the dominant effect at all neutrino energies. For $\overline{\nu}_e$, inverse muon decay can provide some slight additional net number producing opacity at very low neutrino energies and therefore slightly extends the number sphere radius. Thermal pair production by $e^- - e^+$ annihilation, however, remains, next to charged current absorption on nucleons, the primary production process for most energies. For ν_μ and $\overline{\nu}_\mu$, the muonic opacities already show an effect immediately after the bounce and can compete with the thermal pair processes. Especially inverse muon decay is active down to very low energies and absorption on nucleons is active out to the energy sphere for neutrino energies above the muon rest mass.

The mean energy sphere however still remains unaffected, as shown by the similar behavior of ν_μ and ν_τ mean energies. The addition of the new muonic processes, however, allow the ν_μ to be in perfect chemical equilibrium inside the nascent PNS already immediately after the bounce. For $\overline{\nu}_\mu$ the muonic opacities are still too small to have an effect, as antimuons are not yet present. Note that the ν_τ and $\overline{\nu}_\tau$ serve as an excellent proxy for the s20.0-SFHo-standard case representative heavy-lepton neutrino, as the only new neutral-current opacity, neutrino–muon scattering, is weak at best.

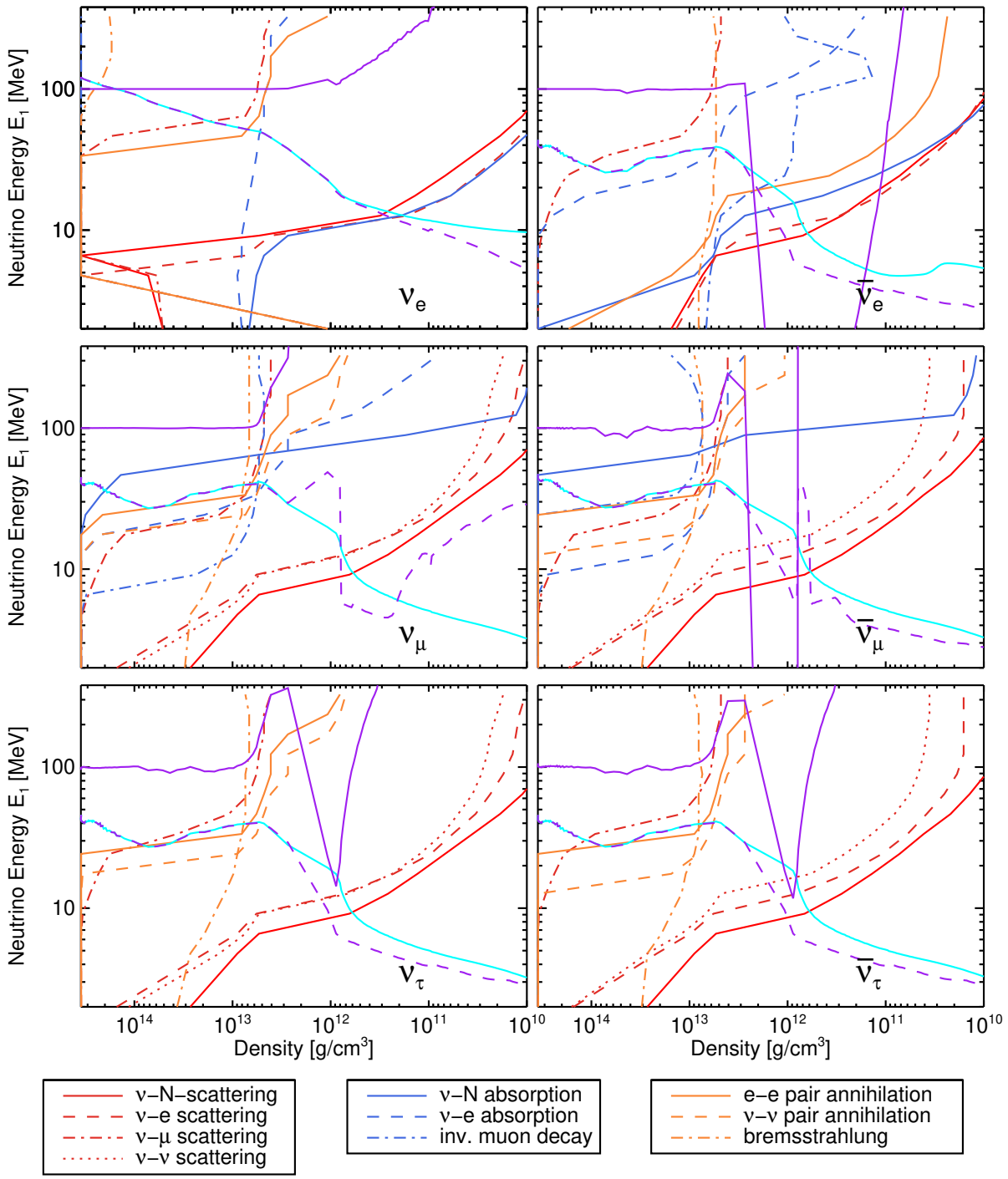

Figure 11.4: Density spheres of last interaction for all neutrinos of case s20.0-SFHo-muons at $t_{\mathrm{pb}} = 0.15\,\mathrm{ms}$. The plots are displayed as a function of density and neutrino energy. The line colors and styles shown in the legend are the densities where the optical depth of the specified interaction becomes smaller than $\tau_{\mathrm{eff}} = \frac{2}{3}$. Neutrino energies above each line still readily interact via the process, whereas below the line the matter has become transparent. Diagnostic quantities are the ratio of the energy integrated number density $\mathcal{J}_\nu^{\mathrm{eq}}/\mathcal{J}_\nu \times 100$ in solid purple; the mean energy of chemical equilibrium in dashed purple; the actual neutrino mean energy in solid cyan. These quantities provide an estimate where the neutrinos leave the local chemical or thermal equilibrium. The termination of an interaction sphere can be determined by the crossing point of the neutrino mean energy and the last active opacity of that sphere.

50 ms postbounce After 50 ms postbounce the two simulations start to diverge in PNS radius and the effects of muonization start to become apparent. The hydrodynamic profiles in Fig. 11.2 are mostly identical, as the muon fraction is still low at only $Y_\mu \approx 0.005$, and temperatures are not high enough to create a sizable thermal muon pair gas. Some of the negative net μ neutrino fraction has already leaked out but it remains negative throughout. The unmodified net τ neutrino fraction has begun developing a sizable positive net number due to weak magnetism as predicted in Ref. [51]. As $\overline{\nu}_\tau$ have a reduced scattering cross section on nucleons compared to ν_τ they can diffuse out of the PNS faster, leaving a temporary surplus of ν_τ localized at the temperature peak. Note, however, that the increased diffusion velocity of $\overline{\nu}_\tau$ inside the PNS also leads to a buildup of negative net τ neutrino number on the denser side of the temperature peak towards smaller radii. The enormous rest mass of tauons, however, prevents production of a charged net tauon number and the surplus $\overline{\nu}_\tau$ will eventually diffuse out once the neutrino energy gradients have equalized. $\overline{\nu}_\mu$ in contrast will preferentially diffuse out from the core, as the developing substantial negative μ neutrino chemical potential leads to a large negative $\overline{\nu}_\mu$ energy density gradient, while ν_μ will tend to flow inwards or be immediately absorbed and converted into muons. The muons are still, to good approximation, in weak chemical equilibrium with μ neutrinos at $\mu_{\nu_\mu} \approx 0$ throughout most of the PNS, and the muon chemical potential additionally is in weak chemical equilibrium with electrons at $\mu_\mu \approx \mu_e$ towards the neutrinosphere of the PNS.

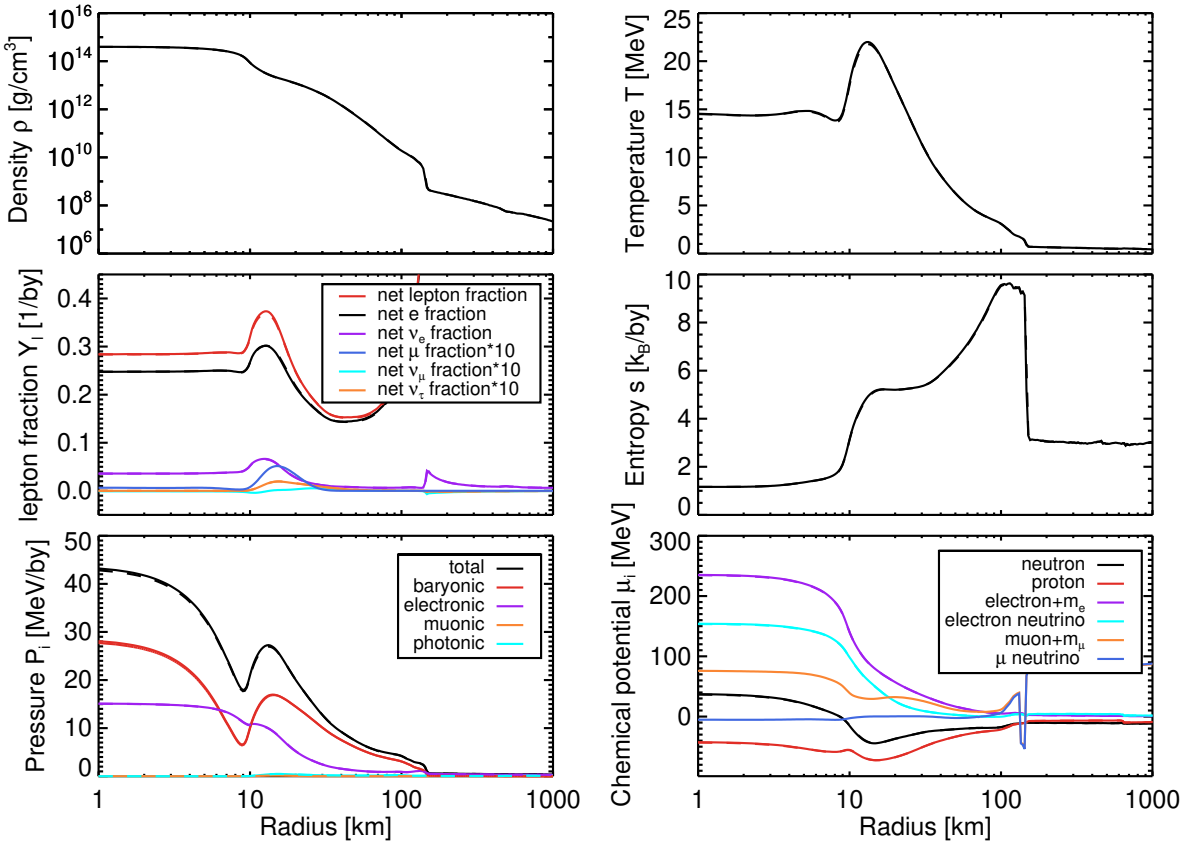

Figure 11.5: Profiles of case s20.0-SFHo-muons in solid lines and s20.0-SFHo-standard in dashed lines at $t_{\mathrm{pb}} = 50\,\mathrm{ms}$. Identical plot content as in Fig. 11.2, except muon fraction and net μ and net τ neutrino fractions are only scaled by a factor of 10.

The spheres of last interaction at $t_{\mathrm{pb}} = 50\,\mathrm{ms}$ are shown in Fig. 11.6 with an extended protoneutron star of approximately 70 km radius. No change is visible for ν_{e} as absorption on nucleons remains the dominant opacity and the number sphere extends out to the PNS surface for all neutrino energies. The muonic opacities are unimportant everywhere and only add a miniscule additional opacity contribution. The $\overline{\nu}_{\mathrm{e}}$ situation is slightly different, as muonic opacities have become competitive with thermal pair processes and inverse muon decay becomes the last number producing opacity for $E_1 \leq 5\,\mathrm{MeV}$. ν_μ is in good chemical equilibrium up to $\rho \sim 3-4 \times 10^{12}\,\mathrm{g/cm^3}$ due to the new opacities with a clear hierarchy of the beta-reaction freezing out first, followed by the absorption on electrons/antimuons and inverse muon decay being the last active opacity. The beneficial effect of nucleon interaction potentials has not been able to increase the opacity of low energy ν_μ yet, but energies of $E_1 \approx m_\mu$ can stay in chemical equilibrium up the PNS surface. Correspondingly, the deviation of the ν_μ number from equilibrium is only slowly increasing. The picture for $\overline{\nu}_\mu$ is quite similar, however here the hierarchy is beta-reactions to inverse antimuon decay to absorption on positrons/muons. Thermal pair production of $\overline{\nu}_\mu$ remain the most significant number producing source, and chemical equilibrium is not maintained significantly better than in the case of ν_τ. For both ν_μ and $\overline{\nu}_\mu$, the traditional ordering of number sphere to energy sphere to scattering sphere remains unchanged at this early time.

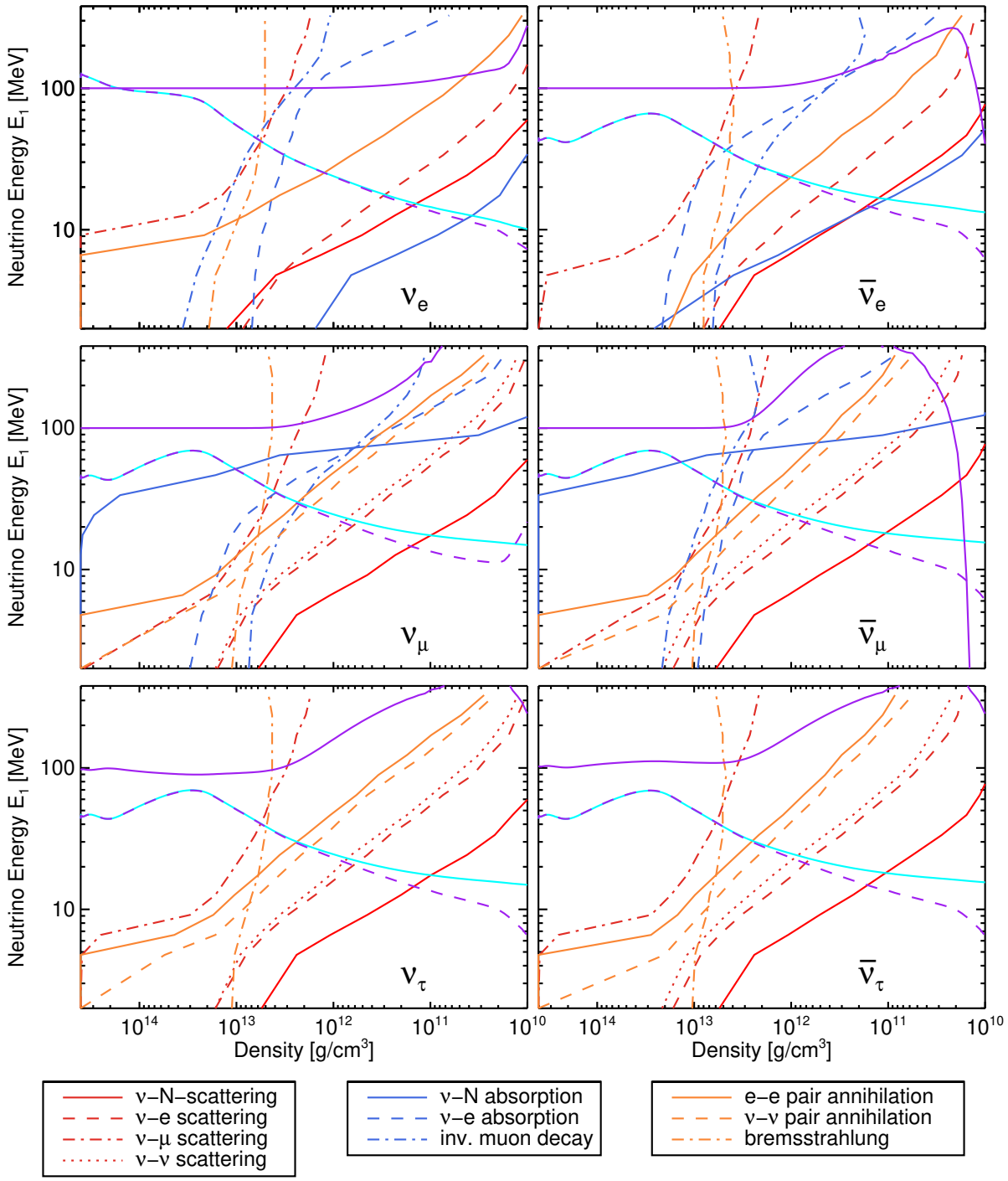

Figure 11.6: Density spheres of last interaction for all neutrinos of case s20.0-SFHo-muons at $t_{\mathrm{pb}} = 50\,\mathrm{ms}$. The figure content is identical to Fig. 11.4.

250 ms postbounce 250 ms postbounce, the effects of muonization have become fully apparent as shown in Fig. 11.7. The density stratification of the inner core has remained mostly unchanged. The hot extended mantle and cooling layer, however, show a steeper density gradient and are located at smaller radii. The protoneutron star radius shows a reduction of 2 km, from 34.6 km to 32.2 km. As the PNS contracts faster, some gravitational potential energy is converted into additional thermal energy, causing the temperature peak to heat up an additional 2 MeV. Note that this increase in temperature would have been larger if a considerable amount of energy had not already been transformed into muon rest mass energy. The net muon fraction around the temperature peak has risen to $Y_\mu = 0.042$, with a slight negative net ν_μ fraction and a positive net ν_τ fraction. The net ν_e and net e^- fraction only show a small reduction, being mostly just compressed into smaller radii. The net lepton fraction, and by extension the proton fraction $Y_\mathrm{p} = Y_\mathrm{e} + Y_\mu$, show a large increase, as degenerate neutrons can be converted to nondegenerate protons more readily by ν_μ absorption than in the Pauli-blocked electronic case. The effect of the increased proton fraction in a muonized PNS compared to the purely electronic case proves to be generic and is maintained during all further phases.

The additional compression of the PNS has increased the amount of pressure support generated by the interacting nucleons, as the electronic contribution becomes less significant. Contrary to the nucleons it remains mostly unchanged, showing that some of the electronic pressure has been converted into muonic pressure. The muonic pressure itself has grown to be larger than the photonic pressure contribution. The muon chemical potential has started to deviate from weak chemical equilibrium and has become strongly negative in the inner core, and slightly negative around the temperature peak. This is a consequence of the loss of $\overline{\nu}_\mu$ number or production of ν_μ not occurring fast enough to allow a production of a sufficient amount of muons. The influence of the $\overline{\nu}_\mu$ number loss can be readily understood by looking at the reaction $\mathrm{n} + \mu^+ \rightarrow \overline{\nu}_\mu + \mathrm{p}$. If there is a surplus of $\overline{\nu}_\mu$ they will be absorbed onto the still large abundance of protons in the dense core and produce antimuons, decreasing the net muon number. This is a consequence of the faster inward diffusion of $\overline{\nu}_\mu$ due to weak magnetism reducing the scattering opacity of high energy antineutrinos. On the other hand, a quicker loss of $\overline{\nu}_\mu$ will lead to a smaller local antineutrino density than demanded by chemical equilibrium. The system will then try to produce $\overline{\nu}_\mu$ to restore chemical equilibrium, by converting antimuons from the thermally produced $\mu^- - \mu^+$ pairs into $\overline{\nu}_\mu$. As the net muon number is $Y_\mu = X_{\mu^-} - X_{\mu^+}$, this naturally leads to an increase.

Naively, one would assume the reduced scattering opacity of $\overline{\nu}_\mu$ by weak magnetism to lead to a faster loss of $\overline{\nu}_\mu$ number. This is, however, not necessarily true. On the outer side of the temperature peak, the spectra of neutrinos and antineutrinos, in the absence of muonic reactions, will adjust themselves to maintain a steady state equilibrium of no net number flux as shown in Ref. [51]. This leads to a hotter $\overline{\nu}_\mu$ spectrum that increases the rate of absorption. This picture will have changed by the inclusion of muons, but the presence of an extended scattering sphere following the number sphere will still lead to a similar effect of the number flux trying to equilibrate. In effect, the ν_μ spectrum will be shifted to lower energies while the $\overline{\nu}_\mu$ spectrum will be boosted to higher energies. As the muon reactions are strongly sensitive to the high energy tail of the spectrum this can have a detrimental effect and suppress net muon production.

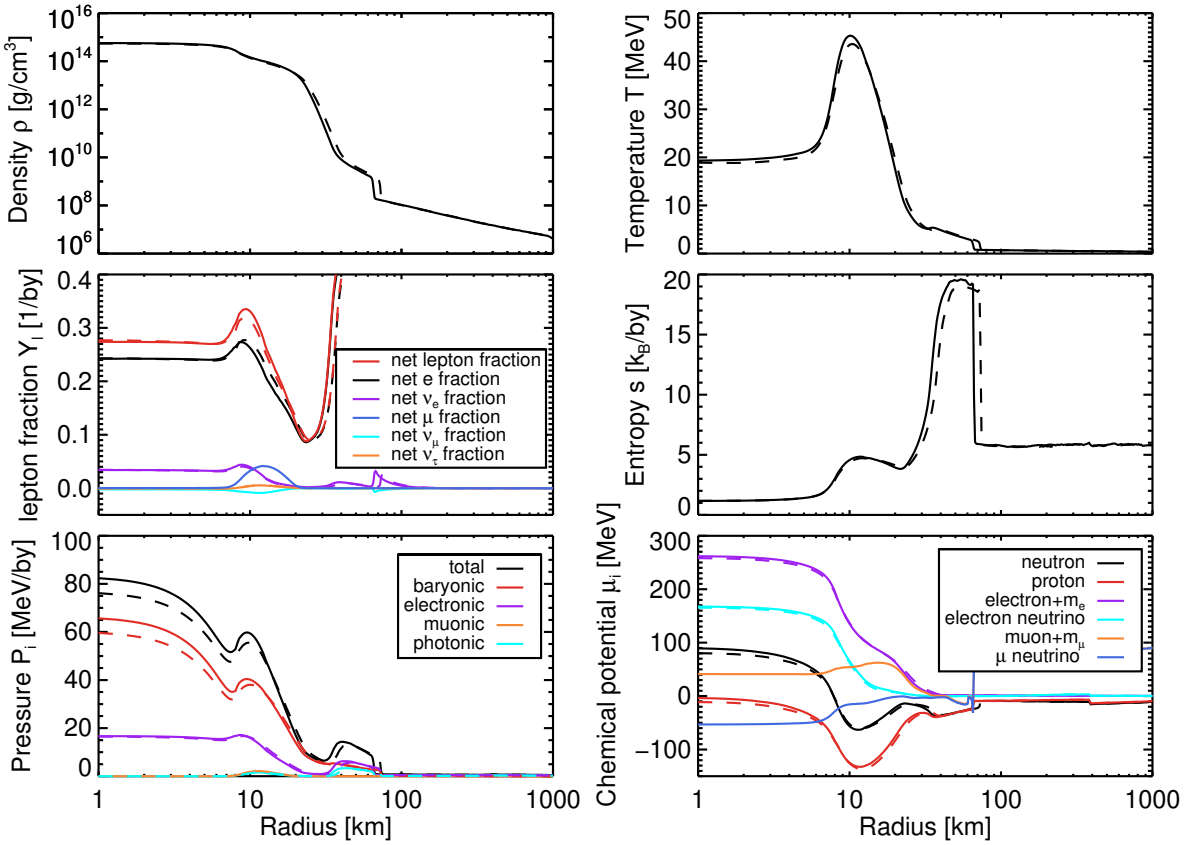

Figure 11.7: Profiles of case s20.0-SFHo-muons in solid lines and s20.0-SFHo-standard in dashed lines at $t_{\rm pb} = 250\,$ms. Identical plot content as in Fig. 11.2 except muon fraction and μ and τ neutrino fractions are not scaled anymore.

The interaction spheres at $t_{\rm pb} = 250\,$ms are shown in Fig. 11.8. The $\nu_{\rm e}$ situation remains mostly unchanged. For $\overline{\nu}_{\rm e}$, inverse muon decay remains essential only for low energy neutrinos but otherwise has little importance. Thermal effects have become apparent for ν_μ and $\overline{\nu}_\mu$, as beta-reactions on nucleons are now open to all neutrino energies even below the nominally hard muon rest mass cutoff. In contrast to electron neutrinos, the μ neutrinos can however still not stay in chemical equilibrium at densities lower than $\rho \sim 10^{13}\,$g/cm^3, followed by an extensive energy and scattering sphere. Any memory of the muonic reactions is therefore destroyed, and a spectral shape very close to ν_τ should be restored. The only effect on the neutrino spectral shape is consequently purely caused by temperature variations in the mantle at the energy-dependent neutrinospheres.

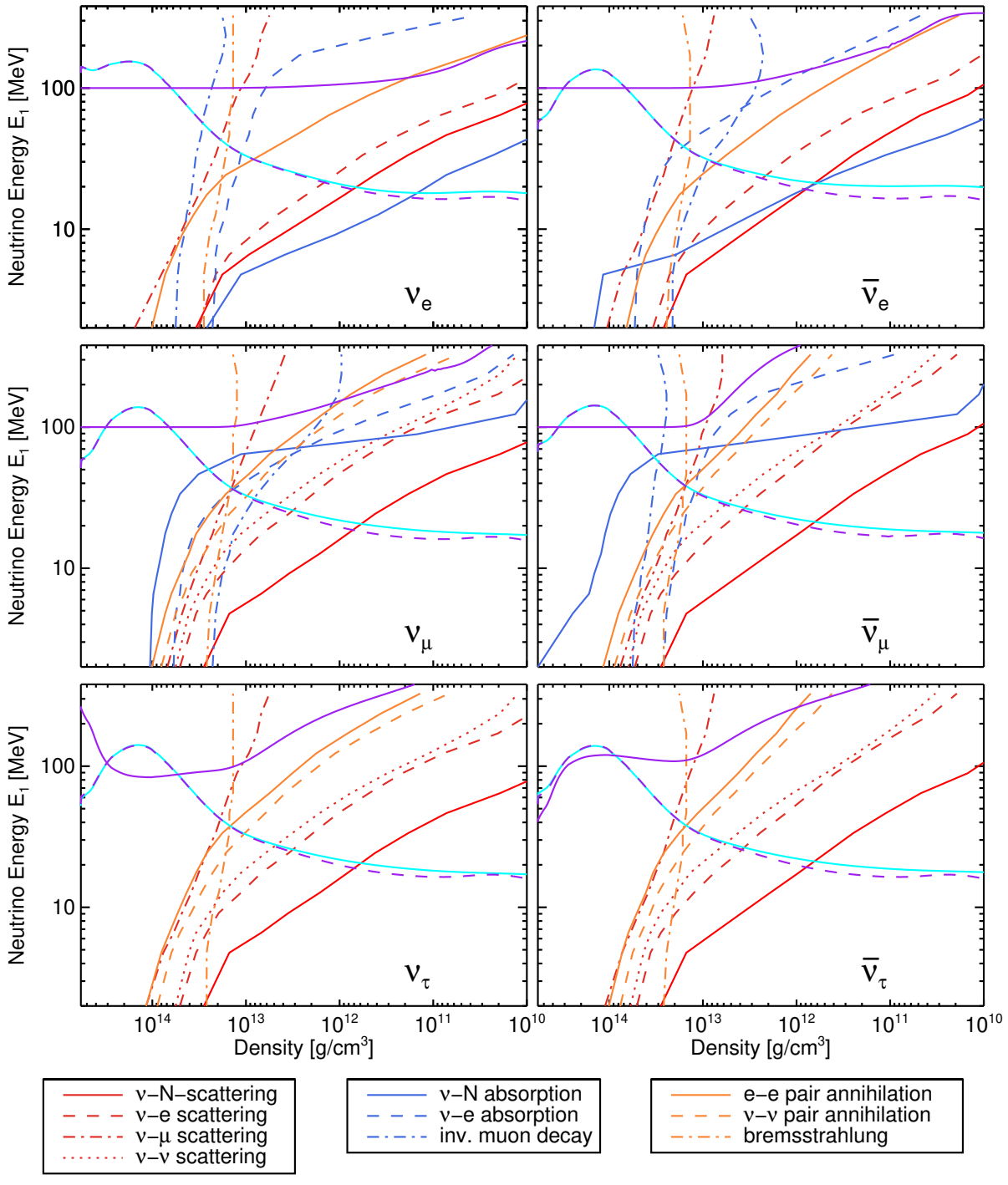

Figure 11.8: Density spheres of last interaction for all neutrinos of case s20.0-SFHo-muons at $t_{\mathrm{pb}} = 250\,\mathrm{ms}$. The figure content is identical to Fig. 11.4.

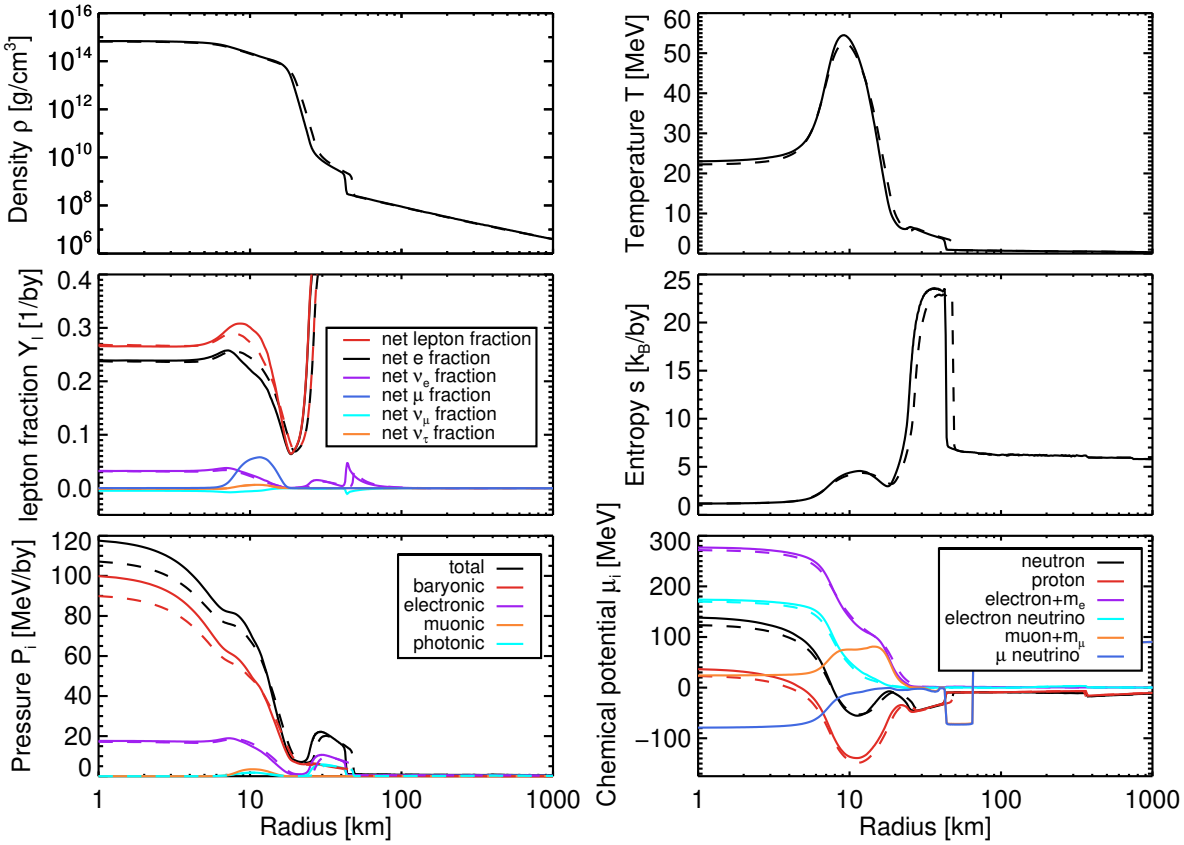

Figure 11.9: Profiles of case s20.0-SFHo-muons in solid lines and s20.0-SFHo-standard in dashed lines at $t_{\mathrm{pb}} = 500\,\mathrm{ms}$. Identical plot content as in Fig. 11.7.

500 ms postbounce At this late stage, the protoneutron star has entered a quasi-steady-state evolution, where neutrino emission perfectly balances the energy gain by gravitational contraction, and the maximum temperature will stay roughly the same for the remaining evolution. The final maximum muon fraction has settled at $Y_\mu \approx 0.058$; the electron fraction shows only a smaller maximum decrease of about $\Delta Y_\mathrm{e} \approx 0.02$, with the result of an increased proton fraction compared to the standard case. The amount of trapped electron fraction seems to be nearly unchanged, except shifted to slightly smaller radii. The increased proton fraction leads to a slight increase in proton chemical potential at the location of the temperature maximum, but only a mild change in neutron chemical potential.

Note that strong nuclear interactions between the nucleons are attractive around saturation density and the chemical potentials are influenced by the symmetry energy J via (see Ref. [32])

$$\mu_\mathrm{n} - \mu_\mathrm{p} \approx 4\beta J\left(T,\,\rho\right)\,, \tag{11.3}$$

where $\beta = 1 - 2Y_\mathrm{p}$ is the asymmetry parameter. Additionally, one can expand the binding energy per baryon at $T = 0\,\mathrm{MeV}$ around saturation density in a power series (see for example Ref. [43]) to be

$$E\left(x,\beta\right) = -E_0 + \frac{1}{18}Kx^2 + \mathcal{O}(x^3) + \beta^2\left(J + \frac{1}{3}Lx + \mathcal{O}(x^2)\right) + \cdots\,, \tag{11.4}$$

where $x = n_\mathrm{B}/n_\mathrm{B}^0 - 1$ is the relative deviation from saturation density, E_0 is the binding energy at saturation density of symmetric matter, K is the bulk incompressibility, J is the symmetry energy, and L is the slope of the symmetry energy. For values of the used SFHo EOS are

(see Ref. [32]): $E_0 = 16.19\,\mathrm{MeV}$, $K = 245\,\mathrm{MeV}$, $J = 31.57\,\mathrm{MeV}$ and $L = 47.1\,\mathrm{MeV}$. The reduction of the asymmetry parameter at the SFHo saturation density of $n_\mathrm{B}^0 = 0.1583\,\mathrm{fm}^{-3} \approx 2.63 \times 10^{14}\,\mathrm{g/cm}^3$, from $\beta = 1 - 2Y_\mathrm{e} \approx 1 - 2 \cdot 0.253 = 0.495$ in the standard case to $\beta = 1 - 2Y_\mathrm{p} \approx 1 - 2 \cdot 0.28 = 0.44$ in the muonic case, reduces the binding energy per nucleon at saturation density by $\Delta E = 1.575\,\mathrm{MeV}$. According to Eq. 11.4, the muonic case would need to increase density by a factor of $x_\mathrm{muons} = 0.2645$ to maintain the same binding energy as the standard case has at saturation density, i.e.,

$$E_\mathrm{muons}\left(x_\mathrm{muons}, \beta_\mathrm{muons}\right) = \frac{K}{18} x_\mathrm{muons}^2 + \beta_\mathrm{muons}^2 \left(J + \frac{L}{3} x_\mathrm{muons}\right) = \beta_\mathrm{standard}^2 J = E_\mathrm{standard}\left(0, \beta_\mathrm{standard}\right) ,$$

if we were neglecting any thermal effects.

Looking at the overall increased pressure everywhere in the PNS is not instructive in determining which exact factor is responsible for the decrease in PNS radius, as the hydrostatic pressure gradient is directly set by gravitational acceleration and density to be

$$\frac{\partial P}{\partial r} = -\frac{\partial \Phi}{\partial r} \rho \,. \tag{11.5}$$

However, the influence of the symmetry energy alone shows that the radius reduction of the PNS depends on all variables simultaneously. If one were to look at the individual components of the EOS in isolation, it would be easy to identify a single cause for the radius reduction. For example, if thermal energy is purely converted into muon pairs at rest, one loses $E_\gamma = 2m_\mu$ of energy and $P_\gamma = \frac{1}{3} E_\gamma$ of pressure, converting it into $E_\mu^\text{rest mass} = 2m_\mu$ and $P_\mu^\text{pair} = 0\,\mathrm{MeV}$. The muons would then quickly thermalize with the surrounding matter, which consumes a further $E_\mu^\text{internal} \approx 2 \cdot \frac{3}{2} T$ to gain $P_\mu^\text{pair} \approx 2T_\text{new}$ in pressure, at a new reduced temperature T_new given by energy conservation. As long as the main pressure contribution does not result from quasi-temperature independent effects like strong interactions or high degeneracy, a reduced temperature leads to an overall reduced pressure of all EOS components. Due to hydrostatic equilibrium, given by Eq. 11.5, this will lead to an increase in central density and a corresponding reduction in PNS radius. Additionally, increased GR corrections to the gravitational potential further magnify the effect. Similarly, converting a degenerate electron with chemical potential $\mu_\mathrm{e} \sim 250\,\mathrm{MeV}$ into a nondegenerate muon, while neglecting neutrinos, converts initial kinetic energy $E_\mathrm{e} \approx \frac{3}{4}\mu_\mathrm{e}$ with pressure $P_\mathrm{e} \approx \frac{1}{4}\mu_\mathrm{e}$ into a partly relativistic muon of energy $E_\mu \approx \frac{3}{4}\mu_\mathrm{e} - m_\mu$ and pressure $P_\mu = \frac{1}{4}\mu_\mathrm{e} - \frac{1}{3} m_\mu$. The final temperature, after the muon has thermalized and lost the surplus energy $\frac{3}{4}\mu_\mathrm{e} - m_\mu - \frac{3}{2} T_\text{neu}$, is likely to be higher than the initial temperature. As the degenerate electron gas is not sensitive to temperature variations, this would, however, still lead to an overall loss of pressure. The PNS will then again contract to restore hydrostatic equilibrium.

To determine the effect muonization has on the EOS at saturation density and temperatures of around $T = 50\,\mathrm{MeV}$, we will compare temperatures and pressures under the constraint of energy and charge conservation if a standard gas of only nucleons, nuclei, electrons and photons is instantaneously supplemented

1. by a gas of pure muon pairs.
2. by the maximum net muon number plus muon pairs we observed in our simulation, via a direct exchange of electron and muon number.
3. by the maximum net muon number plus muon pairs in addition to the original electron number, thereby changing the asymmetry parameter β of Eq. 11.4.

The third column in Table 11.1 shows that adding the pure muon-antimuon gas, equivalent to $\mu_\mu = 0$, reduces the temperature by $1.45\,\mathrm{MeV}$ as thermal energy is converted into muon rest mass energy. The temperature reduction decreases the pressure of all components, which is only partly compensated by the pressure of the new muon pairs. The fourth column shows how releasing electron degeneracy energy can lead to a net gain in temperature as the electron chemical potential is well above the muon rest mass. The loss of electron pressure is, however, larger than the gain in muon pressure, and the total pressure is reduced slightly compared to the unmodified state. The fifth column shows the effect of reducing the asymmetry parameter β by keeping electron number constant and muon production only happening via absorption reactions on neutrons. This shows the lowest temperature and pressure out of all considered variations as the baryonic pressure is significantly reduced and electrons were not able to release any degeneracy energy.

$\rho = 2.63 \times 10^{14}\,\mathrm{g/c}m^3$	$T = 50\,\mathrm{MeV}$	$T = 48.65\,\mathrm{MeV}$	$T = 50.14\,\mathrm{MeV}$	$T = 46.20\,\mathrm{MeV}$
	$Y_\mathrm{p} = 0.25$	$Y_\mathrm{p} = 0.25$	$Y_\mathrm{p} = 0.25$	$Y_\mathrm{p} = 0.308$
	$Y_\mathrm{e} = 0.25$	$Y_\mathrm{e} = 0.25$	$Y_\mathrm{e} = 0.192$	$Y_\mathrm{e} = 0.25$
	$Y_\mu = 0$	only μ^--μ^+pairs	$Y_\mu = 0.058$	$Y_\mu = 0.058$
$E^\mathrm{normalized}_\mathrm{total}$	3.052×10^{34}	3.050×10^{34}	3.054×10^{34}	3.052×10^{34}
$E^\mathrm{normalized}_\mathrm{baryonic}$	1.550×10^{34}	1.494×10^{34}	1.557×10^{34}	1.327×10^{34}
$E_\mathrm{electronic}$	1.414×10^{34}	1.387×10^{34}	1.068×10^{34}	1.342×10^{34}
E_muonic	0	9.057×10^{32}	3.404×10^{33}	3.185×10^{33}
E_photonic	8.572×10^{32}	7.685×10^{32}	8.671×10^{32}	6.251×10^{32}
P_total	1.759×10^{34}	1.732×10^{34}	1.732×10^{34}	1.673×10^{34}
P_baryonic	1.288×10^{34}	1.248×10^{34}	1.292×10^{34}	1.148×10^{34}
$P_\mathrm{electronic}$	4.425×10^{33}	4.366×10^{33}	3.268×10^{33}	4.266×10^{33}
P_muonic	0	2.147×10^{32}	8.406×10^{32}	7.661×10^{32}
P_photonic	2.857×10^{32}	2.563×10^{32}	2.890×10^{32}	2.084×10^{32}

Table 11.1: Energy and pressure of all gas components for the conditions in the top four rows. All energies and pressures are given in [erg/cm^3], and the baryonic and total energy densities have been normalized by $E^\mathrm{normalized} = E^\mathrm{relativistic} - \rho/m_\mathrm{B}\left(m_\mathrm{n} - E_0\right)$ where $E_0 = 9.2\,\mathrm{MeV}$, $m_\mathrm{B} = 1.66 \times 10^{-24}\,\mathrm{g}$ and $m_\mathrm{n} = 939.5731\,\mathrm{MeV}$.

For reference, we also show a similar analysis for conditions further out, at a density of $\rho = 5 \times 10^{13}\,\mathrm{g/cm}^3$ and a temperature of $T = 15\,\mathrm{MeV}$. Here we see that the temperature is too low for muon–antimuon pairs alone to have any effect. Only the cases where net muon number is included show a lower temperature and pressure. One can see that the temperature after conversion of electrons into muons is lowered, as the electron chemical potential is not large enough to compensate for the additional muon rest mass. In these conditions, muonization via net muon number will always lead to a reduction in pressure and temperature and to a contraction of the protoneutron star to maintain hydrostatic equilibrium.

$\rho = 5 \times 10^{13}$ g/cm^3	$T = 15$ MeV	$T = 15$ MeV	$T = 14.91$ MeV	$T = 14.77$ MeV
	$Y_\mathrm{p} = 0.08$	$Y_\mathrm{p} = 0.08$	$Y_\mathrm{p} = 0.08$	$Y_\mathrm{p} = 0.0835$
	$Y_\mathrm{e} = 0.08$	$Y_\mathrm{e} = 0.08$	$Y_\mathrm{e} = 0.0765$	$Y_\mathrm{e} = 0.8$
	No muons	only μ^--μ^+pairs	$Y_\mu = 0.0035$	$Y_\mu = 0.0035$
$E^\mathrm{normalized}_\mathrm{total}$	1.569×10^{33}	1.569×10^{33}	1.569×10^{33}	1.569×10^{33}
$E^\mathrm{normalized}_\mathrm{baryonic}$	1.269×10^{33}	1.269×10^{33}	1.263×10^{33}	1.249×10^{33}
$E_\mathrm{electronic}$	2.925×10^{32}	2.925×10^{32}	2.765×10^{33}	2.906×10^{33}
E_muonic	0	4.878×10^{29}	2.227×10^{31}	2.223×10^{31}
E_photonic	6.952×10^{30}	6.940×10^{30}	6.784×10^{30}	6.529×10^{30}
P_total	6.484×10^{32}	6.481×10^{32}	6.413×10^{32}	6.369×10^{32}
P_baryonic	5.508×10^{32}	5.505×10^{32}	5.466×10^{32}	5.374×10^{32}
$P_\mathrm{electronic}$	9.515×10^{31}	9.513×10^{31}	8.989×10^{31}	9.466×10^{31}
P_muonic	0	5.558×10^{28}	2.551×10^{30}	2.527×10^{30}
P_photonic	2.317×10^{30}	2.314×10^{30}	2.2610×10^{30}	2.176×10^{30}

Table 11.2: Energy and pressure of all gas components for the conditions in the top four rows as in Table 11.1.

In Fig. 11.10 we show all neutrino opacities weighted by the local neutrino energy density via

$$\frac{1}{\lambda}_\mathrm{weighted} = \frac{\int \mathrm{d}E_1 \, J\left(E_1\right) \frac{1}{\lambda}\left(E_1\right)}{\int dE_1 J\left(E_1\right)}, \tag{11.6}$$

where we neglect final phase-space blocking for the case of scattering reactions but take the local partner neutrino spectrum into account for pair reactions. Absorption on nucleons and muonic absorption onto lepton reactions are determined by their respective stimulated opacity and therefore contain equilibrium final phase-space blocking and local emissivity. As the interaction spheres are very similar to the situation at $t_\mathrm{pb} = 0.25$ s of Fig. 11.8, we instead focus here on the local opacities rather than the optical depth. This allows us to identify the local relative importance of the different opacities for the speed of neutrino diffusion, rather than the neutrino spectra forming radii. For ν_e we can see that the muonic opacities cannot compete with the classical opacities anywhere, except in a very localized region around saturation density. As neutrino absorption on nucleons, however, is magnitudes stronger at all densities this does not have any impact. The $\overline{\nu}_\mathrm{e}$ show an interesting property in that $\overline{\nu}_\mathrm{e}$ absorption on electrons outperforms $\overline{\nu}_\mathrm{e}$ absorption on protons above saturation density. This is a consequence of final phase-space blocking of degenerate neutrons, as well as the interaction potential difference penalty. This behavior is maintained throughout the deleptonization phase and suppresses the $\overline{\nu}_\mathrm{e}$ flux from inside the dense core. Inverse muon decay is however unimportant compared to other opacities. The ν_μ plot shows ν_μ absorption on neutrons and ν_μ absorption on electrons to be of roughly equal importance around saturation density and stronger than scattering on nucleons, but they decrease quickly as the local mean neutrino energy becomes too low. Towards lower densities and approaching the PNS surface, the opacities of muonic processes are within one or two magnitudes of each other, at roughly the same strength as the pair processes. Neutrino–muon scattering can also outperform neutrino–electron scattering around the maximum muon density, but quickly becomes as muons abundance decreases towards lower densities. The $\overline{\nu}_\mu$ overall show similar behavior as the ν_μ, except that $\overline{\nu}_\mu$ absorption on

muons can compete with ν_μ absorption on protons down to $\rho = 10^{13}$ g/cm^3. This is however only a consequence of the low proton fraction rather than any particular strength of the absorption on muons process. Overall, neutrino diffusion is still governed by the nucleonic scattering process, but muonic processes take over neutrino production. As ν_τ and $\overline{\nu}_\tau$ remain unmodified, we skip a discussion of their rates.

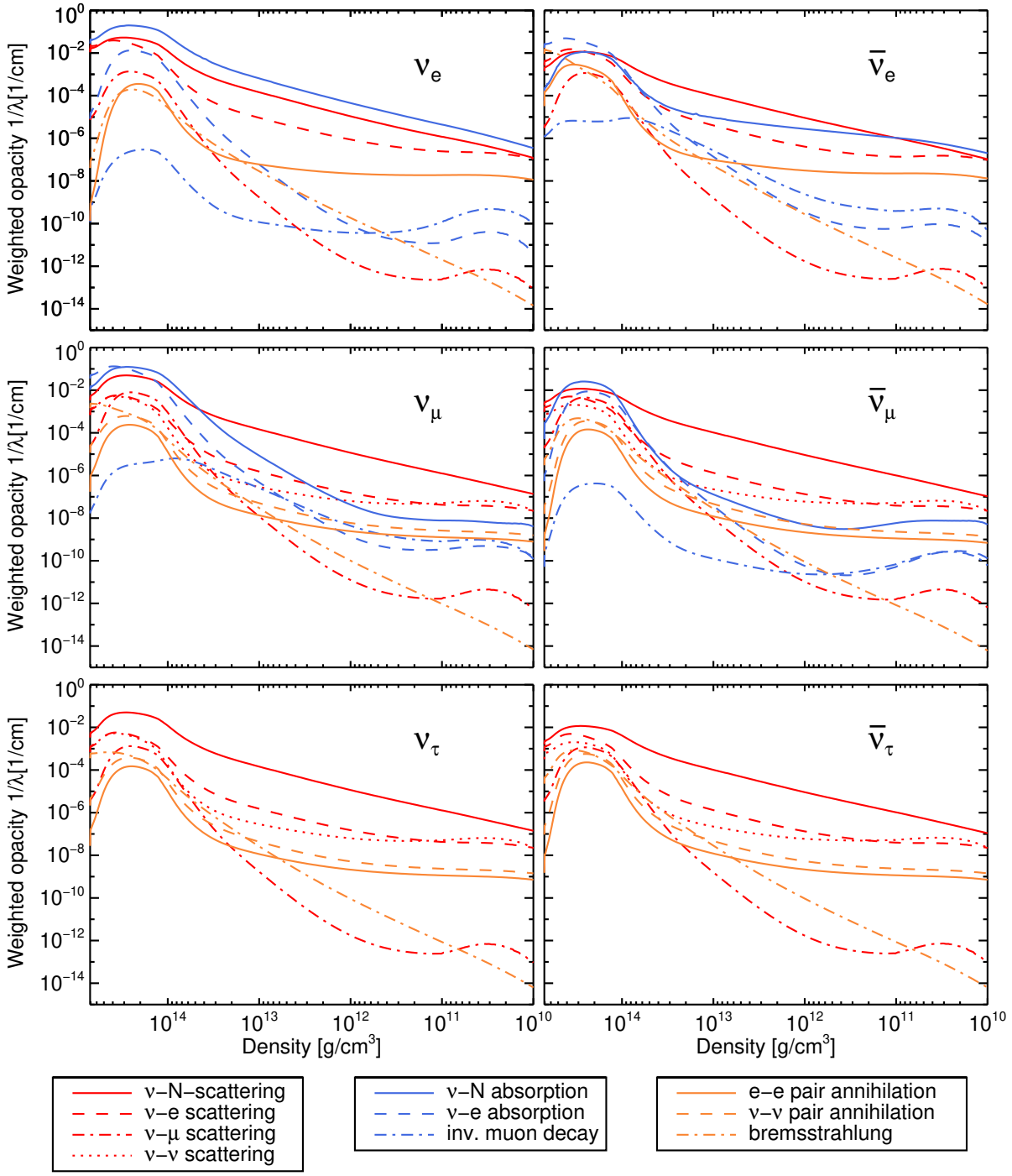

Figure 11.10: Weighted opacities at $t_{\rm pb} = 0.5$ s according to $\frac{1}{\lambda_{\rm weighted}} = \frac{\int \mathrm{d}E_1\, J(E_1) \int \mathrm{d}E_3\, \phi_0^{\rm out}(E_1,E_3)}{\int \mathrm{d}E_1\, J(E_1)}$.

11.1.2 Time evolution

After having analyzed radial profiles at select times, we will now examine the time evolution of specific quantities.

Radii The radius evolution of the PNS in Fig. 11.11 shows a consistent reduction of the radius in the muons case compared to the standard case immediately after the bounce, reaching a maximum contraction of about $\Delta r \approx -2.5$ km after only 200 ms of cooling. As the PNS mantle shrinks and baryonic pressure becomes the dominant pressure contribution everywhere in the PNS, both cases will tend to converge to the same final cold radius.

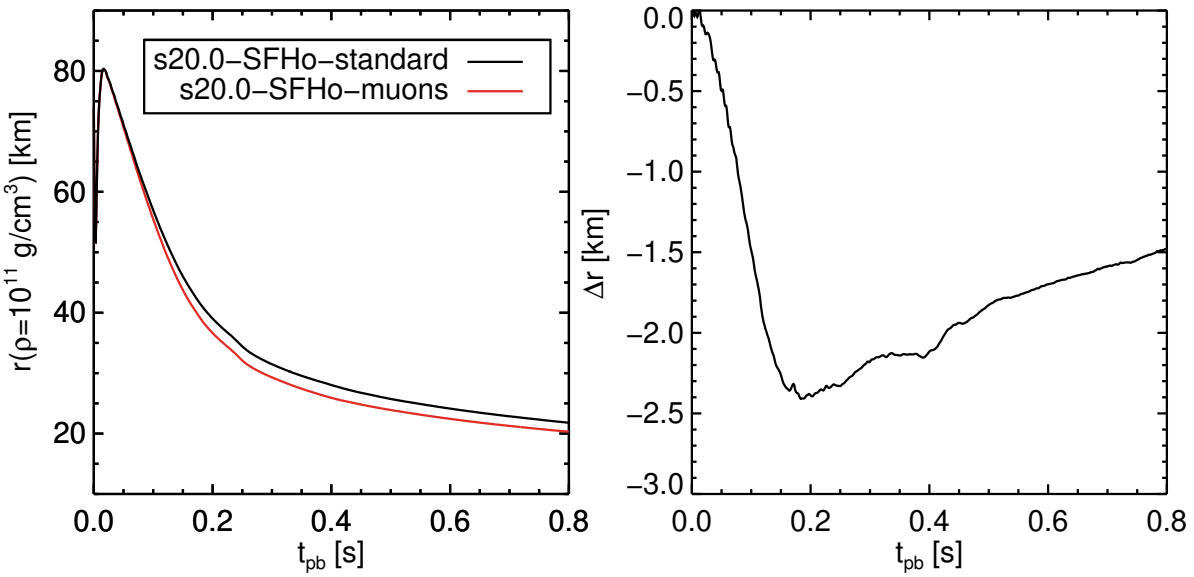

Figure 11.11: On the left, the radius evolution of the PNS defined as the radius where density is equal to $\rho = 10^{11}$ g/cm^3 for cases s20.0-SFHo-standard in black and s20.0-SFHo-muons in red; on the right, the absolute difference of both radii defined as $\Delta r = r_{\mathrm{PNS}}^{\mathrm{muons}} - r_{\mathrm{PNS}}^{\mathrm{standard}}$.

Concomitant with the reduced PNS radius is a reduction of the PNS surface area that is an essential quantity for the neutrino emission properties, plotted in Fig. 11.12. As the PNS surface area is decreased, one would expect a reduction in luminosity of about 15% if the model would otherwise remain unchanged. Due to different PNS temperatures and emission properties, this is not necessarily the case as can be seen as we go on.

The shock radius evolution in Fig. 11.13 is mostly determined by the steady-state shock condition and follows the PNS radius via following relation (see Ref. [57])

$$R_{\mathrm{shock}} \propto \frac{\left(R_{\mathrm{PNS}} T_\nu\right)^{8/3}}{\dot{M}^{2/3} M_{\mathrm{PNS}}^{1/3}}, \tag{11.7}$$

where R_{PNS} is the current radius of the PNS, T_ν is the temperature at the electron neutrino neutrinosphere, $\dot{M}$ is the mass accretion rate onto the shock and M_{PNS} is the PNS gravitational mass. As 1D simulations generally do not explode since they lack the beneficial effects of convection and hydrodynamic instabilities, the shock will, except for special cases of progenitors (e.g., Ref. [84]), always end up in a state of steady-state accretion. As our muonic case does not modify the denominator in any way and only decreases the PNS radius, this will accordingly lead to a reduced shock radius that closely tracks the radius evolution in Fig. 11.11. The transient bump in the shock radius at $t_{\mathrm{pb}} \approx 0.25$ s is caused by the infall of the silicon-oxygen (Si-O) shell

interface that leads to a steep drop in mass accretion rate and concomitant transient shock expansion.

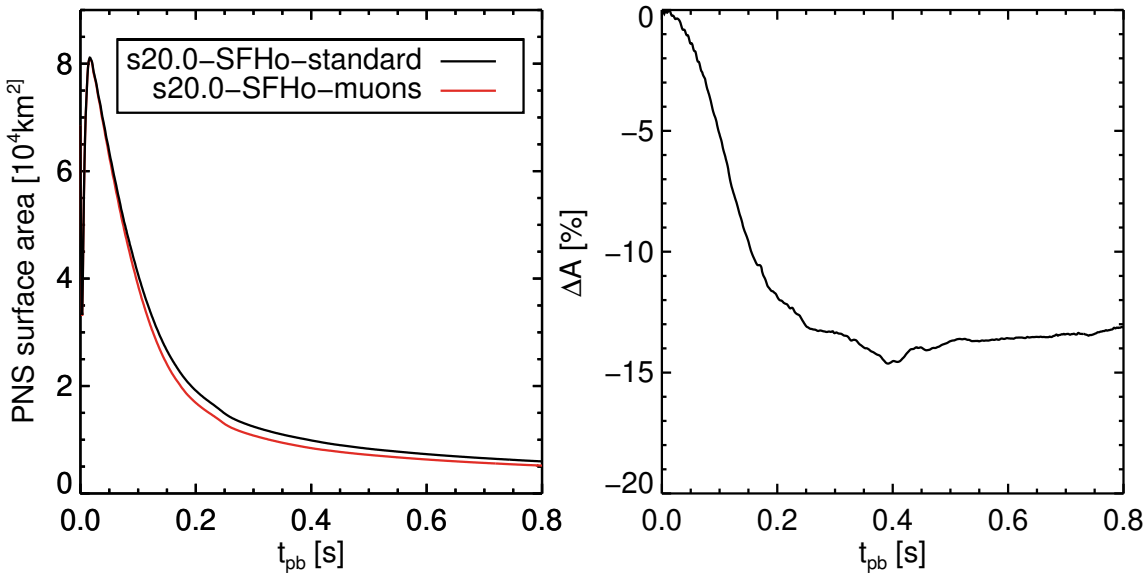

Figure 11.12: On the left, the surface area evolution of the PNS given by $A = 4\pi r_{\rm PNS}^2$ for cases s20.0-SFHo-standard in black and s20.0-SFHo-muons in red; on the right, the relative difference of both surface areas defined as $\Delta A = \frac{A_{\rm PNS}^{\rm muons} - A_{\rm PNS}^{\rm standard}}{A_{\rm PNS}^{\rm standard}} \times 100$.

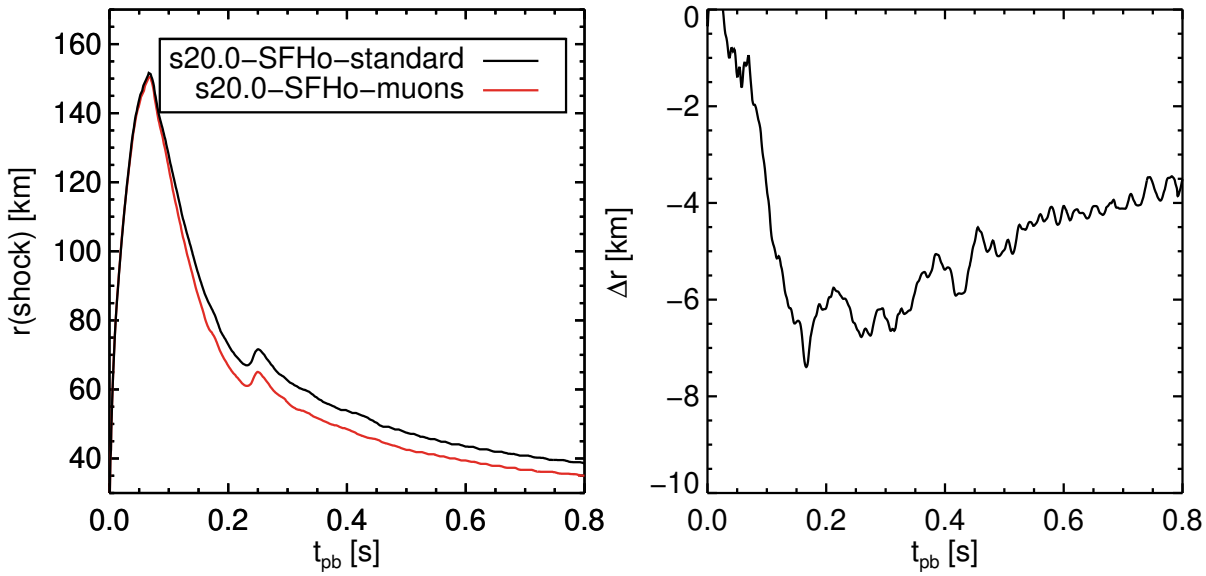

Figure 11.13: On the left, the evolution of the shock radius for cases s20.0-SFHo-standard in black and s20.0-SFHo-muons in red; on the right, the absolute difference of both radii defined as $\Delta r = r_{\rm shock}^{\rm muons} - r_{\rm shock}^{\rm standard}$.

Neutrino heating As there is an additional contribution by the neutrinospheric temperature, we will also plot as a simple approximation the temperature defined at the PNS surface, equivalent to $r\left(\rho = 10^{11}\,\mathrm{g/cm^3}\right)$. As heavy-lepton neutrinos still do not provide significant additional heating, we can neglect their more complicated neutrinosphere locations for now. As visible in Fig. 11.14, the addition of muons has increased the temperature at the PNS surface by up to $\Delta T_\nu \approx 0.4\,\mathrm{MeV}$. This increase is mainly a consequence of the increased PNS contraction rather than modified heating or cooling by heavy-lepton neutrinos, as all new muonic processes have already frozen out at the ν_e neutrinosphere. The increased neutrinospheric temperature enters the steady-state shock condition and can compensate slightly for the reduced PNS radius.

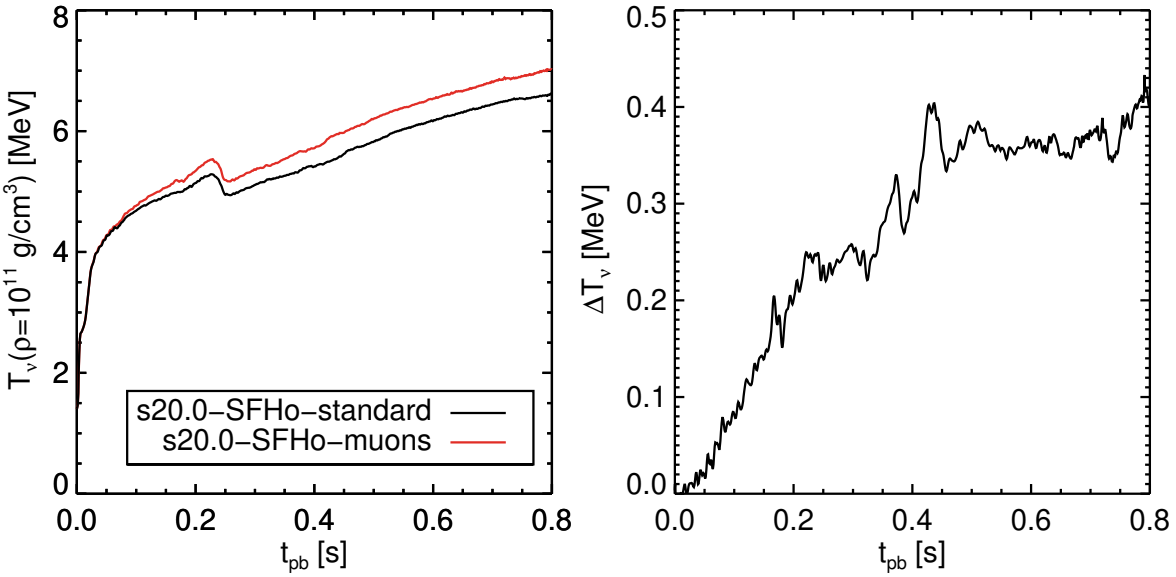

Figure 11.14: On the left, the evolution of the neutrinosphere temperature for cases s20.0-SFHo-standard in black and s20.0-SFHo-muons in red; on the right, the absolute difference of both temperatures defined as $\Delta T_\nu = T_\nu^{\mathrm{muons}} - T_\nu^{\mathrm{standard}}$. For convenience, we use the temperature at the PNS surface, shown in Fig. 11.11, as our electron neutrino neutrinosphere, which is a reasonable approximation.

Another vital quantity to be looked at is the gain radius, where the cooling due to energy loss via neutrino emission of all flavors is balanced precisely by mostly absorption on nucleons by electron neutrinos. This radius demarcates the cooling layer from the gain layer that extends up to the shock. In Fig. 11.15 we show the gain radius defined by the radius where the energy deposition source term by neutrinos changes sign from negative, indicating net cooling, to positive, indicating net heating. This radius strongly correlates with the PNS radius, temperature profile in the cooling layer, and mass accretion rate settling onto the PNS. As we can see, the gain radius retreats to smaller radii, as the PNS contracts faster in the muonic case. As all radii, i.e., PNS radius, gain radius, and shock radius show a contraction compared to the standard case, it is essential to check whether this is beneficial towards increasing neutrino heating. A reduced PNS radius will in general lead to a reduced angle-integrated neutrino luminosity as the neutrino emitting surface decreases. This decrease in PNS radius will need to be compensated by the increased temperature at the respective neutrinosphere, at which the neutrino luminosity roughly scales by $L_\nu \propto R_\mathrm{PNS}^2 T_\nu^4$ in a black-body like fashion.

Furthermore, one needs to compare the volume contained in the gain layer. As the mass accretion rate is unchanged between both standard and muon cases, this will directly relate to the mass held inside the gain layer that can be heated by neutrinos. A large contained

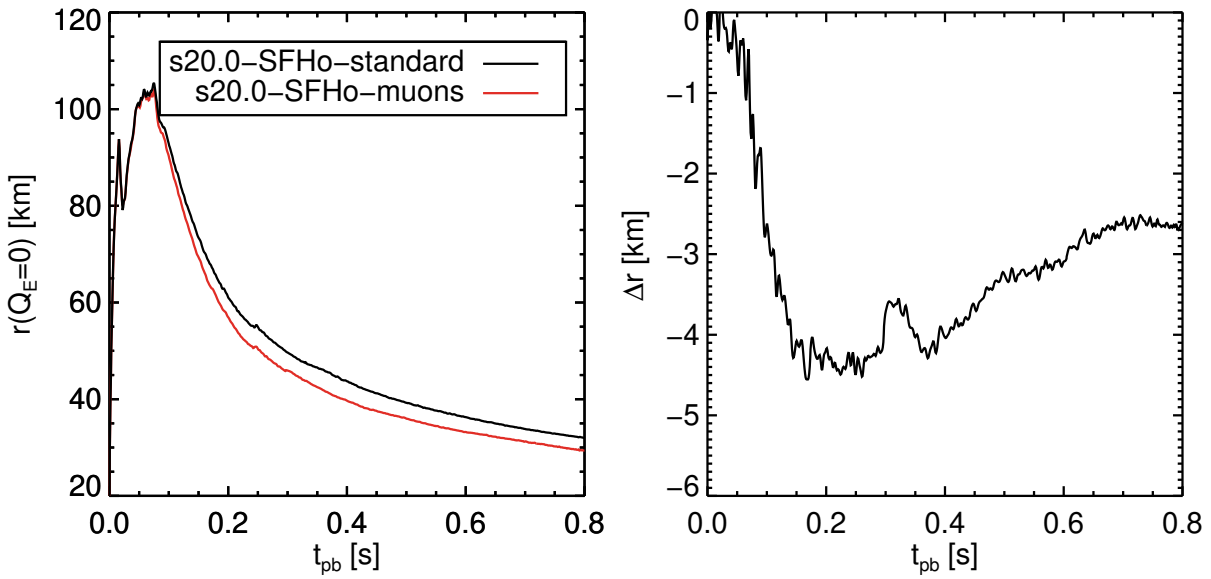

Figure 11.15: On the left, the evolution of the gain radius for cases s20.0-SFHo-standard in black and s20.0-SFHo-muons in red; on the right, the difference of both radii defined as $\Delta r = r_{\text{gain}}^{\text{muons}} - r_{\text{gain}}^{\text{standard}}$.

mass increases the chance of the weakly-interacting neutrinos to interact with the matter, and together with the luminosity and root mean square of the energy is an essential ingredient to improving the neutrino heating efficiency. The contraction of the gain radius as well as of the shock radius might lead to a reduction of the gain layer volume, and thereby to a less optimistic chance of shock revival in the muonic case, if the gain layer volume does not retreat faster than the shock radius. The gain layer volume is calculated by

$$V_{\text{gain}} = 4\pi \int_{r_{\text{gain}}}^{r_{\text{shock}}} \mathrm{d}r\, r^2 \,. \tag{11.8}$$

As can be seen in Figs. 11.16 and 11.17, the muonic case features a 30% reduction of the enclosed volume in the gain layer and therefore also a reduced gain layer mass by up to 20%. Note that the gain layer mass is not decreased as much as the volume itself, as the accreting matter is more compressed inside the gain layer.

The retreating gain radius is directly related to the increased temperature at the PNS surface in Fig. 11.14 as the cooling rate roughly scales with

$$Q_{\text{E}}^{-} \propto T^6 \tag{11.9}$$

(see Ref. [57]), and is therefore extremely sensitive to small temperature variations. As the gain radius is located at the point where the heating rate can just compensate the cooling rate, it will be shifted to higher radii if the temperature profile is shallower in the cooling layer.

The increased cooling rate will need to be compensated by an increase in heating rate, proportional to

$$Q_{\text{E}}^{+} \propto L_\nu \langle E_\nu^2 \rangle \tag{11.10}$$

(see Ref. [57]), where $\langle E_\nu^2 \rangle$ is the mean square of the neutrino energy moment. The mean square reflects the energy scaling behavior of the neutrino cross sections, e.g., the energy source term for absorption reactions is $Q_{\text{E}}^{+} \propto \kappa L_\nu$and $\kappa \propto p_{\text{e}} E_{\text{e}} n_{\text{nuc}} \approx E_\nu^2 n_{\text{nuc}}$ in the elastic approximation.

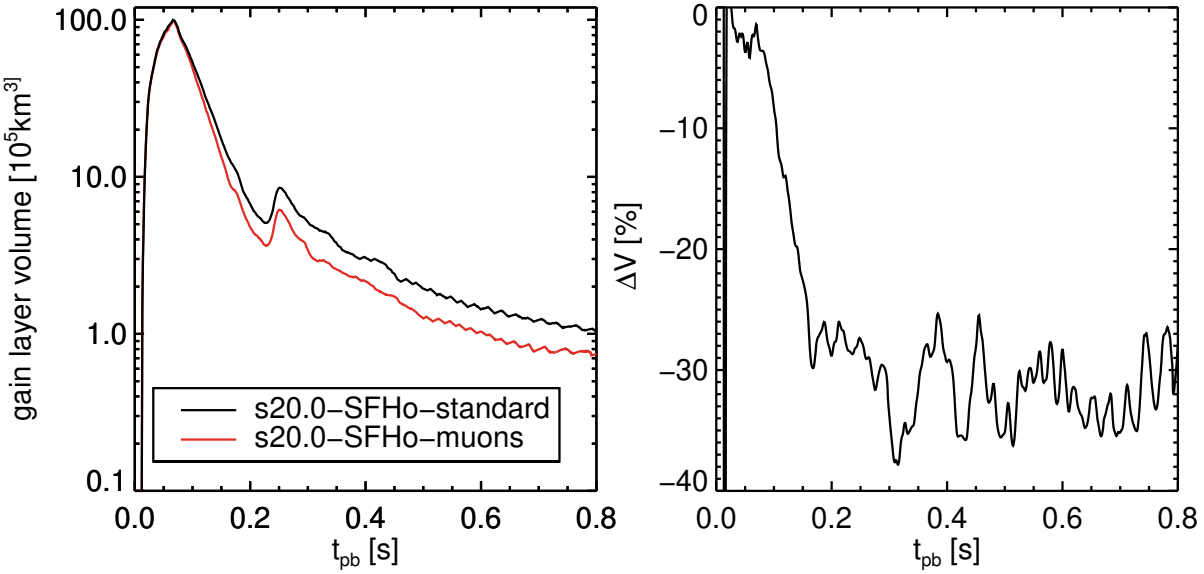

Figure 11.16: On the left, the evolution of the enclosed volume of the gain layer for cases s20.0-SFHo-standard in black and s20.0-SFHo-muons in red; on the right, the relative difference of both volumes defined as $\Delta V = \frac{V_{\rm gain}^{\rm muons} - V_{\rm gain}^{\rm standard}}{V_{\rm gain}^{\rm standard}} \times 100$.

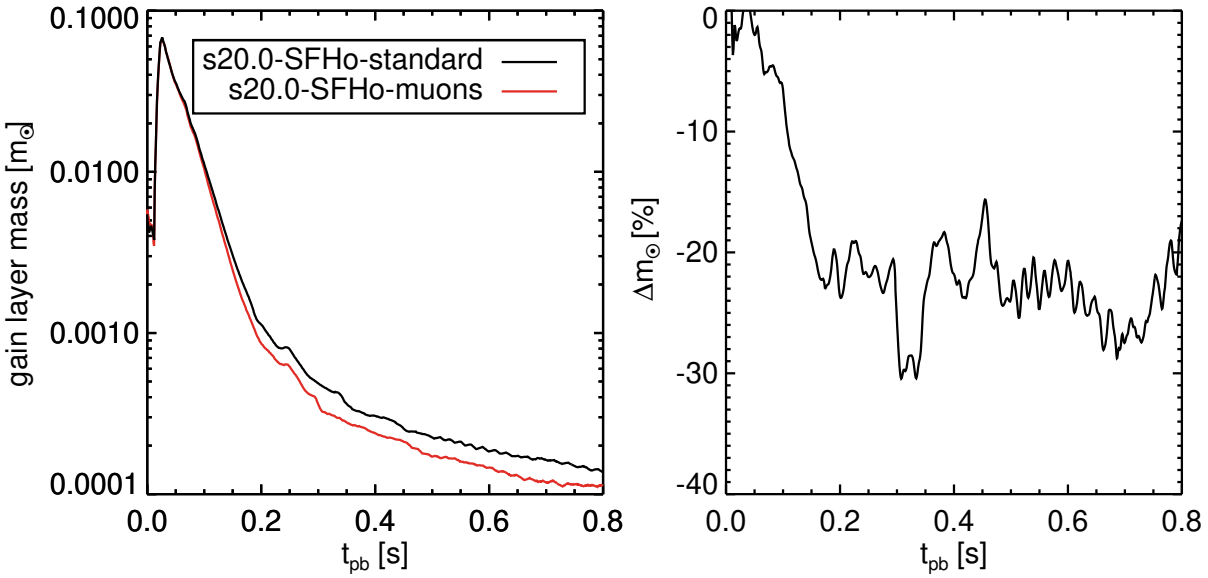

Figure 11.17: On the left, the evolution of the gain layer mass in units of solar mass for cases s20.0-SFHo-standard in black and s20.0-SFHo-muons in red; on the right, the relative difference of both masses defined as $\Delta m = \frac{m^{\rm muons} - m^{\rm standard}}{m^{\rm standard}} \times 100$.

The mean energy of the emitted neutrinos is set by the temperature at the respective energy-dependent energy-sphere of each neutrino species, as depicted in the preceding sections for specific times. As each neutrino decouples at a different radius and temperature, the spectrum will be distorted and "pinched" as described in Ref. [113]. Our inclusion of inelastic nucleon scattering will further deplete the high energy tail and may form an extended scattering-sphere with residual energy transfer.

The mean energy of an isotropic nondegenerate Fermi-Dirac gas in perfect thermal equilibrium with the surrounding gas is given by

$$\langle E \rangle = \frac{\int \mathrm{d}E\, E^3 f_{\mathrm{FD}}\left(E, \eta, T\right)}{\int \mathrm{d}E\, E^2 f_{\mathrm{FD}}\left(E, \eta, T\right)} \,. \tag{11.11}$$

The appearing integrals of the standard Fermi-Dirac distribution of an ultrarelativistic gas of

$$f_{\mathrm{FD}}\left(E, \eta, T\right) = \frac{1}{\exp\left(E/T - \eta\right) + 1} \tag{11.12}$$

can be solved analytically in the case of vanishing degeneracy, $\eta = 0$ (according to Ref. [82]), to be equal to

$$F_k\left(\eta = 0\right) = \left(1 - 2^{-k}\right)\, \Gamma\left(k+1\right)\, \zeta\left(k+1\right) \,, \tag{11.13}$$

where $\int \mathrm{d}E\, E^2 f_{\mathrm{FD}}\left(E, 0, T\right) = F_2\left(0\right)$ and $\int dE\, E^3 f_{\mathrm{FD}}\left(E, 0, T\right) = F_3\left(0\right)$. The resulting mean energy for vanishing neutrino chemical potential is

$$\langle E \rangle_{\mathrm{T}} \approx 3.1514 T_\nu \,. \tag{11.14}$$

This is a valid approximation for the resulting mean energy of the emitted neutrinos, as they have close to vanishing chemical potential at their respective energy-spheres. An increased temperature along the mantle, therefore, leads to hotter mean neutrino energies, regardless of the neutrino species involved. As we wish to evaluate the heating rates over the gain layer, we need to compute the mean energy and root mean square (RMS) of the neutrino energy moment as it enters the gain layer. Trying to estimate neutrino heating from quantities measured at the typical radius of 500 km would lead to an underestimation of the RMS energy present in the gain layer, as absorption onto post-shock nucleons and residual scattering events would further suppress the high energy tail.

The mean neutrino energy of all species, measured at the location of the gain radius in the comoving frame, is shown in Fig. 11.18. The mean neutrino energy is defined as

$$\langle E_\nu \rangle = \frac{\int_0^\infty \mathrm{d}E\, J_\nu\left(E\right)}{\int_0^\infty \mathrm{d}E\, \mathcal{J}_\nu\left(E\right)} \,, \tag{11.15}$$

where $J_\nu\left(E\right)$ is the local neutrino energy density, and $\mathcal{J}_\nu\left(E\right)$ is the local neutrino number density. One could further disentangle the mean energy by separating it into the mean energy of the neutrino energy density $J_\nu\left(E\right)$ of Eq. 11.15, and the mean energy of the neutrino energy flux density $H_\nu\left(E\right)$. The first mean energy is relevant for neutrino heating, whereas the second is relevant for the neutrino transport opacity. At the gain radius, these two quantities will be very similar, as the flux factor $f_{\mathrm{H}}\left(E\right) = H_\nu\left(E\right)/J_\nu\left(E\right)$ is close to unity. In Fig. 11.18 we can see that the mean energy of both ν_{e} and $\overline{\nu}_{\mathrm{e}}$ are increased by $\Delta\langle E \rangle \approx 1\,\mathrm{MeV}$, which correlates well with the increase of T_ν in Fig. 11.14. In combination with Eq. 11.14, an increase of $\Delta T_\nu \approx 0.35\,\mathrm{MeV}$ leads to an increase in mean energy of $\Delta\langle E_\nu \rangle \approx 3.1514 \Delta T_\nu \approx 1.1\,\mathrm{MeV}$. The mean energy of the $\overline{\nu}_{\mathrm{e}}$ being larger than $\langle E \rangle_{T_\nu} \approx 3.1514 T_\nu \approx 3.1514 \cdot 6.2\,\mathrm{MeV} = 19.5\,\mathrm{MeV}$ at $t_{\mathrm{pb}} = 0.5\,\mathrm{s}$ of the muonic case indicates that the temperature difference between muonic and standard case is still maintained at their earlier decoupling radius. As the μ and τ neutrinos are not particularly important for neutrino heating, their quantities will be evaluated later as lab-frame quantities.

The RMS energies relevant to the heating rate are an extension of the mean energy by an increased weighting of the high energy tail by E^2 to better reflect the neutrino cross-section

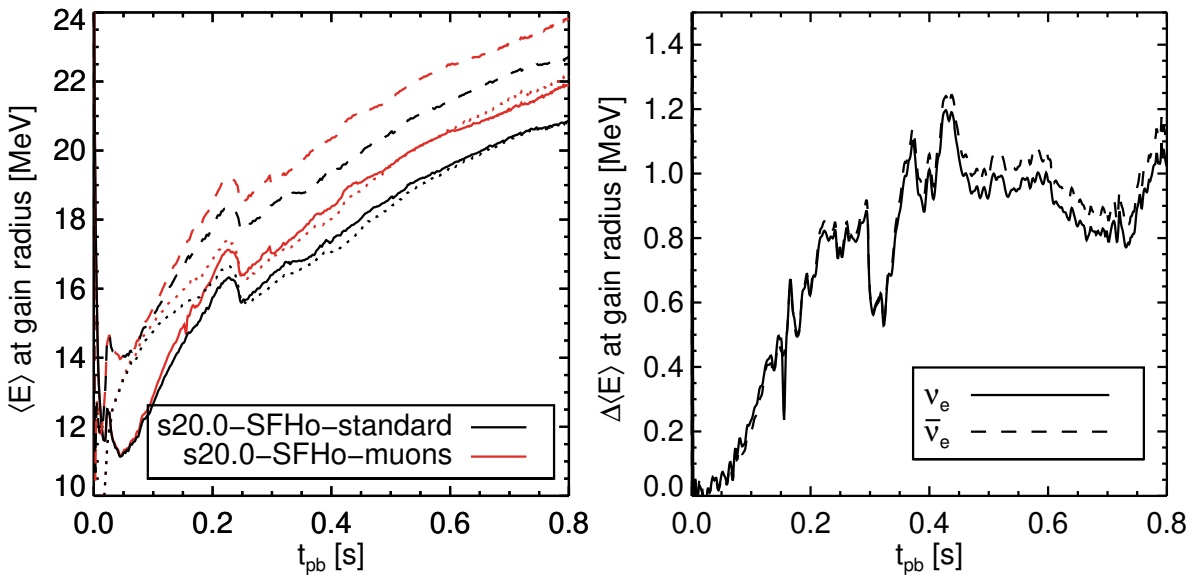

Figure 11.18: On the left, the evolution of the mean comoving energy of the local neutrino energy density at the gain radius defined as $\langle E\rangle = \int \mathrm{d}E\, J\,(E) \,/\, \int \mathrm{d}E\, \mathcal{J}(E)$ for cases s20.0-SFHo-standard in black and s20.0-SFHo-muons in red; on the right, the difference of both mean energies defined as $\Delta\langle E\rangle = \langle E\rangle^{\mathrm{muons}}_{\mathrm{gain}} - \langle E\rangle^{\mathrm{standard}}_{\mathrm{gain}}$. A thermal mean energy computed from the neutrinosphere temperature of Fig. 11.14, according to $\langle E\rangle_{\mathrm{T}} \approx 3.1514 T_\nu$, is plotted as dotted lines on the left panel.

energy dependence. There are various definitions of the RMS energy being used in that they typically either measure the RMS energy of the neutrino energy density,

$$\sqrt{\langle E^2\rangle_{\mathrm{E}}} = \sqrt{\frac{\int \mathrm{d}E\, E^2 J\,(E)}{\int \mathrm{d}E\, J(E)}} = \sqrt{\frac{\int \mathrm{d}E\, E^5 f_\nu\,(E)}{\int \mathrm{d}E\, E^3 f_\nu\,(E)}}\,, \tag{11.16}$$

or the RMS energy of the neutrino number density,

$$\sqrt{\langle E^2\rangle_{\mathrm{N}}} = \sqrt{\frac{\int \mathrm{d}E\, E^2 \mathcal{J}\,(E)}{\int \mathrm{d}E\, \mathcal{J}(E)}} = \sqrt{\frac{\int \mathrm{d}E\, E^4 f_\nu\,(E)}{\int \mathrm{d}E\, E^2 f_\nu\,(E)}}\,. \tag{11.17}$$

As we are interested in the energy deposition by the electron neutrinos and the cross section enhancement, we will focus here on $\sqrt{\langle E^2\rangle_{\mathrm{E}}}$. In Fig. 11.19 one can see that the RMS energy shows an even larger increase of $\Delta\sqrt{\langle E^2\rangle_{\mathrm{E}}} \approx 1.5\,\mathrm{MeV}$. The increased enhancement of the $\overline{\nu}_{\mathrm{e}}$ RMS energy indicates a hotter spectrum compared to ν_{e} and less pinching. One reason for this might be weak magnetism corrections to the neutrino–nucleon scattering opacity that have opposite signs for ν and $\bar{\nu}$. As the $\overline{\nu}_{\mathrm{e}}$ number-sphere lies slightly inside the residual scattering sphere and decouples at higher temperatures, the weakened suppression of the high energy tail leads to a spectral shift as described in Ref. [47] (Sec. Vb). The thermal RMS energy computed according to

$$\sqrt{\langle E^2\rangle_{\mathrm{T}}} = \sqrt{\frac{F_5\,(0)}{F_3\,(0)}} = \frac{\left(1-2^{-5}\right)\,\Gamma\,(6)\,\zeta\,(6)}{\left(1-2^{-3}\right)\,\Gamma\,(4)\,\zeta\,(4)} \approx 4.5622 T_\nu \tag{11.18}$$

compares well to the ν_e spectrum after $t_{pb} = 0.3\,s$, indicating that the ν_e spectral shape has become nearly perfectly thermal. Before this, it shows strong pinching due to absorption onto nuclei and free nucleons.

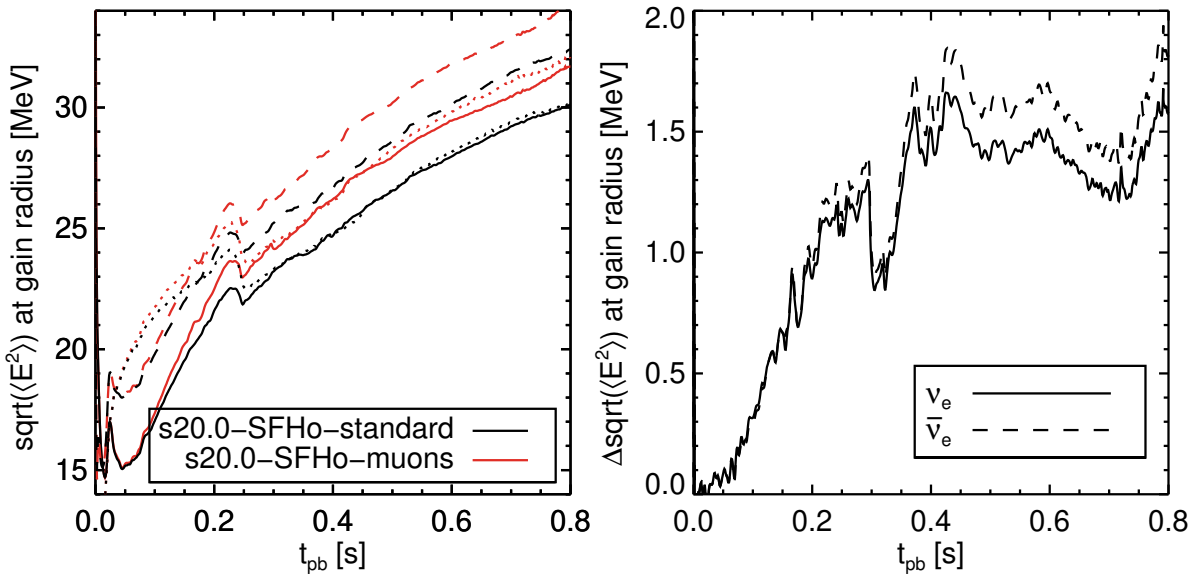

Figure 11.19: On the left, the evolution of the root mean square comoving energy of the local neutrino energy density at the gain radius defined as $\sqrt{\langle E^2\rangle_E} = \sqrt{\int dE\, E^2 J(E) / \int dE\, J(E)}$ for cases s20.0-SFHo-standard in black and s20.0-SFHo-muons in red; on the right, the difference of both RMS energies defined as $\Delta\sqrt{\langle E^2\rangle_E} = \sqrt{\langle E^2\rangle^{muons}_{E,gain}} - \sqrt{\langle E^2\rangle^{standard}_{E,gain}}$. A thermal RMS energy computed from the neutrinosphere temperature of Fig. 11.14, according to $\sqrt{\langle E^2\rangle_T} \approx 4.5622 T_\nu$, is plotted as dotted lines on the left panel.

The comoving luminosity of electron neutrinos as measured at the gain radius is the other necessary quantity in Eq. 11.10 to determine the neutrino heating inside the gain layer and is calculated via

$$L_\nu\left(r_{gain}\right) = 4\pi r^2 \int_0^\infty dE\, 4\pi H(E)\ . \tag{11.19}$$

In Fig. 11.20 we can see that the luminosity of ν_e are quite enhanced by about $\Delta L_{\nu_e} \approx 2-3\,B/s$ compared to the standard case, while the $\bar{\nu}_e$ luminosity remains nearly unchanged and only increases by up to $\Delta L_{\bar{\nu}_e} \approx 1-2\,MeV$. Interestingly both L_{ν_e}, as well as $L_{\bar{\nu}_e}$, are almost identical after $t_{pb} = 0.25\,s$.

As we see an increased mean energy of both ν_e, as well as $\bar{\nu}_e$, this must mean that the number flux has evolved differently, with

$$\mathcal{L}_\nu\left(r_{gain}\right) = 4\pi r^2 \int_0^\infty dE\, 4\pi \mathcal{H}(E)\ . \tag{11.20}$$

In Fig. 11.21 we can see that the ν_e number flux is nearly unchanged. In combination with the increased mean energy, this explains the heightened ν_e luminosity. The $\bar{\nu}_e$ number flux, however, is reduced, which seems to compensate for the increased mean energy and reproduces the standard case $\bar{\nu}_e$ luminosity. We need to remember however that the luminosity is also a function of the surface of the radiating sphere, where $L_\nu \propto T_\nu^4 R_{PNS}^2$ if the emission approaches the Stefan-Boltzmann law of a black-body radiating sphere. As the PNS radius in the muonic

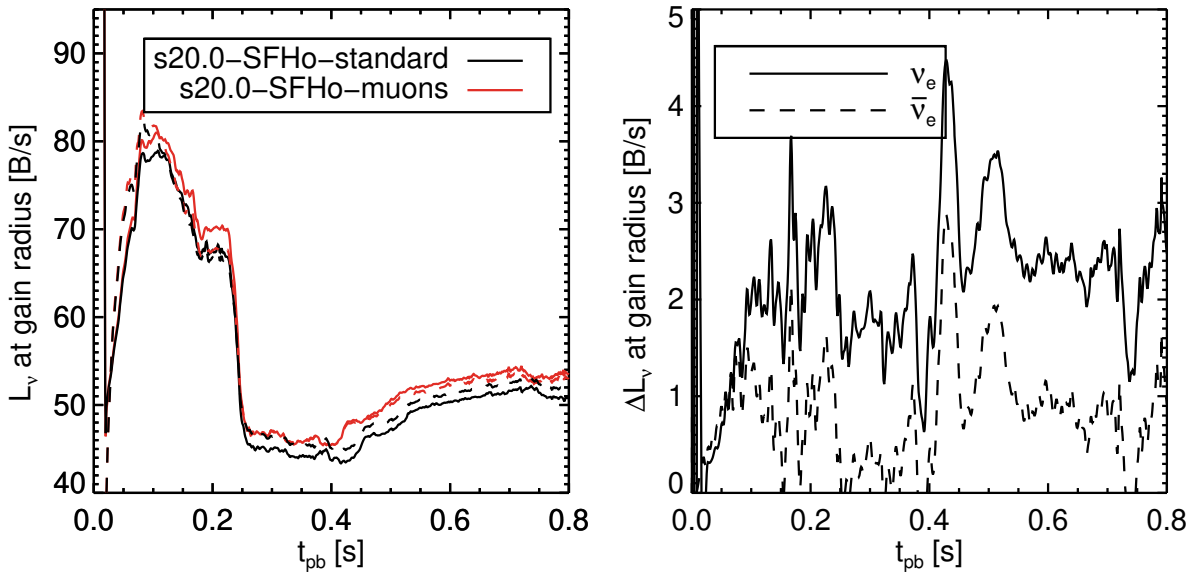

Figure 11.20: On the left, the evolution of the comoving luminosity measured at the gain radius for cases s20.0-SFHo-standard in black and s20.0-SFHo-muons in red; on the right, the difference of both luminosities defined as $\Delta L_\nu = L_\nu^{\text{muons}} - L_\nu^{\text{standard}}$.

case is reduced compared to the standard case, according to Fig. 11.11, this means the muonic case has an increased neutrino flux density at the PNS surface.

Having analyzed all quantities that enter the integrated gain layer heating rate individually, we can now look at the combined result. In Fig. 11.22 it is evident that the muonic case and

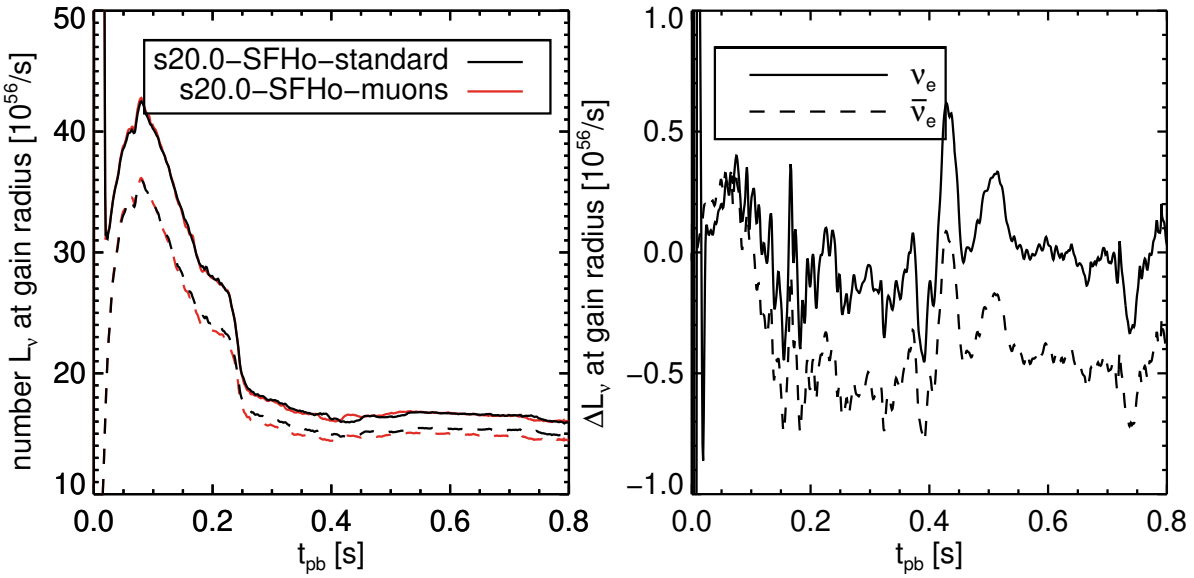

Figure 11.21: On the left, the evolution of the comoving number luminosity measured at the gain radius for cases s20.0-SFHo-standard in black and s20.0-SFHo-muons in red; on the right, the difference of both number luminosities defined as $\Delta \mathcal{L}_\nu = \mathcal{L}_\nu^{\text{muons}} - \mathcal{L}_\nu^{\text{standard}}$.

standard case have nearly identical integrated heating rates according to

$$Q_{\mathrm{E}}^{\mathrm{int}} = 4\pi \int_{r_{\mathrm{gain}}}^{r_{\mathrm{shock}}} \mathrm{d}r\, r^2 Q_{\mathrm{E}}\left(r\right) . \tag{11.21}$$

The reduced gain layer volume somewhat counteracts the increased luminosity and RMS energies of the dominant interacting neutrinos, i.e., ν_{e} and $\overline{\nu}_{\mathrm{e}}$. In the 1D case, the increased luminosity and RMS energy are, at early postbounce times, not able to adequately compensate for the accelerated PNS contraction and the steady-state shock contracting with it. Indeed, Fig. 11.23 shows that the neutrino heating efficiency,

$$Q_{\mathrm{eff}}^{\mathrm{int}} = \frac{Q_{\mathrm{E}}^{\mathrm{int}}}{L_{\nu_{\mathrm{e}}}^{\mathrm{gain}} + L_{\overline{\nu}_{\mathrm{e}}}^{\mathrm{gain}}} \times 100 \tag{11.22}$$

giving the percentage of neutrino energy being deposited in the gain layer, is only increased by up to 5–10% at late times. Note however that this might be improved further if hydrodynamic instabilities, as well as convective energy transport, can efficiently extend the gain layer volume via violent shock motion. A more efficient transfer of energy into the gain layer, as seen in the following 2D section, shows that the muonic case can prove favorable to explosions.

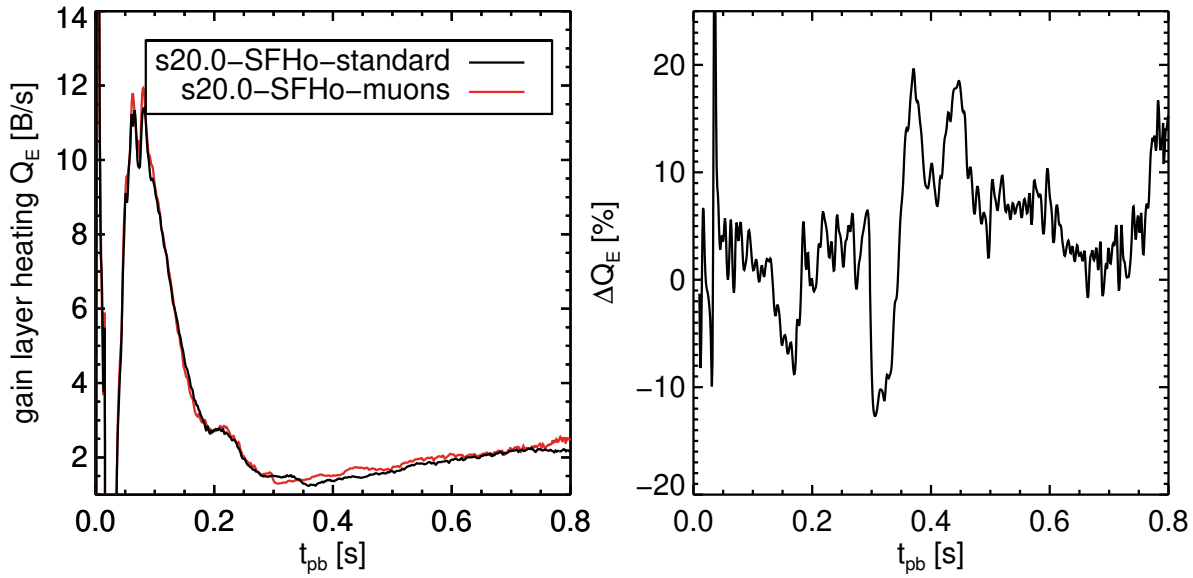

Figure 11.22: On the left, the evolution of the total energy deposition per second by neutrinos in the gain layer for cases s20.0-SFHo-standard in black and s20.0-SFHo-muons in red; on the right, the relative difference of both heating rates defined as $\Delta Q_{\mathrm{E}} = \frac{Q_{\mathrm{E}}^{\mathrm{muons}} - Q_{\mathrm{E}}^{\mathrm{standard}}}{Q_{\mathrm{E}}^{\mathrm{standard}}}$.

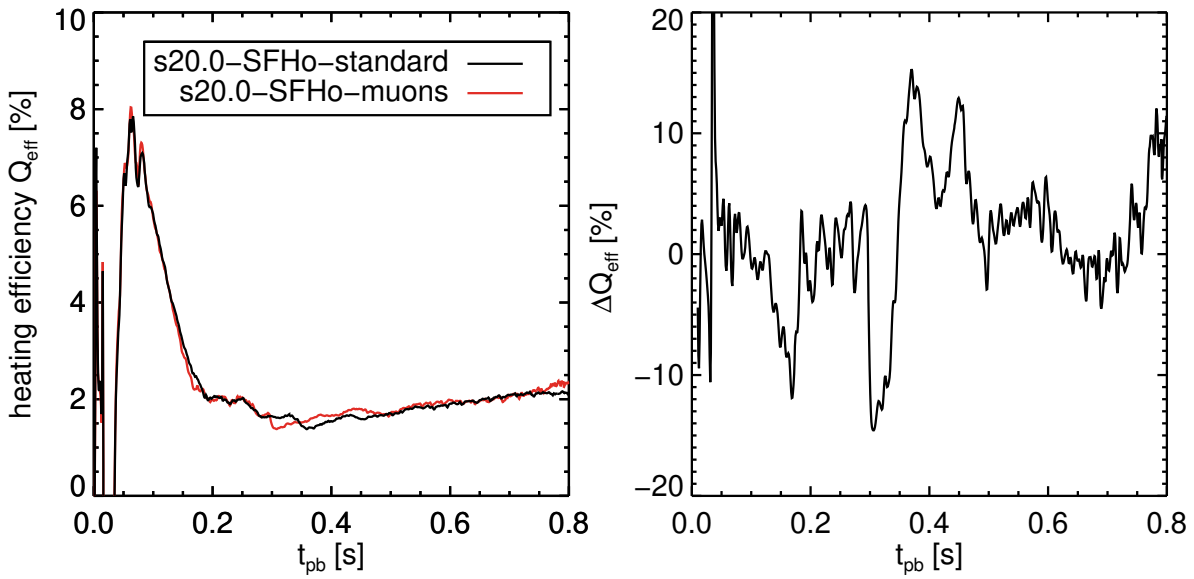

Figure 11.23: On the left, the evolution of the heating efficiency by neutrinos in the gain layer for cases s20.0-SFHo-standard in black and s20.0-SFHo-muons in red; on the right, the relative difference of both efficiencies defined as $\Delta Q_{\text{eff}} = \frac{Q_{\text{eff}}^{\text{muons}} - Q_{\text{eff}}^{\text{standard}}}{Q_{\text{eff}}^{\text{standard}}}$.

Neutrino signal The neutrino signal is evaluated in the lab-frame and extracted at a radius of $r = 400\,\text{km}$ to prevent excessive smearing of the neutrino signal by numerical diffusion. The lab-frame measurement represents the signal as it would be measured by an observer located at an infinite distance and corrected for all Doppler and gravitational redshift effects. The (v/c)-accurate lab-frame transformed luminosity is defined according to Eq. 5.21 by

$$L_\nu^{\text{lab}}\left(r = 400\,\text{km}\right) = 4\pi r^2 e^{\Phi}\left(r\right)\left\{\int_0^\infty \text{d}E\, 4\pi H\left(r,E\right) + \beta\left(r\right)\int \text{d}E\, 4\pi J\left(r,E\right)\left(1 + f_{\text{K}}\left(r,E\right)\right)\right\}, \tag{11.23}$$

where e^{Φ} is the gravitational lapse of our effective GR gravitational potential, accounting for time dilation and gravitational redshift effects. The addition of muons in Fig. 11.24 shows, just as in the comoving quantities evaluated earlier at the gain radius, that the ν_{e} luminosity is enhanced by the accelerated contraction and increased temperature at the neutrinosphere. Interestingly the $\overline{\nu}_{\text{e}}$ luminosity is now practically identical to the ν_{e} luminosity after the drop in mass accretion rate at the point in time when the Si-O shell interface falls through the shock. The $\overline{\nu}_\mu$ luminosity is considerably enhanced by the decay of antimuons or respectively by antimuon capture onto neutrons, whereas the ν_μ luminosity is slightly reduced.

This is a consequence of the muonization of the PNS, where the developing net muon number needs to produce a corresponding net $\overline{\nu}_\mu$ number flux to maintain lepton flavor number conservation. This is more directly related to the number luminosity defined as

$$\mathcal{L}_\nu^{\text{lab}}\left(r = 400\,\text{km}\right) = 4\pi r^2\left\{\int_0^\infty \text{d}E\, 4\pi\mathcal{H}\left(r,E\right) + \beta\left(r\right)\int \text{d}E\, 4\pi\mathcal{J}\left(r,E\right)\right\} \tag{11.24}$$

in Fig. 11.25, which shows that there is a negative net ν_μ number flux by increased emission of $\overline{\nu}_\mu$ compared to ν_μ. This is in contrast to the equal number flux of ν_τ and $\overline{\nu}_\tau$that exhibit the radiating surface reduction in the muonic case . The consequence of differential net ν_μ number flux for lepton flavor conservation and checks thereof will be explored in the long-term cooling simulation. A comparison between ν_μ and ν_τ shows that they are very similar to each other

with not as big a difference as between $\overline{\nu}_\mu$ and $\overline{\nu}_\tau$. This leads to the conclusion that the build-up of net muon number is not primarily caused by increased absorption of ν_μ, which would imply considerable less number flux than the ν_τ, but rather by the preferential emission of $\overline{\nu}_\mu$.

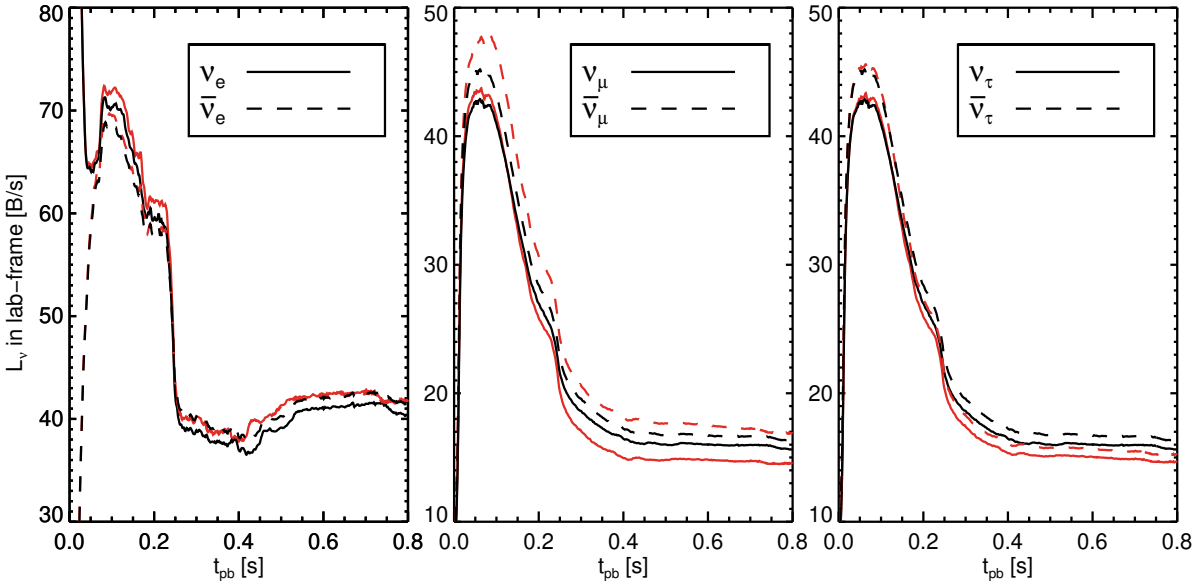

Figure 11.24: On the left, the evolution of the lab-frame luminosity of ν_e and $\overline{\nu}_e$ for cases s20.0-SFHo-standard in black and s20.0-SFHo-muons in red, in the middle of ν_μ and $\overline{\nu}_\mu$ and on the right the same for ν_τ and $\overline{\nu}_\tau$. Note that in the standard case $\nu_\mu = \nu_\tau$ as well as $\overline{\nu}_\mu = \overline{\nu}_\tau$.

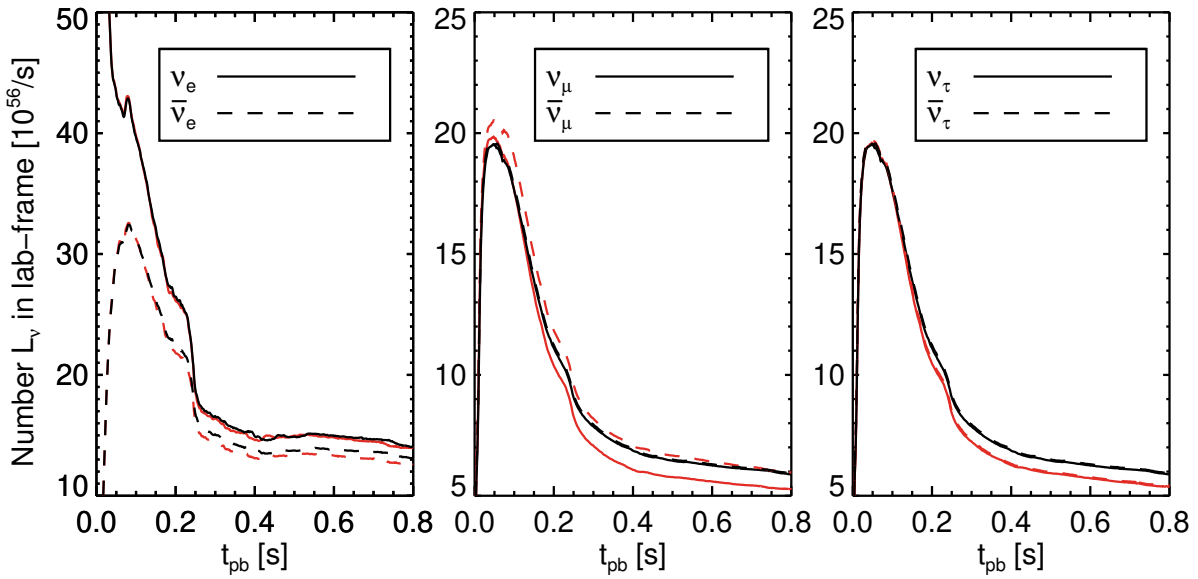

Figure 11.25: On the left, the evolution of the lab-frame number luminosity of ν_e and $\overline{\nu}_e$ for cases s20.0-SFHo-standard in black and s20.0-SFHo-muons in red, in the middle of ν_μ and $\overline{\nu}_\mu$ and on the right the same for ν_τ and $\overline{\nu}_\tau$. Note that in the standard case $\nu_\mu = \nu_\tau$ as well as $\overline{\nu}_\mu = \overline{\nu}_\tau$.

The lab frame mean energies of all considered neutrinos, calculated by

$$\langle E \rangle^{\text{lab}} = \frac{L_\nu^{\text{lab}}\,(r = 400\,\text{km})}{\mathcal{L}_\nu^{\text{lab}}\,(r = 400\,\text{km})}\,, \tag{11.25}$$

show considerable enhancement caused by the increased neutrinosphere temperature. Note that the difference of the ν_e and $\overline{\nu}_e$ mean energy between muonic and standard case is reduced, at only $\Delta E^{\text{lab}}_{\nu_e|\overline{\nu}_e} \approx 0.75\,\text{MeV}$, compared to the comoving quantities evaluated at the gain radius in Fig. 11.18. The reduction is caused by the stronger absorption of the high energy tail in the muonic case. A similar effect happens for the heavy-lepton neutrinos, where mostly neutrino-nucleon, as well as neutrino-electron scattering lead to a small energy loss. The mean energy of ν_μ is increased by $\Delta E^{\text{lab}}_{\nu_\mu} \approx 0.6\,\text{MeV}$, that of $\overline{\nu}_\mu$ by $\Delta E^{\text{lab}}_{\overline{\nu}_\mu} \approx 0.4\,\text{MeV}$. Note that the μ neutrinos show a tiny bit higher mean energy than the τ neutrinos, even though they decouple at least at the same temperature. The exact reason for this, however, cannot be easily determined and might be an artifact caused by the still slightly tighter bound high energy bins of ν_μ and remaining weak magnetism differential transport effects.

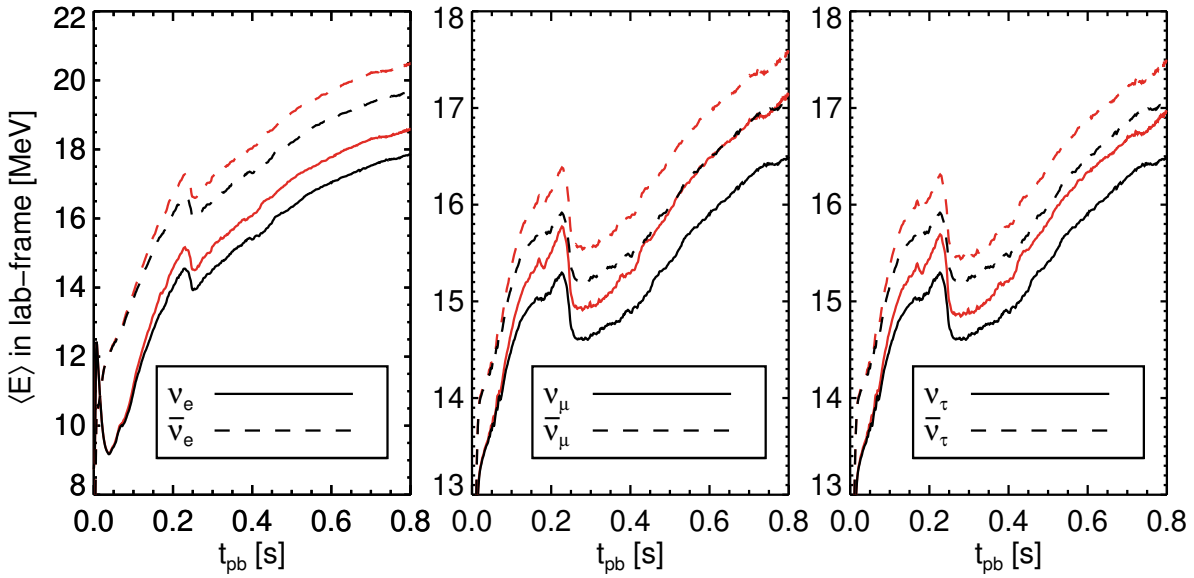

Figure 11.26: On the left, the evolution of the lab-frame mean energy of ν_e and $\overline{\nu}_e$for cases s20.0-SFHo-standard in black and s20.0-SFHo-muons in red, in the middle of ν_μ and $\overline{\nu}_\mu$ and on the right the same for ν_τ and $\overline{\nu}_\tau$. Note that in the standard case $\nu_\mu = \nu_\tau$ as well as $\overline{\nu}_\mu = \overline{\nu}_\tau$.

The mean energy alone is however not sufficient to characterize the spectral shape of the emitted neutrino signal, as the high-energy tail might be significantly nonthermal. One possible method to parameterize the shape of the spectrum is to use the so-called alpha-fit (see Ref. [113]). The alpha parameter here characterizes the width of the spectrum around the mean energy, and is defined by the ratio between the first and second energy moment of the neutrino spectrum

$$\frac{\langle E^2 \rangle}{\langle E \rangle^2} = \frac{2+\alpha}{1+\alpha}\,, \tag{11.26}$$

where the definition of an arbitrary energy moment is

$$\langle E^n \rangle = \frac{\int \mathrm{d}E\, E^{n+2} f_{\text{FD}}\,(E,\eta,T)}{\int \mathrm{d}E\, E^2 f_{\text{FD}}\,(E,\eta,T)}\,. \tag{11.27}$$

The Fermi-Dirac number spectrum

$$f^{\text{N}}_{\text{FD}}\,(E,\eta) = \frac{E^2}{\exp\,(E/T-\eta)+1} \tag{11.28}$$

can then be approximated via

$$f_{\mathrm{FD}}^{\mathrm{N}} \approx f_{\alpha}\left(E, \langle E \rangle, \alpha\right) = \left(\frac{E}{\langle E \rangle}\right)^{\alpha} \exp\left[-\left(-\alpha+1\right)\left(E/\langle E \rangle\right)\right] . \tag{11.29}$$

The alpha-fit can represent a broader range of spectral pinching than an "effective degeneracy" fit can. A Fermi-Dirac spectrum that is purely thermal, i.e., $(\eta = 0)$, then corresponds to $\alpha \approx 2.3$, a Maxwell-Boltzmann spectrum, i.e., $(\eta = -\infty)$, to $\alpha = 2$. The direction of spectral pinching is then given by whether α is larger or smaller than 2.3. $\alpha < 2.3$ yields anti-pinched spectra, which indicates spectra that have a longer high-energy tail than thermal spectra, while $\alpha > 2.3$ yields pinched spectra, which mean spectra that have a shortened high-energy tail when compared to thermal spectra. In Fig. 11.27 the alpha parameter remains nearly unchanged for ν_{e}, which starts out strongly pinched due to absorption on nuclei and nucleons but quickly becomes close to thermal after the accretion of the Si-O interface at $t_{\mathrm{pb}} \approx 0.25\,\mathrm{s}$. Meanwhile, the $\overline{\nu}_{\mathrm{e}}$ also start pinched and remain pinched through most of the simulation time, but with the muonic case coming closest to a purely thermal spectrum. The heavy-lepton neutrinos in both cases start out somewhat pinched but rapidly approach thermal and even strongly anti-pinched spectra, with the muonic case showing a considerably extended high-energy tail for both μ and τ neutrinos. Both ν_{μ} and ν_{τ} are very similar to each other, as the muonic processes have frozen out long before the spectrum stops being formed. In this case, energy redistribution via inelastic scattering events are responsible and lead to identical spectral shapes.

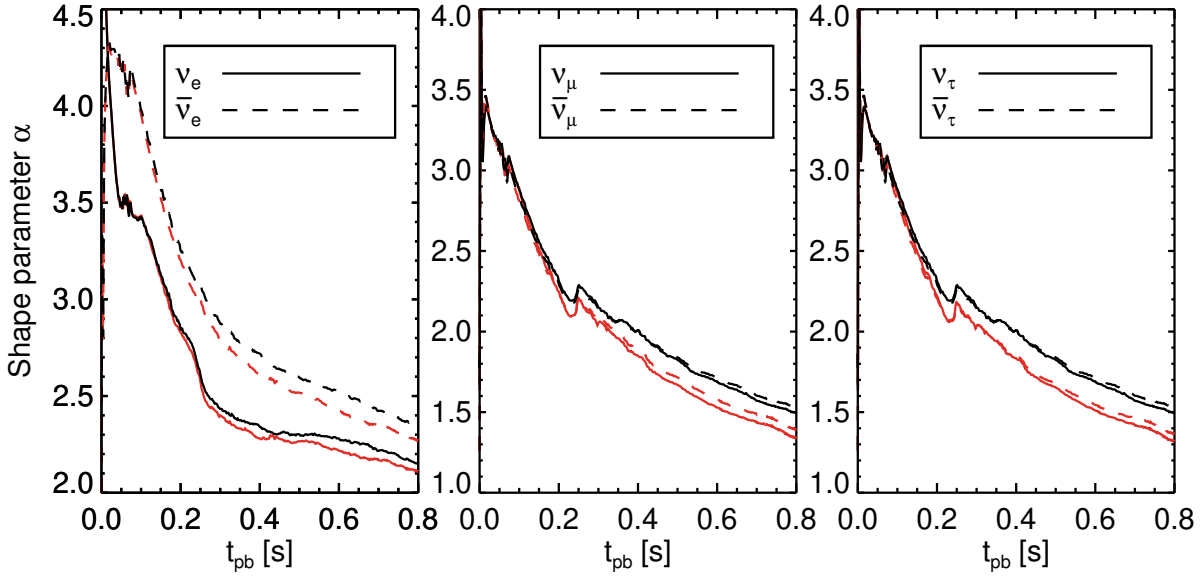

Figure 11.27: On the left, the evolution of the shape parameter α, defined by Eq. 11.26 of ν_{e} and $\overline{\nu}_{\mathrm{e}}$ for cases s20.0-SFHo-standard in black and s20.0-SFHo-muons in red, in the middle of ν_{μ} and $\overline{\nu}_{\mu}$ and on the right the same for ν_{τ} and $\overline{\nu}_{\tau}$. Note that in the standard case $\nu_{\mu} = \nu_{\tau}$ as well as $\overline{\nu}_{\mu} = \overline{\nu}_{\tau}$.

The time-integrated total emitted energy in the form of neutrinos is shown in Fig. 11.28. There we can see that ν_e and $\overline{\nu}_\mu$ show the largest enhancement in emitted energy, whereas ν_μ and τ neutrinos show reduced luminosity compared to the standard case. As the increased energy emitted in the $\overline{\nu}_\mu$ channel is compensated by the reduced ν_μ, ν_τ and $\overline{\nu}_\tau$ luminosity, the largest net difference is in the form of ν_e. The total integrated energy emitted in the form of neutrinos is nearly identical to the standard case, showing that most of the increased PNS contraction is not caused by a more efficient neutrino energy loss, but rather by equation of state effects by muons. Note that the decreased surface area of the PNS, compared to the standard case, should again lead to a nominally decreased angle-integrated luminosity, and the actual flux densities are larger at the PNS surface.

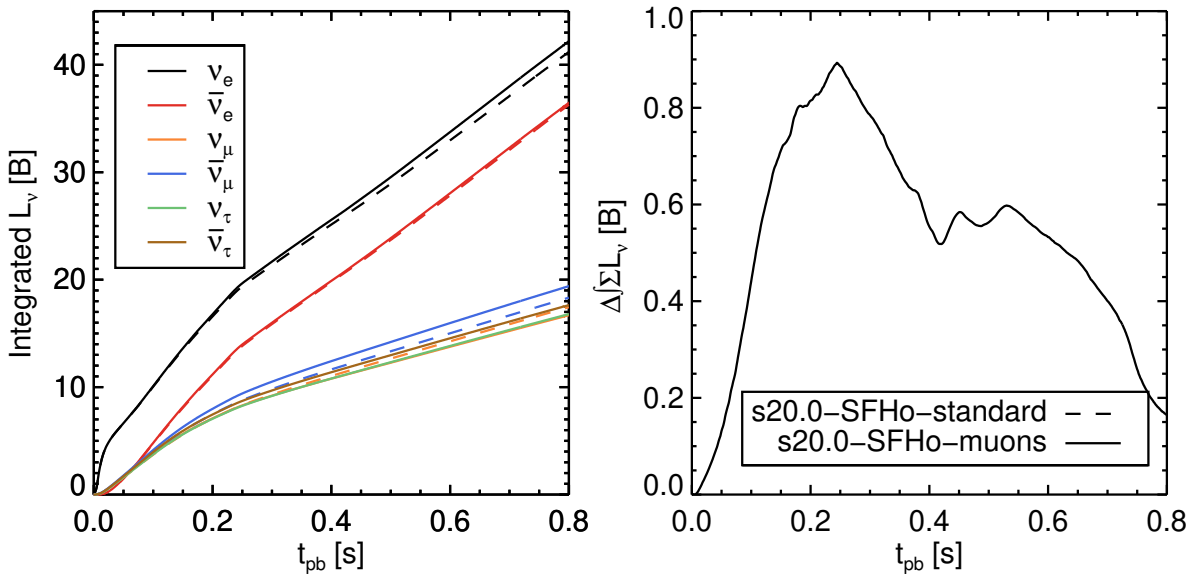

Figure 11.28: On the left, the cumulative time-integrated energy emitted by each neutrino species for s20.0-SFHo-muons in solid lines and s20.0-SFHo-standard in dashed lines. The individual neutrinos are identifiable by the colors in the plot legend. Note that for the standard case, ν_μ and ν_τ and corresponding antineutrinos are identical. On the right, the difference of the total emitted neutrino energy calculated by $\Delta \sum_\nu L_\nu = \sum_\nu L_\nu^{\text{muons}} - \sum_\nu L_\nu^{\text{standard}}$.

Muon number The muon quantity contained in the core is a time-dependent evolved quantity that depends on neutrino transport to conserve the lepton flavor number in the core. Any net muon flavor number in the PNS must be equaled by a corresponding $\overline{\nu}_\mu$ number flux escaping from the PNS, as long as one neglects neutrino oscillations. A similar mechanism has already been analyzed in Ref. [51], who however only evaluated net μ and net τ number generation inside a PNS due to the weak magnetism correction of opposite sign for ν and $\bar{\nu}$ without including muons.

In Fig. 11.29 we plot the net muon flavor number inside the PNS, given by

$$\mathcal{N}_\mu^{\mathrm{PNS}} = 4\pi \int_0^{r_{\mathrm{PNS}}} \mathrm{d}r\, r^2 \left\{ \rho\left(r\right)/m_{\mathrm{B}} Y_\mu\left(r\right) + \mathcal{N}_{\nu_\mu}\left(r\right) - \mathcal{N}_{\overline{\nu}_\mu}\left(r\right) \right\}, \tag{11.30}$$

where $\mathcal{N}_{\nu_\mu}$ and $\mathcal{N}_{\overline{\nu}_\mu}$ are the local ν_μ and $\overline{\nu}_\mu$ number density in [1/cm^3], defined by $\mathcal{N}_\nu = \frac{4\pi}{c}\int_0^\infty \mathrm{d}E\, \mathcal{J}_\nu\left(E\right)$. The net muon flavor number reaches about $\mathcal{N}_\mu^{\mathrm{PNS}} \approx 8 \times 10^{55}$ that is being compensated for by a net $\overline{\nu}_\mu$ flux calculated by

$$\mathcal{L}_{\overline{\nu}_\mu}^{\mathrm{net,sum}}\left(r = 500\,\mathrm{km}\right) = 4\pi r^2 \int_0^t \mathrm{d}t \left\{ \mathcal{L}_{\overline{\nu}_\mu} - \mathcal{L}_{\nu_\mu} \right\}. \tag{11.31}$$

Even though our purely leptonic muonic reactions are only implemented in an approximate manner, the lepton flavor number is conserved very well. This is a consequence of the self-quenching of the muonic reactions, as muon producing reactions freeze out before the neutrinos leave local thermodynamic equilibrium. In the case of muon decay, the neutrino coupling only appears as a Pauli blocking term of the partner neutrino that can be neglected when the nondegenerate neutrinos leave local equilibrium. For comparison, we additionally plot the pure net μ neutrino number inside the PNS for both the standard case as well as the muonic case. As there is a surplus of $\overline{\nu}_\mu$ in the muonic case due to the large negative ν_μ chemical potential, we plot the net $\overline{\nu}_\mu$ number instead. Even though the standard case does not include muonic interactions, the PNS still builds up a macroscopic net ν_μ number following the calculations of Ref. [51] due to the weak magnetism correction. The effect of weak magnetism alone, however, is one magnitude smaller than the case including charged muons.

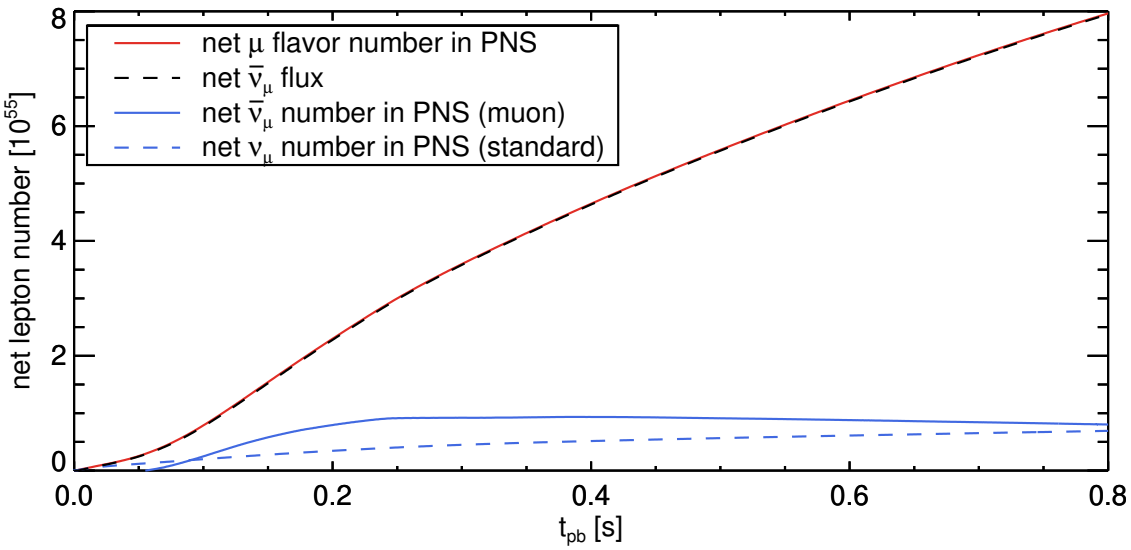

Figure 11.29: A Plot of the volume integrated net muon flavor number contained in the PNS in red defined by $\mathcal{N}_\mu = 4\pi \int_0^{r_{\rm PNS}} {\rm d}r\, r^2 \left\{\rho/m_{\rm B} Y_\mu + \mathcal{N}_{\nu_\mu} - \mathcal{N}_{\bar{\nu}_\mu}\right\}$, where $\mathcal{N}_\nu$ are the local neutrino number densities. To verify the lepton flavor number conservation, the cumulative time-integrated net $\bar{\nu}_\mu$ number flux $= 4\pi r^2 \int_0^t {\rm d}t \left\{\mathcal{L}_{\bar{\nu}_\mu} - \mathcal{L}_{\nu_\mu}\right\}$ is the black dashed line. The net ν_μ number contained in the PNS of the standard case is the blue dashed line.

Neutrinospheres The location of the energy weighted neutrinospheres is computed by combining Eq. 11.2 with Eq. 11.6, according to

$$\tau_{\rm eff}^{\rm weighted} = 2/3 = \int_{r_\tau}^{\infty} {\rm d}r' \sqrt{\frac{1}{\lambda_i^{\rm weighted}\left(r'\right)} \left[\frac{1}{\lambda_{\rm T}^{\rm weighted}\left(r'\right)} + \frac{1}{\lambda_i^{\rm weighted}\left(r'\right)}\right]}, \tag{11.32}$$

where $\lambda_i^{\rm weighted}$ are the summed and weighted opacities of the energy and number sphere, and $\lambda_{\rm T}^{\rm weighted}$ is the transport opacity given by the processes $\nu + {\rm N} \leftrightharpoons \nu' + {\rm N}'$ and $\nu + {\rm A} \leftrightharpoons \nu + {\rm A}$.

The **number sphere** contains the processes

- $\nu_{\rm e} + {\rm n} \leftrightharpoons {\rm e}^- + {\rm p}$
- $\bar{\nu}_{\rm e} + {\rm p} \leftrightharpoons {\rm e}^+ + {\rm n}$
- $\nu + {\rm A_Z} \leftrightharpoons {\rm e}^\mp + {\rm A}_{Z^{\pm 1}}$
- $\bar{\nu}_{\rm e} + {\rm e}^- \leftrightharpoons \bar{\nu}_\mu + \mu^-$
- $\nu_\mu + {\rm e}^- \leftrightharpoons \nu_{\rm e} + \mu^-$
- $\bar{\nu}_{\rm e} + {\rm e}^- + \nu_\mu \leftrightharpoons \mu^-$
- ${\rm e}^- + {\rm e}^+ \leftrightharpoons \nu + \bar{\nu}$
- $\nu_{\rm e} + \bar{\nu}_{\rm e} \leftrightharpoons \nu_{\mu,\tau} + \nu_{\mu,\tau}$
- ${\rm N}' + {\rm N}' \leftrightharpoons {\rm N} + {\rm N} + \nu + \bar{\nu}$

The **energy sphere** contains the processes

- $\nu + e^{\mp} \leftrightharpoons \nu' + e^{\mp\prime}$
- $\nu + \mu^{\mp} \leftrightharpoons \nu' + \mu^{\mp\prime}$
- $\nu_{\mu,\tau} + \nu_e \leftrightharpoons \nu'_{\mu,\tau} + \nu_e{}'$

The **transport sphere** contains the processes

- ν +N$\leftrightharpoons\nu'$+N$'$
- ν +A$\leftrightharpoons\nu$ +A

For the sake of brevity, we omit here some corresponding antiparticle processes but still include them in the calculation. The primed particles indicate an inelastic process which transferred energy. The resulting neutrinospheres are shown in Fig. 11.30, where we skip the standard case as the τ neutrinos can act as a proxy for unmodified heavy-lepton neutrinos. The ν_e number sphere by absorption on nucleons remains the last sphere of interaction and extends past the nominal PNS surface. The $\overline{\nu}_e$ number sphere lies at somewhat higher densities of up to $\rho \sim 3 \times 10^{11}$ g/cm^3. As muonic processes have long frozen out at these densities, we cannot expect a significant change for the PNS accretion phase. The ν_μ number sphere by the muonic processes is now active up to $\rho \sim 10^{13}$ g/cm^3, while the $\overline{\nu}_\mu$ show a weaker enhancement to $\rho \sim 2 \times 10^{13}$ g/cm^3 compared to $\rho \sim 3 \times 10^{13}$ g/cm^3 in the $\overline{\nu}_\tau$ case. The energy and transport sphere for heavy-lepton neutrinos stay unchanged, as no additional process except neutrino-muon scattering has been added. The muonic scattering process is however too weak at the energy sphere to influence the decoupling.

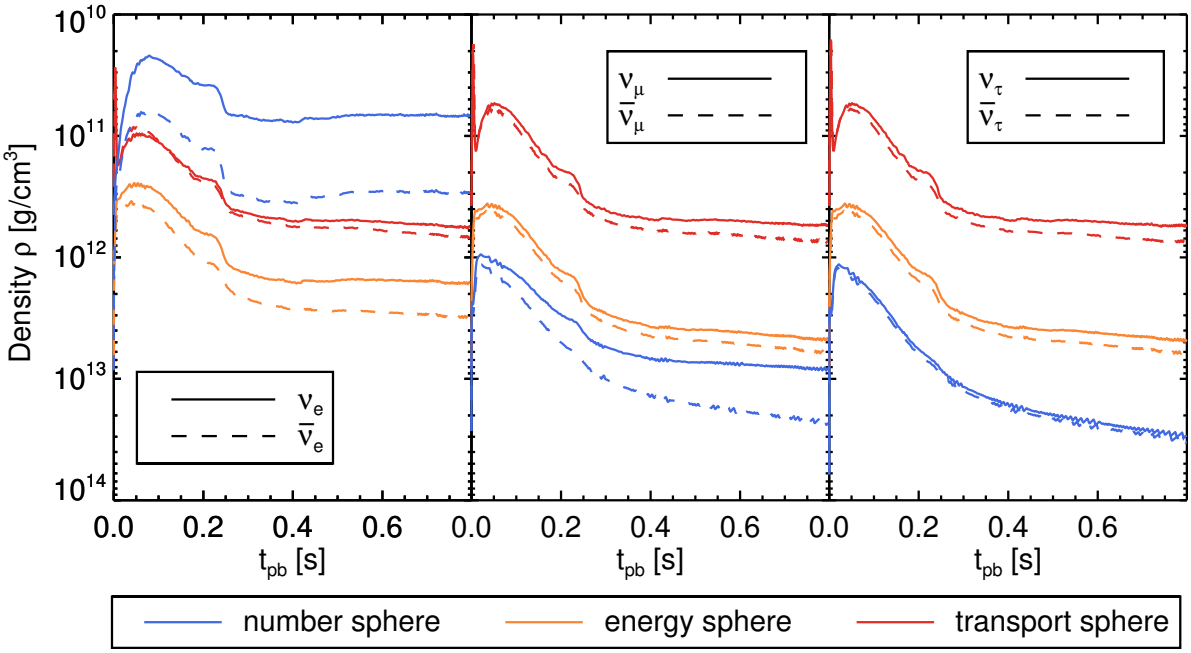

Figure 11.30: On the left, the evolution of the separate neutrinosphere locations of ν_e and $\overline{\nu}_e$ for case s20.0-SFHo-muons, in the middle of ν_μ and $\overline{\nu}_\mu$, and on the right of ν_τ and $\overline{\nu}_\tau$. The number sphere is plotted in blue; the energy sphere in orange; the transport sphere in red. The definition of the transport spheres is given in Par. 11.1.1.

11.1.3 Summary

The results presented in this section are from the first ever self-consistent calculation of muon formation and coupling to neutrino transport using a full set of opacities and an up-to-date neutrino transport method. The effects of muonization on the hydrodynamic evolution of the protoneutron star and the neutrino signal have been examined during the stalled shock phase for several hundred milliseconds. The results show that muon production is sufficiently efficient for μ neutrinos and muons to achieve beta-equilibrium immediately after being switched on at the beginning of the postbounce phase. The further evolution of the net muon number however strongly depends on the individual transport of ν_μ and $\overline{\nu}_\mu$. As the PNS initially starts with zero net muon number, the protoneutron star must compensate for any additional net muon number by a corresponding emission of net $\overline{\nu}_\mu$ number. Analysis of the neutrino signal shows that this net $\overline{\nu}_\mu$ flux happens not via a reduced number flux of ν_μ, but rather by increased diffusion of the degenerate $\overline{\nu}_\mu$ from the muon production sites. While any surplus of ν_μ is probably being absorbed as soon as it is produced via thermal pair production, the emitted number flux of ν_μ develops at densities where muonic processes have already frozen out. The lack of a diffusion component, therefore, has little effect on the neutrino signal. This is not the case for the $\overline{\nu}_\mu$, who have a large negative potential and are present in weakly degenerate conditions inside the PNS core. The number flux of $\overline{\nu}_\mu$ is therefore preferentially directed out of the PNS and already forms at higher densities, so that the diffusion component can overpower the cooling component from the outer edges of the mantle. Nonetheless, the production of ν_μ and the loss of $\overline{\nu}_\mu$ happens too slowly to keep up with the demands of muon production, and beta-equilibrium is not reached during the accretion phase. Muons become abundant inside the PNS after a postbounce time of 100 ms, but fail to efficiently grow further in the dense core. Muonization seems to happen slower in the dense core than a naive interpretation of efficient heavy-lepton neutrino loss might lead one to believe, with mainly the inner 10 km of the PNS moving ever farther away from equilibrium as the PNS contracts. The neutron-proton potential difference increases faster than muon production can keep up.

The muon number, even if not at the theoretical maximum, still has a measurable effect on the PNS dynamics. The accelerated contraction of the PNS by conversion of degenerate electrons into nondegenerate muons, as well as the increased proton fraction's impact on the asymmetry parameter of the baryonic EOS, leads to a reduction of the PNS radius of up to 2 km and can maintain this offset for most of the accretion phase. This reduction is caused by a faster contraction of the hot mantle rather than the inner core. When the mantle contracts it increases in temperature, while it sinks deeper into the gravitational well. The temperature is further raised by the conversion of kinetic energy, of the matter striking the surface, into internal energy. The increase of the temperature by up to $0.4\,\mathrm{MeV}$ at the energy spheres and neutrinospheres of the respective neutrinos, leads to an increased neutrino luminosity of $\Delta L \sim 2.5\,\mathrm{B/s}$ and increased mean energy of the emitted neutrinos by $\Delta\langle E\rangle \sim 1\,\mathrm{MeV}$. The increase is partially counteracted by the reduced emission surface of the shrunken PNS and gain layer region, to have only a small effect on the heating conditions inside the gain layer.

In a simple spherically symmetric simulation, where there can exist no neutrino-driven convection or hydrodynamic instabilities, the effect of muonization is compensated by the system rearranging itself to reach a new steady-state configuration and Mazurek's[①] law is still in full force. As shown in Sec. 12, genuinely multi-dimensional effects can however still break this stalemate and even lead to successful explosions.

The common belief in the core-collapse supernova community that muons can safely be neglected at conditions present in protoneutron stars has been thoroughly refuted. While the

[①] A colloquial law which states that in the CCSN context any small variation of a single aspect is immediately compensated for by strong feedback effects of the coupled system of EOS, hydrodynamics, weak interactions and neutrino transport.

addition of muons indeed is not **the** solution to the supernova problem, the irrefutable presence of muons, already widely accepted in cold neutron stars, the unambiguous classical physics framework, and the measurable dynamical effect of muons, make the common assumption that muons can safely be neglected hard to defend. The approach to the supernova problem has evolved to a point where small changes in microphysics can make or break a successful explosion. A systematic "offset" of the problem by neglecting well-known classical physics can no longer be afforded.

11.2 Kelvin-Helmholtz phase cooling simulations

A fraction of CCSN can achieve revitalization of the stalled shock and reach shock runaway. The expanding shock then drags the surrounding matter with it, quenching the mass accretion onto the protoneutron star. The still hot and radiating protoneutron star remains in the center of the expanding void. The neutrinos diffusing out of the PNS are, however, still able to deposit sufficient energy into the PNS mantle to gravitationally unbind its topmost layers. This ablated material from the PNS forms the neutrino-driven wind, which fills the void left by the propagating shock. Only a small fraction of neutrinos is reabsorbed, however, and nearly all of the energy is lost in the form of neutrino radiation. This marks the beginning of the Kelvin-Helmholtz phase that can last up to several tens of seconds and can be separated into two different epochs.

1. The *deleptonization stage*, in which the trapped electron neutrinos in the dense inner 10 km of the PNS slowly diffuse outward and heat up the PNS core via Joule-heating (cf. Ref. [16]). By emitting these excess electron neutrinos, the PNS decreases electron and proton number and eventually reaches beta-equilibrium. At this point the deleptonization is complete, and the subsequent evolution of the PNS is thermally dominated.

2. The *cooling stage*, in which the now uniformly hot protoneutron star cools and decreases its entropy by emitting neutrinos over its entire volume. Eventually, the PNS becomes cool enough that the thermal mean energies of the neutrinos are so low that neutrino transparency sets in. At this point, neutrino cooling has become inefficient on the relatively short timescale of minutes, and the neutron star will slowly lose energy over the timescale of years and up to millions of years via modified URCA processes, as shown in Ref. [4] for the case including muons.

While we cannot track the evolution of the protoneutron star down to very cold conditions, the quasi-cool conditions of the 3 MeV neutron star we can reach in our simulations already well approximate the final neutron star structure. As we do not adequately treat the formation of pasta phases in the crust anyway (cf. Ref. [48]), we accept this as the end of our simulations.

Recent multi-dimensional simulations of the Kelvin-Helmholtz phase show that there might persist some accretion downflows localized in thin accretion funnels as demonstrated in Ref. [90]. They were able to simulate a low-mass spherically averaged (1D) protoneutron star surrounded by an axisymmetric (2D) or fully 3D environment for up to tens of seconds. These accretion funnels can even temporarily cease all outflow from the protoneutron star surface, but are fortunately found to be a mostly artificial 2D artifact caused by a suppression of shear instabilities (cf. Ref. [90]). Nonetheless, the presence of these persistent downflows over several seconds even in 3D, limit the accuracy of 1D spherical symmetric calculations that by their nature alone can only model uniform in- or outflow.

11.2.1 Numerical setup

In the following, we will compare Kelvin-Helmholtz phase PNS cooling simulations using an identical setup and same progenitor as in Sec. 11.1. The need to accurately track the PNS cooling down to neutrino transparency, as well as to track the expanding shock, however, requires some changes to the numerical setup. The neutrino energy binning has been refined from 15 geometrically spaced bins to 5 linear and 17 geometrically spaced bins. These five linear bins are specifically chosen to better resolve low neutrino energies, as they may carry a large part of the spectrum after the PNS cools down sufficiently. Additionally, the upper extent of the radial grid has been extended from $10000\,\mathrm{km}$ to 6×10^7 km, which now contains most of the pre-collapse stellar structure.

Another change is that for this kind of simulation the mixing-length treatment (MLT) of Ledoux convective instability as described in Ref. [88] is implemented, to take the more rapid deleptonization by convective transport into account. The importance of treating protoneutron star convection adequately is also demonstrated in Ref. [119], who use an approach similar to ours. Note however, that our implementation of the mixing length treatment is made considerably more complicated by the additional inclusion of muons and trapped neutrinos into the formulae for convective energy and lepton number transport, as well as in the Ledoux criterion evaluation. Our treatment in the muonic case still somewhat underestimates convective flux compared to 2D simulations of the same progenitor examined in Sec. 12, and detailed radial profiles and evolved quantities need to be taken with a grain of salt. The long-time muonic cooling simulations, therefore, give only a qualitative assessment of convective effects on the Kelvin-Helmholtz cooling timescale, and will need to be further developed and calibrated against long-time 2D or 3D self-consistent hydrodynamic simulations. The computational expense of even standard physics in PNS cooling simulations, however, precludes this at the moment. The mixing-length treatment in the standard case has, however, been found to be in excellent agreement with multidimensional cooling simulations, as demonstrated in Ref. [88].

As spherical symmetric simulations do not in general lead to neutrino-driven explosions, we need to artificially initiate one. This can be achieved by various methods. Reference [119] for example assigns a mass-cut in their Lagrangian code, after which they remove the pre-collapse stellar structure, therefore, simulating the cessation of accretion in the case of a perfectly symmetric instantaneous shock expansion. This cut is chosen in Ref. [119] to be at $1.42 M_\odot$. This value reproduces a typical neutron star mass determined by observations, but neither takes the specific accretion profile into account nor does it allow for variations in the final baryonic NS mass. Reference [106] applies another method by artificially enhancing heating in the gain layer by heavy-lepton neutrinos. We follow a method similar to Ref. [119] by artificially "ripping" away the mass shells after a set amount of postbounce time. This is however not done instantaneously, but instead simulates a gradual quenching of the accretion flow via a linearly growing suppression factor for the pre-shock density. This approach might not be a very physically motivated method to launch an explosion, and the dynamics are certainly not correct, but it reasonably approximates the neutrino signal of a successful supernova in a phenomenological way. The postbounce time at which we artificially launch the explosion is typically chosen to be $t_{\mathrm{pb}} = 500\,\mathrm{ms}$, but a more accurate way might be to launch an explosion at either the accretion time of the Si-O interface or by reusing the explosion times of parameterized calibrated simulations of Ref. [28]. In our case, the standard time of 500 ms fits well with the results of the 2D simulations in Sec. 12, and no further fine-tuning of the explosion time is necessary.

Figure 11.31: Plot of the density before (black) and after (red) scaling to initiate the explosion. The dashed lines mark the start and the end of the scaling region, in which the density is linearly reduced by up to a factor of 30.

11.2.2 Time evolution

As our mixing-length treatment for the muonic case is not yet fully calibrated to reproduce multi-dimensional hydrodynamic calculations, we avoid over-analyzing the early phase when protoneutron star convection strongly influences the radial profile evolution of the PNS, and instead focus on later times when convection is a slower less dynamic process. For the first $500\,\mathrm{ms}$ we refer to the 2D section, where the early evolution is demonstrated in more detail. The evolution of the PNS radius in the muonic case in Fig. 11.32 converges quite rapidly towards the standard case after two seconds, as the previously expanded hot mantle shrinks and becomes more and more dominated by the baryonic pressure component. After this point, the temperature maximum has reached the center of the PNS in the standard case, and the PNS begins to cool over the entirety of its volume. This point in time is plotted in Fig. 11.33, when the temperature in the center has reached its maximum value of $T_{\mathrm{standard}} \approx 65\,\mathrm{MeV}$. At this time, the muonic case shows a slowed "deleptonization wave" (cf. Ref. [119]), caused by a steeper lepton fraction gradient in the Ledoux criterion of convective instability

$$C_{\mathrm{ledoux}} = \left(\frac{\partial \rho}{\partial s}\right)_{P,Y_\ell} \frac{\mathrm{d}s}{\mathrm{d}r} + \left(\frac{\partial \rho}{\partial Y_\ell}\right)_{P,s} \frac{\mathrm{d}Y_\ell}{\mathrm{d}r} > 0\,.$$

The decreased diffusion velocity of the $\overline{\nu}_{\mathrm{e}}$ into the core due to the new muonic purely-leptonic opacities, as well as the appearance of muons itself, increases the deleptonization timescale. The steep gradient of Y_{e} and $Y_{\nu_{\mathrm{e}}}$ at the inner boundary of the convective zone cannot be softened as fast as in the standard case by additional $\overline{\nu}_{\mathrm{e}}$ diffusion into this boundary region, and in addition, any decrease in Y_{e} is immediately countered by an increase in Y_μ. This feedback delays the deleptonization by about one second compared to the standard case. Note however, that the size of this effect might change if our MLT implementation were correctly calibrated for the muonic case. As the deleptonization wave moves inwards, the trapped lepton fraction is released and the PNS quickly reaches weak equilibrium in respect to electron neutrinos at the local temperature, i.e., $\mu_{\nu_{\mathrm{e}}} \approx 0$. It transiently even overshoots weak equilibrium slightly to reach a marginally negative ν_{e} chemical potential. Note however, that reaching weak equilibrium does not mean that the PNS has reached its minimum lepton fraction, since a hot PNS has a larger equilibrium Y_{p} than a cold neutron star. Additionally, the PNS does not reach weak equilibrium

in respect to electron neutrinos and μ neutrinos at the same time, as the equilibration timescale of μ neutrinos is considerably longer. The μ neutrinos only reach weak equilibrium when the PNS has practically reached its quasi-cold configuration and efficient neutrino cooling has ceased. The μ neutrinos remain at a substantial negative chemical potential of about half its previous value, $\mu_{\nu_\mu}^{\text{delep}} \approx -40\,\text{MeV}$, even after the deleptonization wave has passed. They are only in complete weak equilibrium, i.e., $\mu_{\nu_\mu} \approx 0$ and $\mu_\text{e} \approx \mu_\mu$, at the outer fringes of the PNS, where all neutrinos have already decoupled.

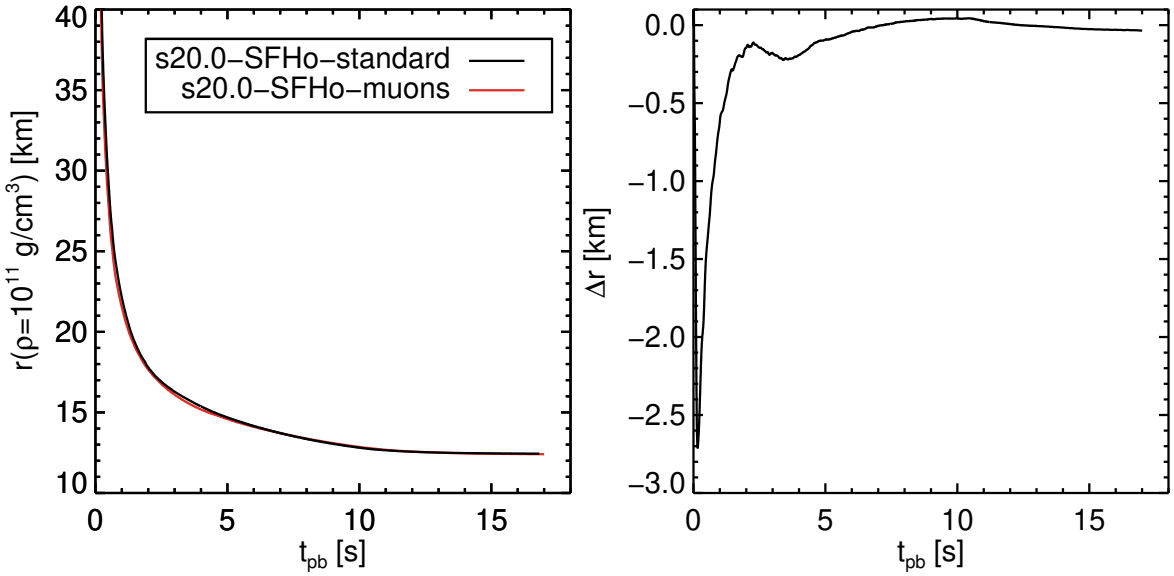

Figure 11.32: On the left, the radius evolution of the PNS defined as the radius where density is equal to $\rho = 10^{11}$ g/cm^3 for cases s20.0-SFHo-standard in black and s20.0-SFHo-muons in red; on the right, the absolute difference of both radii defined as $\Delta r = r_{\text{PNS}}^{\text{muons}} - r_{\text{PNS}}^{\text{standard}}$.

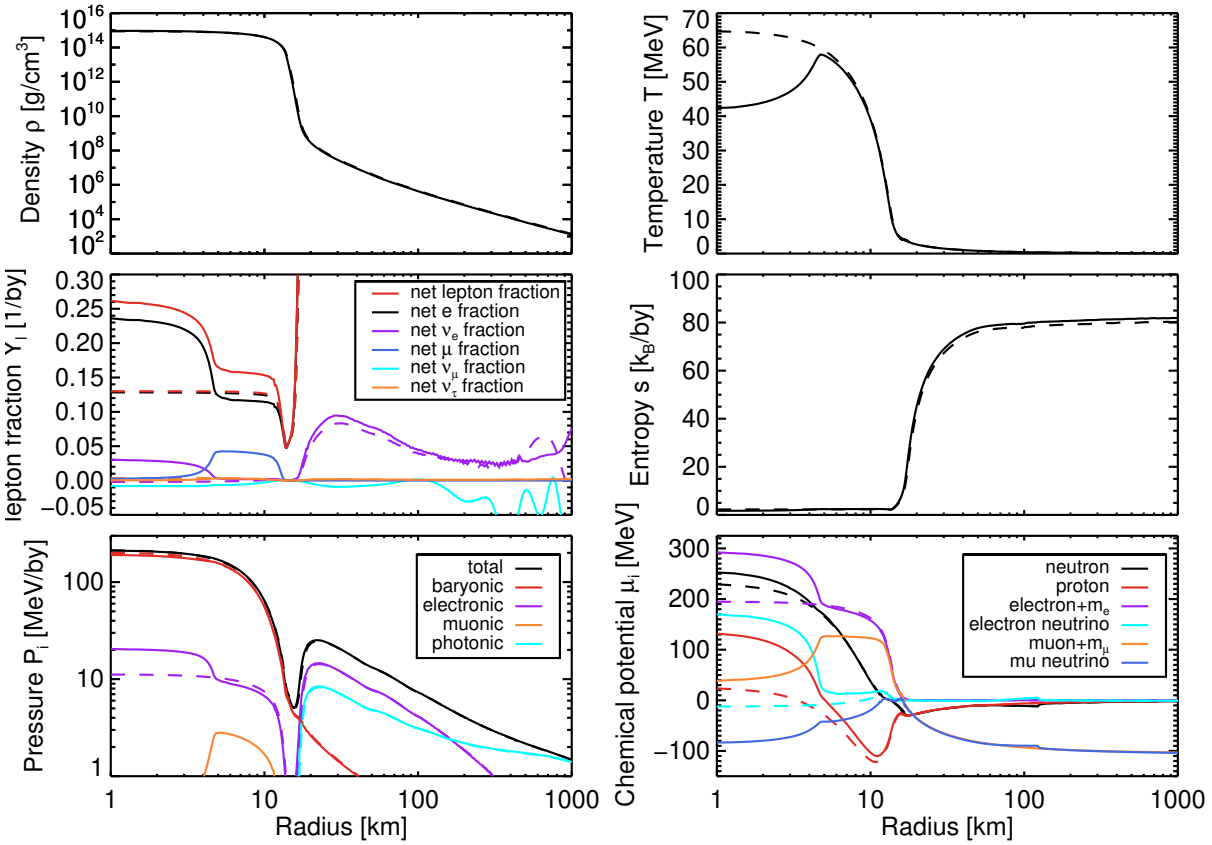

Figure 11.33: Profiles of case s20.0-SFHo-muons in solid lines and s20.0-SFHo-standard in dashed lines at $t_{\rm pb} = 3.2\,$s. Identical plot content as in Fig. 11.7.

At $t_{\rm pb} = 5\,$s, the muonic case has also entered the homogeneous cooling phase, and does not reach as hot a central temperature as the standard case in Fig. 11.34 as a result of decreased Joule heating (cf. Ref. [16]). Reasons for this are first, that an increased amount of thermal and degenerate energy is trapped in the abundant newly produced muons; second, the slower progression of the deleptonization wave gives the PNS more time to radiate energy and lepton number away in the form of neutrinos. As energy is being temporarily stored in the thermally produced muon pairs, as well as thermally excited net muons, this delayed form of energy needs to be radiated away when the PNS has cooled down further. The thermal muon pairs will recombine at lower temperatures, and muons decay to electrons. This reservoir fuels the neutrino luminosity at late times and supplies additional internal energy that slows down the cooling of the PNS. The total maximum energy stored in the muonic gas amounts to 27 bethe as shown in Fig. 11.35, and is maintained until the deleptonization wave has reached the center. It then decreases down to 13 bethe in the cold PNS, stored in the form of nearly pure muon rest mass. The difference needs to be emitted in the form of neutrinos, and the muons act as a kind of energy "battery". The concomitant additional gravitational relativistic "weight" of the muons can be compensated in the cold PNS by a small increase of the central density. At maximum, the 27 bethe correspond to $0.015 M_\odot$, and the final 13 bethe correspond to $0.007 M_\odot$, using the well known relativistic mass $E/c^2 = m$. The profiles in Fig. 11.36 show a uniform muon fraction of $Y_\mu^{\rm muons} \approx 0.035$ that, together with the uniform electron fraction of $Y_{\rm e}^{\rm muons} \approx 0.095$, leads to a proton fraction of $Y_{\rm p}^{\rm muons} \approx 0.13$. This is larger than $Y_{\rm p}^{\rm standard} \approx 0.105$ in the standard case, and decreases the asymmetry parameter β of Eq. 11.4. Note also that the electron chemical potential does not feature the same negative overshoot as in the standard case, because the electron chemical potential can also equilibrate using the additional ν_μ and $\overline{\nu}_\mu$ channels. The

muon chemical potential does not seem to benefit in the same way though, as the μ neutrino chemical potential remains negative throughout.

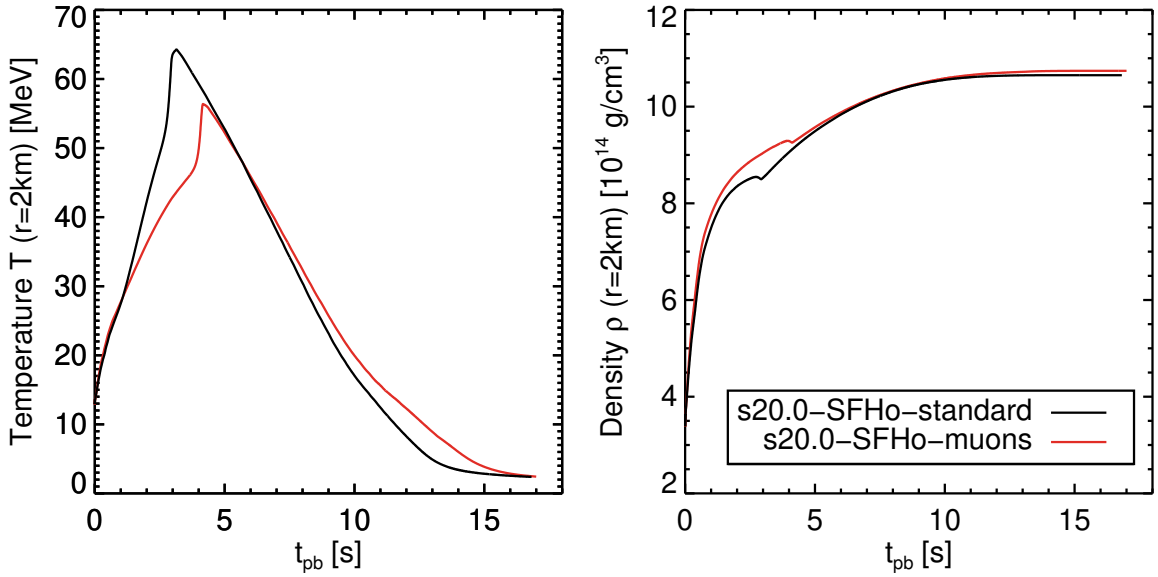

Figure 11.34: On the left, the evolution of the temperature at the PNS center evaluated at $r = 2$ km for cases s20.0-SFHo-standard in black and s20.0-SFHo-muons in red; on the right the evolution of the central density.

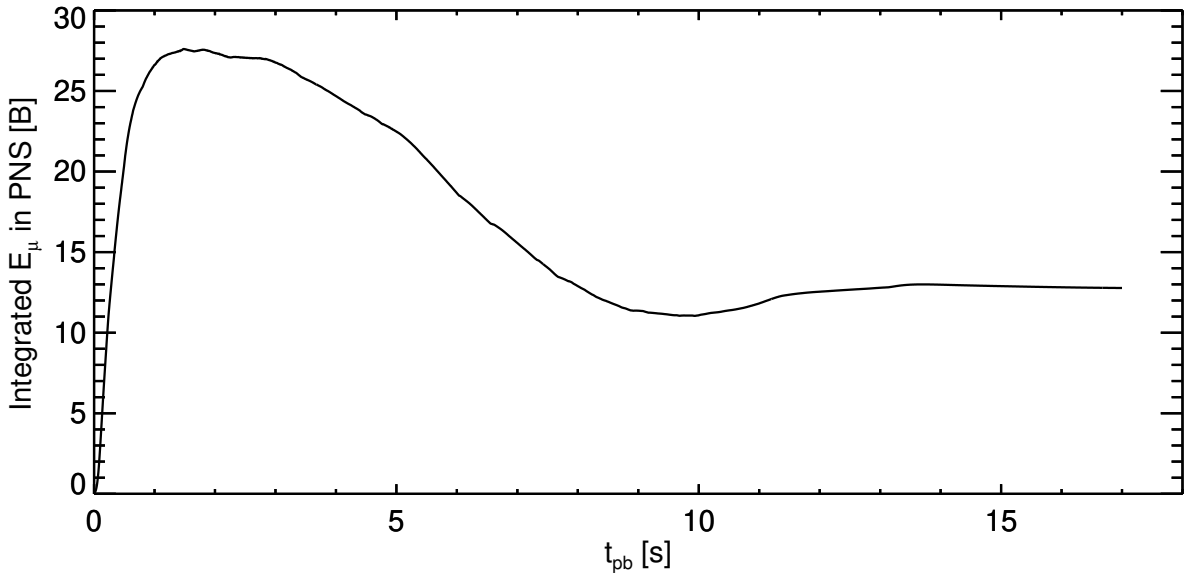

Figure 11.35: The total internal plus rest mass energy contained in the muonic gas inside the PNS given in bethe for model s20.0-SFHo-muons as a function of time.

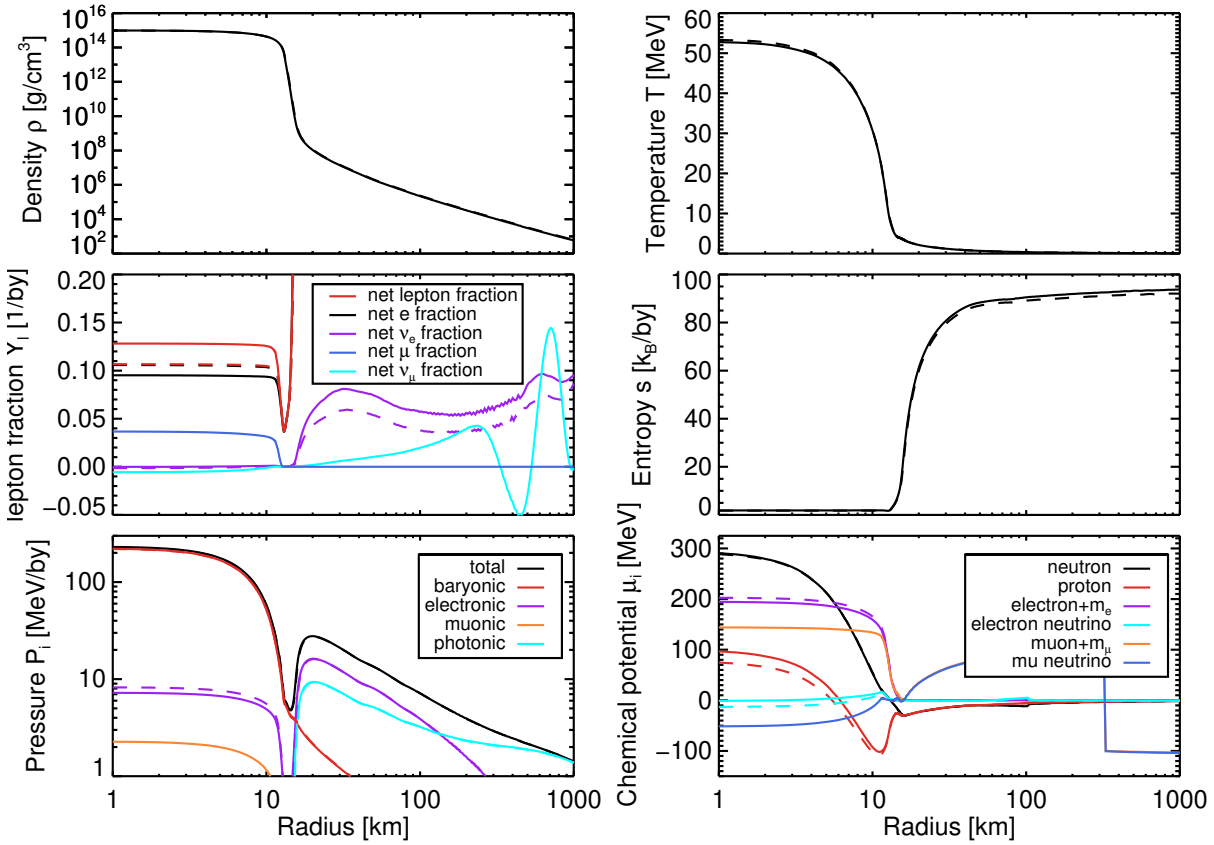

Figure 11.36: Profiles of case s20.0-SFHo-muons in solid lines and s20.0-SFHo-standard in dashed lines at $t_{\mathrm{pb}} = 5\,\mathrm{s}$. Identical plot content as in Fig. 11.7, except the net ν_τ fraction is not plotted.

At $t_{\mathrm{pb}} = 10\,\mathrm{s}$, the PNS has reached the point of neutrino transparency, as visible by the steep drop in neutrinosphere locations in Fig. 11.37. The number and energy sphere of all neutrinos begin to freeze out except ν_{e}, which notably stay active throughout most of the PNS during the entire cooling evolution. At this point, the energy loss via neutrinos slows down, as they cannot be produced in sufficient numbers anymore. The number sphere has retreated to the deepest layers of the PNS, indicated by the light gray dotted lines in the plot. Muonic opacities become relevant in this phase for $\overline{\nu}_{\mathrm{e}}$, as shown by the difference between the blue dashed and blue dot-dashed number sphere location. The dashed line includes muonic opacities by inverse muon decay and absorption on electrons, whereas the dot-dashed line only comprises standard opacities. Not directly visible here is also the effect muonic opacities have on $\overline{\nu}_{\mathrm{e}}$ diffusion inside the PNS, whose flux consists mostly of low energy neutrinos. Muonic opacities fill the low energy gap caused by the nucleon interaction potential energy penalty, and diffusion is slowed considerably. Especially ν_μ show the extensive modification by muonic opacities as expected, with the number sphere coming close to or even exceeding the energy sphere. This keeps ν_μ in good equilibrium nearly everywhere in the star for up to seven seconds, after which both energy and number sphere retreat at roughly the same pace. $\overline{\nu}_\mu$ only show a small modification, as their opacities are dependent on an abundant amount of either muons or antimuons to interact with.

The evolution of the different lepton and proton fractions at the PNS center, as well as the maximum (or minimum) value of either sign inside the PNS, are plotted in Fig. 11.38. The electron and muon fraction in the center are directly related, as the presence of highly degenerate ν_{e} prevents the efficient formation of muons by back-reactions. What is apparent is also the

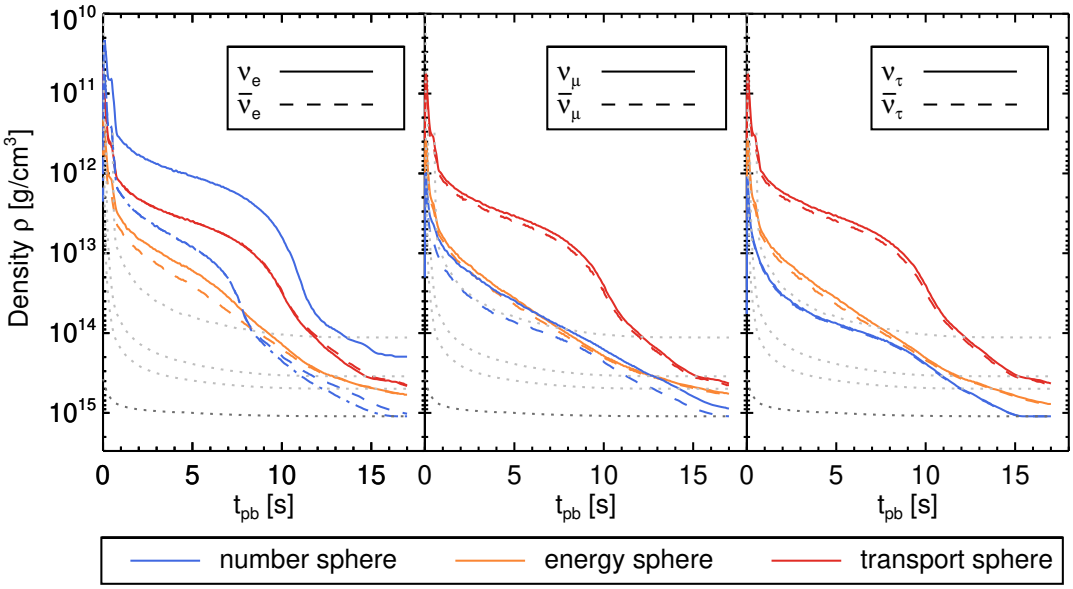

Figure 11.37: On the left, the evolution of the separate neutrinosphere locations for ν_e and $\overline{\nu}_e$ for case s20.0-SFHo-muons, in the middle of ν_μ and $\overline{\nu}_\mu$, and on the right the same for ν_τ and $\overline{\nu}_\tau$,with definitions as in Fig. 11.30. The light gray lines are from top to bottom, the densities where the enclosed mass exceeds 99%, 90% and 75% of the total PNS mass at that time. Additionally, the maximum PNS density is plotted in dark gray to show when an interaction sphere has completely frozen out.

increased proton fraction when muons are included, as well as the large net $\overline{\nu}_\mu$ fraction while μ_{ν_μ} is still negative and large in the PNS core. The muon fraction at the temperature peak sets the maximum number fraction and is moving to higher and higher densities as the deleptonization wave sweeps through the PNS. The maximum muon fraction eventually becomes identical to the central muon fraction once the distribution of muons in the PNS becomes homogeneous. The dip in the muon fraction around nine seconds is related to the system reaching weak equilibrium with respect to electron neutrinos but still being out of equilibrium with respect to μ neutrinos. After this point, the electron chemical potential is relatively fixed, and the muons increase in number until also weak equilibrium in respect to μ neutrinos is reached, and $\mu_e = \mu_\mu$ everywhere in the PNS. In the standard case without muons, the PNS slightly releptonizes after ten seconds by an increase in electron fraction, whereas in the muonic case the electron fraction sinks throughout and the muon fraction instead maintains beta equilibrium.

The evolution of the chemical potentials in Fig. 11.39 show this in more detail. The assumption that muon number is describable everywhere by a simple weak equilibrium chemical potential using $\hat{\mu} = \mu_n - \mu_p = \mu_\mu$ is only valid after 13 s. Note that this is only true for the dense PNS core, where there is still a significant trapped ν_e number. The weak equilibrium assumption is acceptable in the outer mantle region, where neutrinos are not trapped and the system can reach weak equilibrium easily. This means the simple equilibrium assumption could model the hydrodynamical evolution of the PNS mantle without explicitly needing to incorporate muons into the neutrino sector. This simplification would, however, have the caveat of breaking lepton flavor number conservation, shown in Sec. 11.3, and only being valid when the accretion and hydrodynamic evolution are relatively slow and the mantle is in good steady-state equilibrium with the neutrino transport.

Neutrino-driven wind The neutrino-driven wind is only weakly affected by the addition of muons, as the luminosity of ν_e and $\overline{\nu}_e$ is nearly unchanged during the cooling phase. The Y_e in

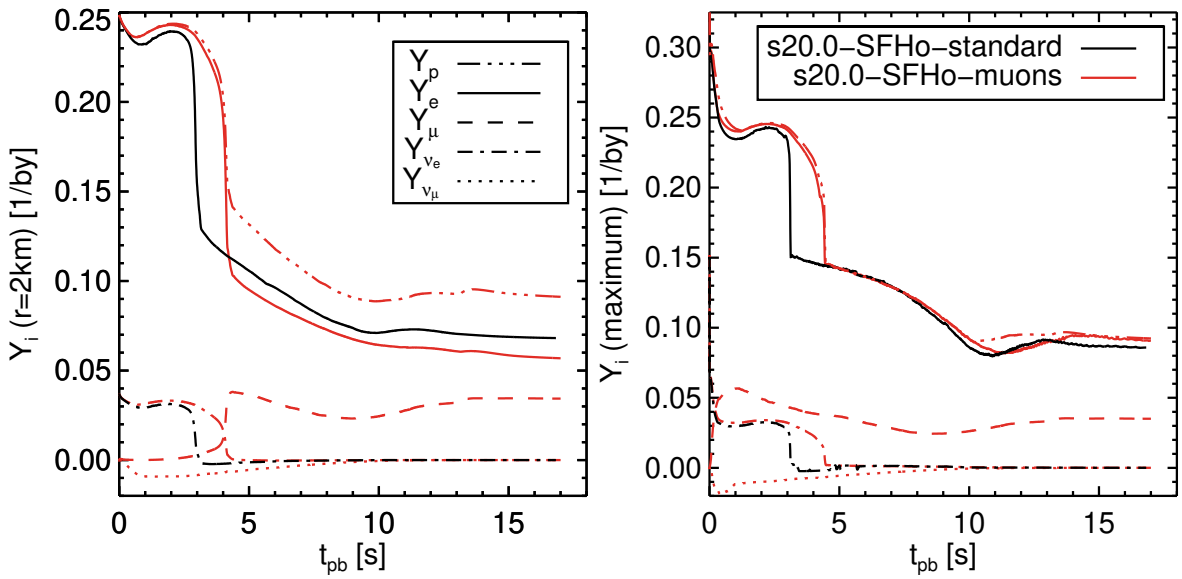

Figure 11.38: On the left, the evolution of the electron and muon fraction at the PNS center evaluated at $r = 2$ km for cases s20.0-SFHo-standard in black and s20.0-SFHo-muons in red; on the right, the evolution of the maximum values of the respective fractions inside the PNS.

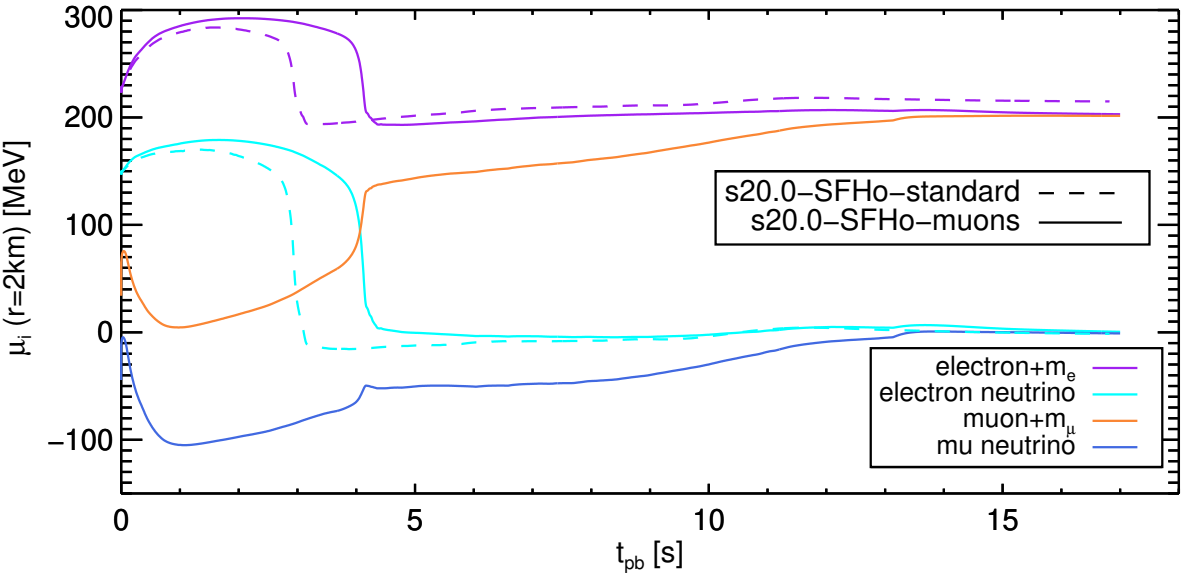

Figure 11.39: The evolution of the leptonic chemical potentials at the PNS center evaluated at $r = 2$ km for cases s20.0-SFHo-standard in black and s20.0-SFHo-muons in red. The charged lepton chemical potentials are including the lepton rest masses.

the ejecta only shows the influence of the delayed PNS deleptonization by a more smeared out Y_e peak while the deleptonization wave propagates through the PNS. The wind entropy shows a very slight enhancement at five seconds as a consequence of the colder PNS and the resulting slower wind velocities. Note that the entropy becomes very noisy at late times as a result of our mixing-length algorithm identifying the now subsonic weak wind as being convectively unstable. Furthermore, the wind outflow has reversed at the 12 s mark and turned into fallback, leading to the plateau phase from then on.

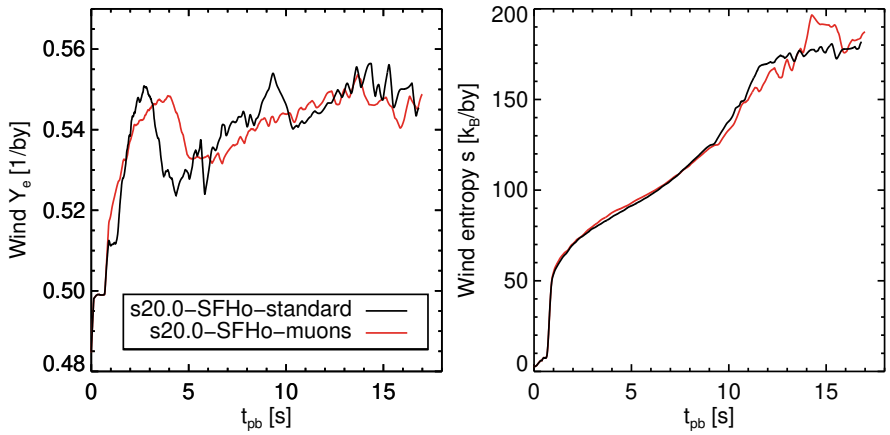

Figure 11.40: On the left, the evolution of the electron fraction contained in the neutrino-driven wind for cases s20.0-SFHo-standard in black and s20.0-SFHo-muons in red; on the right, the evolution of the wind entropy.

Neutron star mass The neutron star mass of both the standard and muonic case are nearly identical, except for some very minute differences in the evolution. The gravitational mass of the muonic case is slightly heavier throughout most of the cooling phase, as more energy is trapped in the PNS in the form of muons that also act gravitationally through their relativistic energy. The final gravitational and baryonic mass of the muonic case is ever so slightly smaller than the standard case. This lowered gravitational mass is a result of the raised Y_p in the cold NS due to the decreased asymmetry parameter. This allows the NS to contract more and liberate a bit more gravitational binding energy. The difference in baryonic mass can be attributed to uncertainties during the initiation of the artificial explosion and is not an effect of the muonic gas. The final baryonic masses are $m_{\text{Bary.}}^{\text{muons}} = 1.9466 M_\odot$ and $m_{\text{Bary.}}^{\text{standard}} = 1.9469 M_\odot$; the final gravitational masses are $m_{\text{Grav.}}^{\text{muons}} = 1.7312 M_\odot$ and $m_{\text{Grav.}}^{\text{standard}} = 1.7321 M_\odot$.

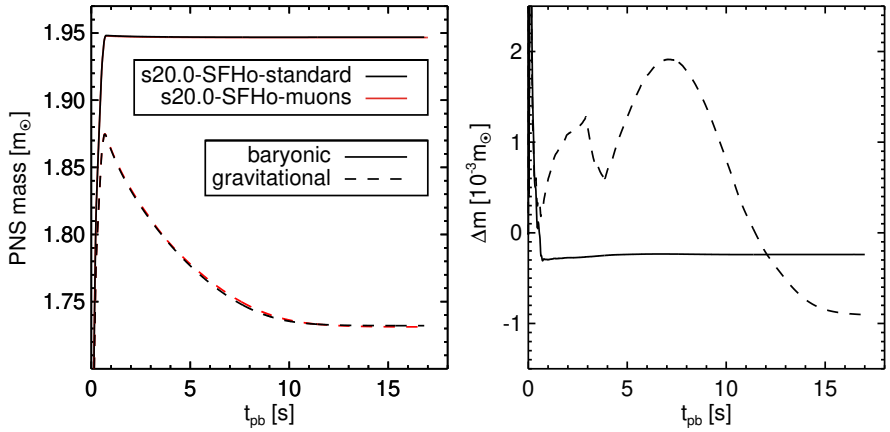

Figure 11.41: On the left, the evolution of the baryonic and gravitational PNS mass for cases s20.0-SFHo-standard in black and s20.0-SFHo-muons in red; on the right, the difference of both cases defined as $\Delta m_{\text{B/G}} = m_{\text{B/G}}^{\text{muons}} - m_{\text{B/G}}^{\text{standard}}$.

Neutrino signal The changes in the total emitted neutrino energy in Fig. 11.42 reflect the differences in the temperature evolution. When the temperature reduction is slower after $t_{\text{pb}} \approx 5\,\text{s}$ in the muonic case, the neutrino emission is reduced and just catches up after $t_{\text{pb}} \approx 11\,\text{s}$.

The final emitted neutrino energy only shows a slight increase by $\Delta \int_t \sum_\nu L_\nu \approx 2.2\,\mathrm{B}$, caused by the neutron star having found a slightly lower energy configuration. Muon generation reduces some of the electron degeneracy, and the more compact PNS can liberate some additional gravitational binding energy. This additional energy seems to be emitted mostly in the form of $\overline{\nu}_\mu$.

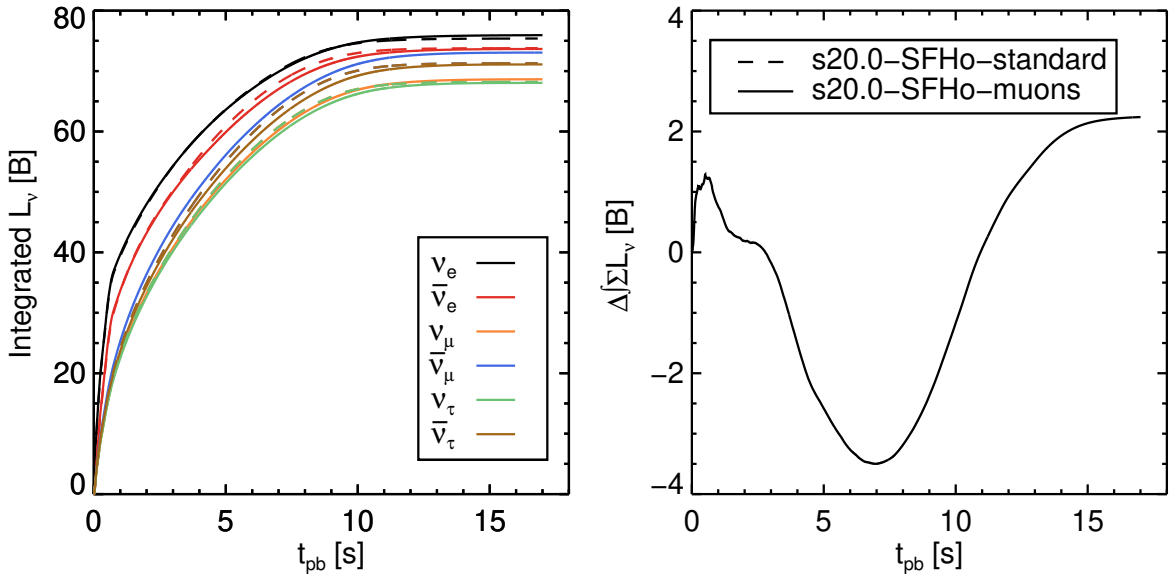

Figure 11.42: On the left, the evolution of the time integrated lab-frame luminosity for cases s20.0-SFHo-standard in dashed and s20.0-SFHo-muons in solid lines; on the right, the difference of the time-integrated and summed total neutrino emission defined as $\Delta \int_t \sum L_\nu = \int_t \sum_\nu L_\nu^{\mathrm{muons}} - \int_t \sum_\nu L_\nu^{\mathrm{standard}}$. Note that the standard case μ and τ neutrino luminosity are overlaid on each other.

The total number of muons inside the PNS is shown in Fig. 11.43, indicating excellent agreement in lepton flavor number conservation. There is a small mismatch during the very dynamic phase from 2–5 s, while the deleptonization wave sweeps through the protoneutron star and the neutrino signal is erratic. This erratic signal might cause inaccuracies in the discrete data points used in the time-integration, in addition to the possible error induced by the missing strict lepton flavor coupling used in our stimulated opacity implementation. The error, however, remains well bound and follows the correct trend. The net neutrino number flux of ν_μ shows the secular changes in luminosity tracking the muon number evolution.

The luminosity and mean energy of all neutrinos follow the expected behavior and show a longer tail in the muonic case, as the cooling is delayed compared to the standard case. As the energy to be radiated is roughly the same, energy conservation implies that less luminosity in the deleptonization phase from 2–6 s needs to be compensated by increased luminosity in the cooling phase from 6–18 s.

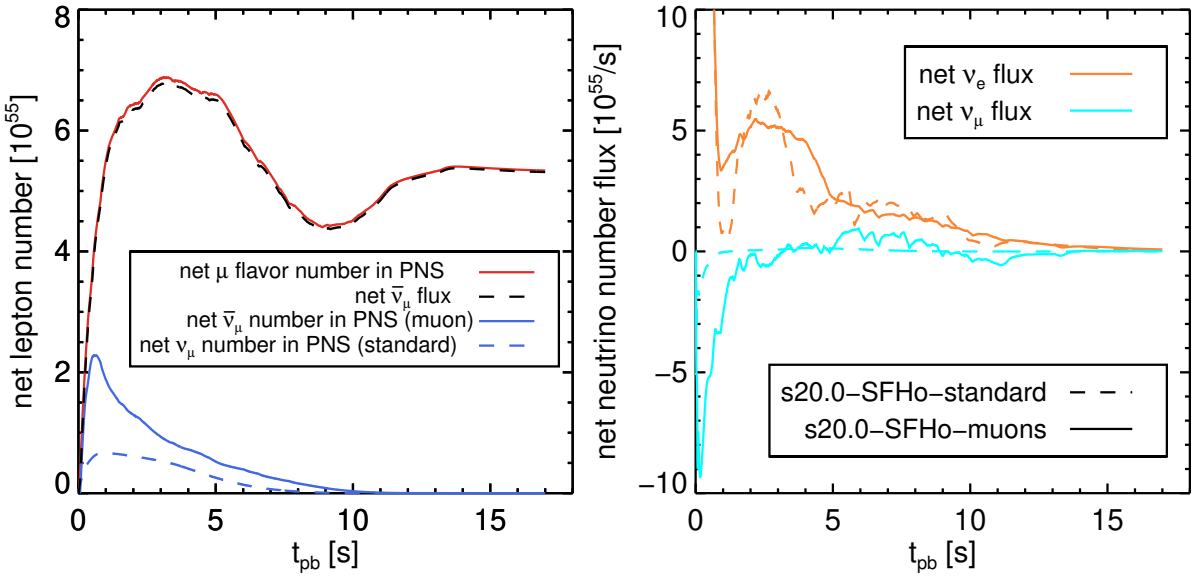

Figure 11.43: On the left, a plot of the volume integrated net muon flavor number contained in the PNS with definitions as in Fig.11.29; on the right, the net neutrino number flux of ν_e and ν_μ defined by net-$\mathcal{L}_\nu = \mathcal{L}_\nu - \mathcal{L}_{\bar{\nu}}$ for s20.0-SFHo-muons in filled and s20.0-SFHo-standard in dashed lines.

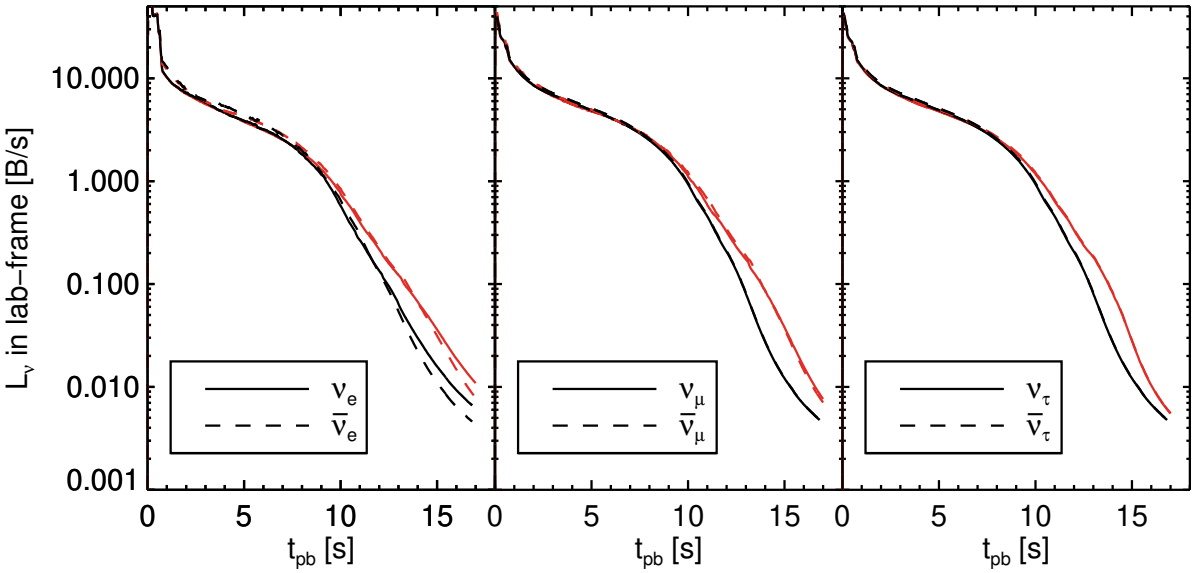

Figure 11.44: On the left, the evolution of the lab-frame luminosity of ν_e and $\overline{\nu}_e$ for cases s20.0-SFHo-standard in black and s20.0-SFHo-muons in red, in the middle of ν_μ and $\overline{\nu}_\mu$, and on the right of ν_τ and $\overline{\nu}_\tau$. Note that in the standard case $\nu_\mu = \nu_\tau$ as well as $\overline{\nu}_\mu = \overline{\nu}_\tau$.

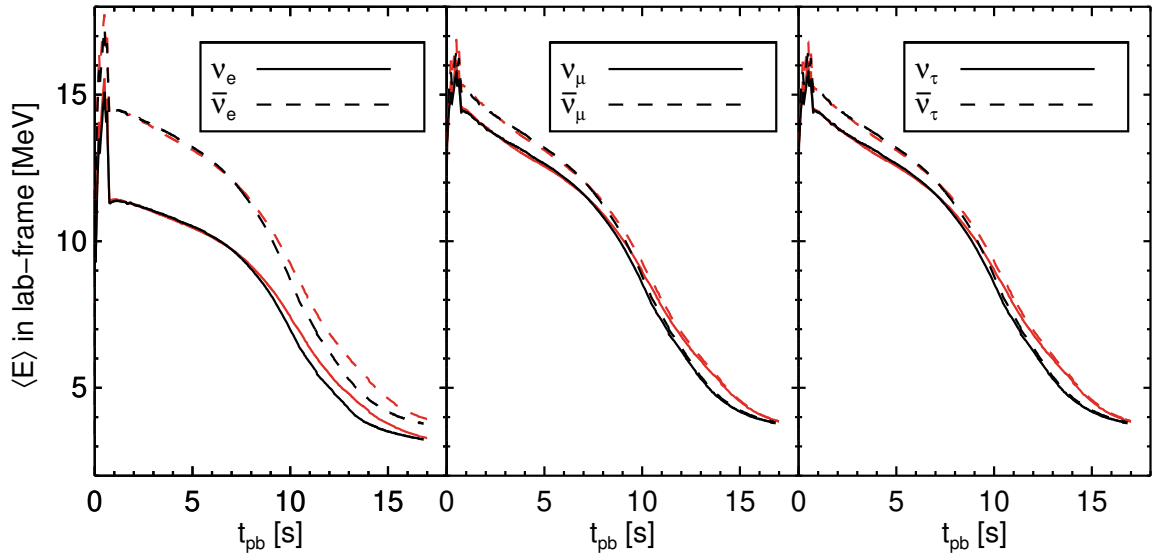

Figure 11.45: On the left, the evolution of the lab-frame mean energy of ν_e and $\overline{\nu}_e$ for cases s20.0-SFHo-standard in black and s20.0-SFHo-muons in red, in the middle of ν_μ and $\overline{\nu}_\mu$, and on the right of ν_τ and $\overline{\nu}_\tau$. Note that in the standard case $\nu_\mu = \nu_\tau$ as well as $\overline{\nu}_\mu = \overline{\nu}_\tau$.

The shape parameter α in Fig. 11.46 shows the largest change in the late neutrino signal with, in general, more pinched spectra compared to the standard case. The spectrum of the $\overline{\nu}_e$ shows a sizable modification, as the mean neutrino energy has become small enough that muonic opacities start to become relevant to $\overline{\nu}_e$ spectrum generation, visible in Fig. 11.37. The spectra of ν_μ and ν_τ show an interesting difference in that the muonic ν_μ and $\overline{\nu}_\mu$ spectra only show a delayed spectral evolution compared to the standard case, whereas the ν_τ and $\overline{\nu}_\tau$ are noticeably more pinched compared to the standard case.

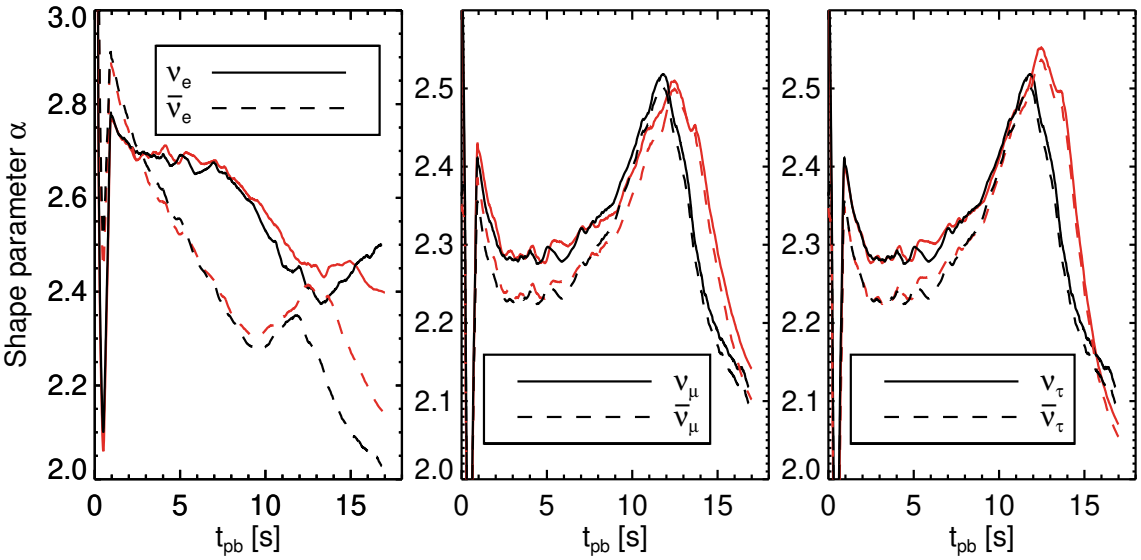

Figure 11.46: On the left, the evolution of the shape parameter α, defined by Eq. 11.26, of ν_e and $\overline{\nu}_e$ for cases s20.0-SFHo-standard in black and s20.0-SFHo-muons in red, in the middle of ν_μ and $\overline{\nu}_\mu$, and on the right of ν_τ and $\overline{\nu}_\tau$. Note that in the standard case $\nu_\mu = \nu_\tau$ as well as $\overline{\nu}_\mu = \overline{\nu}_\tau$.

11.2.3 Summary

The present Kelvin-Helmholtz phase cooling simulation is, just as the stalled accretion shock phase simulation presented in Sec. 11.1, the first of its kind to include all muonic opacities and muons as an out of beta-equilibrium component in a state-of-the-art transport simulation. We have simulated a $20M_{\odot}$ ZAMS progenitor through the stalled shock phase, and have achieved shock revival via artificial quenching of the mass inflow after 500 ms postbounce time. The following Kelvin-Helmholtz phase was tracked up to 18 s using mixing-length convection, to simulate protoneutron star convective overturn. We have seen that the presence of muons affects the deleptonization timescale due to decreased diffusive inward transport of $\overline{\nu}_{\mu}$ number and a steepening of the trapped lepton gradient that suppresses convectively unstable regions according to the Ledoux criterion. As soon as trapped electron neutrinos are convectively transported to the surface, freshly produced muons take the place of the decaying surplus electrons and prevent a softening of the lepton gradient. In addition to the net muons produced via weak processes, additional thermal muon pairs are created as the temperature rises steeply in these now deleptonized areas by Joule heating. A significant amount of this thermal energy is converted into inert muon rest mass that stores large amounts of energy. This effect reduces the maximum temperature of the PNS, and muon decay only slowly releases the energy stored in their rest mass. This reservoir lets the muon gas act similar to an energy "battery" that supplies additional energy for the very late cooling phase. The produced net muons are however still far from beta-equilibrium, even when the deleptonization wave has passed and electrons have already achieved beta-equilibrium. Full equilibration and the PNS entering beta-equilibrium with respect to both electrons and muons, i.e., $\hat{\mu} = \mu_{\mathrm{n}} - \mu_{\mathrm{p}} = \mu_{\mathrm{e}} = \mu_{\mu}$ is only achieved after 13 s of cooling when the PNS becomes transparent to neutrinos.

The results of this section show that muons can also affect the Kelvin-Helmholtz cooling phase by the additional degree of leptonic freedom that can store thermal energy and release it slowly in a delayed manner. This prolongs the effective measurable neutrino signal. Further effects of muonization on the way to a completely cold NS on the megayear timescale are explored for example in Refs. [4, 2].

11.3 Muons in beta-equilibrium

In addition to the self-consistent buildup of muon number we examined in the previous sections, we will now also shortly address the possibility of treating the muon number as an equilibrium component of the EOS. This requires a vanishing μ neutrino chemical potential, $\mu_{\nu_\mu} = 0$, as well as a fixed muon chemical potential, $\mu_\mu = \mu_\mathrm{n} - \mu_\mathrm{p} + Q$, where μ_n and μ_p are the nonrelativistic chemical potentials and $Q = m_\mathrm{n} - m_\mathrm{p}$. This approximation is valid under the assumption that the creation of muons is perfectly efficient, transport of ν_μ and $\overline{\nu}_\mu$ is unhindered, and any surplus of μ neutrinos is instantaneously lost. A simple way to assure that no μ neutrino chemical potential can form is by only simulating the single averaged heavy-lepton neutrino, as is common in most CCSN simulation codes. This approach however wholly neglects lepton flavor number conservation and further effects on neutrino spectra, except by changes in temperature.

11.3.1 EOS generation

As muon number is not an equilibrium component of any publicly available EOS, we modified the SFHo EOS to contain a beta-equilibrium muon number.

The needed steps are as follows.

1. We use the pure baryonic component of the high-density EOS as the base and calculate for every tabulated grid point in ρ, T, Y_p an equilibrium muon number, using the local muon chemical potential
$$\mu_\mu\left(\rho, T, Y_\mathrm{p}\right) = \mu_\mathrm{n}\left(\rho, T, Y_\mathrm{p}\right) - \mu_\mathrm{p}\left(\rho, T, Y_\mathrm{p}\right) + Q$$
as required by beta-equilibrium. Note that here the proton fraction Y_p is equivalent to the positive charge fraction bound in nuclei and as free protons.

2. After inverting the muon chemical potential to get the muon fraction $Y_\mu\left(\rho, T, Y_\mathrm{p}\right)$, we use the constraint of charge neutrality,
$$Y_\mathrm{e}\left(\rho, T, Y_\mathrm{p}\right) = Y_\mathrm{p} - Y_\mu\left(\rho, T, Y_\mathrm{p}\right) , \tag{11.33}$$
to determine the still missing electron fraction of each grid point.

3. Calculate the electron and muon gas quantities from the tabulated data created in Chapter II.

4. Add the leptonic components e and μ to the baryonic component B to create the new table μbeta.
$$e^{\mu\mathrm{beta}}\left(\rho, T, Y_\mathrm{p}\right) = e_\mathrm{B}\left(\rho, T, Y_\mathrm{p}\right) + e_\mathrm{e}^\mathrm{tot}\left(T, \rho Y_\mathrm{e}\left(\rho, T, Y_\mathrm{p}\right)\right) + e_\mu^\mathrm{tot}\left(T, \rho Y_\mu\left(\rho, T, Y_\mathrm{p}\right)\right) ,$$
$$P^{\mu\mathrm{beta}}\left(\rho, T, Y_\mathrm{p}\right) = P_\mathrm{B}\left(\rho, T, Y_\mathrm{p}\right) + P_\mathrm{e}^\mathrm{tot}\left(T, \rho Y_\mathrm{e}\left(\rho, T, Y_\mathrm{p}\right)\right) + P_\mu^\mathrm{tot}\left(T, \rho Y_\mu\left(\rho, T, Y_\mathrm{p}\right)\right) ,$$
$$s^{\mu\mathrm{beta}}\left(\rho, T, Y_\mathrm{p}\right) = s_\mathrm{B}\left(\rho, T, Y_\mathrm{p}\right) + s_\mathrm{e}^\mathrm{tot}\left(T, \rho Y_\mathrm{e}\left(\rho, T, Y_\mathrm{p}\right)\right) + s_\mu^\mathrm{tot}\left(T, \rho Y_\mu\left(\rho, T, Y_\mathrm{p}\right)\right) ,$$
$$\mu_\mathrm{e}^{\mu\mathrm{beta}}\left(\rho, T, Y_\mathrm{p}\right) = \mu_\mathrm{e}\left(T, \rho Y_\mathrm{e}\left(\rho, T, Y_\mathrm{p}\right)\right) ,$$
$$\mu_\mu^{\mu\mathrm{beta}}\left(\rho, T, Y_\mathrm{p}\right) = \mu_\mathrm{n}\left(\rho, T, Y_\mathrm{p}\right) - \mu_\mathrm{p}\left(\rho, T, Y_\mathrm{p}\right) + Q = \mu_\mu\left(T, \rho Y_\mu\left(\rho, T, Y_\mathrm{p}\right)\right) ,$$
$$\mu_{\nu_\mathrm{e}}^{\mu\mathrm{beta}}\left(\rho, T, Y_\mathrm{p}\right) = \mu_\mathrm{e}^{\mu\mathrm{beta}}\left(\rho, T, Y_\mathrm{p}\right) + \mu_\mathrm{p}^{\mu\mathrm{beta}}\left(\rho, T, Y_\mathrm{p}\right) - \mu_\mathrm{n}^{\mu\mathrm{beta}}\left(\rho, T, Y_\mathrm{p}\right) - Q ,$$
$$Y_\mathrm{e}^{\mu\mathrm{beta}}\left(\rho, T, Y_\mathrm{p}\right) = Y_\mathrm{p} - Y_\mu\left(\rho, T, Y_\mathrm{p}\right) ,$$
$$Y_\mu^{\mu\mathrm{beta}}\left(\rho, T, Y_\mathrm{p}\right) = Y_\mu\left(\rho, T, Y_\mathrm{p}\right) .$$

5. Copy the remaining unmodified baryonic quantities over into the new table μbeta.

6. As the table is still tabulated as a function of proton number, i.e., $\left(\rho, T, Y_{\mathrm{p}}\right)$, we need to interpolate the table from the fixed ρ, T, Y_{p} grid to a fixed ρ, T, Y_{e} grid. This step is necessary as the electron fraction and not the proton fraction is the conserved quantity in our transport.

7. The resulting table has a positive charge fraction that is not equal to the electron fraction, as in a normal general-purpose EOS table, anymore. The positive charge fraction is now a function of the conserved electron fraction and the state dependent muon fraction, resulting in
$$Y_{\mathrm{p}}^{\mu\mathrm{beta}}\left(\rho, T, Y_{\mathrm{e}}\right) = Y_e + Y_{\mu}^{\mu\mathrm{beta}}\left(\rho, T, Y_{\mathrm{e}}\right) \ .$$

The effect of the muonic negative charge is now captured in the proton and neutron fraction being able to deviate from the electron fraction. This feeds back onto the nucleon chemical potentials that enter the electron neutrino chemical potential via $\mu_{\nu_{\mathrm{e}}}^{\mu\mathrm{beta}}\left(\rho, T, Y_{\mathrm{e}}\right) = \mu_{\mathrm{e}}^{\mu\mathrm{beta}}\left(\rho, T, Y_{\mathrm{e}}\right) + \mu_{\mathrm{p}}^{\mu\mathrm{beta}}\left(\rho, T, Y_{\mathrm{e}}\right) - \mu_{\mathrm{n}}^{\mu\mathrm{beta}}\left(\rho, T, Y_{\mathrm{e}}\right) - Q$, as neutron and proton chemical potential also depend on $Y_{\mu}\left(\rho, T, Y_{\mathrm{e}}\right)$. When ρ, T at constant Y_{e} moves towards a state where muon number increases, there will be a simultaneous increase in protons and a decrease in neutrons that shifts the ν_{e} chemical potential to a different value, as the left-hand side of

$$\mu_{\mathrm{p}} - \mu_{\mathrm{n}} = \mu_{\nu_{\mathrm{e}}} - \mu_{\mathrm{e}} + Q \tag{11.34}$$

will change accordingly. The electron neutrinos will then try to re-equilibrate to the new chemical equilibrium, which will reduce or increase electron fraction as a result of our transport solution. Muonization of the PNS is therefore treated consistently in the electron sector, but is completely neglected for μ neutrinos. An example plot of how the muon fraction might develop for a fixed $Y_{\mathrm{e}} = 0.2$ is shown in Fig. 11.47. The corresponding approximate proton fraction can be found by adding the color encoded muon fraction back onto the constant electron fraction. Note the large uniform dark red area where the equilibrium muon fraction per baryon can become very large and lead to nonphysical proton fractions exceeding the maximum original tabulated value of $Y_{\mathrm{p}} = 0.6$. These areas cause the interpolation to break down, but are in effect not accessible to the gas, as the energy penalty associated with entering these regions is excessive and the transport will self-correct back to physical regions beforehand.

11.3.2 Comparisons

The model with the beta equilibrium muon fraction will be called s20.0-SFHo-μbeta and run with the three neutrino species, ν_{e}, $\overline{\nu}_{\mathrm{e}}$, and a heavy-lepton neutrino ν_{x}. It will be compared to our full physics muonic case s20.0-SFHo-muons using the same numerical setup as in the accretion model. We only use the single heavy-lepton neutrino here, as the effect of weak magnetism would otherwise lead to the buildup of a net heavy-lepton number and a nonzero ν_{μ} chemical potential in the PNS that would be inconsistent with our requirement of $\mu_{\nu_{\mu}} \equiv \mu_{\mathrm{x}} = 0$.

The radii and heating rates in the full physics case and our simplified model in Fig. 11.48 show good agreement in all three radii, demonstrating that the radius reduction is as expected an effect of the muonic component in the EOS. Of course, the manner in which this net muon number is produced is simplified, but the PNS mantle in our full physics simulations was already in good muonic beta-equilibrium during most of the accretion phase. Our simplified model is accordingly suitable to model the PNS mantle evolution. Nonetheless, the heating rate in case μbeta is slightly reduced due to differences in the neutrino spectra.

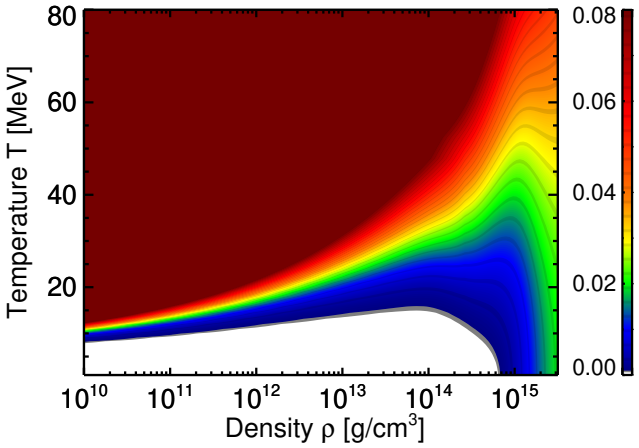

Figure 11.47: A plot of the equilibrium muon fraction Y_μ for $Y_e = 0.2$ and variable density and temperature. The muon fraction is color coded according to the color bar given on the right.

The electron neutrino luminosity of our simplified model in Fig. 11.49 fit well to the full physics muonic model, but there are of course some variations in the μ and τ neutrino sector. The assumption of a single heavy-lepton neutrino ν_x does not allow any differential weak magnetism effects, species dependent neutrinosphere location or number production variations to change the neutrino signal, and it only contains an averaged representation of some of these effects. The ν_x luminosity, therefore, lies in the middle and slightly above our ν_τ and $\overline{\nu}_\tau$ luminosity, and does not exhibit the lepton flavor conservation effects on the $\overline{\nu}_\mu$ and ν_μ luminosity. Thermal energy loss of the PNS proceeds less by neutrino emission and more by additional muon rest mass production. The PNS, therefore, stores more energy at earlier times in the muonic gas than seen in our full physics simulation. The slightly increased luminosity of the ν_x compared

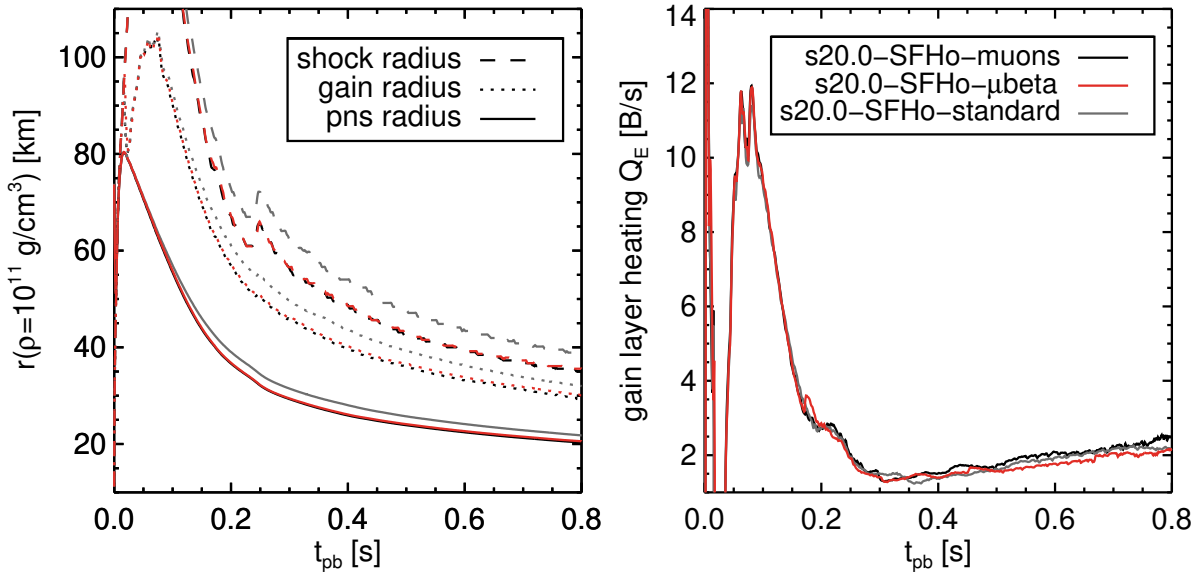

Figure 11.48: On the left, the evolution of the shock radius in dashed, the gain radius in dotted and the PNS radius in solid lines for cases s20.0-SFHo-muons in black and s20.0-SFHo-μbeta in red; on the right, the volume integrated heating rate in the gain layer for both models. The model s20.0-SFHo-standard is shown in gray for reference.

to our full physics ν_τ and $\overline{\nu}_\tau$ show that the PNS temperature stratification is different at their number and energy spheres.

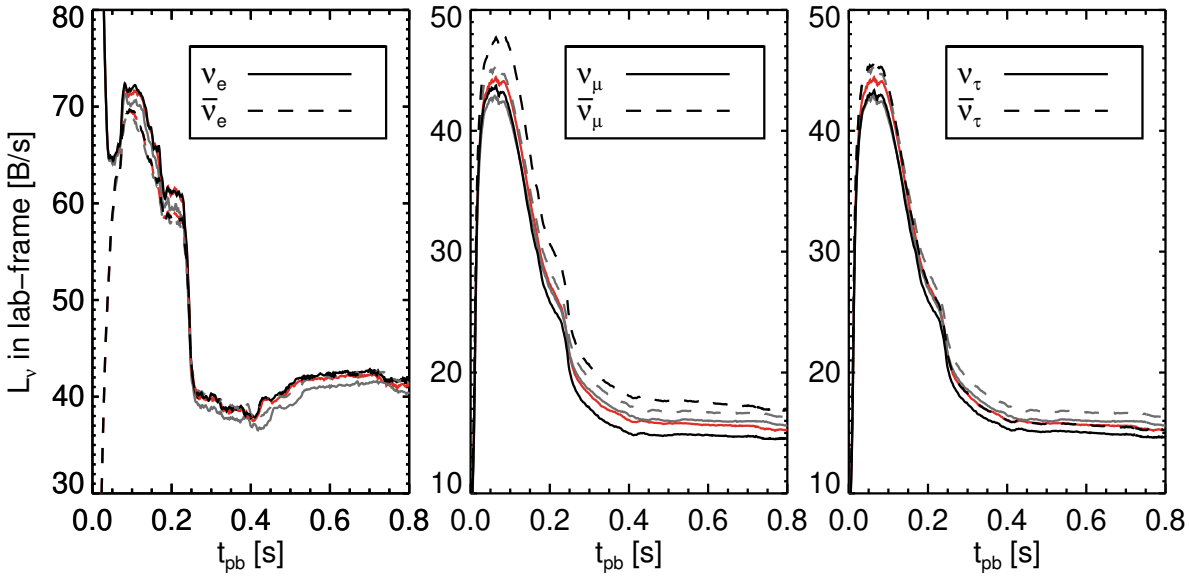

Figure 11.49: On the left, the evolution of the lab-frame luminosity of ν_e and $\overline{\nu}_e$ for cases s20.0-SFHo-muons in black and s20.0-SFHo-μbeta in red, in the middle of ν_μ and $\overline{\nu}_\mu$ and on the right the same for ν_τ and $\overline{\nu}_\tau$. Note that in the μbeta case there only exists the averaged heavy-lepton neutrino ν_x, serving as a stand-in for both μ/τ neutrinos and antineutrinos. The model s20.0-SFHo-standard is shown in gray for reference.

Similarly, the mean energies in Fig. 11.50 show good agreement for the ν_e and $\overline{\nu}_e$ neutrinos at early times but become slightly lower at late times. The ν_x do not exhibit the spectral splitting caused by weak magnetism, and the ν_x should sit in the middle of the ν_τ and $\overline{\nu}_\tau$ mean energy if the emission conditions were identical. As the mean energy of the ν_x even passes below the $\overline{\nu}_\tau$ mean energy, the temperature at the ν_x energy sphere must be lower than in the full physics case, which is further proof that more energy is stored in muon rest mass.

The shape parameter α shows that the spectra of all neutrinos are slightly more pinched than in the full physics muonic case and resemble the standard physics case without muons.

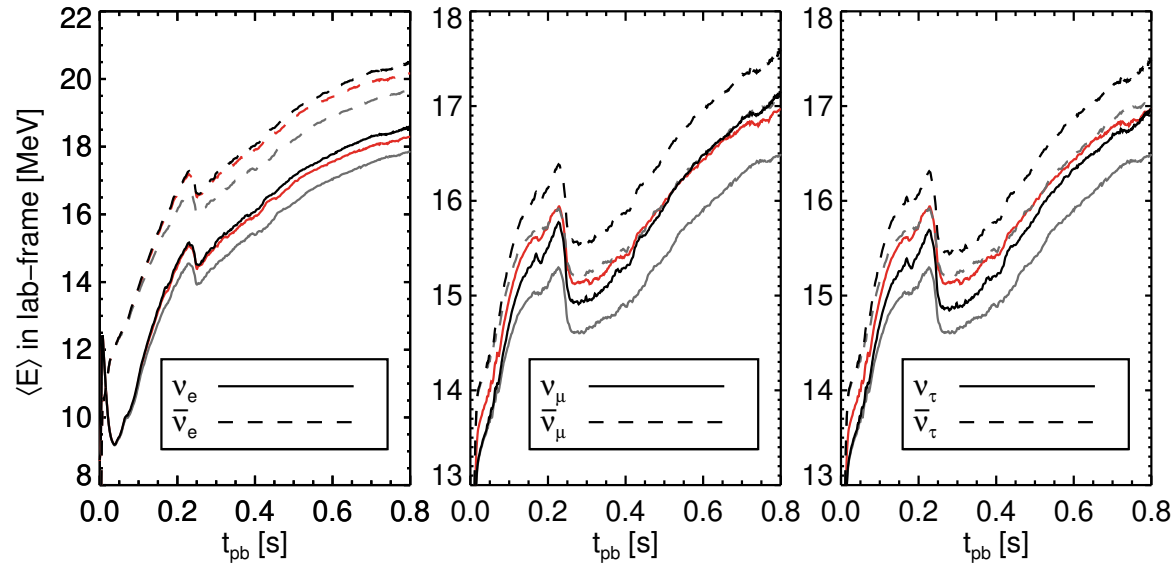

Figure 11.50: On the left, the evolution of the lab-frame mean energy of ν_e and $\overline{\nu}_e$ for cases s20.0-SFHo-muons in black and s20.0-SFHo-μbeta in red, in the middle of ν_μ and $\overline{\nu}_\mu$, and on the right the same for ν_τ and $\overline{\nu}_\tau$. The model s20.0-SFHo-standard is shown in gray for reference.

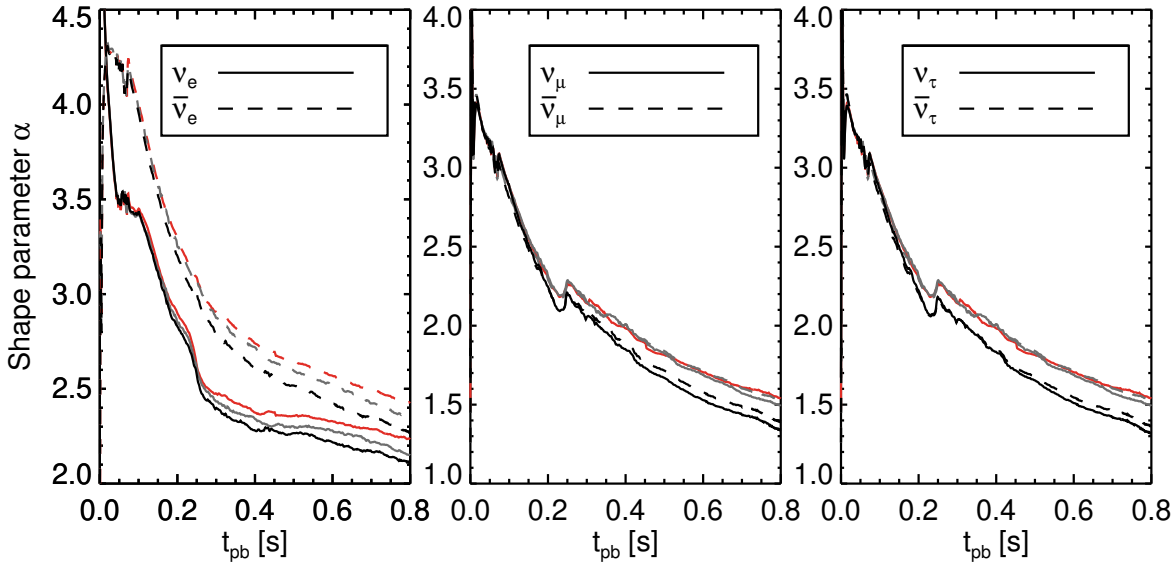

Figure 11.51: On the left, the evolution of the shape parameter α, defined by Eq. 11.26 of ν_e and $\overline{\nu}_e$ for cases s20-SFHo-muons in black and s20.0-SFHo-μbeta in red, in the middle of ν_μ and $\overline{\nu}_\mu$, and on the right the same for ν_τ and $\overline{\nu}_\tau$. The model s20.0-SFHo-standard is shown in gray for reference.

The largest error of our approximation is seen, as expected, in the net muon number, which features a relatively constant offset in the beta-equilibrium case in Fig. 11.52. It shows a significant overproduction of muons in the protoneutron star due to there being no neutrino back-reactions and neutrino blocking present in the dense PNS core, which would otherwise suppress muonization. Correspondingly, more energy being stored in muon rest mass results in less emitted neutrino energy.

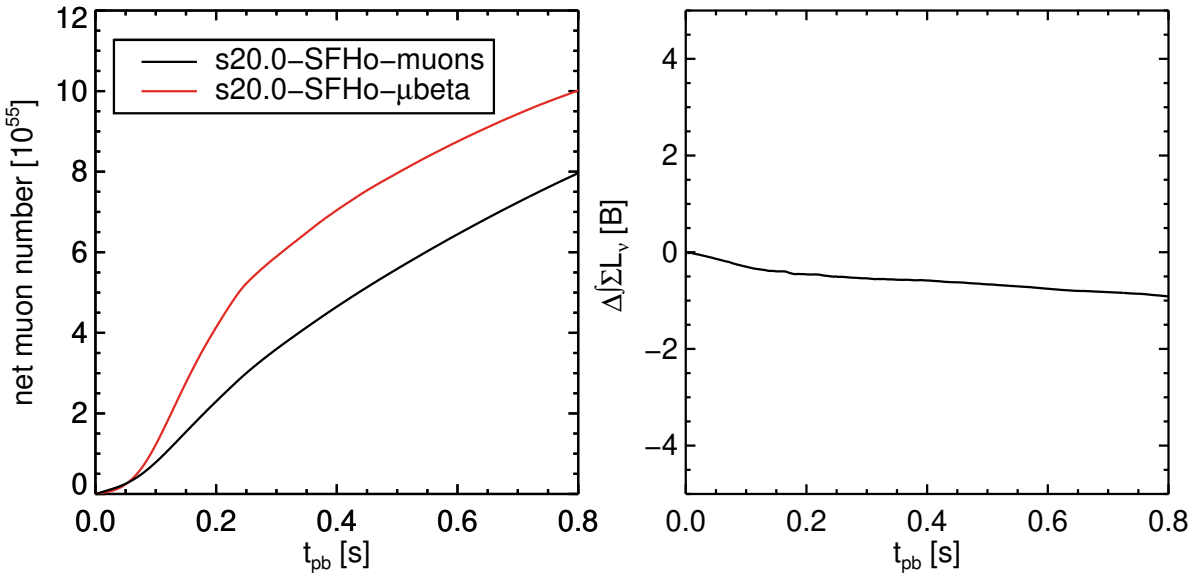

Figure 11.52: On the left, the evolution of the volume integrated net muon number in the PNS for cases s20.0-SFHo-muons in black and s20.0-SFHo-μbeta in red; on the right, the difference of the time-integrated and summed total emitted neutrino luminosity calculated by $\Delta \int_t \sum_\nu L_\nu = \int_t \sum_\nu L_\nu^{\mu\text{beta}} - \int_t \sum_\nu L_\nu^{\text{muons}}$.

11.3.3 Summary

In this section, we have compared our full physics muonic simulation of Sec. 11.1 with a simplified model, where muons are assumed to be in perfect beta-equilibrium with vanishing net ν_μ number. This was achieved by modifying an existing general-purpose equation of state table to include muons as an equilibrium component while still maintaining electron flavor conservation. This allows for easy implementation into existing supernova codes and for a first estimate of the sensitivity of accretion simulations to muonization. The shortfall of this approach is that our simulations show that the initial premise of this approximation, that μ neutrino number can efficiently escape from the PNS, is not assured everywhere. Muons interior to the mantle region do not reach an equilibrium distribution, and in fact, deviate farther from equilibrium during the accretion phase, requiring tens of seconds after shock-revival until achievement of beta-equilibrium. This causes the μbeta case to depart from our full physics case after a few hundred milliseconds, showing reduced gain layer heating, luminosity and mean energy of all neutrinos. The hydrodynamic contraction of the PNS is, however, well reproduced even though the total number muon number is exceeded by $\sim 20\%$.

In conclusion, a muon weak equilibrium table is a useful tool for exploring the sensitivity of CCSN to muonization, but a self-consistent calculation is still required to get the full effect.

12 2D simulations

12.1 Accretion phase and shock revival

In this section we have attached a refereed journal paper submitted to Physical Review Letters and accepted under reference PRL 119, 242702 (2017) and DOI: 10.1103/PhysRevLett.119.242702. (Ref. [9]). The 2D simulations published in this letter demonstrate the sensitivity of multi-dimensional simulations to muonic effects. The problematic 1D shortfalls of steady-state quasi-hydrostatic post-shock and PNS stratification are avoided, and genuine multidimensional effects like the standing accretion shock instability and neutrino-driven convection can lift the shock surface to higher radii. This allows the increased neutrino energies in the muonic case to deposit sufficient energy to revitalize the stalled shock, leading to shock runaway and explosion. This is conclusively demonstrated in the case s20.0-SFHo-Muons that achieves shock runaway while the standard case fails to explode. This demonstrates that muons can, contrary to our first pessimistic outlook in the 1D case, aid in the neutrino-driven explosion mechanism and cannot be neglected in first-principle self-consistent calculations of core-collapse supernovae.

12.1.1 Introduction

First state-of-the-art three-dimensional simulations have recently yielded successful supernova explosions by the neutrino-driven mechanism (see Refs. [130, 83, 84, 71, 58, 117, 91, 94]). But the explosions turned out to be more delayed than in two-dimensional calculations and sensitive to neutrino effects even on the $10-20\%$ level (cf. Ref. [83]). Accurate physics in the neutrino and nuclear sectors is therefore demanded to investigate the viability of the neutrino-driven mechanism by self-consistent, first-principle neutrino-hydrodynamical simulations.

While the presence of muons is well known to play a role in cold neutron stars (NSs; e.g., Refs. [124, 2]), it is traditionally ignored in SN matter based on the argument that the high muon rest mass ($m_\mu c^2 \approx 105.66\,\mathrm{MeV}$) suppresses their formation. This reasoning, however, is not well justified (cf. Ref. [73]) because the electron chemical potential in newly formed NSs exceeds the muon rest mass, and the peak temperatures rise above $30\,\mathrm{MeV}$ after roughly $100\,\mathrm{ms}$ after core bounce, when the thermal distributions of photons and neutrinos reach well beyond $100\,\mathrm{MeV}$. These conditions enable the production of significant numbers of muons and anti-muons (μ^-, μ^+) via electromagnetic interactions such as $\mathrm{e}^- + \mathrm{e}^+ \leftrightharpoons \mu^- + \mu^+$ and $\gamma + \gamma \leftrightharpoons \mu^- + \mu^+$ (γ denotes high-energy photons), via weak reactions that couple the e-lepton and μ-lepton sectors, and via beta-processes between nucleons and μ neutrinos and antineutrinos (ν_μ, $\overline{\nu}_\mu$), which are created in the SN core through thermal pair processes.

While the new-born NS loses electron-lepton number by radiating a slight excess of electron neutrinos (ν_e) compared to electron antineutrinos ($\overline{\nu}_\mathrm{e}$), it also gradually builds up net muon-lepton number ("muonizes") by emitting more muon antineutrinos than muon neutrinos. Electrons and muons thus share the negative charge that compensates the positive reservoir of protons (and of some e^+ and μ^+). Here we show that the rearrangements in the stellar medium and the neutrino emission that are associated with the appearance of muons have an important impact on the evolution of the proto-NS by accelerating its contraction. This facilitates the development of SN explosions by the neutrino-driven mechanism. Muons therefore must be included in self-consistent, first-principle models of the SN phenomenon.

12.1.2 Neutron star formation with muons.

Assuming neutrino-flavor oscillations do not play a role, conservation equations for the lepton numbers (i.e., the numbers of the charged leptons plus their neutrinos minus those of the corresponding anti-particles) for all three flavors hold individually. During stellar core collapse neutrinos get trapped and equilibrate at about one percent of the nuclear saturation density

($\rho_0 \approx 2.7 \times 10^{14}\,\mathrm{g/cm^3}$ or baryon density $n_0 \approx 0.16\,\mathrm{fm}^{-3}$). Subsequently, they diffuse out of the newly formed NS only over a time scale of several seconds. The NS, which begins to form at core bounce, thus inherits a large concentration of electron-lepton number from the progenitor core with an initial electron-flavor lepton fraction of ~ 0.30 electrons plus electron neutrinos per baryon (see Ref. [78]). The diffusive loss of ν_e then drives the evolution to the final neutron-rich state of a cold NS with its small remaining content of protons.

In contrast, the trapped μ and τ-lepton numbers are zero initially. The tauon density remains extremely small at all times because of the huge rest mass of the tauons ($m_\tau c^2 \approx 1777\,\mathrm{MeV}$), which is much bigger than both the temperature and electron chemical potential in the NS. Therefore the ν_τ and $\overline{\nu}_\tau$ numbers are initially equal and the chemical potentials $\mu_{\nu_\tau} = -\mu_{\overline{\nu}_\tau} = 0$ with high precision. However, since the cross section for neutral-current scattering on nucleons, $\nu + \mathrm{N} \leftrightharpoons \nu + \mathrm{N}$ $(\mathrm{N} = \mathrm{n},\, \mathrm{p})$, is somewhat larger for neutrinos than for anti-neutrinos due to weak-magnetism corrections (of order $E/\left(m_\mathrm{N} c^2\right)$ with neutrino energy E and nucleon mass m_N (see Ref. [47]), ν_τ diffuse out faster and the proto-NS is expected to (transiently) develop a considerable τ-lepton number in the neutrino sector ($\mu_{\nu_\tau} > 0$) even though the formation of tauons is negligible (see Ref. [51]).

Different from τ neutrinos, but analogously to ν_e and $\overline{\nu}_\mathrm{e}$, ν_μ and $\overline{\nu}_\mu$ participate in beta-reactions,

$$\nu_\ell + \mathrm{n} \leftrightharpoons \mathrm{p} + \ell^- \,, \tag{12.1}$$

$$\overline{\nu}_\ell + \mathrm{p} \leftrightharpoons \mathrm{n} + \ell^+ \,, \tag{12.2}$$

with their charged leptons, ℓ (standing for e or μ), when a significant population of thermally excited μ^- and μ^+ appears (cf. Ref. [73]). Beta equilibrium for both flavors implies the usual relation

$$\Delta\mu \equiv \mu_\mathrm{n} - \mu_\mathrm{p} = \mu_\ell - \mu_{\nu_\ell} \tag{12.3}$$

between the chemical potentials (including particle rest-mass energies) of neutrons, protons, charged leptons, and the corresponding neutrinos. Since the highly degenerate Fermi sea of e^- partially converts to μ^-, and since initially the trapped muon number is zero, an excess of μ^- over μ^+ is compensated by an opposite excess of $\overline{\nu}_\mu$ over ν_μ. Therefore the diffusive flux of $\overline{\nu}_\mu$ will dominate that of ν_μ, leading to a gradual build-up of muon number. The easier escape of $\overline{\nu}_\mu$ compared to ν_μ is aided by the lower neutral-current scattering cross section for $\overline{\nu}_\mu$ mentioned above and by the higher opacity for beta-reactions of ν_μ compared to $\overline{\nu}_\mu$ in analogy to the electron-flavor. The accumulation of net muon number in the proto-NS, i.e., the process of muonization that leads to an excess of μ^- over μ^+ in the final NS, is facilitated by the reactions of Eqs. (12.1 and 12.2). Also other interactions that couple the e-lepton and μ-lepton sectors

$\nu + \mu^- \leftrightharpoons \nu' + \mu^{-\prime}$	$\nu + \mu^+ \leftrightharpoons \nu' + \mu^+$
$\nu_\mu + \mathrm{e}^- \leftrightharpoons \nu_\mathrm{e} + \mu^-$	$\overline{\nu}_\mu + \mathrm{e}^+ \leftrightharpoons \overline{\nu}_\mathrm{e} + \mu^+$
$\nu_\mu + \overline{\nu}_\mathrm{e} + \mathrm{e}^- \leftrightharpoons \mu^-$	$\overline{\nu}_\mu + \nu_\mathrm{e} + \mathrm{e}^+ \leftrightharpoons \mu^+$
$\overline{\nu}_\mathrm{e} + \mathrm{e}^- \leftrightharpoons \overline{\nu}_\mu + \mu^-$	$\nu_\mathrm{e} + \mathrm{e}^+ \leftrightharpoons \nu_\mu + \mu^+$
$\nu_\mu + \mathrm{n} \leftrightharpoons \mathrm{p} + \mu^-$	$\overline{\nu}_\mu + \mathrm{p} \leftrightharpoons \mathrm{n} + \mu^+$

Table 12.1: Neutrino reactions with muons.

enhance the muonization rate and thus increase both the ν_μ and $\overline{\nu}_\mu$ fluxes.

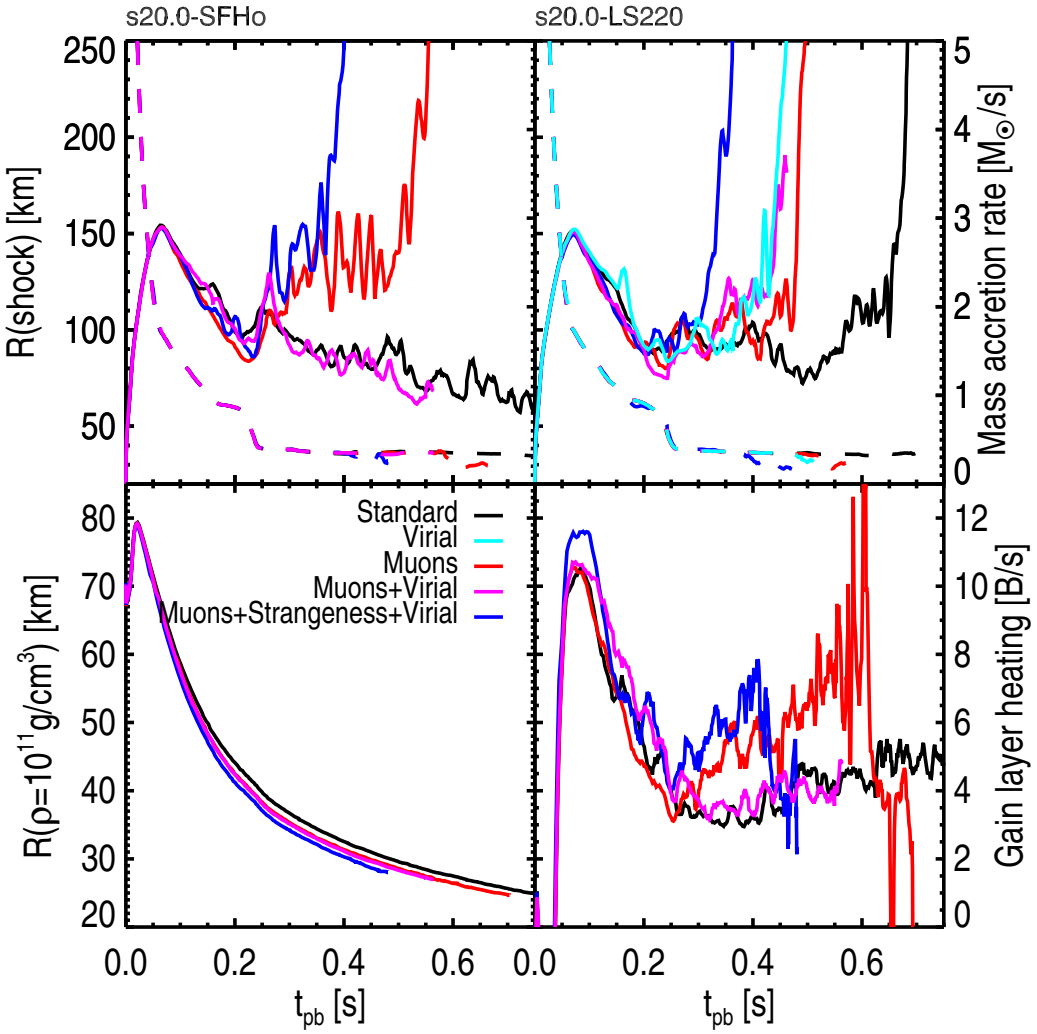

Figure 12.1: *Upper row:* Angle-averaged shock radii (solid) and mass-infall rates (at 400 km; dashed) vs. post-bounce time for our sets of models with SFHo (*left*) and LS220 EOS (*right*). *Lower row:* Time evolution of NS radii (measured at an average density of 10^{11} g/cm^3; *left)* and net heating rate integrated over the gain layer (in 1 B/s $= 10^{51}$ erg/s; *right*) for models with SFHo EOS.

Muonization might play a non-negligible role during all stages of the SN post-bounce (p.b.) evolution and NS as well as black-hole (BH) formation. In the following we discuss its effects on the initiation of SN explosions by neutrino-energy deposition.

12.1.3 Numerical modeling

Our SN simulations were performed with the Prometheus-Vertex neutrino-hydrodynamics code (see Refs. [114, 14]) with an approximate treatment of general relativistic gravity by the effective gravitational potential of Case A of Ref. [77]. The Prometheus hydrodynamics module solves the equations of nonrelativistic hydrodynamics (continuity equations for mass, momentum, energy, lepton number, and nuclear composition) with an explicit, directionally-split, higher-order Godunov scheme of Ref. [38]. The transport module Vertex integrates the energy-dependent evolution equations of energy and momentum for all six neutrino species (ν_e, $\overline{\nu}_e$, ν_μ, $\overline{\nu}_\mu$, ν_τ, $\overline{\nu}_\tau$) in the comoving frame of the stellar fluid to order v/c (v is the fluid velocity, c the speed of light), including corrections due to general relativistic redshift and time dilation. The closure is provided by an Eddington factor based on the solution of a

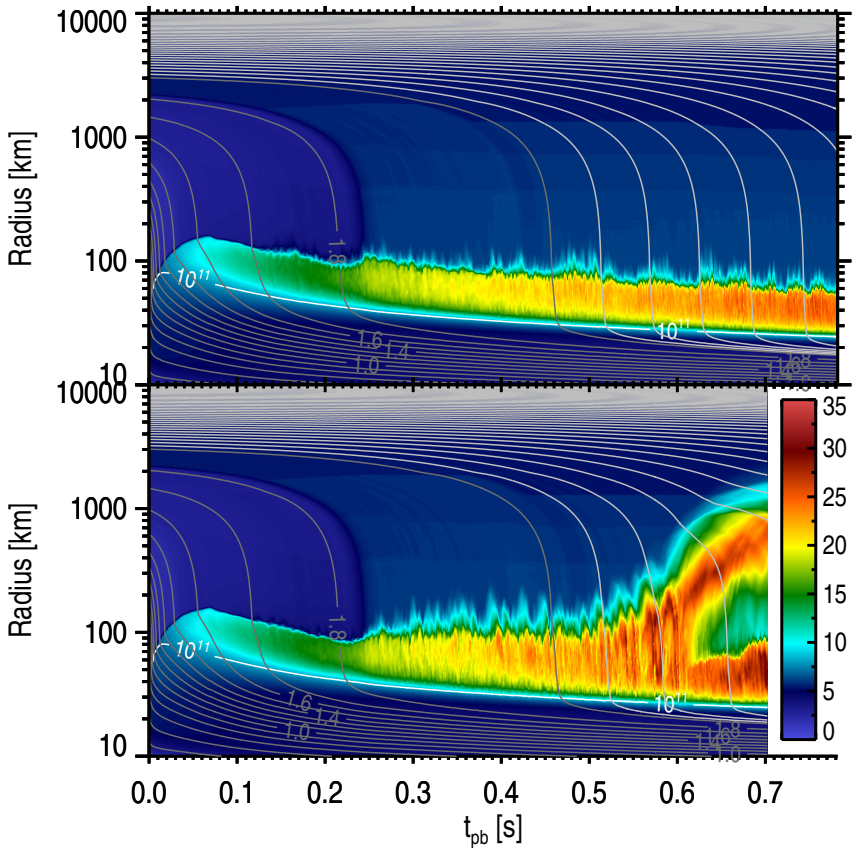

Figure 12.2: Evolution of angle-averaged specific entropy (color; in k_B per nucleon vs. post-bounce time for model s20.0-SFHo-standard (*top*) and s20.0-SFHo-muons (*bottom*). The outer boundary of the light blue-green-yellow region follows the average radius of the SN shock. The gray lines mark "mass shells" (radii of constant enclosed baryonic mass), the white line corresponds to an average density of 10^{11} g/cm^3.

model-Boltzmann equation, iterated for convergence with the set of two-moment equations of Ref. [114]. Neutrino transport in multi-dimensional simulations employs the ray-by-ray plus approximation of Ref. [14].

We upgraded the Prometheus-Vertex code for including all effects of μ^- and μ^+ in the hydrodynamics and equation of state (EOS) of the stellar plasma, the effective relativistic gravity potential, and in the neutrino transport. This implies the solution of conservation equations for electron and muon lepton number:

$$\frac{\partial \rho Y_\ell}{\partial t} + \vec{\nabla}\left(\rho Y_\ell \vec{v}\right) = Q_\ell \tag{12.4}$$

(here, relativistic corrections are omitted for simplicity). $Y_\ell = Y_{\ell^-} - Y_{\ell^+}$ is the net number of charged leptons per nucleon, ρ the baryon-mass density and Q_ℓ the source rate that is associated with all processes emitting and absorbing ν_ℓ and $\bar{\nu}_\ell$. The EOS depends on Y_e and Y_μ, i.e., $P = P\left(\rho, T, Y_e, Y_\mu, \{Y_k\}_{k=1,\ldots,N_{nuc}}\right)$ and $e^{int} = e^{int}\left(\rho, T, Y_e, Y_\mu, \{Y_k\}_{k=1,\ldots,N_{nuc}}\right)$ for pressure P and specific energy density e^{int} (T is the medium temperature, N_{nuc} the number of nuclear species). Analog to e^- and e^+, μ^- and μ^+ provide an additive contribution to P and e^{int} and are treated as ideal Fermi gases of arbitrary degeneracy and arbitrary degree of relativity. In nuclear statistical equilibrium (NSE) the mass fractions of nuclei and nucleons, Y_k, are determined by the Saha equations and hence $Y_k = Y_k\left(\rho, T, Y_e, Y_\mu\right)$ holds; otherwise they follow from evolution equations similar to Eq. 12.4 with Q_ℓ being replaced by source terms for nuclear reaction rates.

With ρ, $e^{\rm int}$, $Y_{\rm e}$ and Y_μ given as solutions of the hydrodynamics and Y_k ($k = 1, \ldots, N_{\rm nuc}$) being determined either by NSE or Eq. 12.4, T and the chemical potentials $\mu_{\rm e}$, μ_μ, $\mu_{\rm n}$, $\mu_{\rm p}$, and μ_k for all k can be determined under the constraint of charge neutrality, $\sum_k Z_k Y_k = Y_{\rm e} + Y_\mu$, with Z_k being the nuclear charge number of species k.

Accounting for the presence of muons and the differences of the ν and $\bar{\nu}$ scattering cross sections with nucleons due to nucleon-recoil and weak-magnetism of Ref. [47], we generalized the neutrino-transport module VERTEX to an energy-dependent six-species treatment, tracking $\nu_{\rm e}$, $\overline{\nu}_{\rm e}$, ν_μ, $\overline{\nu}_\mu$, ν_τ, and $\overline{\nu}_\tau$ individually. Besides our "standard" set of neutrino reaction rates listed in table 1 of Ref. [57], we also implemented all relevant neutrino interactions with μ^- and μ^+ as listed in Table 12.1. The detailed kinematics (energy and momentum exchange between reaction partners) were fully taken into account, describing charged leptons as arbitrarily relativistic and arbitrarily degenerate fermions and nucleons as nonrelativistic fermions. Neutral and charged-current interactions between neutrinos and nucleons were handled by the formalism of Refs. [17, 18], which includes the effects of nucleon correlations by a random-phase approximation (RPA). We generalized the treatment to also include corrections due to neutron and proton mean-field potentials in the beta-processes (see Refs. [115, 81, 120]) and due to the large rest masses of μ^- and μ^+. Weak-magnetism corrections according to Ref. [47] were implemented for all neutral-current neutrino-nucleon scattering reactions (cf. Ref. [14]) but only for charged-current reactions of $\nu_{\rm e}$ and $\overline{\nu}_{\rm e}$ with nucleons (because lepton-mass dependence was neglected in Ref. [47]). Neutral and charged-current reactions of neutrinos with nucleons bound in light nuclei (^{2}H, ^{3}H, ^{3}He) were approximated by using the neutrino-nucleon interactions of Ref. [10], which slightly overestimates (mainly at low energies) the collective opacity of these reactions compared to the detailed description in Ref. [33]. When specified, we included in neutrino-nucleon scatterings virial corrections for the axial response of nuclear matter at low densities (see Ref. [50]) and/or applied a strangeness-dependent contribution to the axial-vector coupling coefficient (see Ref. [47]) with a value of $g_{\rm A}^{\rm s} = -0.1$, consistent with experimental constraints of Ref. [45]). The virial corrections were implemented via an effective interaction in the RPA that was stronger at low densities. This yielded results similar to those in Ref. [50].

Our SN simulations were performed in 2D for a nonrotating $20 M_\odot$ progenitor model of Ref. [136] with the Lattimer-Swesty EOS (LS220) with nuclear incompressibility $K = 220\,$MeV of Ref. [70] and the SFHo EOS of Refs. [43, 123] (models s20.0-LS220 and s20.0-SFHo, respectively). After bounce, at densities below $10^{11}\,$g/cm^3, we employed a 23-species NSE solver at $T > 0.5\,$MeV for infalling and $T > 0.34\,$MeV for expanding, high-entropy matter, and nuclear "flashing" (see Ref. [114]) at lower temperatures. For the polar coordinate grid we used a time-dependent number of 400–650 radial zones and 160 lateral zones with a refinement to 320 lateral zones outside of the gain radius (i.e., the radius exterior to which neutrino heating dominates), and for the neutrino transport 15 geometrically distributed energy bins with $E_{\rm max} = 380\,$MeV.

12.1.4 Results

Besides conducting simulations for the two employed nuclear EOS with our standard set of neutrino processes (Table 1 in Ref. [57]), we also investigated cases where we included (a) the virial corrections in ν–N-scattering, (b) all muon effects, (c) both muon and virial effects, and (d) muons, virial effects, and a strangeness correction in ν–N-scattering. Fig. 12.1 displays the time evolution of the average shock radii for the models with SFHo (top left) and LS220 EOS (top right). It is obvious that muon formation enables an explosion for the SFHo model, which does not explode with standard neutrino physics, and it allows for a clearly earlier onset of the explosion with the LS220 EOS.

Figure 12.2 compares the evolution of angle-averaged radial profiles of the entropy per baryon (superimposed in color on mass-shell trajectories) for the two SFHo-models. After the

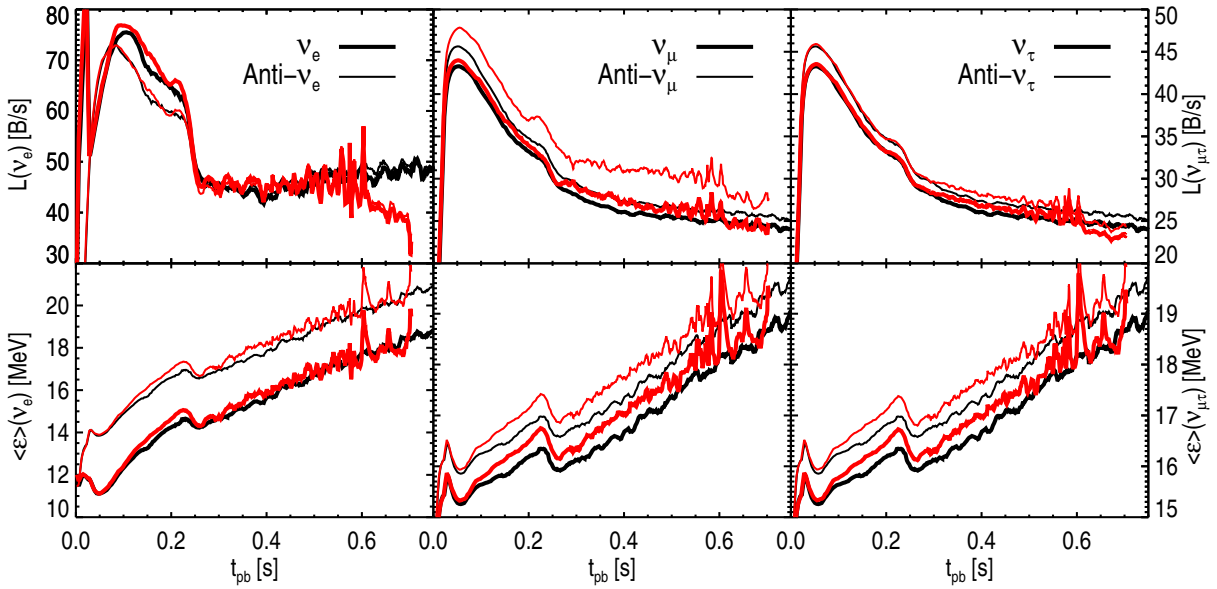

Figure 12.3: Neutrino luminosities (*upper row*) and radiated mean neutrino energies (defined as ratio of neutrino energy density to number density; *lower row*) vs. post-bounce time, evaluated in the laboratory frame at the average gain radius s20.0-SFHo-standard (black) and s20.0-SFHo-muons (red).

arrival of the interface between silicon-shell and oxygen-rich Si-layer at the shock at $t_{\rm pb} \sim 240\,$ms, the shock radius in the muonic case is considerably larger than in the standard case, leading to an explosion, despite the inverse order of the shock radii at earlier times (Fig. 12.1). The lower panels of Fig. 12.1 provide an explanation: with muons the proto-NS contracts notably faster (left). The creation of μ^- and μ^+ effectively softens the EOS by conversion of thermal and degeneracy energy of $\rm e^-$ into rest-mass energy of muons. In addition, it significantly raises the emission of $\overline{\nu}_\mu$ and, on a lower level, also of ν_μ (Fig. 12.3, middle panels). The accelerated shrinking of the NS leads to higher temperatures at given densities and correspondingly increased luminosities and mean energies of the emitted electron- and τ-flavor neutrinos, which are shown in Fig. 12.3 (left and right panels) at the gain radius, where $\nu_{\rm e}$ and $\overline{\nu}_{\rm e}$ differences are relevant for the neutrino heating. As a consequence, the neutrino-heating rate, per baryon as well as integrated over the gain layer (i.e., the region between gain radius and shock), becomes sizably greater in the model with muons at $t \gtrsim 240\,$ms (Fig. 12.1, lower right panel). Muons therefore have a similar overall effect as the strangeness-dependent reduction of neutrino-nucleon scattering discussed in Ref. [83].

Figure 12.4 documents the appearance of significant charged-muon number (up to $Y_\mu \sim 0.05$) (at the expense of $\rm e^-$) correlated with a temperature maximum in the NS between $\sim 7\,$km ($\sim 4 \times 10^{14}\,$g/cm^3) and $\sim 21\,$km ($\sim 2 \times 10^{13}\,$g/cm^3). While in the model without muons ν_μ are more abundant than $\overline{\nu}_\mu$, equivalent to the situation for ν_τ and $\overline{\nu}_\tau$ discussed above, the situation is reversed when muons are included: Y_{ν_μ} drops in its peak to about half of the abundance in the standard case, whereas the number of $\overline{\nu}_\mu$ more than doubles ($Y^{\rm max}_{\overline{\nu}_\mu} \gtrsim 0.02$).

Including also strangeness corrections in ν–N-scattering leads to even faster explosions (Fig. 12.1, upper panels), because muon and strangeness effects drive the system in the same direction, namely a faster contraction of the NS (Fig. 12.1, lower left panel). The situation for virial effects is ambiguous. While the LS220 model with virial corrections explodes faster than the standard case and evolves similar to the simulation with muons, virial effects in addition to muons make little difference (Fig. 12.1, upper right panel). In contrast, an SFHo model including virial corrections and strangeness $g^{\rm s}_{\rm A} = -0.1$ (not shown) explodes only later than 600 ms due

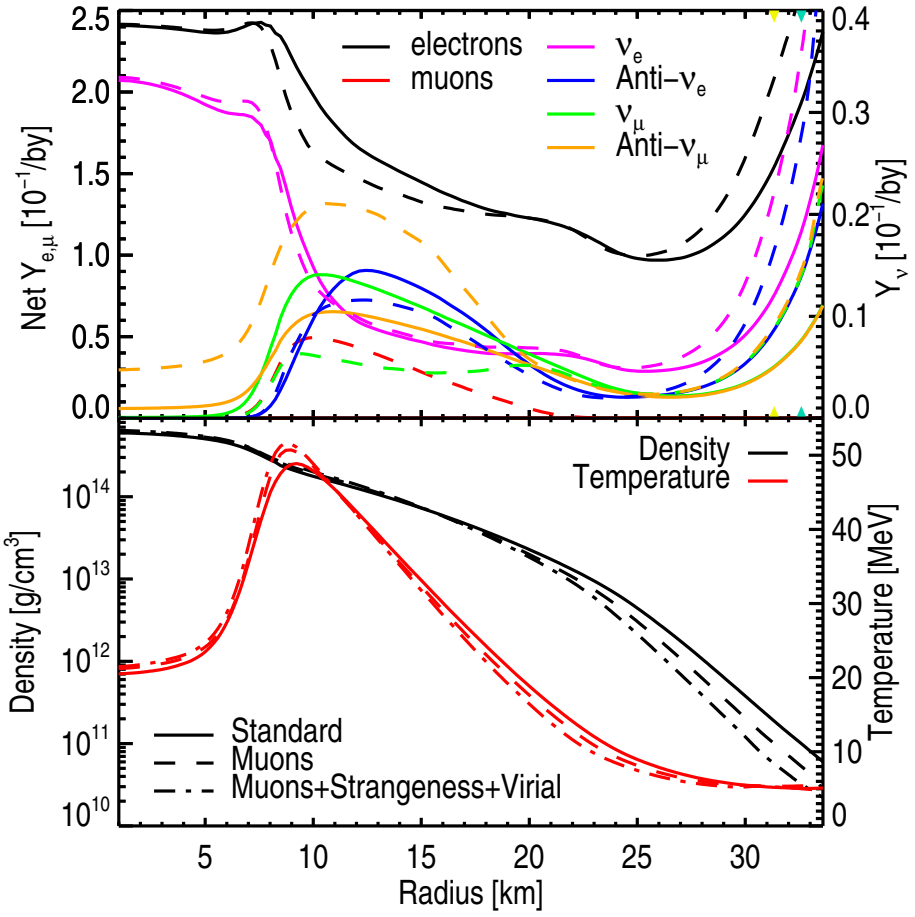

Figure 12.4: *Top:* Radial profiles at 0.4 s after bounce of the net numbers of charged leptons (left-hand scale) and neutrinos (right-hand scale) per baryon for s20.0-SFHo-standard (solid) and s20.0-SFHo-muons (dashed). *Bottom:* Radial profiles of density (black) and temperature (red) for three cases with SFHo EOS.

to the strangeness effects, whereas the SFHo model with muons and virial response fails to explode. For relevant temperatures ($T \approx 5$–10 MeV) virial effects lead to a reduction of the ν–N-scattering opacity compared to RPA results only at densities below $\sim (0.01, \ldots, 0.03)\rho_0$. This is so low that there is a visible (1–2%) increase of the heavy-lepton neutrino emission but hardly any correspondingly accelerated contraction of the NS radius (Fig. 12.1, lower left panel). Virial effects are therefore subtle, because they can extract energy in the ν_μ and ν_τ sector without explosion-favoring consequences for the ν_e and $\overline{\nu}_e$ emission.

12.1.5 Conclusion

We have demonstrated by 2D simulations that the appearance of muons in the hot medium causes enhanced neutrino emission and faster contraction of the proto-NS with supportive effects on the neutrino-energy deposition behind the stalled shock and the onset of neutrino-driven explosions. The ongoing muonization of the new-born NS may also lead to stronger heating of matter that is still accreted and re-ejected after the onset of the explosion (see Ref. [94] and references therein) and could therefore raise the explosion energy. Muonization mainly affects more massive and thus hotter NSs and should have less impact on SN explosions of low-mass progenitors with less massive NSs. Final conclusions about their detailed role in the explosion will require 3D simulations. Since muon formation effectively softens the NS EOS at high densities, it also has important implications for the collapse of hot NSs to BHs. Therefore

muons cannot be ignored in detailed models of the SN explosion mechanism and NS formation. For a rigorously self-consistent description, this requires —and we have implemented— a full six-species treatment of neutrino transport, which couples the production of electron- and muon-flavor neutrinos. Since all six neutrino species differ in their spectra, corresponding transport results may offer interesting new aspects for neutrino oscillations. Muons may also have to be included in simulations of NS–NS mergers, because the compactness of the merger remnant and its time scale for a possible collapse to a BH is sensitive to muon formation in the hot nuclear medium.

12.2 Rapid accretion induced collapse

To gauge the effect muonization has in the extreme case of rapid accretion and collapse to a black hole, we have simulated an ultra-low metallicity $75M_\odot$ ZAMS progenitor star with a $3M_\odot$ iron core from the 2002 model set by Woosley&Heger [138], henceforth called u75.0. The numerical setup of our muonic case is identical to the common numerical setup established in Sec. 10 and preceding sections, to ensure comparability in cause and effect. The minimum angular resolution in θ is $1.125°$, increasing to $0.5625°$ in the gain layer as described in Sec. 10. The numerical setup of the standard case is almost identical to the common numerical setup, except evolving only three neutrino species $\nu \in [\nu_e, \overline{\nu}_e, \nu_x]$, where ν_x is the averaged heavy-lepton neutrino as in Sec. 11.3. The employed EOS are the LS220 nonrelativistic liquid-drop EOS by Ref. [70], and the SFHo relativistic mean field EOS by Ref. [123].

Even though the multi-dimensional collapse to a black hole might ordinarily be expected to stay mostly spherically symmetric with only marginal neutrino-driven convection in the gain layer, the presence of hydrodynamic instabilities like SASI may lead to extremely rapid and violent high-frequency shock oscillation around the PNS. Furthermore, the presence of violent protoneutron star convection and other genuinely multi-dimensional effects in the PNS core make two-dimensional simulations worthwhile. However, due to the computational cost associated with modeling a failed supernova through a long accretion phase of possibly several seconds to eventual collapse, we have to choose a more tractable model. The extremely short collapse timescale of the selected u75.0 progenitor of only ca. 200 ms to 300 ms, depending on the employed EOS, allows quick 2D and even 3D simulations. Similar studies regarding additional nonbaryonic particle degrees of freedom in the EOS have been undertaken most recently in Ref. [107], who simulated the collapse of an s40.0 progenitor from Ref. [136] using the LS220 EOS supplemented by an ideal Bose-Einstein gas of pions and a neutrino leakage scheme. Additional work on combining hadronic and leptonic degrees of freedom have been undertaken in Ref. [101], who however only simulated the direct collapse of perturbed unstable muonized neutron stars to black holes without thermal effects or neutrino transport. Here we aim to extend on these short excursions by modeling the whole evolutionary track towards black hole formation. As black hole collapse is a physical manifestation of a strongly GR dominated event, we need to rely on the accuracy of our effective GR TOV potential, implemented in Ref. [77]. This potential has however been demonstrated in Refs. [55, 88] to be in good agreement with full GR calculations. As the PNS in our model is nonrotating and there are no large-scale deviations from spherical symmetry present in the PNS, we expect the gravitational potential to be dominated by the monopole component and our 2D results to remain as accurate as the 1D results. The analyzed simulations are named u75.0-LS220-standard and u75.0-LS220-muons for the LS220 EOS case, and u75.0-SFHo-standard and u75.0-SFHo-muons for the SFHo EOS case

12.2.1 Progenitor

The progenitor u75.0 has an extremely heavy iron-core at its center that is not purely supported by electron degeneracy pressure alone, but also by photonic pressure. This allows the iron-core mass to exceed the cold Chandrasekhar mass of $1.45727 \times \left(2Y_e\right)^2 M_\odot$ by more than a solar mass. The extended $\sim 2.5M_\odot$ iron-core already even exceeds the cold TOV mass of both the employed LS220 EOS and the SFHo EOS. The mapping of the initial progenitor profiles onto our chosen numerical grid is shown in Fig. 12.5, and the treatment of the thermodynamic quantities is as in Sec. 11.1.

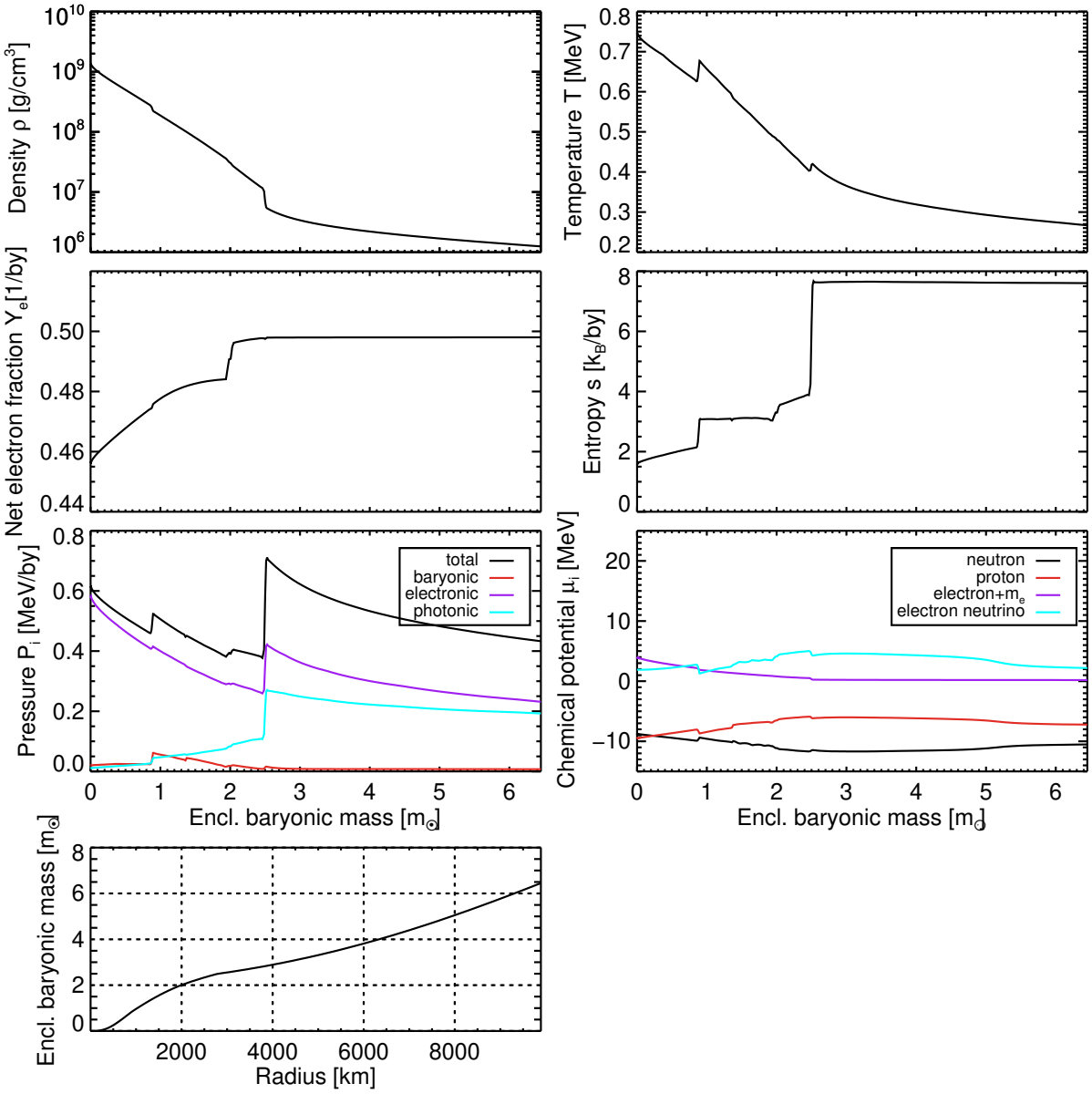

Figure 12.5: Initial profiles of the u75.0 progenitor mapped onto our numerical grid as a function of enclosed baryonic mass using the LS220 EOS. Shown are the density, temperature, electron fraction, entropy per baryon, pressure per baryon, chemical potentials, and the location of each enclosed mass shell. The pressure has been further subdivided into its individual components.

12.2.2 Time evolution

Radii The radii evolution of both the LS220 model and SFHo model are depicted in Fig. 12.7, showing a very rapid shrinking of the PNS radius in both cases. The point of gravitational instability and collapse to a BH is reached after $t^{\text{muons}}_{\text{pb,LS220}} \approx 150\,\text{ms}$ in the LS220 muonic case, and $t^{\text{standard}}_{\text{pb,LS220}} \approx 200\,\text{ms}$ in the LS220 standard case. In the LS220 standard case, the final baryonic mass is $2.520 M_\odot$ and the final gravitational mass is $2.474 M_\odot$. In the LS220 muonic case, the final baryonic mass is $2.458 M_\odot$ and the final gravitational mass is $2.416 M_\odot$. The SFHo shows a slightly later collapse at $t^{\text{muons}}_{\text{pb,SFHo}} \approx 230\,\text{ms}$ in the muonic case, and $t^{\text{standard}}_{\text{pb,SFHo}} \approx 290\,\text{ms}$ in the standard case. In the SFHo standard case, the final baryonic mass is $2.593 M_\odot$ and the final gravitational mass is $2.532 M_\odot$. In the SFHo muonic case, the final baryonic mass is $2.542 M_\odot$ and the final gravitational mass is $2.489 M_\odot$.

The spread of collapse time between muonic and standard physics case for both EOS is roughly around 50-60 ms. The overall longer collapse time for the SFHo case, even though the maximum cold TOV mass is nearly identical in both EOS, is probably due to differences in thermal effects on the EOS. The muonic models in both cases show a very rapid decrease in protoneutron star radius that does not converge towards the nearly constant offset seen in lighter progenitors. This can be an indication that the formation of muons has reached a region of instability, where muon production is a self-reinforcing cycle analogous to the electron pair-instability in hypernovae. In contrast to the muonic models that already collapse before or immediately after the in-fall of the Si-O interface, the standard case models of LS220 and SFHo show signs of shock revival shortly before the collapse. Reason being the extreme neutrino luminosity from the rapidly shrinking protoneutron star being sufficient to revitalize the shock temporarily, as the Si-O interface arrives and the mass accretion rate slows down to a still formidable $1 M_\odot$ per second.

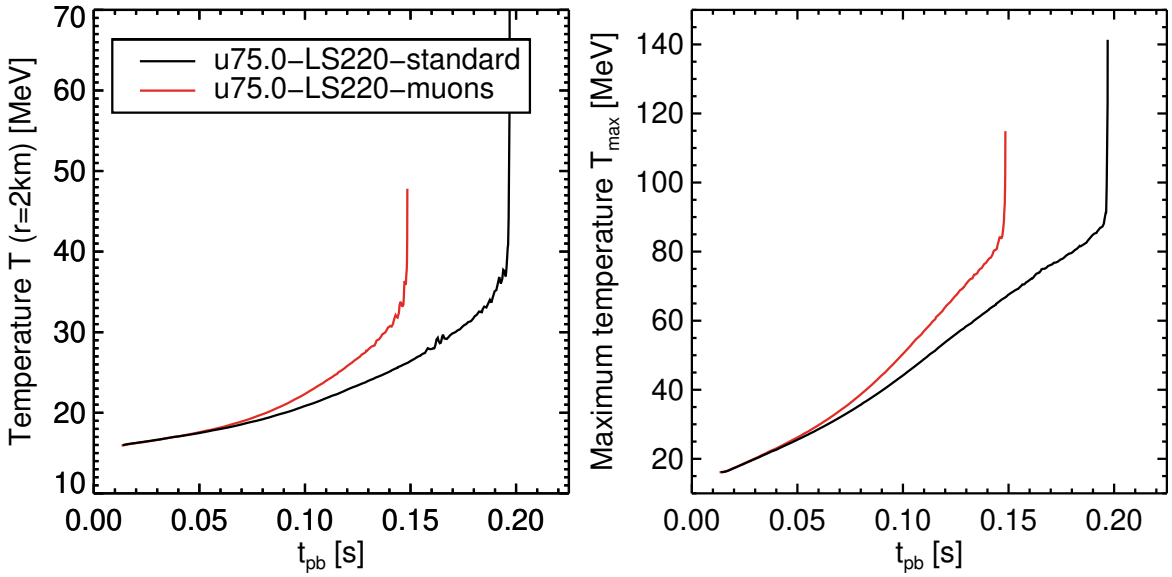

Figure 12.6: On the left, the central temperature of u75.0-LS220-muons in red and u75.0-LS220-standard in black; on the right, the maximum temperature inside the PNS with the same color assignments as on the left.

Similar behavior was already seen in Refs. [104, 19], where a solar metallicity $40 M_\odot$ ZAMS progenitor of the Ref. [136] set showed shock expansion before the final collapse to a black hole. In both our u75.0 and the s40.0 model in Ref. [104] this shock expansion is however not fast enough to be counted as a successful explosion. The BH collapse and following rarefaction of the post-shock region will eventually lead the explosion to fail and the remaining still gravitationally bound surrounding progenitor to be accreted into the growing black hole, whereas the results of Ref. [19] indicate a very weak explosion and ejection of the outer hydrogen envelope. Note however, that a calculation up to the BH singularity is not possible with our Newtonian hydrodynamics code, and our simulation crashes once the collapsing PNS reaches the limits of our tabulated EOS. A demonstration of a dynamical simulation of shock failure and following accretion is therefore not possible to accurately simulate with PROMETHEUS-VERTEX.

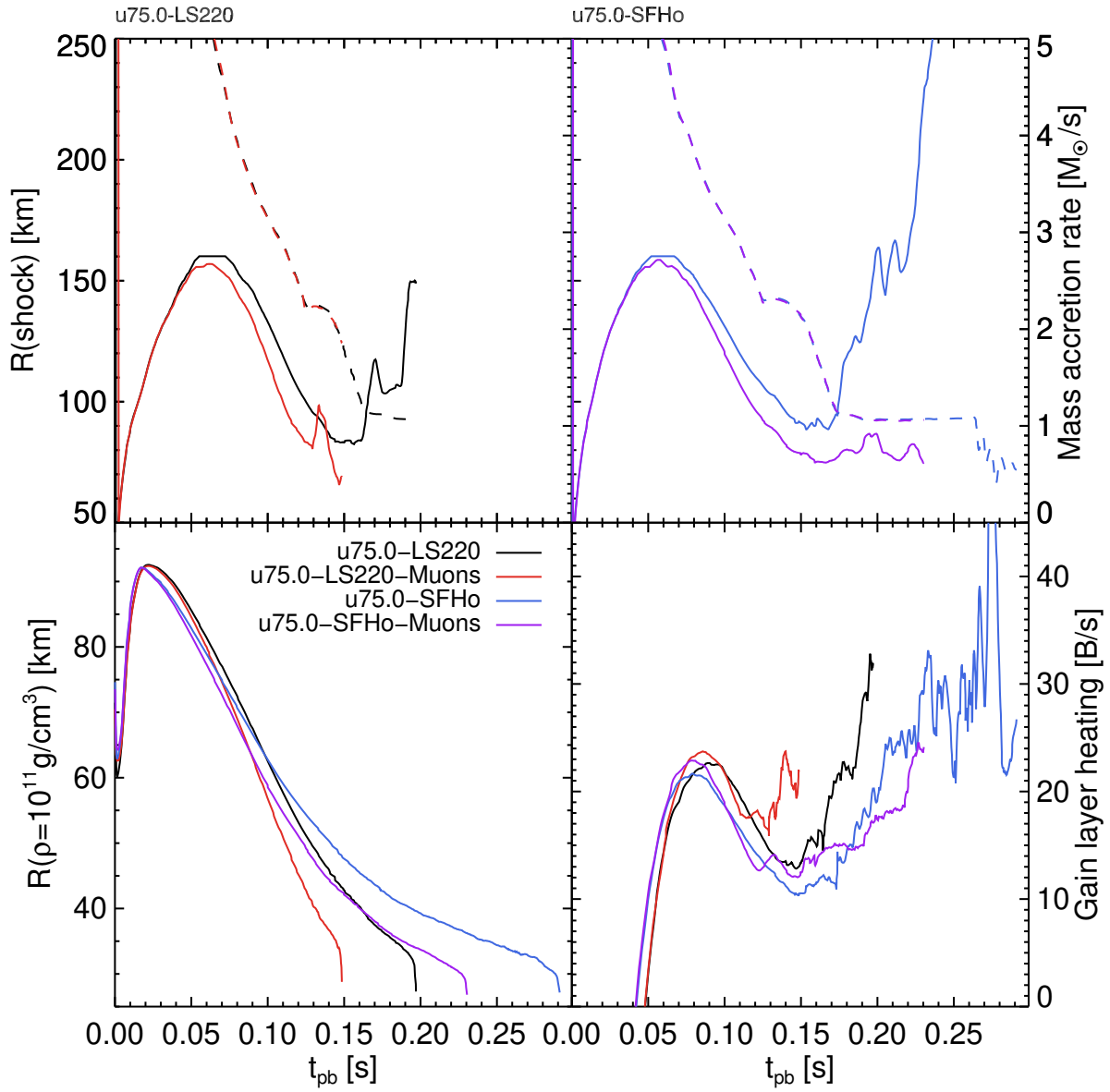

Figure 12.7: Plots of u75.0-LS220 and u75.0-SFHo radii evolution and gain layer heating as a function of time. The top left plot shows the shock radii of the u75.0-LS220-standard case in black and the u75.0-LS220-muons case in red. The dashed lines are the corresponding mass accretion rates. On the right, the plot content is identical to the left plot, except the u75.0-SFHo-standard case in blue and the u75.0-SFHo-muons case in purple is depicted. The lower left plot shows the PNS radii of the four mentioned models; the right plot shows the volume-integrated neutrino net energy source term over the gain layer as in Eq. 11.21.

Muon number The total energy contained in the muonic gas in the PNS of model u75.0-LS220-muons in Fig. 12.8 shows continuous growth, reaching up to 80 bethe before BH collapse, equivalent to $\sim 0.045 M_\odot$ in extra gravitational mass. This means there is about as much energy stored in the muonic gas as has been lost in the form of neutrino radiation up to the collapse. This can explain the more rapid collapse of the protoneutron star, as thermal energy is continuously converted into fresh muon pairs and net muons, drastically reducing thermal pressure support. The PNS, therefore, reaches its last stable configuration much earlier than if it had to wait for energy loss by neutrinos to reach the same point. The net muon number in the PNS is in fact produced so fast that the $\overline{\nu}_\mu$ number is not lost fast enough. The net muon flavor number, i.e., $Y_\mu = Y_{\mu^-} + Y_{\nu_\mu}$ in the PNS is accordingly significantly smaller than the net muon number, as shown in Fig. 12.9. The net muon number in the star is therefore suppressed by neutrino back-reactions, and beta-equilibrium is not reached. We would, therefore, expect our beta-equilibrium comparison run in Sec. 12.3 to exhibit even faster collapse.

It would be instructive in future studies to isolate the effect of loss of thermal pressure support compared to prolonged accretion, by artificially quenching mass accretion once both models have exceeded an identical fixed baryonic mass. As the PNS in the u75.0-LS220-standard case continues to accrete a further $0.05 M_\odot$, it is not possible to ascertain whether the standard case could maintain thermal pressure support even longer if the final baryonic mass were identical to the muonic case.

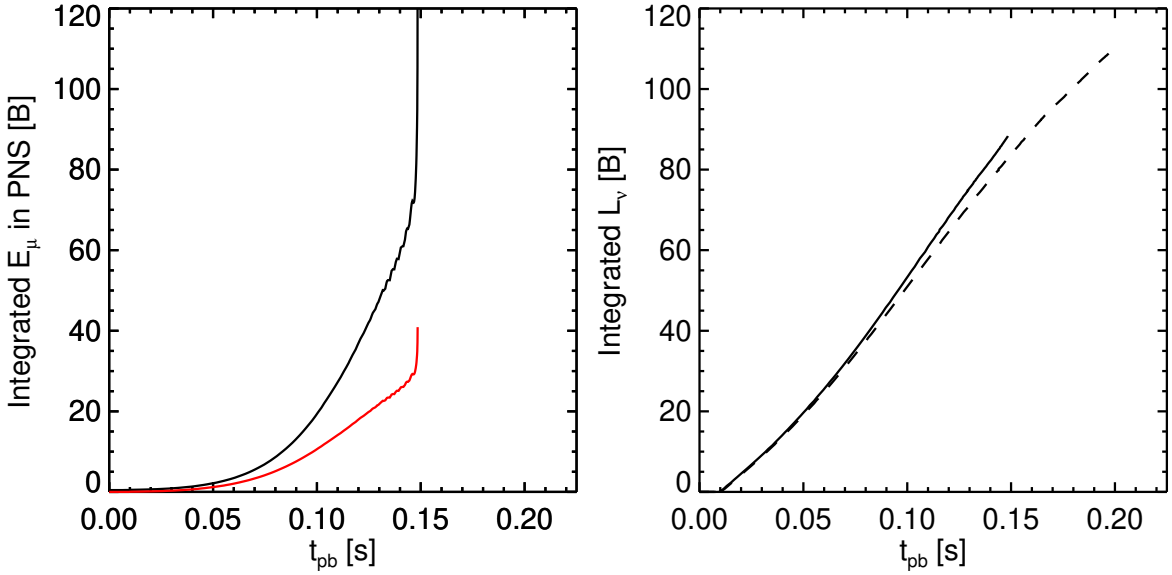

Figure 12.8: On the left, the total internal plus rest mass energy contained in the muonic gas inside the PNS given in bethe for model u75.0-LS220-muons as a function of time; on the right, the time-integrated and summed neutrino luminosity. The red line on the left plot is the pure muon rest mass energy; the dashed line on the right is model u75.0-LS220-standard.

Neutrino signal The neutrino signal is obviously cut short by the early onset of collapse, but the rapid PNS contraction strongly increases both the neutrino luminosity as well as the mean energy, as shown in Fig. 12.10. The ν_e luminosity shows an increase of ~ 10 B/s, while the ν_μ and $\overline{\nu}_\mu$ show an increase of ~ 5 B/s and ~ 20 B/s respectively. Note that the standard case only transports a single averaged heavy-lepton neutrino and therefore does not exhibit a spectral splitting due to weak magnetism effects. A realistic increase, compensating for weak magnetism, is therefore closer to ~ 10 B/s and ~ 15 B/s respectively. The same holds true for the ν_τ and $\overline{\nu}_\tau$ luminosity, showing an increase of ~ 5 B/s and ~ 15 B/s respectively. The true value

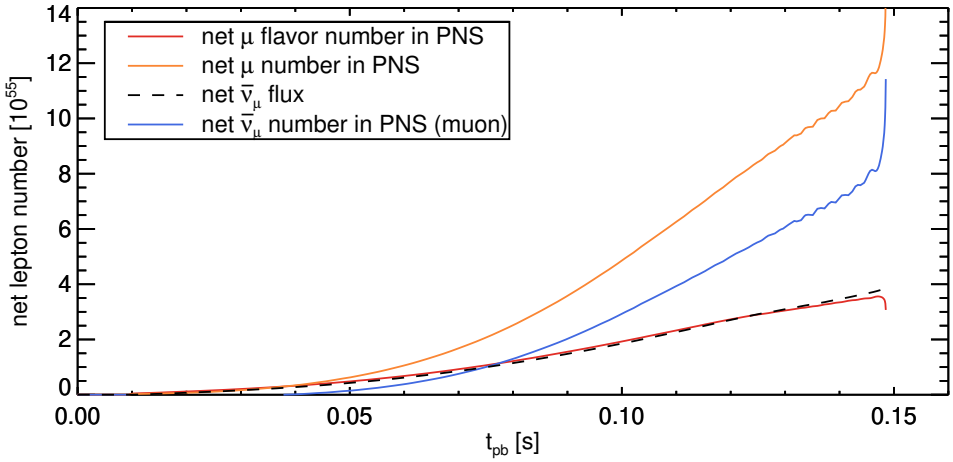

Figure 12.9: Plot of the volume integrated net muon flavor number contained in the PNS of u75.0-LS220-muons in red defined by $\mathcal{N}_\mu = 4\pi \int_0^{r_{\mathrm{PNS}}} \mathrm{d}r\, r^2 \left\{\rho/m_{\mathrm{B}} Y_\mu + \mathcal{N}_{\nu_\mu} - \mathcal{N}_{\bar{\nu}_\mu}\right\}$, where $\mathcal{N}_\nu$ are the local neutrino number densities. The cumulative time integrated net $\bar{\nu}_\mu$ number flux $\mathcal{L}^{\mathrm{net}}_{\bar{\nu}_\mu} = 4\pi r^2 \int_0^t \mathrm{d}t \left\{\mathcal{L}_{\bar{\nu}_\mu} - \mathcal{L}_{\nu_\mu}\right\}$ is plotted in black dashed lines; the net muon number $\mathcal{N}_{\mu^-} = 4\pi \int_0^{r_{\mathrm{PNS}}} \mathrm{d}r\, r^2 \left\{\rho/m_{\mathrm{B}} Y_\mu\right\}$ is plotted in solid orange lines.

should be closer to $\sim 10\,$B/s for both. A new effect by the addition of muons is a sudden sharp increase of the luminosity just as the PNS becomes unstable and begins its collapse. As this also occurs for the τ neutrinos, this effect is not caused by any rapid muonization or demuonization alone. Furthermore, as the neutrinos are trapped and dragged with the collapsing PNS, any changes in the deep PNS cannot propagate to the surface in time. A similar effect was already observed in Refs. [34, 72], and was attributed to a shift of the main heavy-lepton neutrino production sites to lower densities where emission properties are more beneficial. Analysis of the temperature profiles at the time of the collapse to a BH of each case shows a temperature dip at the PNS surface relative to the surrounding matter in the standard case, compared to no dip and constantly increasing temperature in the muonic case. The cause of this is simply that in the muonic case the PNS contraction outpaces the energy loss by neutrinos, as the PNS mantle does not shrink by the emission of neutrinos but by progressive softening of the EOS. At the point in time when the PNS begins its collapse to a black hole, the shock reaction is delayed compared to the rapid PNS contraction and the distance between shock and PNS surface increases. As the entire post-shock volume is a cooling layer for heavy-lepton neutrinos, an increase of this volume leads to a larger volume-integrated neutrino emission. Furthermore, as there is no temperature dip at the PNS surface and the luminosity scales roughly with $L_\nu \propto T^4$, the increased volume at higher temperatures can lead to a disproportionate gain in luminosity. Similarly, the mean energies of ν_{e} and $\bar{\nu}_{\mathrm{e}}$ show an increase of $\sim 1-1.5\,$MeV on average during collapse, as their neutrinospheric temperature increases. The mean energies of the heavy-lepton neutrinos show a significantly larger increase of $\sim 2-3\,$MeV, as their number and energy sphere lie deeper in the PNS.

The enhanced neutrino luminosity is, however, only able to increase the total emitted neutrino energy by 6 B in the 50 ms left until collapse, as shown in Fig. 12.11. The extra gravitational energy liberated by the PNS contraction is instead mostly stored in the muon gas, outstripping the additional neutrino energy loss by more than one magnitude, cf. Fig. 12.8.

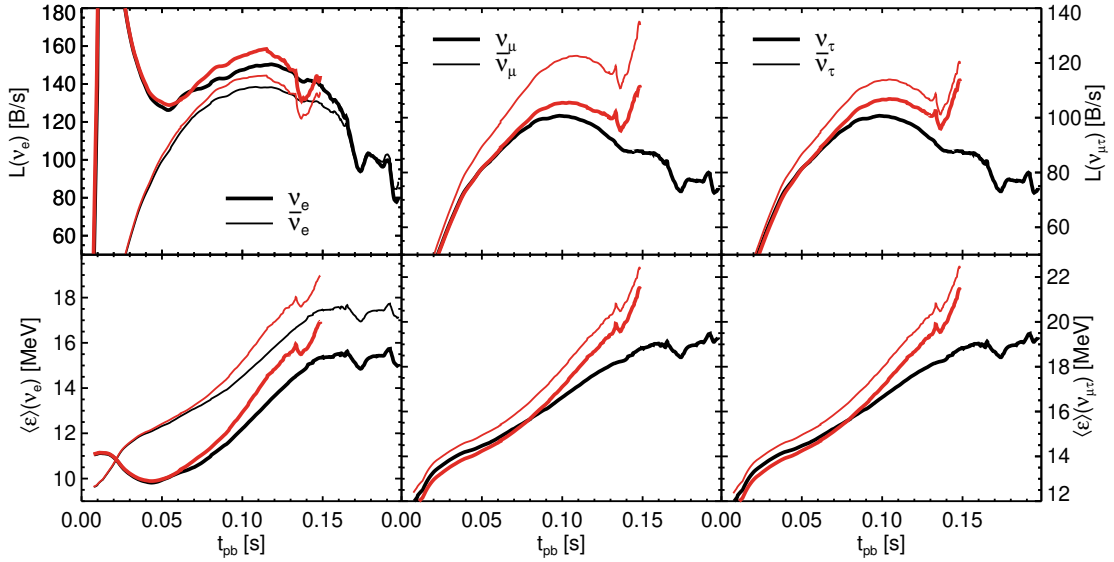

Figure 12.10: The evolution of the lab-frame neutrino luminosity in the top row and the mean neutrino energies in the bottom row, evaluated at a radius of 400 km. The red lines are the u75.0-LS220-muons case; the black lines are the u75.0-LS220-standard case. The thick lines are for the ν, and the thin lines are for the $\bar{\nu}$ of each neutrino flavor. Note that for the u75.0-LS220-standard case there exists only a single averaged heavy-lepton neutrino representing both μ and τ neutrinos.

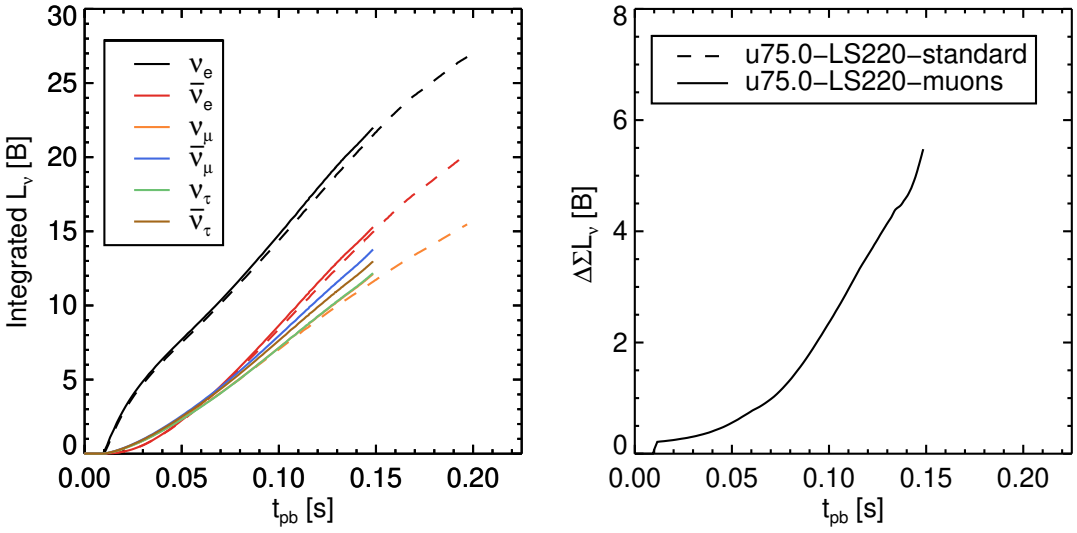

Figure 12.11: On the the left, the cumulative time-integrated energy emitted by each neutrino species for model u75.0-LS220-muons in solid lines and model u75.0-LS220-standard in dashed lines. Note that u75.0-LS220-standard only has a single heavy-lepton neutrino as in Fig. 12.10. On the right, the difference of the total emitted neutrino energy calculated by $\Delta \int_t \sum_\nu L_\nu = \int_t \sum_\nu L_\nu^{\text{muons}} - \int_t \sum_\nu L_\nu^{\text{standard}}$.

12.2.3 Snapshots

Radial profiles of select quantities immediately before BH collapse of model u75.0-LS220-muons are shown in Fig. 12.12. The net muon fraction is still mostly compensated for by the net ν_μ fraction as shown in Fig. 12.9, and the net lepton fraction of the muon and standard case are very similar to each other. Notably, the electron neutrino fraction becomes negative and decreases the net lepton fraction of the standard case. Neutrino transport is therefore not fast enough, as shown in the previous sections, to efficiently transport even electron lepton number away from the PNS.

The temperature and density profiles in Fig. 12.13 show that the PNS of both the standard case and muonic case are very similar to each other at the moment when the gravitational instability of each PNS occurs. This similarity is a result of the unchanged high-density nucleonic pressure support. Note that the temperature in the standard case is larger at the point of collapse, as the PNS had more time to redistribute energy inside the PNS via convection and neutrino transport. The reduced accretion rate and longer collapse time scale of the standard case also allows the extended mantle to contract further against the stabilizing dense PNS core, leading to a steeper density profile.

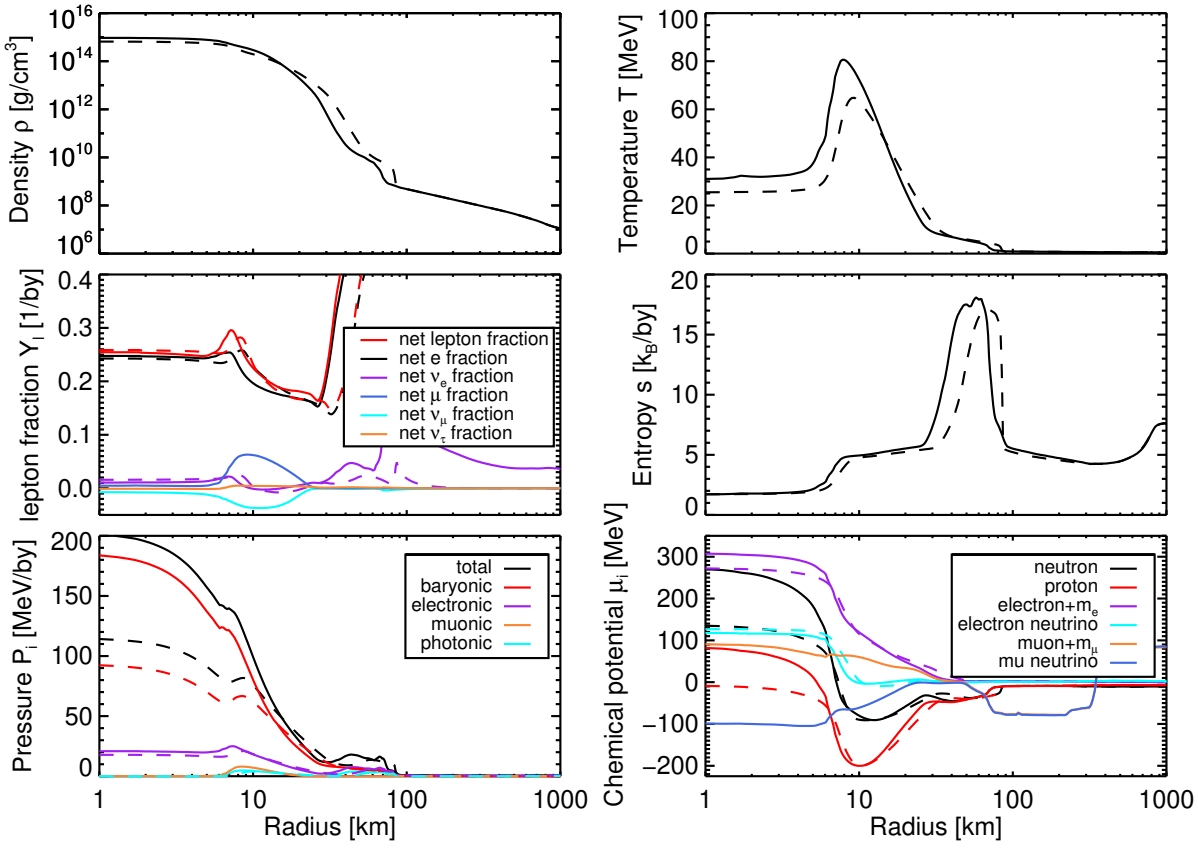

Figure 12.12: Profiles of case u75.0-LS220-muons in solid lines and u75.0-LS220-standard in dashed lines at 4 ms pre-BH collapse of the muonic case at $t_{\rm pb}^{\rm muons} = t_{\rm pb}^{\rm standard} = 148\,{\rm ms}$. The plots are displayed as a function of the logarithmic radial coordinate from 1 km to 1000 km, to capture both the PNS as well as the gain layer and pre-shock region. Note that the standard case does not have any net heavy-lepton neutrino number as there is only a single averaged neutrino.

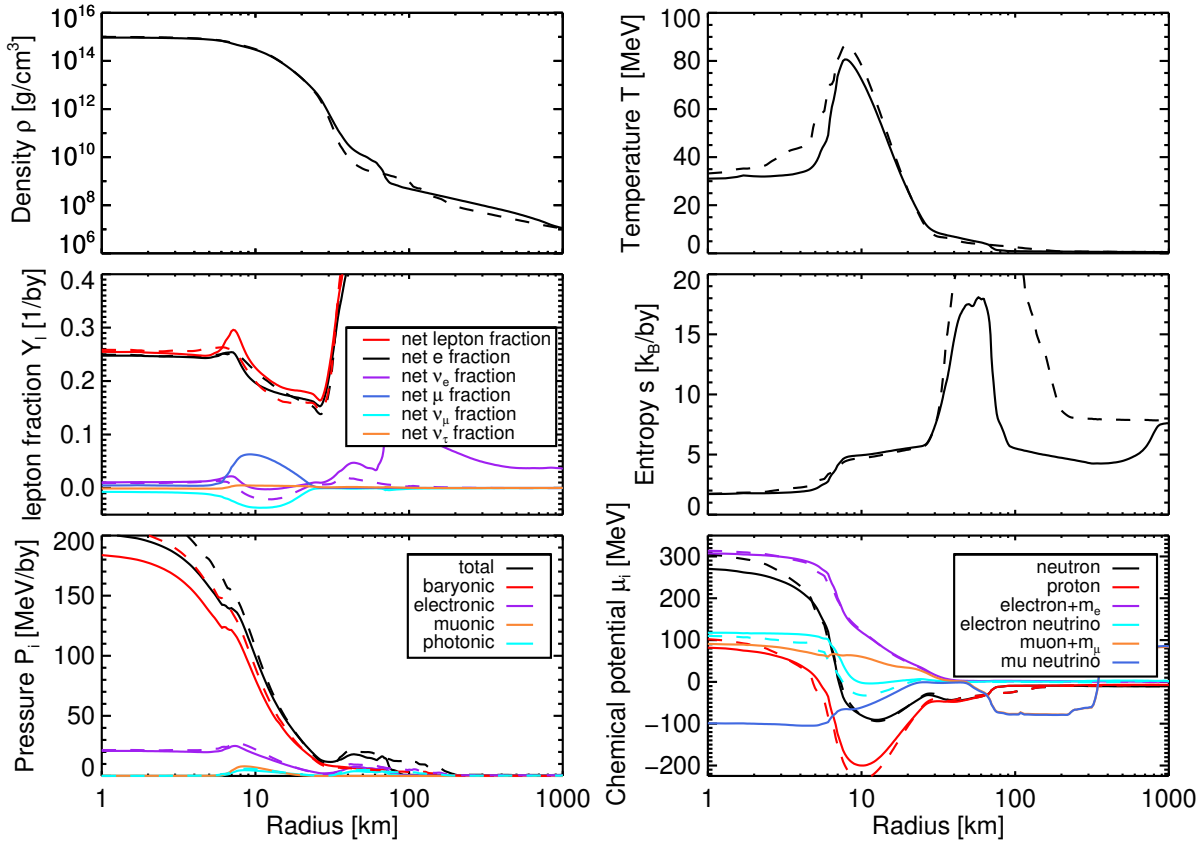

Figure 12.13: Profiles of case u75.0-LS220-muons in solid lines and u75.0-LS220-standard in dashed lines at 4 ms pre-BH collapse of each case at $t_{\rm pb}^{\rm muons} = 148$ ms and $t_{\rm pb}^{\rm standard} = 193$ ms respectively. Plot content is as in Fig. 12.12.

12.2.4 Summary

Calculations of black hole formation have long been performed in 1D, but current state-of-the-art simulations have recently progressed to two-dimensional calculations. An interesting property is that many of these calculations show shock expansion shortly before the BH collapse of the s40.0 progenitor of the 2007 Woosley&Heger model set explored in Refs. [104, 19]. We can confirm these findings here also for the u75.0 progenitor of the 2002 model set using the standard physics case. Even though the mass accretion rate still exceeds $1M_{\odot}$/s, it can achieve shock expansion before the final collapse to a black hole for both the examined LS220 EOS and SFHo EOS. Adding a self-consistent treatment of muonization into the calculations however changes these results, as BH collapse is reached before the Si-O Interface and the concomitant rapid drop in mass accretion rate can arrive. These results are in accordance with preliminary simulations in Ref. [107], who have simulated an LS220 EOS supplemented by an ideal Bose-gas of pions and they saw a similar shortening of the collapse timescale.

We find in our simulations that the time to BH collapse is reduced by roughly $\sim 50-60\,\mathrm{ms}$ when adding muonization, compared to the standard case with only neutrons, protons, and electrons. This decrease in collapse timescale is caused by the extremely rapid contraction of the PNS, aided by the addition of muons. Compared to the lighter progenitors explored in the preceding section, the PNS never enters a steady-state between neutrino cooling and contraction. Instead, it remains highly dynamic in a rapid contraction that liberates gravitational binding energy faster than neutrino radiation can react. The temperature inside the PNS continually increases during the accelerated contraction, compared to the standard case, but a significant amount of the released energy is stored in the form of muon rest mass in the muonic gas. Muons are therefore a massive net sink of internal energy, which do not contribute significantly to the stabilization of the PNS. In fact muons, due to their large mass of$\sim 10\%$ of the nucleon mass, actually act gravitationally on the collapse. During the accretion phase, the useful energy being lost in the form of neutrinos is not significantly increased compared to the standard case and in fact, the trapped μ neutrino number is lost too slowly compared to the rate of muon production. The resulting net muon flavor number in the PNS therefore remains close to zero and muon production is suppressed by back-reactions. An additional feature of the muonic case is a peak both in luminosity and mean energy at the moment of gravitational collapse, caused by the effect of the rapid PNS contraction not being balanced by increased neutrino luminosity. The changed temperature stratification in the post-shock layer leads to a disproportionately large increase in temperature at the heavy-lepton neutrino production sites.

In conclusion, muons are shown to be an important addition to the simulation of failed core-collapse supernovae. Their appearance modifies both the measurable neutrino signal as well as the stability of the thermally stabilized hot PNS before their collapse. They are therefore also relevant for the case of NS-NS merger events where similar temperatures and conditions can be reached during the brief lifespan of the massive merger remnant. Muons, therefore, must be treated consistently in BH formation simulations and may thereby also influence the diffuse supernova neutrino background.

12.3 BH collapse with muons in beta-equilibrium

As in Sec. 11.3, we will again look at whether the muonization of the PNS can be modeled by a muon gas that is assumed to be in strict beta-equilibrium, i.e., $\mu_\mu = \mu_\mathrm{e} = \mu_\mathrm{n} - \mu_\mathrm{p}$ at all times. As the PNS in the rapid collapse scenario presented in Sec. 12.2 remained far from beta-equilibrium, and there was a substantial trapped $\overline{\nu}_\mu$ number suppressing net muon formation, we would expect the equilibrium treatment to vastly overstate the net muon number in the PNS. The net muon number, however, might not be a critical factor at extremely high temperature. Instead, the number of muon-antimuon pairs created by the large thermal energy might be dominant. This would reduce the relative influence of net muon number on the dynamics, and the PNS might behave similar as in the full muonic calculation. As in Sec. 12.2, the assumption that any net heavy-lepton neutrino number can escape the PNS unhindered and muon production is efficient, is maintained by simulating only the single averaged heavy-lepton neutrino. The condition $\mu_{\nu_\mu} = \mu_{\nu_\tau} = 0$ is then automatically fulfilled at all times, while neglecting lepton flavor number conservation.

12.3.1 Comparisons

The new beta-equilibrium muon fraction model will be called u75.0-SFHo-μbeta, and has a collapse time of $t^{\mu\,\mathrm{beta}}_{\mathrm{pb,SFHo}} \approx 226\,\mathrm{ms}$. The final baryonic mass of the PNS is $2.534 M_\odot$, and the final gravitational mass is $2.484 M_\odot$. These values fit the full calculation well, with only a slightly earlier collapse. The shock radius evolution in Fig. 12.14 shows significant deviation, with shock revitalization happening at the same time as in the standard case of Fig. 12.7. The full muon calculation shows no sign of shock revitalization, even though the gain layer heating rates are favorable compared to the standard case. This might be the result of 2D stochasticity or differences in the PNS structure. The PNS itself initially shows slightly faster contraction, up to $\Delta r \approx 2\,\mathrm{km}$, until the initiation of shock expansion at $t_\mathrm{pb} \approx 150\,\mathrm{ms}$ quenches the mass accretion onto the PNS and contraction slows down. For the PNS to contract faster, more thermal energy needs to be stored in the muon gas as shown in Fig. 12.15. The difference of energy contained in the muon gas between the full muon physics case in dashed and the μbeta case in solid lines rapidly grows to more than 30 bethe, while the neutrino luminosity remains unchanged compared to the full physics case. The maximum temperature inside the PNS is slightly hotter in the μbeta case by $\sim 2\,\mathrm{MeV}$ as shown in Fig. 12.16, indicating that still more gravitational energy has been liberated than absorbed in the muon gas. This might be helped by the additional reduction of degenerate electron neutrinos, as more of the negative charge is provided by muons. The net muon number contained in the PNS has grown by nearly a factor of two in Fig. 12.17 compared to the full physics case. As the energy contained in the muon gas only raises by a factor of ~ 1.6, and temperature is also still somewhat increased, there must be a significant pair contribution to the muon gas.

12.3.2 Summary

In this section, we have compared the results of a simple strict beta-equilibrated muon approximation to our full physics set as in Sec. 11.3 for the case of BH formation. We have seen that the initial premise of beta-equilibrium is never fulfilled, as there is a significant trapped μ neutrino number inside the PNS that would otherwise suppress muon production. Nonetheless, as the temperatures inside the unstable PNS rise above the muon pair-production threshold, the accurate determination of net muon number is subdominant compared to the vast amount of energy stored in the muon pairs. The overall behavior of the protoneutron star is therefore somewhat similar and thermally dominated.

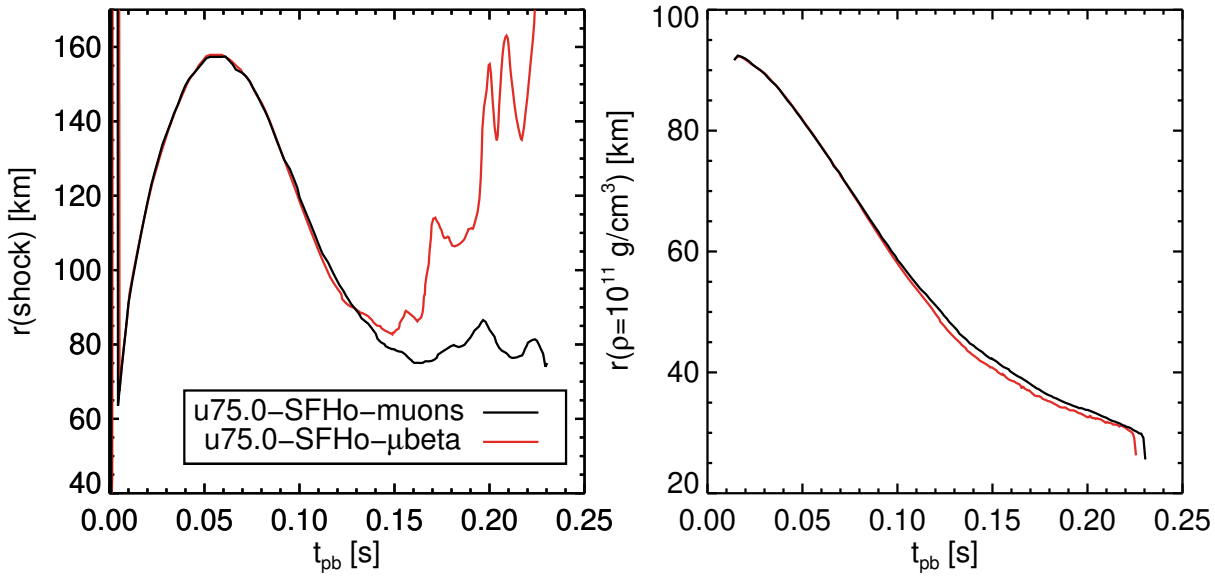

Figure 12.14: On the left, the shock radius of u75.0-SFHo-μbeta in red and u75.0-SFHo-muons in black; on the right, the PNS radius with the same color assignments as on the left.

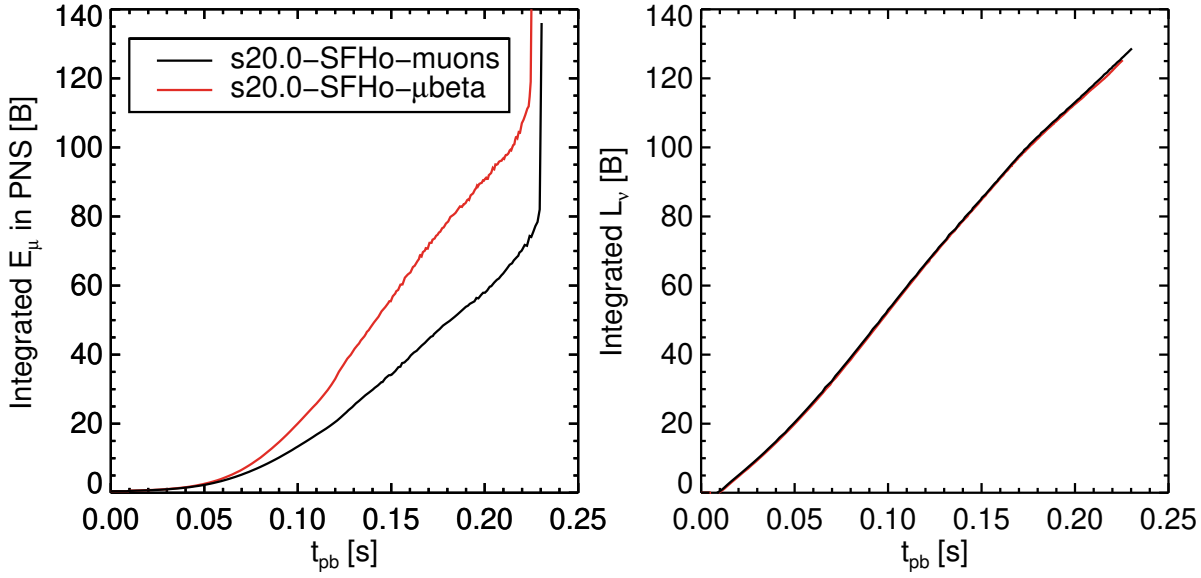

Figure 12.15: On the left, the total internal plus rest mass energy contained in the muonic gas inside the PNS given in bethe for model u75.0-SFHo-μbeta in black and u75.0-SFHo-muons in red; on the right, the time-integrated and summed neutrino luminosity.

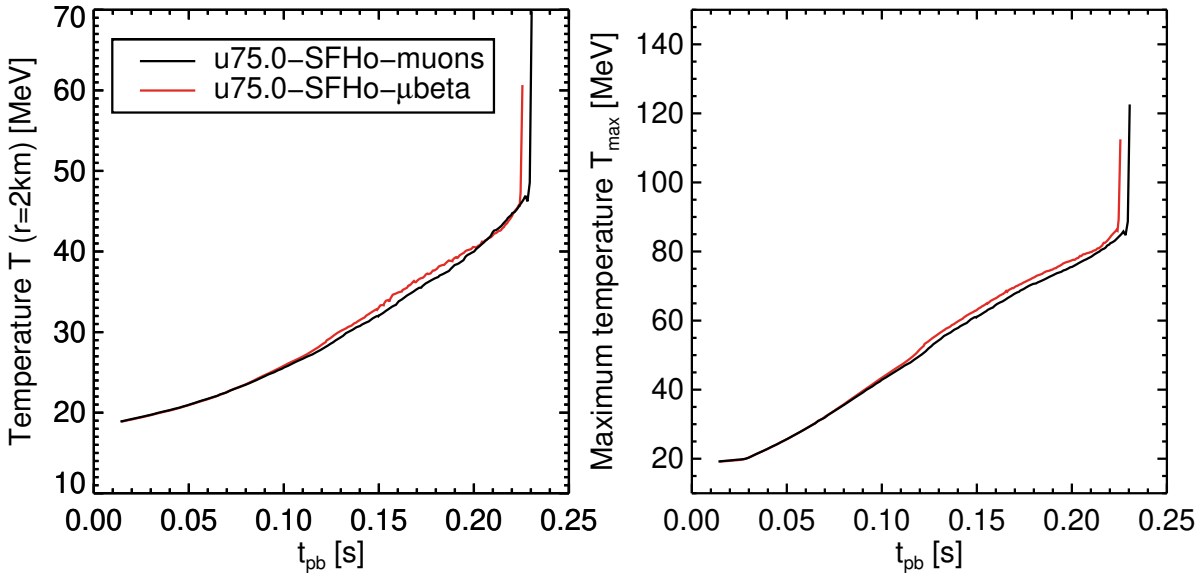

Figure 12.16: On the left, the central temperature of u75.0-SFHo-μbeta in red and u75.0-LS220-muons in black; on the right, the maximum temperature inside the PNS with the same color assignments as on the left.

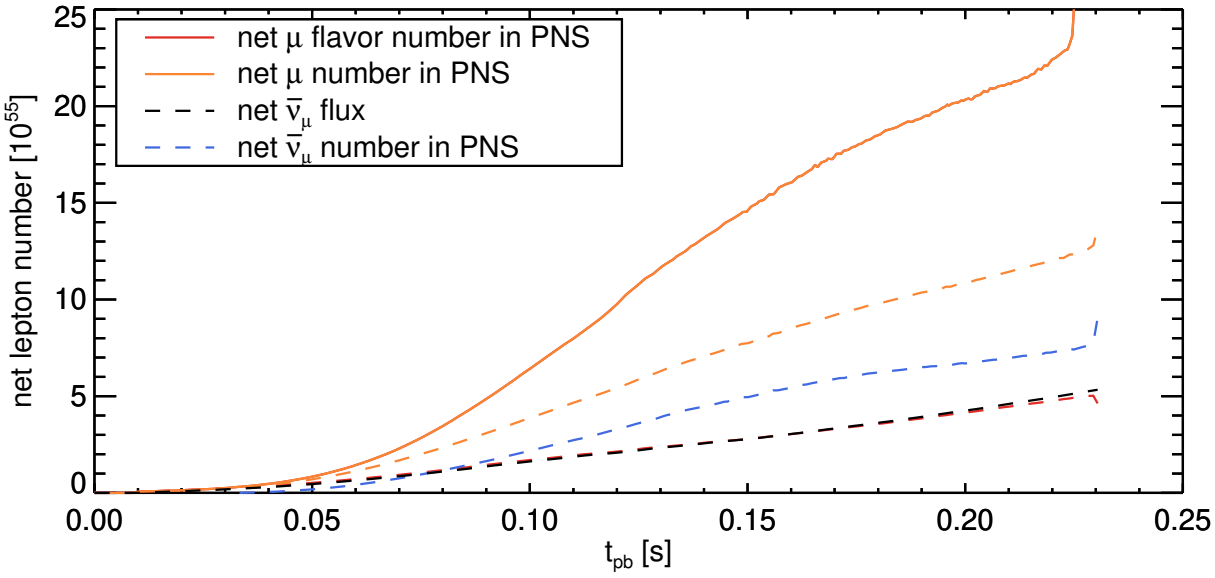

Figure 12.17: Plot content is as in Fig. 12.17, but here the solid lines are for case u75.0-SFHo-μbeta and the dashed lines are for case u75.0-SFHo-muons.

Chapter VII
Conclusions

In this thesis, we have performed the first self-consistent implementation of a second family of charged leptons, i.e., of muons, into the core-collapse supernova simulations, including the necessary full coupling between neutrino transport and hydrodynamics. While the eventual appearance of muons in beta-equilibrium in neutron stars is part of the standard theoretical picture of cold neutron stars (cf. static NS profiles in Ref. [109]), there has been no previous effort of investigating the feedback between ongoing muonization and the dynamical evolution of supernovae and hot protoneutron stars.

Here we have improved on the beta-equilibrated picture of muonic effects, only valid for cold and neutrino-transparent neutron stars, by also taking the lepton number evolution, constrained by conservation equations, fully into account. This requires, in contrast to the beta-equilibrated approach, a direct coupling between the appearance of a net number of muons and the corresponding opposite change in net number of μ-flavor neutrinos, whose evolution requires a transport description. The benefit of this more involved treatment is that it allows us to track muonization in phases where neutrino feedback cannot yet be neglected. This is a prerequisite to investigating the muonization of a protoneutron star from the moment of birth to cold beta-equilibrium conditions, without requiring any prior assumptions on the muon or μ neutrino chemical potential.

Developing an arbitrary muon fraction in the protoneutron star requires the implementation of a new lepton equation of state into general-purpose high-density baryonic equations of state currently available. As the thermodynamics of noninteracting ideal leptons are largely independent of those of baryons (Ref. [70]), we can easily extend any purely hadronic equation of state to an arbitrary distribution of charge balance between the positive charge carriers, e.g., protons, Σ^+ or π^+, and the leptonic negative charge carriers of electrons and muons. As expected from experience with equations of state developed explicitly for cold beta-equilibrated neutron star matter, our modified general-purpose equations of state still fulfill the observational mass constraint of pulsar PSRJ0348+0432 (Ref. [3]). This is expected, because muons only increase the leptonic degrees of freedom, but leave the hadronic degrees of freedom unchanged. Protoneutron stars at birth, however, are surrounded by an extended hot mantle, supported by degenerate electron and thermal nucleon pressure support. Muons, with their large rest mass, can "soften" the equation of state in the sensitive mantle region, and alter the evolution of the hot protoneutron star during the crucial initial second of a core-collapse supernova. Compared to other possible additional particle degrees of freedom, the muon contribution has no theoretical uncertainties and remained the next logical step in extending the current treatment of the description of matter around nuclear saturation density.

To investigate the muonization of protoneutron stars, we have extended the well-tested neutrino radiation-hydrodynamics code Prometheus-Vertex to solve the transport equations of all six neutrino species, and added new evolution equations for the muon number with corresponding muon neutrino sourceterms; the necessary number and energy source terms associated with muons are implemented for particles of arbitrary mass and degeneracy. The hurdle of the large muon rest mass, requiring a minimum incoming neutrino energy, can be overcome in the presence of high temperature, large electron chemical potential, and with nuclear self-interaction potential differences characteristic of neutron stars. The opacity set extended by the muon beta-processes, lepton flavor exchange, lepton flavor conversion and inverse muon decay, allow muon interactions at nearly any incoming neutrino energy above a matter density of $\rho \sim 10^{12} - 10^{13}$ g/cm^3. Muon beta-reactions are shown to be most effective close to saturation density and high temperatures, where muons become most abundant. Towards

lower densities, the purely leptonic processes of flavor exchange and conversion can harness the considerable electron chemical potential, and assist μ-flavor neutrinos, and to some extent also $\overline{\nu}_{\mathrm{e}}$, to stay in chemical equilibrium. The still present process of inverse muon decay sets a base floor opacity for muon creation, as it is nearly independent of incoming neutrino energy and mostly depends on the electron chemical potential; in addition, it performs the natural process of muon decay. We find these new opacities to efficiently drive the muon and μ-flavor neutrino phase space distributions to their equilibrium spectra.

Using the modified PROMETHEUS-VERTEX code, we examined the process of muonization in spherically symmetric (1D) and axisymmetric (2D) models of stellar core-collapse evolution to explosion or black hole formation and obtained the following results.

1. We found that the production of muon number effectively softens the EOS in the density and temperature domain most sensitive to modifications in the leptonic sector. The protoneutron star is found to contract more rapidly in the case where muons are included, as thermal pressure and electron degeneracy are continuously reduced by converting energy into inert muon rest mass; furthermore, the equilibrium isospin asymmetry is shifted to slightly more proton-rich conditions, as the reduction of μ_{e} leads to a larger beta-equilibrium $\mu_{\mathrm{p}} = \mu_{\mathrm{n}} - \mu_{\mathrm{e}}$[①], and the increased negative charge fraction required for charge neutrality is provided by muons with $\mu_{\mu} \leq \mu_{\mathrm{e}}$. Since the nuclear pressure around saturation density depends on the isospin asymmetry parameter J according to $P \propto (1 - 2Y_{\mathrm{p}})^2 J$, an increased proton fraction reduces the available pressure. This process begins as early as 100 ms post-bounce. The faster contraction of the protoneutron star mantle increases the temperature at the neutrinospheres, leading to an increase of the mean energies of all neutrinos by $\sim 1\,\mathrm{MeV}$.

2. The muonization of the protoneutron star proceeds efficiently in the mantle region below nuclear saturation density, as neutrinos can escape efficiently and Pauli-blocking is negligible. This results in a considerably enhanced net $\overline{\nu}_{\mu}$ number flux that is the largest observable signature of the muonization, as demanded by muon lepton number conservation. The muonization of the inner core of the PNS above saturation density is, however, suppressed by strong back-reactions of highly degenerate ν_{e} and the long trapping of a large number of $\overline{\nu}_{\mu}$. The result is that the muon chemical potential reaches and stays very close to beta-equilibrium $\mu_{\mathrm{e}} = \mu_{\mu}$ in the PNS mantle after only a few milliseconds post-bounce, but remains far from beta-equilibrium in the PNS core during the explosion phase. The inner core only achieves full muonization after several ten seconds of post-explosion PNS cooling.

3. The increased luminosity and mean energy of all neutrinos, by the developing muonization, can influence the critical accretion phase and can make conditions more favorable to explosions. In multi-dimensional (2D) simulations, the muonic model shows an earlier explosion time for the LS220 baryonic equations of state. In the case of the "stiffer" SFHo EOS, the effect of muonization is even able to lift a model above the explosion threshold, turning a dud without muons into a successful explosion. The genuinely multi-dimensional hydrodynamic motions, which increase the matter dwell time[②] compared to the 1D case, remain a crucial ingredient, as the effect of muonization on the shock dynamics stays marginal in 1D. Whether the beneficial influence of muonization carries over into full 4π simulations (3D) remains to be investigated, but the successful 2D results give hope that muons might provide a needed boost to reach the critical luminosity condition also in 3D (cf. Ref. [128]).

[①] $\mu_{\mathrm{n}} - \mu_{\mathrm{p}} \approx 4(1 - 2Y_{\mathrm{p}})^2 J(T, \rho)$ (Ref. [32]) further links the chemical potential difference to the proton fraction Y_{p} and symmetry energy J, which leads to Y_{p} being anticorrelated to μ_{e} in beta-equilibrium.

[②] The time a fluid element spends in the neutrino heating layer.

4. We have further examined the influence of muonization during the Kelvin-Helmholtz phase; i.e., the cooling period of $\sim 20\,\mathrm{s}$ from a hot thermally supported extended PNS to a warm, compact, nuclear pressure supported quasi-NS. We find the appearance of muons to strongly modify the temperature evolution of the protoneutron star during the deleptonization phase, i.e., during the loss of trapped electron neutrino number, because a fair fraction of the electron degeneracy energy is converted into inert muon rest mass rather than being transformed into thermal energy. When the PNS reaches beta-equilibrium with respect to electron neutrinos, i.e., $\mu_{\nu_e} \approx 0\,\mathrm{MeV}$, it still has very high temperatures and continues to lose charged lepton number while it cools due to neutrino emission; reason being that the equilibrium proton-fraction typically decreases with matter temperature. The muon fraction, produced at high temperatures at the end of the deleptonization phase, stores a large part of the liberated electron degeneracy energy. As some of these muons decay, their stored kinetic and large rest mass energy will be released in the form of high energy neutrinos and electrons. In this way, the muon gas acts as an energy "battery" that is rapidly charged during the initial deleptonization phase, and slowly discharged during the following cooling phase. Accordingly, we find muonization to uniformly increase the luminosity and mean energy of all neutrinos in the cooling phase after 10 s of post-bounce time.

5. The degree of muonization depends sensitively on the temperature evolution of the PNS and thereby also on the mass accretion rate. Progenitors with massive iron-cores and high core compactness correspondingly favor muon formation compared to progenitors with less compact cores. Progenitor stars of failed supernovae, which collapse to black holes already during the accretion phase, therefore, show a significant influence of muonization on the lifetime of the doomed thermally stabilized protoneutron stars forming at their center. In the examined case of an ultra-low metallicity $75M_\odot$ progenitor, the lifetime of the central protoneutron star is only on the order of $\sim 200\,\mathrm{ms}$ and radiative neutrino energy losses are inefficient. The continuously growing temperature of the protoneutron star leads to abundant thermal production of muon-antimuon pairs acting as an additional energy sink. As the collapse timescale is too short for neutrino diffusion from the muon-producing regions to be efficient, the production of net muon number is suppressed by the trapped large $\overline{\nu}_\mu$ number, and the initially vanishing net μ-flavor number is maintained nearly up to collapse. This means that increased additional total energy loss by neutrino radiation does not accelerate the collapse, but rather the aforementioned production of thermal muon pair rest mass does. The effect of muonization on the stability of such hot protoneutron stars, in this case, is similar to the initial collapse of very massive ($\gtrsim 100M_\odot$) stars by the electron-positron pair-instability, in which stabilizing thermal energy is rapidly converted into electron pair rest mass. This instability is self-reinforcing, as the muon pairs continually drain thermal pressure support from the contracting protoneutron star, which leads to further contraction. Accordingly, the muonic case reaches the point of gravitational instability $\sim 50\,\mathrm{ms}$ earlier than the nonmuonic case, with a correspondingly earlier shut off of the neutrino signal.

Having presented the results of typical scenarios encountered in core-collapse supernovae, we have challenged the standard assumption of muons being irrelevant in the early phase of stellar core-collapse and supernova explosions. Muons are shown to macroscopically impact the evolution of hot protoneutron stars already shortly after birth and not only late in their cooling evolution as previously assumed. The formation of a muon gas can be seen as assured, as the matter temperature and electron chemical potential practically force their presence from simple energetic considerations. These environmental factors leading to muon formation are not limited to the CCSN scenario, but include all events which form similarly hot neutron stars.

One possible further candidate scenario where muons might play a dynamically relevant role are NS – NS mergers. The temperature at the interface of the two colliding NSs can easily exceed the threshold temperature for muon formation, and the possible hypermassive metastable NS remnant will have a stabilizing thermal pressure contribution. Whether the softening effects of a muonic component in the equation of state can shorten the lifetime of the centrifugally supported hot supra-massive or hypermassive neutron stars will require dedicated studies, but as seen for the case of BH collapse, the survival timescale of these hot metastable compact remnants might be shortened. These effects might affect the measurable future gravitational wave signals from future events, following the recent very first detection of a gravitational wave of a NS–NS merger in the case of GW170817 (Ref. [1]). Changes of the neutrino emission due to the presence of muons might also affect the nucleosynthesis and r-process conditions in the merger ejecta, which caused the kilonova (AT2017gfo; Ref. [30]) discovered in association with GW170817 and the accompanying gamma-ray burst (GRB1709817A; Ref. [29]). Since the formation of the heaviest elements in the universe, for which NS–NS mergers are currently considered as the most promising sources, sensitively depends on the final electron fraction in the ejecta, muons might also be interesting for scientists studying the nuclear processes in the merger ejecta (see e.g. Refs. [60, 135]).

As the inclusion of muons also leads to a nonzero chemical potential for the μ-flavor neutrinos, neutrino oscillations in CCSNe might be altered. Especially the increased flux of muon antineutrinos might be detectable in a measured electron antineutrino signal from a future galactic SN, as those have the largest detection probability in current neutrino detectors.

While implementing muons into current radiation-hydrodynamics codes can be cumbersome, their impact on the core-collapse scenario is of a similar magnitude as other considered theoretical uncertainties. Their effect on the "explodability" of core-collapse supernovae, however, requires further study in full 3D simulations, which remove the artificial effect of the symmetry axis of 2D models. This is, however, the subject matter for future work.

Appendix

A Implications of neglecting the electron rest mass for low-mass progenitors

The implementation of inelastic neutrino-electron scattering in VERTEX-PROMETHEUS in the formalism developed in ref. [139] for ultrarelativistic massless electrons is analytically exact in the scattering angle integration but neglects the rest mass of the charged lepton. Here we wish to show the errors that treating electrons as ultrarelativistic during all phases of a low-mass supernova progenitor collapse can cause, as well as the advantages of our new implementation of the NES scattering kernel including all rest mass terms introduced in section 6.1 for the particular case of the z9.6 progenitor by Woosley&Heger ([137]). This progenitor features a low-temperature extended envelope with temperatures where electrons become nonrelativistic. $\beta_\mathrm{e} = m_\mathrm{e}/T$ can give a measure of the degree of relativistic effects on electrons, where $\beta_\mathrm{e} \to 0$ implies that the particle has become ultrarelativistic and $E_\mathrm{e} \simeq p_\mathrm{e}$. On the other hand β_e of order unity and above require the correct relativistic energy dispersion $E_\mathrm{e} = \sqrt{p_\mathrm{e}^2 + m_\mathrm{e}^2}$, which for very low temperatures approaches the classical nonrelativistic case of $E_\mathrm{e} \simeq p_\mathrm{e}^2/2m_\mathrm{e}+m_\mathrm{e}$. Figure A.1 shows the initial temperature and β_e profiles of the z9.6 progenitor, where we can see that electrons quickly become nonrelativistic at relatively small radii, which are still inside the computationally relevant domain where the accurate calculation of neutrino source terms and opacities remain essential.

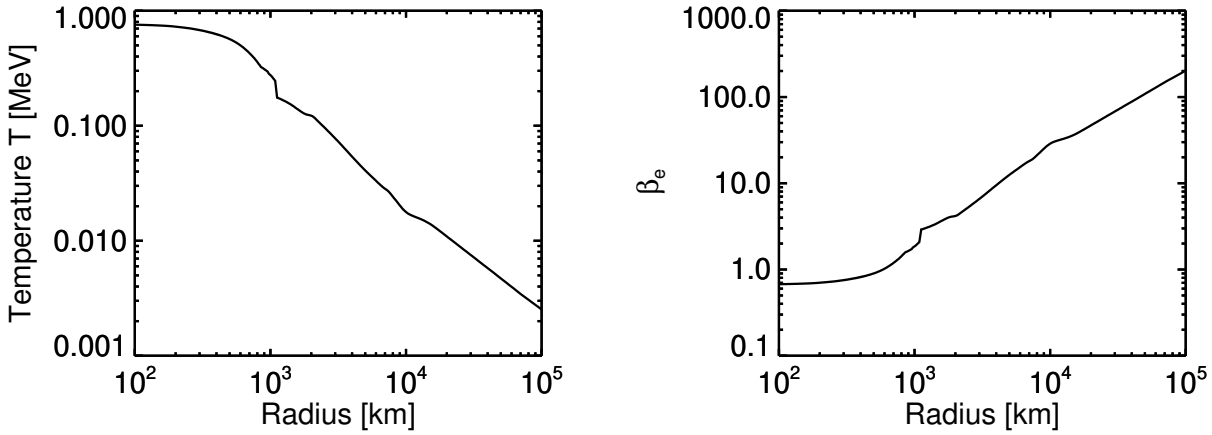

(a) Pre-collapse temperature in MeV.

(b) Pre-collapse parameter β_e.

Figure A.1: Initial profiles of z9.6 progenitor ([137]).

Neglecting the electron mass in the Fermi-Integrals appearing in the Yueh & Buchler ([139]) Legendre expansion typically used in most codes results in a significant overestimation of the electron number densities for regions where $\beta_\mathrm{e} > 1$. The reason for this can easily be understood by comparing the formulae for the number density of a Fermi-Dirac gas of an ultrarelativistic and nonrelativistic Fermi-Dirac gas.

The number density of an ultrarelativistic gas is proportional to

$$n_\mathrm{e}^\mathrm{UR} \propto \int_0^\infty \frac{E_\mathrm{e}^2}{\exp\left(\left(E_\mathrm{e} - \mu_\mathrm{e}\right)/T\right) + 1} \mathrm{d}E\,, \tag{A.1}$$

where the relativistic electron chemical potential $\mu_e = \mu_e^{kin} + m_e$ including rest mass is used, which for low temperatures converges towards the electron rest mass. As E_e here itself does not contain any term accounting for the electron rest mass, the relativistic chemical potential causes the Fermi-Dirac distribution to appear fully degenerate at low-temperatures, resembling a constant electron number density regardless of the physical density. As the scattering opacity is in effect the cross-section of an individual electron times the density of scattering targets, this also results in a constant neutrino scattering opacity. In contrast the nonrelativistic number density,

$$n_e^{NR} \propto \int_0^\infty \frac{p_e^2}{\exp\left(\left(p_e^2/2m_e + m_e - \mu_e\right)/T\right) + 1} \mathrm{d}p\,, \tag{A.2}$$

correctly captures the low-temperature limit of the number density as the rest mass term in the nonrelativistic dispersion relation cancels the rest mass term in the chemical potential but does not treat the intermediate regime correctly. It is therefore necessary to apply the arbitrarily relativistic formulation of the number density,

$$n_e^{AR} \propto \int_0^\infty \frac{p_e^2}{\exp\left(\left(\sqrt{p_e^2 + m_e^2} - \mu_e\right)/T\right) + 1}\,, \tag{A.3}$$

when temperatures are at 1 MeV or lower in regions of interest.

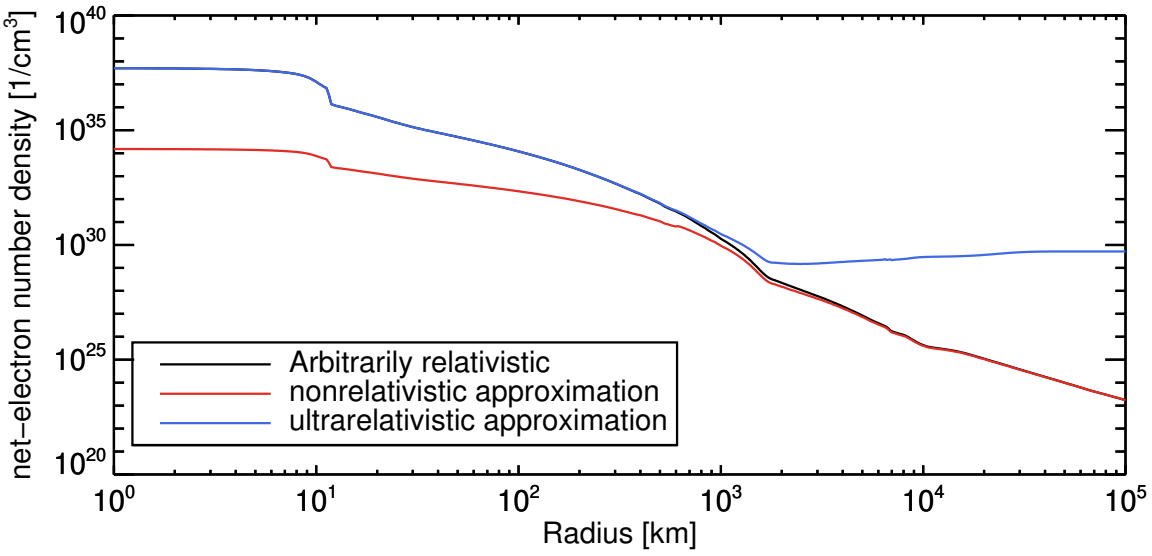

Figure A.2: Number densities of electrons as calculated using different approximations compared to physical electron number density of z9.6-LS220 model at the time of bounce. Note that arbitrarily relativistic and physical number density are identical and so only one is plotted.

In Fig. A.2 one can see that the ultrarelativistic approximation fails to accurately reproduce the physical number density Y_e at a radius of 1000 km and above, which in turn leads to a scattering opacity that is nonphysically increasing with a decreasing matter density. This leads to a nonphysical neutrino heating rate that only depends on neutrino luminosity according to roughly $Q_E^+ \propto r^2$. Depending on the density gradient of the progenitor this can lead to significant neutrino heating where neutrinos should nominally be completely decoupled

from matter. In Fig. A.3 we demonstrate the effect this has on the z9.6 progenitor structure with its very steep density falloff. The internal energy source term per baryon is seen to nonphysically increase again when the numerical electron density uncouples from the physical electron density. This can lead to significant preheating of the pre-shock matter and can in extreme cases deposit sufficient energy into the outer layers to gravitationally unbind them. This problem is especially evident in simulations of white-dwarf like stellar structures of the oxygen-neon-magnesium ECSN progenitors, e.g., refs. [97, 98], where excessive neutrino heating can lead to spontaneous fusion and deflagration of the extremely degenerate white-dwarf core mantle and atmosphere (c.f. refs. [53, 54]) before collapse due to electron capture onto neon can even proceed.

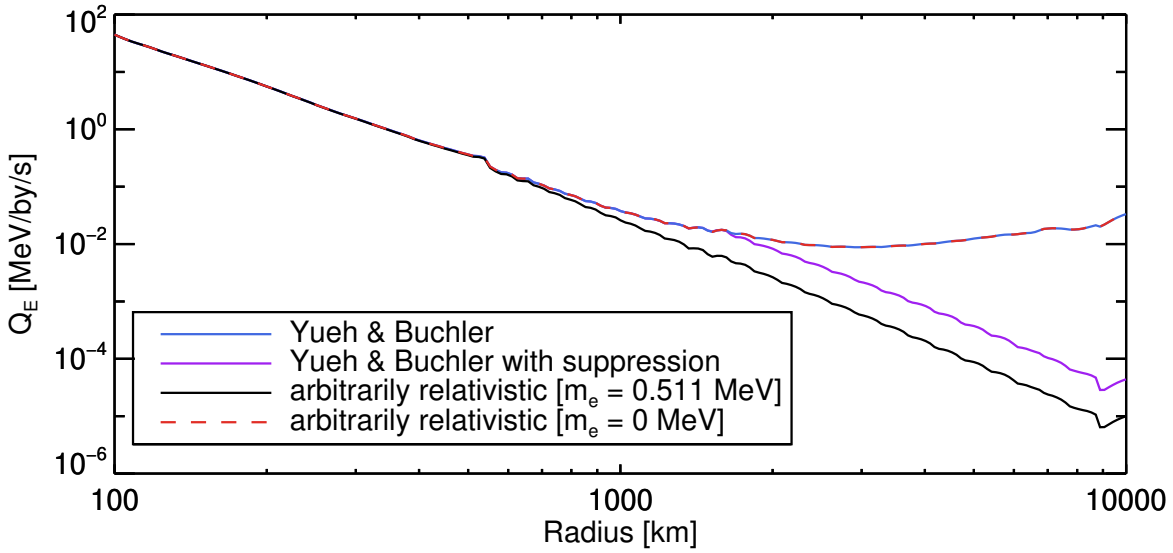

Figure A.3: Net integrated internal energy source term per baryon for z9.6 progenitor at the time of bounce. The blue line is the matter-energy source term using the Yueh&Buchler scattering kernel; The purple line is the Yueh&Buchler scattering kernel suppressed using Eq. A.4; The black line is the source term utilizing the implementation detailed in Sec. 6.1 and the dashed red line is the same implementation using mass-less electrons. Note that the plotted source term, as output from our code, contains interpolation wiggles and is only calculated up to a radius of 10000 km as that is the outer boundary of our neutrino transport grid.

A simple interim solution to this problem that resembles the true physical behavior is to extrapolate the NES inverse mean free path from the point, where the error of the ultrarelativistic integrals is still of order unity by assigning a scaling operator based on the change of the physical net neutrino number density. A small complication is the dependency of the scattering cross section on the helicity of neutrinos which is relevant for the accuracy of the $\overline{\nu}_e - e^-$ scattering opacity. This reaction is in general roughly one-third the strength of the $\nu_e - e^-$ scattering opacity for nondegenerate electrons, as demonstrated in Tubbs & Schramm (1975) Fig. 2 (ref. [133]). One therefore has to balance the accuracy of the relative $\overline{\nu}_e - e^-/\nu_e - e^-$ scattering opacity with the absolute scattering opacity. For our purposes, we have chosen a cut-off parameter $\beta_e = 4$ which gives a reasonable balance between the two. The neutrino-electron scattering opacity is then suppressed according to the following formula,

$$\phi_l^{\text{in/out}}(r, E_1, E_3) = \phi_l^{\text{in/out}}(r, E_1, E_3) \cdot \frac{n_e(r)}{n_e(\beta_e = 4)}, \tag{A.4}$$

where n_e is the local net electron density and $n_e\left(\beta_e = 4\right)$ is the net electron density at the last point where $\beta_e \leq 4$, which mimics the scaling of the scattering opacity with the number of available scattering centers under the assumption of vanishing positron density. To verify our approximate suppression factor, we plot in Fig. A.4 the scattering opacity of electron neutrinos for the ultrarelativistic case of ref. [139], our suppressed modification of ref. [139] and our arbitrarily relativistic scattering kernel of Eq. 6.1. For the sake of comparison of the integration accuracy of our arbitrarily relativistic scattering kernel, we additionally plot an opacity where we neglect the electron rest mass that reproduces the behavior of ref. [139].

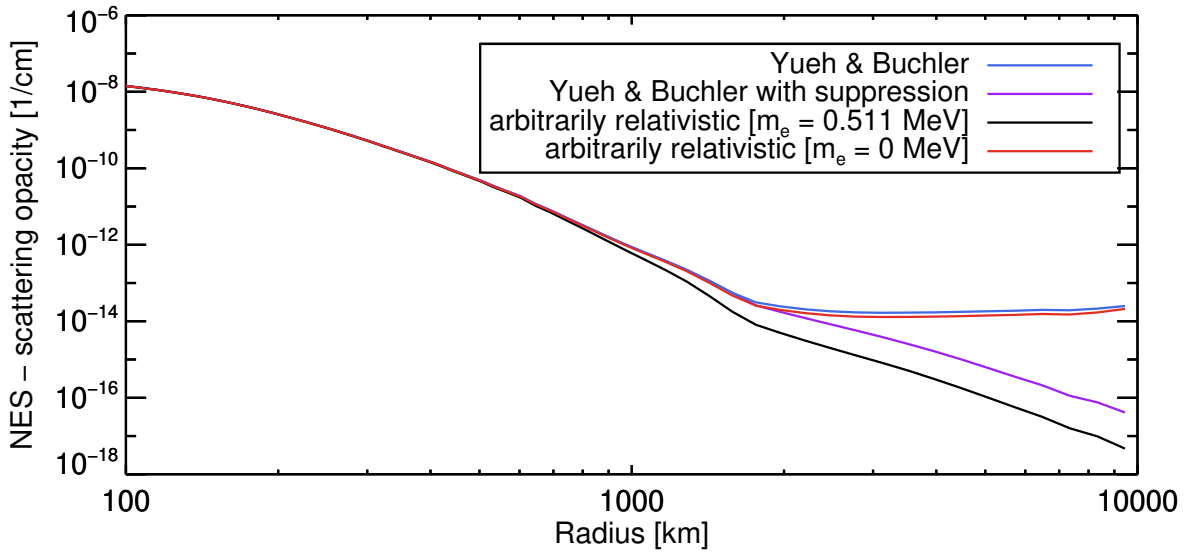

Figure A.4: Scattering opacity comparison of different kernels for z9.6 progenitor at $E_1 = 13\,\mathrm{MeV}$.

We note further that the limitations of the ultrarelativistic scattering kernel do not only apply to the particular case of very low-mass progenitors but is in general problematic for all phases of the neutrino-driven wind phase. The overestimated heating rate leads to sustained heating and entropy generation in the neutrino-driven wind as well as higher velocity of the expanding material, which can have consequences for the nucleosynthesis properties. An illustration of this behavior is shown in Fig. A.5, where the additional entropy generation caused by the ultrarelativistic approximation is visible compared to our arbitrarily relativistic kernel of Sec. 6.1. We additionally examine the resulting entropy using our artificially suppressed ultrarelativistic kernel according to Eq. A.4 and find that both the suppressed and arbitrarily relativistic kernel are in good agreement.

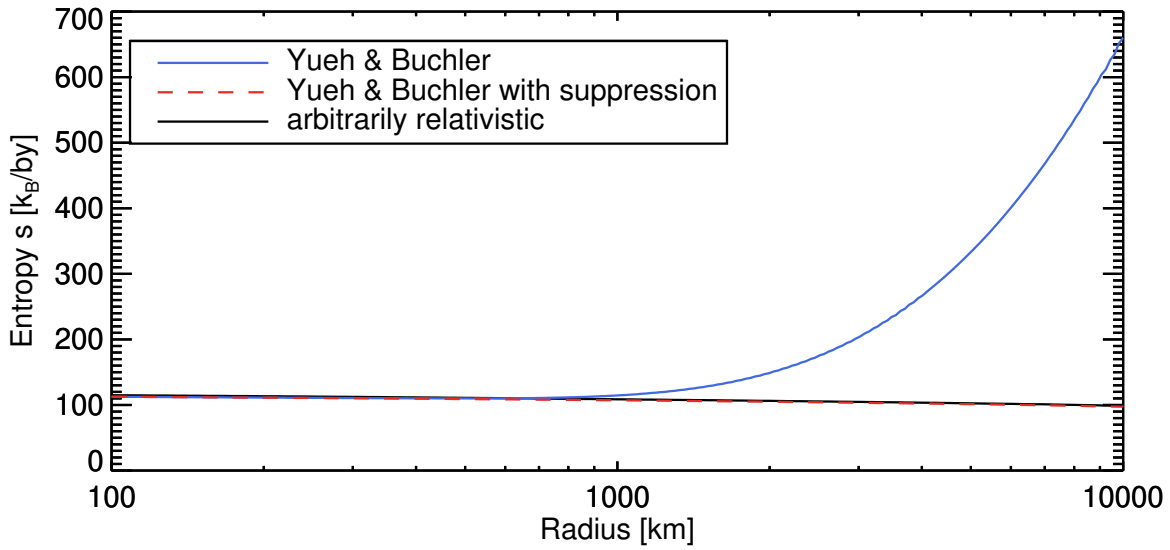

Figure A.5: Comparison plot of z9.6 progenitor matter outflow entropy in the late neutrino-driven wind phase at $t_{\mathrm{pb}} = 8.7\,s$.

References

[1] B. P. et al. Abbott, LIGO Scientific Collaboration, and Virgo Collaboration. Gw170817: Observation of gravitational waves from a binary neutron star inspiral. *Physical Review Letters*, 119(16):161101, October 2017.

[2] M. G. Alford and G. Good. Leptonic contribution to the bulk viscosity of nuclear matter. Phys. Rev. C, 82(5):055805, November 2010.

[3] J. Antoniadis, P. C. C. Freire, N. Wex, T. M. Tauris, R. S. Lynch, M. H. van Kerkwijk, M. Kramer, C. Bassa, V. S. Dhillon, T. Driebe, J. W. T. Hessels, V. M. Kaspi, V. I. Kondratiev, N. Langer, T. R. Marsh, M. A. McLaughlin, T. T. Pennucci, S. M. Ransom, I. H. Stairs, J. van Leeuwen, J. P. W. Verbiest, and D. G. Whelan. A massive pulsar in a compact relativistic binary. *Science*, 340:448, April 2013.

[4] M. Bejger, D. G. Yakovlev, and O. Y. Gnedin. Cooling of superfluid neutron stars with muons. *Acta Physica Polonica B*, 34:233, January 2003.

[5] H. A. Bethe. Supernova mechanisms. *Reviews of Modern Physics*, 62(4):801–866, October 1990.

[6] H. A. Bethe and J. R. Wilson. Revival of a stalled supernova shock by neutrino heating. *ApJ*, 295:14–23, August 1985.

[7] J. M. Blondin and A. Mezzacappa. Pulsar spins from an instability in the accretion shock of supernovae. Nature, 445:58–60, January 2007.

[8] J. M. Blondin, A. Mezzacappa, and C. DeMarino. Stability of standing accretion shocks, with an eye toward core–collapse supernovae. *ApJ*, 584(2):971–980, February 2003.

[9] R. Bollig, H.-T. Janka, A. Lohs, G. Martínez-Pinedo, C. J. Horowitz, and T. Melson. Muon creation in supernova matter facilitates neutrino-driven explosions. *Phys. Rev. Lett.*, 119(24):242702, Dec 2017.

[10] S. W. Bruenn. Stellar core collapse - numerical model and infall epoch. ApJS, 58:771–841, August 1985.

[11] S. W. Bruenn and A. Mezzacappa. Ion screening effects and stellar collapse. *Phys. Rev. D*, 56(12):7529–7547, December 1997.

[12] S. W. Bruenn, A. Mezzacappa, W. R. Hix, E. J. Lentz, O. E. B. Messer, E. J. Lingerfelt, J. M. Blondin, E. Endeve, P. Marronetti, and K. N. Yakunin. Axisymmetric ab initio core-collapse supernova simulations of 12-25 m $_\odot$ stars. ApJ, 767(1):L6, April 2013.

[13] R. Buras, H.-T. Janka, M. T. Keil, G. G. Raffelt, and M. Rampp. Electron neutrino pair annihilation: A new source for muon and tau neutrinos in supernovae. ApJ, 587:320–326, April 2003.

[14] R. Buras, M. Rampp, H.-T. Janka, and K. Kifonidis. Two-dimensional hydrodynamic core-collapse supernova simulations with spectral neutrino transport. i. numerical method and results for a 15 $m_\odot$ star. A&A, 447(3):1049–1092, March 2006.

[15] A. Burrows. Colloquium: Perspectives on core-collapse supernova theory. *Reviews of Modern Physics*, 85(1):245–261, January 2013.

[16] A. Burrows and J. M. Lattimer. The birth of neutron stars. ApJ, 307:178–196, August 1986.

[17] A. Burrows and R. F. Sawyer. Effects of correlations on neutrino opacities in nuclear matter. Phys. Rev. C, 58:554–571, July 1998.

[18] A. Burrows and R. F. Sawyer. Many-body corrections to charged-current neutrino absorption rates in nuclear matter. Phys. Rev. C, 59:510–514, January 1999.

[19] C. Chan, B. Müller, A. Heger, R. Pakmor, and V. Springel. Black hole formation and fallback during the supernova explosion of a $40\mathrm{M}_{\odot}$ star. *ArXiv e-prints*, October 2017.

[20] J. Chernohorsky. Symmetries in neutrino-electron scattering. ApJ, 433:247–249, September 1994.

[21] P. Colella and P. R. Woodward. The Piecewise Parabolic Method (PPM) for Gas-Dynamical Simulations. *Journal of Computational Physics*, 54(1):174–201, September 1984.

[22] S. A. Colgate and R. H. White. The Hydrodynamic Behavior of Supernovae Explosions. *ApJ*, 143:626–+, March 1966.

[23] S. M. Couch, E. Chatzopoulos, W. D. Arnett, and F. X. Timmes. The three-dimensional evolution to core collapse of a massive star. ApJ, 808(1):L21, July 2015.

[24] S. M. Couch and C. D. Ott. Revival of the stalled core-collapse supernova shock triggered by precollapse asphericity in the progenitor star. ApJ, 778:L7, November 2013.

[25] P. B. Demorest, T. Pennucci, S. M. Ransom, M. S. E. Roberts, and J. W. T. Hessels. A two-solar-mass neutron star measured using shapiro delay. Nature, 467:1081–1083, October 2010.

[26] D. A. Dicus. Stellar energy-loss rates in a convergent theory of weak and electromagnetic interactions. Phys. Rev. D, 6(4):941–949, August 1972.

[27] J. C. Dolence, A. Burrows, and W. Zhang. Two-dimensional core-collapse supernova models with multi-dimensional transport. ApJ, 800:10, February 2015.

[28] T. Ertl, H.-T. Janka, S. E. Woosley, T. Sukhbold, and M. Ugliano. A two-parameter criterion for classifying the explodability of massive stars by the neutrino-driven mechanism. ApJ, 818:124, February 2016.

[29] Abbott et al. Gravitational waves and gamma-rays from a binary neutron star merger: Gw170817 and grb 170817a. ApJ, 848:L13, October 2017.

[30] Abbott et al. (LIGO Scientific Collaboration and Virgo Collaboration). Estimating the contribution of dynamical ejecta in the kilonova associated with gw170817. ApJ, 850:L39, December 2017.

[31] A. L. Fetter and J. D. Walecka. *Quantum theory of many-particle systems*. 1971.

[32] T. Fischer, M. Hempel, I. Sagert, Y. Suwa, and J. Schaffner-Bielich. Symmetry energy impact in simulations of core-collapse supernovae. *European Physical Journal A*, 50:46, February 2014.

[33] T. Fischer, G. Martínez-Pinedo, M. Hempel, L. Huther, G. Röpke, S. Typel, and A. Lohs. Expected impact from weak reactions with light nuclei in corecollapse supernova simulations. In W.-P. Liu, Z.-H. Li, Y.-B. Wang, B. Guo, and Y.-P. Shen, editors, *European Physical Journal Web of Conferences*, volume 109 of *European Physical Journal Web of Conferences*, page 06002. EDP Sciences, February 2016.

[34] T. Fischer, S. C. Whitehouse, A. Mezzacappa, F.-K. Thielemann, and M. Liebendörfer. The neutrino signal from protoneutron star accretion and black hole formation. A&A, 499:1–15, May 2009.

[35] T. Fischer, S. C. Whitehouse, A. Mezzacappa, F.-K. Thielemann, and M. Liebendörfer. Protoneutron star evolution and the neutrino-driven wind in general relativistic neutrino radiation hydrodynamics simulations. A&A, 517:A80, July 2010.

[36] T. Foglizzo. Non–radial instabilities of isothermal Bondi accretion with a shock: Vortical–acoustic cycle vs. post–shock acceleration. *A&A*, 392(1):353–368, September 2002.

[37] T. Foglizzo, R. Kazeroni, J. Guilet, F. Masset, M. González, B. K. Krueger, J. Novak, M. Oertel, J. Margueron, J. Faure, N. Martin, P. Blottiau, B. Peres, and G. Durand. The explosion mechanism of core-collapse supernovae: Progress in supernova theory and experiments. PASA, 32:e009, March 2015.

[38] B.A. Fryxell, E. Müller, and W.D. Arnett. Hydrodynamics and nuclear burning. preprint MPA–449, Max Planck Institut für Astrophysik, Garching, apr 1989.

[39] F. Hanke, A. Marek, B. Müller, and H.-T. Janka. Is strong sasi activity the key to successful neutrino-driven supernova explosions? ApJ, 755:138, August 2012.

[40] F. Hanke, B. Müller, A. Wongwathanarat, A. Marek, and H.-T. Janka. Sasi activity in three-dimensional neutrino-hydrodynamics simulations of supernova cores. ApJ, 770:66, June 2013.

[41] Florian Hanke. *Two- and Three-Dimensional Simulations of Core-Collapse Supernova Explosions of Massive Stars Applying Neutrino Hydrodynamics*. PhD thesis, Technische Universität München, 2014.

[42] S. Hannestad and G. Raffelt. Supernova neutrino opacity from nucleon-nucleon bremsstrahlung and related processes. ApJ, 507(1):339–352, November 1998.

[43] M. Hempel, T. Fischer, J. Schaffner-Bielich, and M. Liebendörfer. New equations of state in simulations of core-collapse supernovae. ApJ, 748:70, March 2012.

[44] M. Hempel and J. Schaffner-Bielich. A statistical model for a complete supernova equation of state. *Nuclear Physics A*, 837:210–254, June 2010.

[45] T. J. Hobbs, M. Alberg, and G. A. Miller. Role of nucleon strangeness in supernova explosions. Phys. Rev. C, 93(5):052801, May 2016.

[46] C. J. Horowitz. Neutrino trapping in a supernova and the screening of weak neutral currents. *Phys. Rev. D*, 55(8):4577–4581, April 1997.

[47] C. J. Horowitz. Weak magnetism for antineutrinos in supernovae. Phys. Rev. D, 65(4):043001, February 2002.

[48] C. J. Horowitz, D. K. Berry, M. E. Caplan, T. Fischer, Z. Lin, W. G. Newton, E. O'Connor, and L. F. Roberts. Nuclear pasta and supernova neutrinos at late times. *ArXiv e-prints*, November 2016.

[49] C. J. Horowitz, E. F. Brown, Y. Kim, W. G. Lynch, R. Michaels, A. Ono, J. Piekarewicz, M. B. Tsang, and H. H. Wolter. A way forward in the study of the symmetry energy: experiment, theory, and observation. *Journal of Physics G Nuclear Physics*, 41(9):093001, September 2014.

[50] C. J. Horowitz, O. L. Caballero, Z. Lin, E. O'Connor, and A. Schwenk. Neutrino-nucleon scattering in supernova matter from the virial expansion. Phys. Rev. C, 95(2):025801, February 2017.

[51] C. J. Horowitz and G. Li. The mu and tau number of supernovae. *Physics Letters B*, 443:58–62, December 1998.

[52] C. J. Horowitz and K. Wehrberger. Neutrino interactions in a dense plasma. *Physical Review Letters*, 66(3):272–275, January 1991.

[53] L. Hüdepohl, B. Müller, H.-T. Janka, A. Marek, and G. G. Raffelt. Neutrino signal of electron-capture supernovae from core collapse to cooling. *Physical Review Letters*, 104(25):251101, June 2010.

[54] Lorenz Hüdepohl. personal communication.

[55] Lorenz Hüdepohl. *Neutrinos from the Formation, Cooling, and Black Hole Collapse of Neutron Stars*. Dissertation, Technische Universität München, München, 2014.

[56] C. Ishizuka, A. Ohnishi, K. Tsubakihara, K. Sumiyoshi, and S. Yamada. Tables of hyperonic matter equation of state for core-collapse supernovae. *Journal of Physics G Nuclear Physics*, 35(8):085201, August 2008.

[57] H.-T. Janka. Explosion mechanisms of core-collapse supernovae. *Annual Review of Nuclear and Particle Science*, 62(1):407–451, November 2012.

[58] H.-T. Janka, T. Melson, and A. Summa. Physics of core-collapse supernovae in three dimensions: A sneak preview. *Annual Review of Nuclear and Particle Science*, 66:341–375, October 2016.

[59] H.-Th. Janka. unpublished, 1999.

[60] O. Just, A. Bauswein, R. Ardevol Pulpillo, S. Goriely, and H.-T. Janka. Comprehensive nucleosynthesis analysis for ejecta of compact binary mergers. MNRAS, 448:541–567, March 2015.

[61] O. Just, M. Obergaulinger, and H.-T. Janka. A new multidimensional, energy-dependent two-moment transport code for neutrino-hydrodynamics. MNRAS, 453(4):3386–3413, November 2015.

[62] W. Keil. *Konvektive Instabilitäten in entstehenden Neutronensternen*. PhD thesis, Technische Universität München, 1997.

[63] W. Keil, H.-T. Janka, and E. Mueller. Ledoux Convection in Protoneutron Stars—A Clue to Supernova Nucleosynthesis? ApJ, 473:L111, December 1996.

[64] K. Kifonidis, T. Plewa, H.-Th. Janka, and E. Müller. Non–spherical core collapse supernovae. I. Neutrino–driven convection, Rayleigh–Taylor instabilities, and the formation and propagation of metal clumps. *A&A*, 408(2):621–649, September 2003.

[65] Kurt Siegfried Kölbig, JA Mignaco, and E Remiddi. On nielsen's generalized polylogarithms and their numerical calculation. *BIT Numerical Mathematics*, 10(1):38–73, 1970.

[66] R. H. Kraichnan. Inertial ranges in two-dimensional turbulence. *Physics of Fluids*, 10(7):1417–1423, July 1967.

[67] T. Kuroda, T. Takiwaki, and K. Kotake. Gravitational wave signatures from low-mode spiral instabilities in rapidly rotating supernova cores. Phys. Rev. D, 89(4):044011, February 2014.

[68] K. Langanke, G. Martínez–Pinedo, J. M. Sampaio, D. J. Dean, W. R. Hix, O. E. Messer, A. Mezzacappa, M. Liebendörfer, H.-Th. Janka, and M. Rampp. Electron capture rates on nuclei and implications for stellar core collapse. *Physical Review Letters*, 90(24):241102–+, June 2003.

[69] K. Langanke, G. Martínez-Pinedo, B. Müller, H.-T. Janka, A. Marek, W. R. Hix, A. Juodagalvis, and J. M. Sampaio. Effects of Inelastic Neutrino-Nucleus Scattering on Supernova Dynamics and Radiated Neutrino Spectra. *Physical Review Letters*, 100(1):011101–+, January 2008.

[70] J. M. Lattimer and F. Douglas Swesty. A generalized equation of state for hot, dense matter. *Nuclear Physics A*, 535(2):331–376, December 1991.

[71] E. J. Lentz, S. W. Bruenn, W. R. Hix, A. Mezzacappa, O. E. B. Messer, E. Endeve, J. M. Blondin, J. A. Harris, P. Marronetti, and K. N. Yakunin. Three-dimensional core-collapse supernova simulated using a 15 m $_{\odot}$ progenitor. ApJ, 807:L31, July 2015.

[72] M. Liebendörfer, O. E. B. Messer, A. Mezzacappa, S. W. Bruenn, C. Y. Cardall, and F.-K. Thielemann. A finite difference representation of neutrino radiation hydrodynamics in spherically symmetric general relativistic spacetime. ApJS, 150:263–316, January 2004.

[73] A. Lohs, G. Martínez-Pinedo, and T. Fischer. Charged current interactions of numu neutrinos in supernova. In *XIII Nuclei in the Cosmos (NIC XIII)*, page 118, 2014.

[74] Andreas Lohs. personal communication.

[75] Andreas Lohs. *Neutrino Reactions in Hot and Dense Matter*. PhD thesis, Technische Universität Darmstadt, Darmstadt, Februar 2015.

[76] D. Lonardoni, A. Lovato, S. Gandolfi, and F. Pederiva. Hyperon puzzle: Hints from quantum monte carlo calculations. *Physical Review Letters*, 114(9):092301, March 2015.

[77] A. Marek, H. Dimmelmeier, H.-T. Janka, E. Müller, and R. Buras. Exploring the relativistic regime with newtonian hydrodynamics: an improved effective gravitational potential for supernova simulations. A&A, 445:273–289, January 2006.

[78] A. Marek, H.-T. Janka, R. Buras, M. Liebendörfer, and M. Rampp. On ion-ion correlation effects during stellar core collapse. A&A, 443:201–210, November 2005.

[79] A. Marek, H.-T. Janka, and E. Müller. Equation-of-state dependent features in shock-oscillation modulated neutrino and gravitational-wave signals from supernovae. A&A, 496:475–494, March 2009.

[80] B. Margalit and B. D. Metzger. Constraining the maximum mass of neutron stars from multi-messenger observations of gw170817. ApJ, 850:L19, December 2017.

[81] G. Martínez-Pinedo, T. Fischer, A. Lohs, and L. Huther. Charged-current weak interaction processes in hot and dense matter and its impact on the spectra of neutrinos emitted from protoneutron star cooling. *Physical Review Letters*, 109(25):251104, December 2012.

[82] J. McDougall and E. C. Stoner. The computation of fermi-dirac functions. *Philosophical Transactions of the Royal Society of London Series A*, 237(773):67–104, February 1938.

[83] T. Melson, H.-T. Janka, R. Bollig, F. Hanke, A. Marek, and B. Müller. Neutrino-driven explosion of a 20 solar-mass star in three dimensions enabled by strange-quark contributions to neutrino-nucleon scattering. ApJ, 808(2):L42, August 2015.

[84] T. Melson, H.-T. Janka, and A. Marek. Neutrino-driven supernova of a low-mass iron-core progenitor boosted by three-dimensional turbulent convection. ApJ, 801(2):L24, March 2015.

[85] Tobias Fabian Melson. *Modeling neutrino-driven core-collapse supernova explosions in three dimensions*. Dissertation, Technische Universität München, München, 2016.

[86] A. Mezzacappa and S. W. Bruenn. Stellar core collapse - a boltzmann treatment of neutrino-electron scattering. ApJ, 410:740–760, June 1993.

[87] D. Mihalas and B.W. Mihalas. *Foundations of Radiation Hydrodynamics*. Oxford University Press, 1984.

[88] A. Mirizzi, I. Tamborra, H.-T. Janka, N. Saviano, K. Scholberg, R. Bollig, L. Hüdepohl, and S. Chakraborty. Supernova neutrinos: production, oscillations and detection. *Nuovo Cimento Rivista Serie*, 39:1–112, 2016.

[89] Peter J. Mohr, David B. Newell, and Barry N. Taylor. CODATA recommended values of the fundamental physical constants: 2014. *Reviews of Modern Physics*, 88(3), sep 2016.

[90] B. Müller. The dynamics of neutrino-driven supernova explosions after shock revival in 2d and 3d. MNRAS, 453:287–310, October 2015.

[91] B. Müller. The status of multi-dimensional core-collapse supernova models. PASA, 33:e048, September 2016.

[92] B. Müller and H.-T. Janka. Non-radial instabilities and progenitor asphericities in core-collapse supernovae. MNRAS, 448:2141–2174, April 2015.

[93] B. Müller, H.-T. Janka, and H. Dimmelmeier. A New Multi-dimensional General Relativistic Neutrino Hydrodynamic Code for Core-collapse Supernovae. I. Method and Code Tests in Spherical Symmetry. *ApJs*, 189:104–133, July 2010.

[94] B. Müller, T. Melson, A. Heger, and H.-T. Janka. Supernova simulations from a 3d progenitor model - impact of perturbations and evolution of explosion properties. MNRAS, 472:491–513, November 2017.

[95] B. Müller, M. Viallet, A. Heger, and H.-T. Janka. The last minutes of oxygen shell burning in a massive star. ApJ, 833:124, December 2016.

[96] K. Nakamura, T. Kuroda, T. Takiwaki, and K. Kotake. Impacts of rotation on three-dimensional hydrodynamics of core-collapse supernovae. ApJ, 793:45, September 2014.

[97] K. Nomoto. Evolution of 8-10 solar mass stars toward electron capture supernovae. i - formation of electron-degenerate o + ne + mg cores. ApJ, 277:791–805, February 1984.

[98] K. Nomoto. Evolution of 8-10 solar mass stars toward electron capture supernovae. ii - collapse of an o + ne + mg core. ApJ, 322:206–214, November 1987.

[99] E. O'Connor and S. Couch. Two dimensional core-collapse supernova explosions aided by general relativity with multidimensional neutrino transport. *ArXiv e-prints*, November 2015.

[100] E. O'Connor and C. D. Ott. Black hole formation in failing core-collapse supernovae. ApJ, 730:70, April 2011.

[101] M. Oertel, A. F. Fantina, and J. Novak. Extended equation of state for core-collapse simulations. Phys. Rev. C, 85(5):055806, May 2012.

[102] M. Oertel, F. Gulminelli, C. Providência, and A. R. Raduta. Hyperons in neutron stars and supernova cores. *European Physical Journal A*, 52:50, March 2016.

[103] M. Oertel, M. Hempel, T. Klähn, and S. Typel. Equations of state for supernovae and compact stars. *Reviews of Modern Physics*, 89(1):015007, January 2017.

[104] C. D. Ott, L. F. Roberts, A. da Silva Schneider, J. M. Fedrow, R. Haas, and E. Schnetter. The progenitor dependence of three-dimensional core-collapse supernovae. *ArXiv e-prints*, December 2017.

[105] K.-C. Pan, M. Liebendörfer, M. Hempel, and F.-K. Thielemann. Two-dimensional core-collapse supernova simulations with the isotropic diffusion source approximation for neutrino transport. ApJ, 817:72, January 2016.

[106] A. Perego, M. Hempel, C. Fröhlich, K. Ebinger, M. Eichler, J. Casanova, M. Liebendörfer, and F.-K. Thielemann. Pushing core-collapse supernovae to explosions in spherical symmetry i: the model and the case of sn 1987a. ApJ, 806:275, June 2015.

[107] B. Peres, M. Oertel, and J. Novak. Influence of pions and hyperons on stellar black hole formation. Phys. Rev. D, 87(4):043006, February 2013.

[108] J. A. Pons, J. A. Miralles, and J. M. Ibanez. Legendre expansion of the neutrino - anti-neutrino <—> e+ e- kernel: Influence of high order terms. *Astron. Astrophys. Suppl. Ser.*, 129:343, 1998.

[109] M. Prakash, I. Bombaci, M. Prakash, P. J. Ellis, J. M. Lattimer, and R. Knorren. Composition and structure of protoneutron stars. Phys. Rep., 280:1–77, 1997.

[110] D. Radice, E. Abdikamalov, C. D. Ott, P. Moesta, S. M. Couch, and L. F. Roberts. Turbulence in core-collapse supernovae. *ArXiv e-prints*, October 2017.

[111] D. Radice, A. Burrows, D. Vartanyan, M. A. Skinner, and J. C. Dolence. Electron-Capture and Low-Mass Iron-Core-Collapse Supernovae: New Neutrino-Radiation-Hydrodynamics Simulations. *ArXiv e-prints*, February 2017.

[112] D. Radice, C. Ott, E. Abdikamalov, S. Couch, R. Haas, and E. Schnetter. Neutrino-driven turbulent convection in stalled supernova cores. In *APS April Meeting Abstracts*, April 2015.

[113] G. G. Raffelt. Mu- and tau-neutrino spectra formation in supernovae. ApJ, 561:890–914, November 2001.

[114] M. Rampp and H.-T. Janka. Radiation hydrodynamics with neutrinos. variable eddington factor method for core-collapse supernova simulations. A&A, 396:361–392, December 2002.

[115] S. Reddy, M. Prakash, and J. M. Lattimer. Neutrino interactions in hot and dense matter. Phys. Rev. D, 58(1):013009, July 1998.

[116] S. Reddy, M. Prakash, J. M. Lattimer, and J. A. Pons. Effects of strong and electromagnetic correlations on neutrino interactions in dense matter. Phys. Rev. C, 59:2888–2918, May 1999.

[117] L. F. Roberts, C. D. Ott, R. Haas, E. P. O'Connor, P. Diener, and E. Schnetter. General-relativistic three-dimensional multi-group neutrino radiation-hydrodynamics simulations of core-collapse supernovae. ApJ, 831:98, November 2016.

[118] L. F. Roberts and S. Reddy. Charged current neutrino interactions in hot and dense matter. *ArXiv e-prints*, December 2016.

[119] L. F. Roberts and S. Reddy. Neutrino signatures from young neutron stars. *ArXiv e-prints*, December 2016.

[120] L. F. Roberts, S. Reddy, and G. Shen. Medium modification of the charged-current neutrino opacity and its implications. Phys. Rev. C, 86(6):065803, December 2012.

[121] P. J. Schinder. Exact expressions and improved approximations for interaction rates of neutrinos with free nucleons in a high-temperature, high-density gas. ApJS, 74:249–273, September 1990.

[122] P. J. Schinder and S. L. Shapiro. Neutrino emission from a hot, dense, plane-parallel atmosphere in hydrostatic equilibrium. II - Numerical methods and interaction functions. *ApJs*, 50:23–37, September 1982.

[123] A. W. Steiner, M. Hempel, and T. Fischer. Core-collapse supernova equations of state based on neutron star observations. ApJ, 774:17, September 2013.

[124] A. W. Steiner, M. Prakash, J. M. Lattimer, and P. J. Ellis. Isospin asymmetry in nuclei and neutron stars [review article]. Phys. Rep., 411:325–375, June 2005.

[125] C. Sullivan, E. O'Connor, R. G. T. Zegers, T. Grubb, and S. M. Austin. The sensitivity of core-collapse supernovae to nuclear electron capture. ApJ, 816:44, January 2016.

[126] K. Sumiyoshi and S. Yamada. Neutrino transfer in three dimensions for core-collapse supernovae. i. static configurations. ApJS, 199:17, March 2012.

[127] A. Summa, F. Hanke, H.-T. Janka, T. Melson, A. Marek, and B. Müller. Progenitor-dependent explosion dynamics in self-consistent, axisymmetric simulations of neutrino-driven core-collapse supernovae. ApJ, 825:6, July 2016.

[128] A. Summa, H.-T. Janka, T. Melson, and A. Marek. Rotation-supported neutrino-driven supernova explosions in three dimensions and the critical luminosity condition. *ArXiv e-prints*, August 2017.

[129] K. Takahashi, M. F. El Eid, and W. Hillebrandt. Beta transition rates in hot and dense matter. A&A, 67:185–197, July 1978.

[130] T. Takiwaki, K. Kotake, and Y. Suwa. A comparison of two- and three-dimensional neutrino-hydrodynamics simulations of core-collapse supernovae. ApJ, 786:83, May 2014.

[131] T. Takiwaki, K. Kotake, and Y. Suwa. Three-dimensional simulations of rapidly rotating core-collapse supernovae: finding a neutrino-powered explosion aided by non-axisymmetric flows. MNRAS, 461:L112–L116, September 2016.

[132] F. X. Timmes and D. Arnett. The accuracy, consistency, and speed of five equations of state for stellar hydrodynamics. ApJS, 125(1):277–294, November 1999.

[133] D. L. Tubbs and D. N. Schramm. Neutrino astrophysics at high temperatures and densities. In *Bulletin of the American Astronomical Society*, volume 7 of BAAS, page 546, September 1975.

[134] J. Vollinga and S. Weinzierl. Numerical evaluation of multiple polylogarithms. *Computer Physics Communications*, 167:177–194, May 2005.

[135] S. Wanajo, Y. Sekiguchi, N. Nishimura, K. Kiuchi, K. Kyutoku, and M. Shibata. Production of all the r-process nuclides in the dynamical ejecta of neutron star mergers. ApJ, 789:L39, July 2014.

[136] S. E. Woosley and A. Heger. Nucleosynthesis and remnants in massive stars of solar metallicity. Phys. Rep., 442:269–283, April 2007.

[137] S. E. Woosley and A. Heger. The remarkable deaths of 9-11 solar mass stars. ApJ, 810:34, September 2015.

[138] S. E. Woosley, A. Heger, and T. A. Weaver. The evolution and explosion of massive stars. *Reviews of Modern Physics*, 74(4):1015–1071, November 2002.

[139] W. R. Yueh and J. R. Buchler. Neutrino processes in dense matter. Ap&SS, 41(1):221–251, May 1976.